# Electron Bernstein Wave Current Drive Modeling in Toroidal Plasma Confinement

by

Joan Decker

Master of Science in Electrical Engineering and Computer Science
Massachusetts Institute of Technology (2002)

Ingénieur Diplômé de l'Ecole Polytechnique
Ecole Polytechnique, Palaiseau, France (2000)



Submitted to the Department of
Electrical Engineering and Computer Science
in partial fulfillment of the requirements for the degree of

Doctor of Philosophy

at the

MASSACHUSETTS INSTITUTE OF TECHNOLOGY

June 2005



Author .....
Department of
Electrical Engineering and Computer Science
May 19, 2005

Certified by .....
Abraham Bers
Professor of Electrical Engineering and Computer Science
Thesis Supervisor

Accepted by ... .....
Arthur C. Smith
Chairman, Department Committee on Graduate Students

# Electron Bernstein Wave Current Drive Modeling in Toroidal Plasma Confinement

by Joan Decker

Submitted to the Department of
Electrical Engineering and Computer Science
on May 20, 2005, in partial fulfillment of the
requirements for the degree of Doctor of Philosophy

## Abstract

The steady-state confinement of tokamak plasmas in a fusion reactor requires non-inductively driven toroidal currents. Radio frequency waves in the electron cyclotron (EC) range of frequencies can drive localized currents and are thus particularly attractive for control of the current profile. In the high-$\beta$ regimes of spherical tokamaks (ST) such as NSTX and MAST, heating and current drive (CD) by conventional electron cyclotron waves is not possible. However, electron Bernstein waves (EBW) have been proposed as an alternative for CD in these overdense devices. Given the important role predicted for CD by EBWs in high-$\beta$ STs, a detailed study of EBWCD must be undertaken.

In this thesis a systematic analysis of EBWCD is provided. In particular, the characteristics of EBWs, the physics of resonant wave-particle interaction, and the CD mechanisms are investigated in detail. The CD efficiency and the current deposition profile are calculated using the numerical code *DKE*, which solve the drift-kinetic equation. Two scenarios for EBWCD are identified. The first scenario consists of approaching a harmonic of the EC resonance from a lower $B$-field region and drives current in the plasma core using the Fisch-Boozer mechanism. The other scenario consists of approaching a harmonic of the EC resonance from a higher $B$-field region and drives current off-axis on the outboard side using the Ohkawa mechanism. Both schemes drive current in the toroidal direction opposite to the parallel wave vector. The EBWCD efficiency is found to be higher than ECCD efficiency because the EBW power is deposited in the tail of the electron distribution function. The results of this thesis confirm the important role of EBWs for driving currents in high-$\beta$ plasmas.

The analytical and numerical tools developed as part of this thesis can be used to design, predict, and analyze future EBWCD experiments. Among these tools is the kinetic solver *DKE*, which can be used for electron current drive calculations in toroidal plasmas for different types of radio-frequency waves, such as lower hybrid and electron cyclotron waves.

Thesis Supervisor: Abraham Bers
Title: Professor of Electrical Engineering and Computer Science

# Acknowledgments

I would like to thank my research supervisor, Abraham Bers, for giving me the opportunity to work in plasma physics on the exciting topics of plasma waves and current drive. In particular, I am grateful to him for initiating and encouraging the collaboration with Dr. Yves Peysson from the CEA-Cadarache center in France. Yves has been a fantastic research mentor and partner, and the numerical kinetic code *DKE* is the major accomplishment of our common work. Our collaboration - and friendship - has grown stronger with time despite the distance, and I am happily joining him in Cadarache for a post-doc to continue this exciting research. I am also very grateful to Dr. Abhay Ram, whose guidance and insight have greatly helped me in this thesis work. I will miss our long discussions and heated debates, and remember his kindness.

These five years spent in Cambridge have changed my life. Here I have met my wife, Philippa, and a number of friends that I will miss greatly. Thanks to Anastassia, Andrea, Anukool, Athicha, Craig C., Craig R., Flo, Guy, Jeremy, Ludo, Maya, Mary Lee, Markus, Rahul, Richard, Sonya, Suzuko, Thien-Loc and Vadim for making my stay here such a enjoyable experience.

# Contents

# List of Figures

# List of Tables

# Chapter 1

# Introduction and Background

## 1.1 Motivation, Objectives and Outline

### 1.1.1 Motivation

Electron Bernstein Waves (EBW) have been theoretically predicted [1] and experimentally identified [2] more than forty years ago. Recently [3] [4] [5], they have received much consideration for heating and current drive (CD) in spherical tokamaks (ST) such as NSTX, MAST and CDX-U.

STs are small aspect ratio toroidal devices that differ from conventional tokamaks by their ability to achieve high-$\beta$ regimes, where $\beta = 2\mu_0 \langle p \rangle / B^2$ is the ratio of the kinetic pressure to the magnetic pressure ($\langle p \rangle$ is the volume-averaged pressure and $B$ is the toroidal magnetic field on axis). In complement to the large bootstrap current (BC) fraction expected in these high-$\beta$ plasmas, sustaining a steady-state operation in STs requires one to drive non-inductive currents. For that matter, radio-frequency (RF) CD in the electron-cyclotron (EC) range of frequency is particularly attractive because of its ability to drive very localized currents, and thus to provide an accurate control of the $q$-profile and a means to stabilize MHD modes such as neoclassical tearing modes [6].

However, high-$\beta$ plasmas in STs are typically very overdense, meaning that the electron plasma frequency $\omega_{pe}$ is several times larger than the electron cyclotron fre-

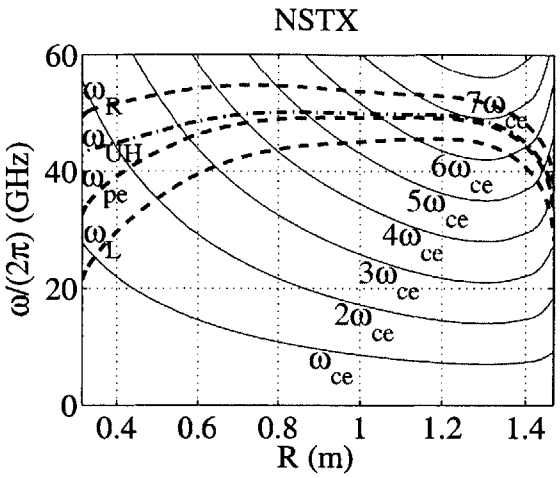


Figure 1-1: Radial profile of characteristic frequencies in a NSTX high-$\beta$ plasma. Solid lines correspond to harmonics of the EC frequency, while dashed lines represent the R, O and L cut-off frequencies $\omega_R$, $\omega_{pe}$, and $\omega_L$ respectively. The dash-dotted line shows the upper-hybrid frequency $\omega_{UH}$.

quency $\omega_{ce}$, except near the edge of the plasma. In that case, heating and current drive by electromagnetic EC waves (O- and/or X-mode), which have been used extensively in low-$\beta$ tokamaks, becomes very difficult because ECWs can propagate only above the cut-off frequencies $\omega_R$ (X-mode) and $\omega_{pe}$ (O-mode), several times above the cyclotron harmonics. Unfortunately, ECWs experience little if any damping at high harmonics of the cyclotron frequency. To illustrate these observations, a radial profile of characteristic frequencies in a overdense high-$\beta$ NSTX plasma is shown in Fig. 1-1.

However, lower frequency ECWs can be mode-converted to EBWs at the upper-hybrid resonance (UHR) near the edge [7] [8], and EBWs can propagate into the overdense plasma at frequencies below the electromagnetic cut-offs. In addition, they are completely damped at any harmonic of the cyclotron frequency [8].

Although EBWCD has been demonstrated in toroidally confined fusion plasmas [9] [10] and numerical prediction of EBWCD can be found in the litterature [11] [10] [12], no systematic description of EBWCD has been given. Given the important role predicted for EBWCD in high-$\beta$ STs, a thorough understanding of EBWCD

mechanisms and an extensive calculation of CD efficiency and localization are much needed. In addition, analytical and numerical tools must be developped in order to design and analyze future EBW experiments.

### 1.1.2 Objectives

The goal of this thesis is to provide an extensive analysis and understanding of EBWCD. I will identify the possible scenarios and mechanisms of EBWCD. For each of the two EBWCD scenarios considered in this work, I will study the parametric dependence of the current drive localization and efficiency. Several ways to optimize the CD efficiency will be discussed. The possible locations of EBWCD and the extent of the current deposition region will be calculated. More generally, I will investigate the robustness of EBWCD with respect to variations in plasma and wave parameters.

A systemetic calculation of EBWCD requires to study extensively the properties of EBWs and the kinetic calculation of RFCD in toroidal plasmas, with numerical developments. These topics are addressed in separate chapters of the thesis, which are fairly independent and could be used in different areas of research.

In addition, the set of analytical and numerical tools developed in this thesis could be used to design, predict and analyze EBWCD experiments.

The present work focuses on high-$\beta$ STs, because the possible role of EBWCD in these devices is clearly apparent, and because the particular magnetic geometry of high-$\beta$ STs is suitable to study different scenarios for EBWCD. However, most of the results and analyses are also applicable to other overdense toroidal plasmas in a magnetic field. In particular, EBWCD could also be an attractive method for CD in high-$\beta$ conventional tokamaks.

### 1.1.3 Outline

In the rest of this introductory chapter, I outline a more general approach to the EBWCD problem, and give a review, with historical perspective, of the research on EBW excitation, description of wave-particle interaction and numerical calculations

of RFCD. Then, the particular magnetic geometry of high-$\beta$ STs is introduced, and two possible EBWCD scenarios in STs, schematically illustrated on Fig. 1-2, are proposed (Section 1.3):

- The low $B$-field (LBF) approach, in which the EBW (with frequency $\omega$) approaches the $n^{\text{th}}$ cyclotron harmonic resonance from a lower field region ($n\omega_{ce} < \omega$), and which typically takes place in the core of the plasma.
- The high $B$-field (HBF) approach, in which the EBW approaches the $n^{\text{th}}$ cyclotron harmonic resonance from a higher field region ($n\omega_{ce} > \omega$), and which typically takes place off-axis on the outboard side of the plasma.

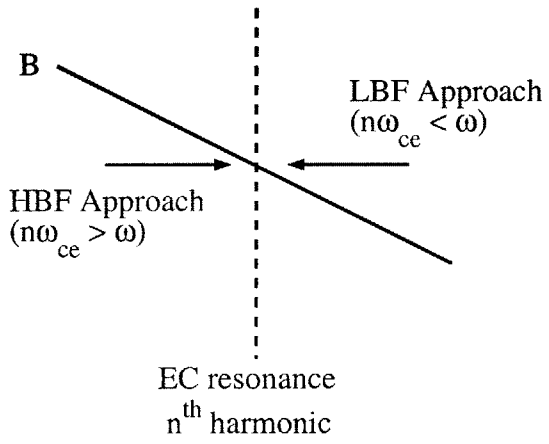


Figure 1-2: Illustration of the LBF and HBF schemes.

In Chapter 2, the characteristics of EBWs are studied in details. Because EBWs are kinetic waves that do not exist in the cold plasma description, the basic concepts of the linear kinetic theory of waves are reviewed (Section 2.1). This theory is applied specifically to EBWs in the electrostatic approximation (Section 2.2), which allows one to carry approximate analytical calculations of EBW characteristics, thus providing useful insight on the behavior of EBW. In particular, characteristics of EBWs in the vicinity of cyclotron harmonic resonances are very different depending on whether the resonance is approached from a LBF or a HBF region. Then, in Section 2.3, the

exact dispersion relation for EBWs is solved using the numerical dispersion solver *R2D2* developed by A.K. Ram [13], and the relevant wave parameters for studing EBWCD are calculated.

Current drive by radio-frequency (RF) waves, such as EBWs, results from the combined effects of three physical mechanisms:

- The resonant interaction between the waves and particles in the plasma. In the case of high frequency waves in the electron cyclotron range of frequencies, such as EBWs, the interaction is between the waves and electrons.
- The collisions between particles, which involve energy and momentum exchange.
- The motion of particles in the toroidal magnetic field, including effects of trapped particle orbits and particle drifts.

Although the motion of particles and the interaction with RF waves can generally be described from the perspective of a single particle moving in an electromagnetic field, the essential role of collisions requires a collective description of the plasma, such as provided by kinetic theory, which we adopt in the present work. The motion of electrons in a toroidal magnetic plasma, the wave-particle interaction, and the collisions between particles are described in Chapter 3 where the appropriate electron kinetic equation including these three mechanisms is derived. This equation accounts for the particle radial drifts, which generate the bootstrap current. Therefore, RFCD and the bootstrap current are kinetically calculated self-consistently, and possible synergistic effects can be investigated.

This equation can only be solved numerically, and a kinetic code, named *DKE*, was developed in close collaboration with Yves Peysson from CEA-Cadarache, France, to solve the electron kinetic equation and calculate the distribution function describing electrons in a toroidal plasma in the presence of collisions, interaction with RF waves, and the particles radial drifts that generate the bootstrap current. This code and its application to solving the kinetic equation for EBWCD are described in Chapter 4.

EBWCD calculations are presented in Chapter 5. The mechanisms of the interaction between EBWs and electrons are studied in detail and the EBW power deposition

is calculated. This description is used to analyze the results of CD calculations, which are presented separately for the two EBWCD scenarios (LBF and HBF approach).

## 1.2 Introduction to Electron Bernstein Wave Current Drive

The problem of modeling current drive by RF waves can be generally divided into three main aspects:

- *Excitation from a launching structure*, such as waveguides, antennas and mirrors. One investigates the launching efficiency (what fraction of the incoming RF power will actually propagate in the mode under consideration) and the characteristics of the wave in the excitation region: spectral properties and spatial power distribution. This work requires a modeling of the launching structures and knowledge of the plasma edge physics. In the case of indirect launching - as for EBWs - this work includes the modeling of mode-conversion and sometimes requires the study of non-linear effects, such as parametric instabilities where different modes are non-linearly coupled and power can be transmitted from one to another.

- *Propagation of the RF wave* through the plasma to the region of absorption and current drive. The evolution of the wave characteristics along its propagation needs to be calculated, which typically involves ray-tracing or full-wave calculation techniques. In addition, the problem of accessibility investigates whether all or part of the power in the wave is reflected (for example, at a cut-off) or mode-converted (for example, at a propagation resonance) instead to reaching the region of wave-particle resonance.

- *Wave-particle interaction, power absorption and current drive.* Wave-particle interaction can occur when the resonance condition

$$\omega - k_{\parallel} v_{\parallel} - n\Omega = 0 \tag{1.1}$$

is satisfied for some particle velocity $v_{\|} < c$ , some wave frequency $\omega$ and parallel wave number $k_{\|}$ (with respect to the magnetic field), and some harmonic number $n$ at some location where the particle's gyrofrequency is $\Omega = q_e B/\gamma m_e$. Here $B$ is the magnetic field and $\gamma$ is the relativistic factor. The effect of wave-particle interaction is the exchange of energy and momentum between the wave and the particles. This exchange can modify the distribution function of the particles and therefore lead to current drive if this distribution becomes asymmetric in $v_{\|}$.

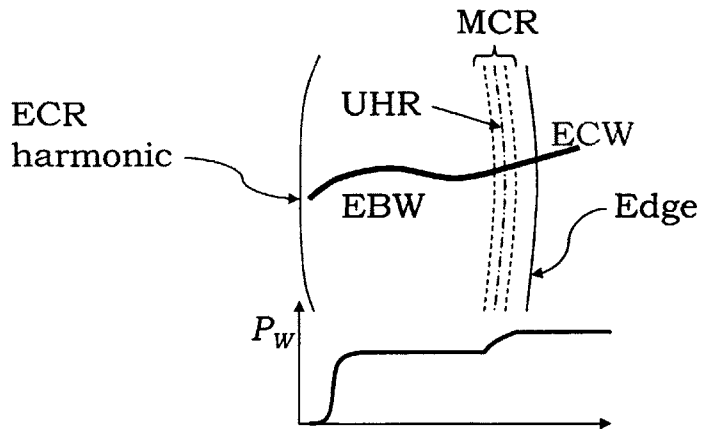


Figure 1-3: General scheme of the EBWCD problem.

EBWs are excited by mode conversion at the upper-hybrid frequency and damped at the Doppler-shifted location of cylotron resonance harmonics. The general scheme of EBWCD is illustrated in Fig. 1-3.

The present work does not encompass the study of EBW excitation and propagation. Rather, previous work on EBW excitation and propagation will be used to extract the information relevant to the present study, which is focusing on the vicinity of the EBW damping region in the plasma and addresses the wave-particle interaction, power absorption and current drive problems.

### 1.2.1 Excitation and propagation of electron Bernstein waves

#### Historical background

The existence of electrostatic waves in the electron cyclotron frequency range, propagating perpendicularly to the magnetic field and not subject to Landau damping, was first shown by I. Bernstein [1], who gave the corresponding dispersion relation. The experimental verification of EBW was done by F.W. Crawford, *et al.* [2]. Because EBWs do not exist in vacuum, they need to be excited either by an in-plasma antenna structure or by MC from the slow electromagnetic extraordinary mode (SX) at the upper-hybrid resonance (UHR). Among the MC methods with launching from the low field side (LFS) - the only ones applicable to STs - the O-SX-B scheme [7] was first experimentally demonstrated in a linear device [14], and then at high harmonics [15]. It has been successfully used for ECH on Wendelstein 7-AS [16]. A second scheme, noted FX-SX-B [17] [4], has been demonstrated first on linear devices [18] and then on STs [19] [20]. These two MC schemes have been extensively studied in [8]. Because of the symmetry properties of the MC process [21], significant knowledge has been gained from the theoretical [22] and experimental [16] study of EBW emission (EBE). EBWCD in tokamaks was first demonstrated on COMPASS-D [9], showing the high dependence of EBW properties, such as the parallel index of refraction, on the propagation path, as predicted in [8].

#### Description of EBW excitation

The FX-SX-B and O-SX-B schemes for EBW excitation are described on Fig. 1-4, where propagating modes are shown in the vicinity of the upper-hybrid resonance (UHR), represented by a vertical dashed line. These modes are characterized by their perpendicular wave number $N_\perp\left(\omega, N_\parallel\right)$, calculated by solving the dispersion relation (2.16) assuming a fixed frequency $\omega/\left(2\pi\right) = 14$ GHz and using the full non-relativistic kinetic plasma susceptibility tensor (2.65) $\mathbb{X}_{\mathrm{M}}\left(\mathbf{k}, \omega\right)$ in (2.10) and (2.15). The solution is obtained using the code *R2D2* [13], which solves the dispersion relation. The wave number is defined as $\mathbf{N} = \mathbf{k}c/\omega$.

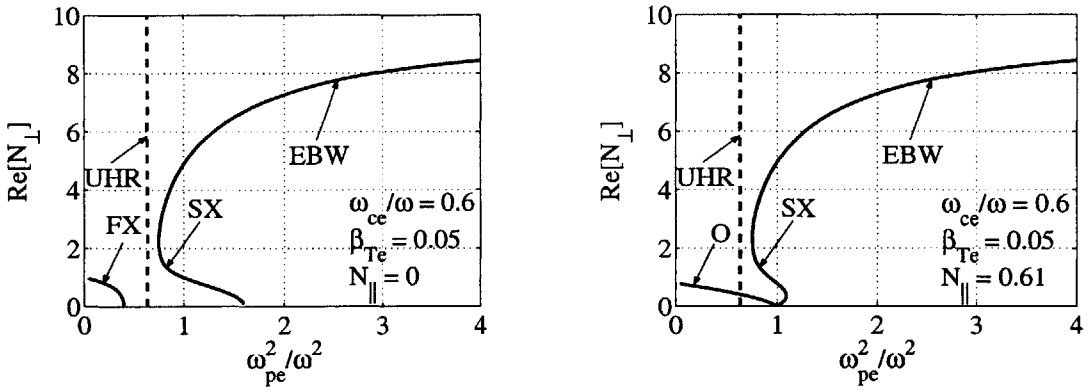


Figure 1-4: ECW and EBW roots $N_\perp$ (real part) as a function of $\alpha = \omega_{pe}^2/\omega^2$ for (a) perpendicular ($N_\parallel = 0$) and (b) oblique ($N_\parallel = N_{\parallel 0}$) propagation. The dashed vertical line corresponds to the location $\alpha_{\mathrm{UHR}}$ of the upper-hybrid resonance.

The mode-conversion region is typically located very near the edge where the wave characteristics are dominated by the strong density variations. A scan of the mode conversion region is therefore obtained by varying the electron density normalized to the frequency, $\alpha^2 = \omega_{pe}^2/\omega^2$, keeping all other plasma parameters constant, including the temperature ($T_{e0} = 1.3$ keV) and the magnetic field amplitude ($B = 0.3$ T). The upper-hybrid resonance is obtained for $\alpha^2 = \alpha_{\mathrm{UHR}}^2 \equiv 1 - (\omega_{ce}/\omega)^2$. The roots of the dispersion relation ($N_\perp$) are shown on Fig. 1-4, where two separate values of $N_\parallel$ are considered:

- Graph (a): $N_\parallel = 0$ for perpendicular propagation. This is a case where FX-SX-B mode conversion is favored. In that case, if an ECW is launched into the plasma with X-mode polarization, it reaches a cut-off (R) where part of the wave power is reflected and part of the power is tunneled across the evanescent region between the cut-off and the UHR to the slow X mode. The power is then reflected at the L cut-off and propagates back to the UHR when it can be mode-converted to the EBW. In fact, the FX-SX-B scheme present a resonator configuration [8], and under some favorable conditions, up to 100 % of the wave power can be mode-converted to the EBW.

- Graph (b): $N_{\|} = N_{\|0} \equiv (1 + \omega/\omega_{ce0})^{-1/2} \simeq 0.61$, for oblique propagation. $N_{\|0}$ is the value for which the O- and L- cut-offs coincide, and therefore where O-SX-B mode conversion is favored. In that case, if an ECW is launched obliquely into the plasma with O-mode polarization and $N_{\|} = N_{\|0}$, it reaches the plasma cutoff (O) where $\omega = \omega_{pe}$, which coincide with the L cut-off. Part of the power is transmitted to the SX mode, which propagates back towards the UHR where the power can be mode-converted to the EBW.

Detailed calculations of the mode-conversion processes [8] show that the FX-SX-B scheme is favored by steep density gradients, such that the evanescent region is narrower and more power can tunnel though. These conditions are typically found very near the edge, and thus the FX-SX-B scheme is better at lower frequencies. By contrast, the O-SX-B scheme is favored by smaller density gradients, such that little if any power is tunneling back to a FX mode at the UHR after conversion from O to SX mode. This scheme requires the UHR to be located farther away from the edge, and is thus adapted for larger frequencies.

### 1.2.2 Description of wave-particle interaction

The idea of using radio-frequency (RF) waves to drive currents in tokamak plasmas goes back to the 1970's. It was shown that lower-hybrid waves (LHW) could be used to transfer parallel momentum to the electrons [23] [24], and that LHWs with sufficiently high power lead to the creation of a plateau in the parallel momentum direction in distribution function, and drive a large current [25]. Important 2D effects (in momentum space) in LHCD, due to collisional pitch-angle scattering, were later described [26] [27].

Waves in the electron cyclotron (EC) range of frequency are attractive for heating and current drive, because they are easily coupled to the plasma and the location of their damping, at the Doppler-shifted cyclotron resonance or its harmonics, can be precisely controlled and adjusted with mirrors. While ECW transfer mostly perpendicular momentum to the electrons, it is possible to use them for driving parallel

current through several mechanisms:

- One method was described by Fisch & Boozer (FB) [28] and shows that asymmetric (in $p_{||}$) perpendicular heating of the distribution function leads to an asymmetric resistivity of electrons, since hotter particles are less collisional. More precisely, if electrons with $p_{||} > 0$ are heated, ions collide more frequently with electrons going in the opposite direction ($p_{||} < 0$) and there is a net ion momentum gain in the $p_{||} < 0$ direction. By reaction, there must be a net (opposite and equal in magnitude) electron momentum gain in the $p_{||} > 0$ direction. Although both species then drive a current in the same direction (in that case, $p_{||} < 0$, since electrons carry a negative charge), the contribution from electrons to the current is dominant because they are much lighter. Note that no current could be generated without collisions of electrons with ions, in which case the total parallel momentum of electrons would be conserved.

- Another method, proposed by Ohkawa (OK) [29], uses electron magnetic trapping to drive current. Indeed, perpendicular heating near the trapped/passing boundary leads to the magnetic trapping of barely passing electrons. Because of the fast bounce motion of trapped electrons, the collisional detrapping of electrons is quasi-symmetric in $p_{||}$. In steady state, the RF and collisional fluxes through the trapped/passing boundaries must compensate, so that there must be a depletion of passing electrons with negative $p_{||}$, along with an accumulation of both trapped electrons and passing electrons with positive $p_{||}$. These effects combine to drive a current in the same direction as the resonant electrons, since electrons carry a negative charge. Note that a more accurate description of the Ohkawa effect should account for the radial pinch effect associated with the trapping of electrons, in order to conserve toroidal canonical momentum.

To sum up, the FB effect drives a current in the opposite parallel direction to the resonant electrons, while the OK effect drive a current in the same parallel direction as the resonant electrons. A schematic representation of the Fisch-Boozer and Ohkawa effects is shown in Fig. 1-5 on graphs (a) and (b) respectively. While all experiments

in tokamaks have relied on - and optimized - the FB effect in ECCD, we have shown that the OK method for CD may be more efficient when current is needed far off-axis [30], as it is often the case in recent advanced tokamak (AT) scenarios. We gave a precise description of the kinetic mechanisms of ECCD in the presence of magnetic trapping [31].

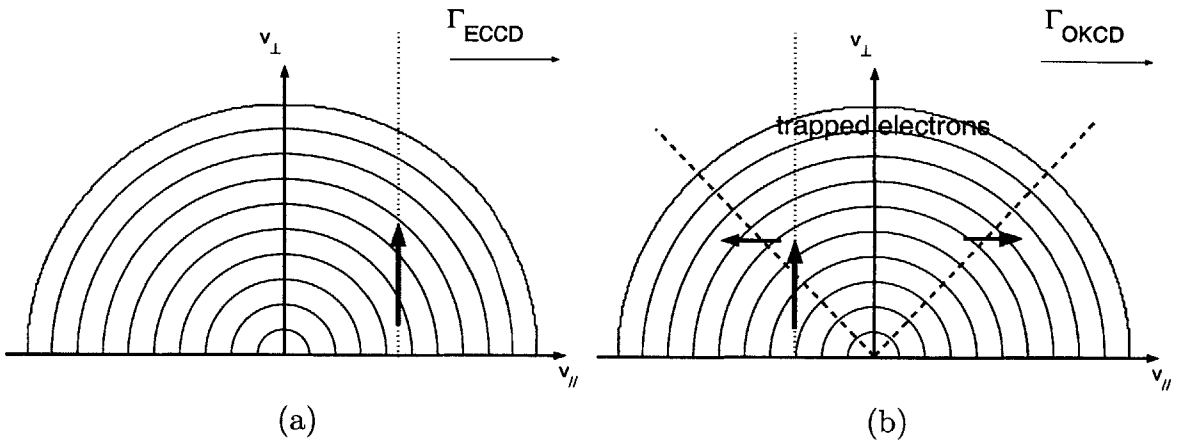


Figure 1-5: Schematic illustration of the Fisch-Boozer (a) and Ohkawa (b) mechanisms for ECCD.

The first kinetic description of the kinetic interaction between BC and LHCD was given by S. Schultz [32]. We further studied this interaction [33], showing the positive effect of temperature gradient on the synergism between LHCD and BC, and also investigated the synergism of FBCD and OKCD with the BC [34][30][35].

### 1.2.3 Numerical Calculations of Radio-Frequency Current Drive

An accurate calculation of RFCD requires one to solve a kinetic equation including the effect of collisions and RF fields [36]. Collisions are well described by a Fokker-Planck operator, which accounts for the cumulative effect of small angle bilinear collisions, which is the dominant collisional process. A differential expression for the fully relativistic Fokker-Planck collision operator has been developed by Braams and Karney [37] by expanding Rosenbluth potentials in spherical harmonics.

RFCD calculations also use the so-called adjoint method to describe the effect of RF waves [38]. This description, which calculates the current drive efficiency analytically in the linear limit where the distribution function remains close to a Maxwellian, ignores the effects of particle trapping, which are very important in small aspect ratio toroidal devices like STs. Modifications to the adjoint method that include the effect of magnetic trapping have been proposed [39] [40]. However, analytical calculations of the current drive efficiency are then no longer possible and numerical calculations are needed. Quasilinear theory, which accounts for distorsions of the distribution function to calculate the densities of current and power dissipated self consistently, is more appropriate to describe the effect of externally imposed RF waves. A quasilinear operator was developed by Kennel and Engelmann [41], and extended to relativistic plasmas by Lerche [42]. However, these operators apply only to infinite uniform plasmas, and are not immediately suitable for simulations in tokamaks and STs. A quasilinear operator for slab and mirror plasmas was later derived [43]. Operators were also derived for toroidal plasmas by using a direct approach to reduce the kinetic equation by averaging over fast gyro- and wave frequencies [44], and also by using a Hamiltonian approach to adiabatically remove these fast time scales [45] [46]. However, these operators were only applicable to plasmas without toroidal magnetic field.

It is necessary to use numerical tools to solve the 2D Fokker-Planck equation (FPE) with quasilinear diffusion. Such solvers have been developed by Kerbel and McCoy [47] also with Killeen [48], and their work was continued by Harvey and McCoy [49]. Other solvers were developed independently by Karney and Fisch [50], Giruzzi, *et al.* [51], Bizarro, *et al.* [52], Shoucri and Schkarofski [53] [54], and also Peysson and Shoucri [55]. A good review paper on FP QL codes was written by Karney [56].

## 1.3 High-$\beta$ Plasmas and EBWCD Scenarios

### 1.3.1 Magnetic field configuration in STs

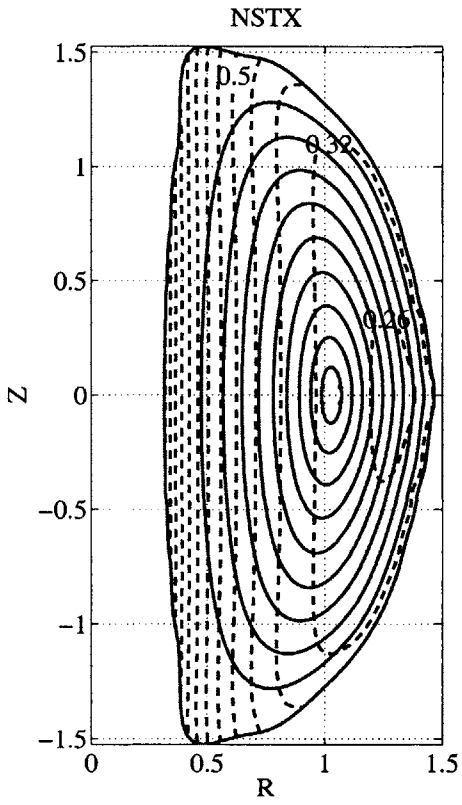


Figure 1-6: NSTX high-$\beta$ plasma poloidal cross section. The red solid contours are flux-surfaces labeled by $\rho = 0, 0.1, \cdots 1$ and the blue labeled dashed lines are contours of constant magnetic field magnitude (in Tesla).

The tight geometry of STs rules out the possibility of inboard launching. The only remaining possibilities are top launching and outboard launching. However, in a ST, launching from the outboard horizontal midplane does not necessarily imply that the resonance region is approached from a low-field region, as it would be in a conventional tokamak. Indeed, because of the important contribution of the poloidal magnetic field in a ST with sufficiently high $\beta$, the lower field region is generally not at the point farthest outboard, but somewhere between the core and the edge near the outboard horizontal midplane.

To illustrate this, we show the poloidal cross-section of our sample NSTX plasma on Fig. 1-6 where the red solid contours are flux-surfaces labeled by $\rho = 0, 0.1, \cdots 1$ and the blue labeled dashed lines are contours of constant magnetic field magnitude. Here $\rho$ is the normalized distance form the magnetic axis, measured along the outboard horizontal midplane. The enclosed magnetic well on the outboard side is clearly apparent, and is centered at the point $X_{\mathrm{M}}$ of minimum magnetic field, which is lo-

cated at ($R = 1.31$ m, $Z = 0$) where the corresponding radial coordinate is $\rho = 0.63$. The important contribution of $B_P$ to the total magnetic field magnitude appears on Fig. 1-7 which shows a profile of the magnetic field components along the horizontal mid-plane ($Z = 0$). Near the outboard edge, the poloidal component of the magnetic field becomes comparable and even larger than the toroidal component.

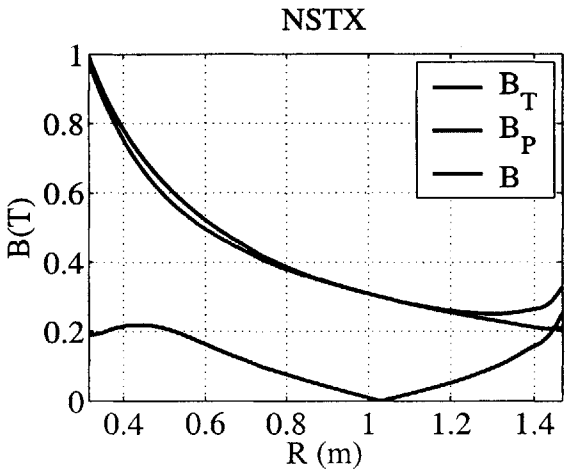


Figure 1-7: Toroidal (red), poloidal (blue) and total (black) magnetic field amplitudes along the $Z = 0$ horizontal midplane.

As we show in Section 2.2, the EBWs are strongly absorbed at any Doppler-shifted electron cyclotron harmonic. Because of the particular magnetic field configuration of high-$\beta$ STs, with a dip in the field magnitude profile as shown on Fig. 1-7, it should be possible, with outboard launch only, to approach a Doppler-shifted electron cyclotron harmonic from either a low $B$-field (LBF) region ($n\omega_{ce} < \omega$), or a high $B$-field (HBF) region ($n\omega_{ce} > \omega$), depending on the propagation path, the angular frequency $\omega$, and the parallel wave vector $k_{\|}$. These schemes are illustrated in Fig. 1-2. The terms low-field side and high field side are not used here because of the confusion with conventional tokamaks where they are also used to describe outboard and inboard sides, respectively. We will show in Chapter 2 that the EBW characteristics differ greatly upon whether the wave approaches a resonance from a LBF or a HBF region. As a consequence, as will be shown later, these two scenarios for wave-particle interaction

are very different and should be treated separately.

### 1.3.2 Equilibrium profiles

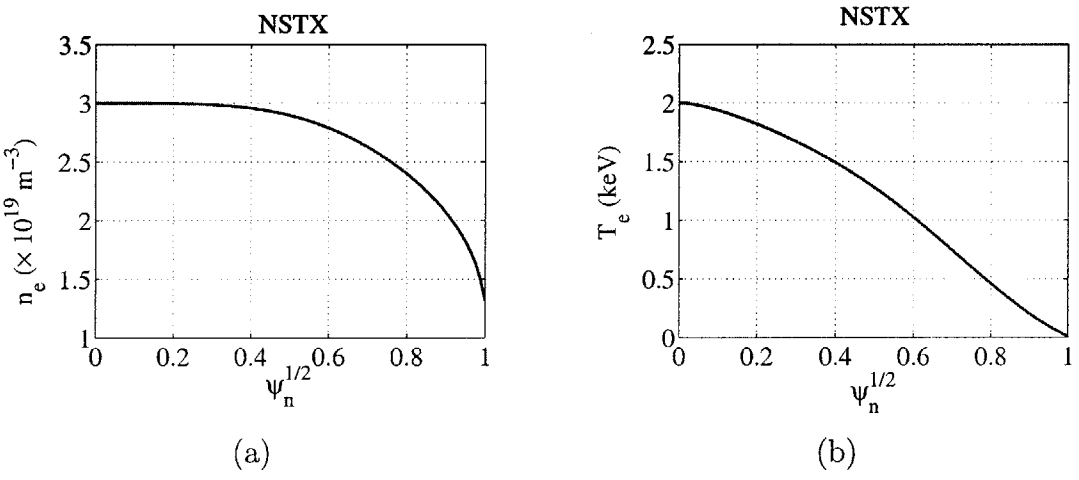


Figure 1-8: Density (a) and temperature (b) profiles in NSTX, as a function of $\sqrt{\psi_n}$ where $\psi_n = \psi/\psi_a$ is the normalized flux function.

The calculations presented in this thesis are based on a $\beta = 42\%$ NSTX equilibrium with the magnetic configuration presented in Section 1.3.1 and equilibrium profiles calculated consistently with a MHD code [57]. The electron temperature and density profiles are shown on Fig. 1-8. The effective charge is $Z_{\text{eff}} = 2$ and is assumed to be uniform across the plasma.

### 1.3.3 Accessibility

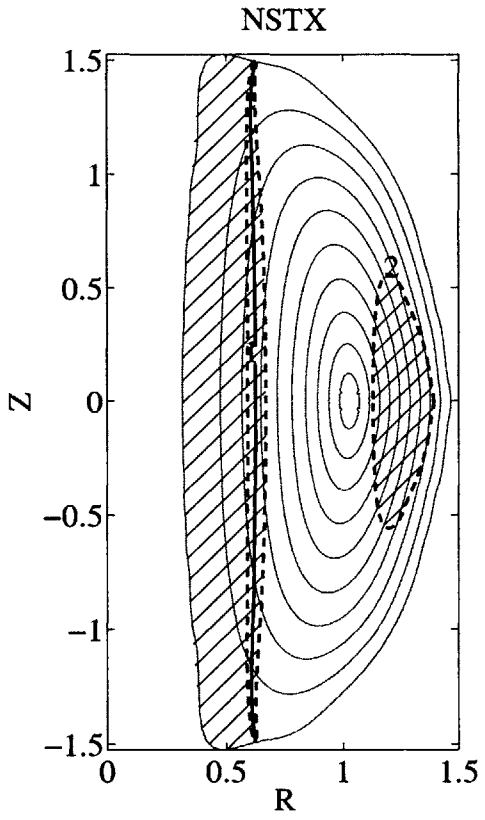


Figure 1-9: NSTX high-$\beta$ plasma poloidal cross section. The red solid contours are flux-surfaces labeled by $\rho = 0, 0.1, \cdots 1$. The thick solid line give the location of the first cyclotron harmonic for the frequency $f_{\mathrm{M}} = 14$ GHz, and the blue dashed lines are the corresponding Doppler-shifted harmonics $\omega = n\omega_{ce} \pm 3v_{Te}k_{\|}$ for $N_{\|} = 0.5$.

Because EBWs are generated - mode converted from EC modes - at the upper-hybrid resonance where $\omega^2 = \omega_{ce}^2 + \omega_{pe}^2$, the EBW frequency is necessarily higher than the electron cyclotron frequency. In order to choose a suitable launching frequency, $N_{\|}$ spectrum and location for EBWCD generation, it is important to know which regions of the plasma are accessible to a given frequency and what type of CD scenario is associated with the wave propagation (HBF or LBF). In our case, we define a plasma location to be *inaccessible* to an EBW, characterized by their frequency $\omega$ and their parallel wave number $N_{\|}$, either if EBWs do not propagate in this region (where $\omega_{ce} < \omega$), or if the wave is completely damped before reaching this location. In any other case, the location is said to be *accessible* to this EBW, regardless of the existence of an actual propagation path, from a region where mode-conversion is possible, to the location under consideration. Because we do not address the problems of EBW mode-conversion and propagation in this work, additional studies would be required to determine whether a

location defined here as accessible can indeed be reached in an experiment and what the EBW characteristics - in particular $N_{\|}$ - would be in that case.

On Fig. 1-9, we show the same the poloidal cross section as in Fig. 1-6, where the location of cyclotron harmonics for the frequency $f_{\mathrm{M}} = 14$ GHz is shown as labeled (by the harmonic number) solid black lines. In addition, dashed blue lines show the location of the Doppler-shifted resonances, calculated for $N_{\|} = 0.5$ by

$$\omega = n\omega_{ce} \pm 3v_{Te}k_{\|} \tag{1.2}$$

where $v_{Te} = \sqrt{T_e/m_e}$ is derived from the local temperature (See Fig. 1-8-b), and the strong damping condition is given by $v_{\|} = 3v_{Te}$, which is the typical value for EBWs as we will show in Section 5.1.6. The striped regions represent the plasma locations that are inaccessible to this wave, either because $\omega < \omega_{ce}$ (on the inboard side) or because the location is enclosed by Doppler-shifted cyclotron harmonics, where complete damping of the wave occurs. In principle, any Doppler-shifted cyclotron harmonic resonance location (dashed blue lines) which borders an accessible region of the plasma is a possible location for EBW damping and CD, and the type of scenario for EBWCD - HBF or LBF - depends on whether the magnetic field in the bordering accessible region is higher or lower, respectively, than it is at the location of the harmonic. For example, in the case considered on Fig. 1-9, HBF EBWCD is possible in principle at locations along the second harmonic Doppler-shifted resonance on the outboard side, while LBF EBWCD is possible on the first harmonic Doppler-shifted resonance on the inboard side.

Such general investigation of accessibility and possible scenarios is easily done for any frequency $\omega$ and parallel wave number $N_{\|}$, by drawing the poloidal cross section of the (axisymmetric) plasma and showing the locations of Doppler-shifted harmonic resonances. To illustrate this, we show on Fig. 1-10 the accessible regions corresponding to two frequencies often mentioned in the NSTX design plan, which are $f_{\mathrm{PR1}} = 21$ GHz (graph (a)) and $f_{\mathrm{PR2}} = 28$ GHz (graph(b)), still with $N_{\|} = 0.5$. At $f = 21$ GHz, outboard launching would in principle give access to HBF CD at

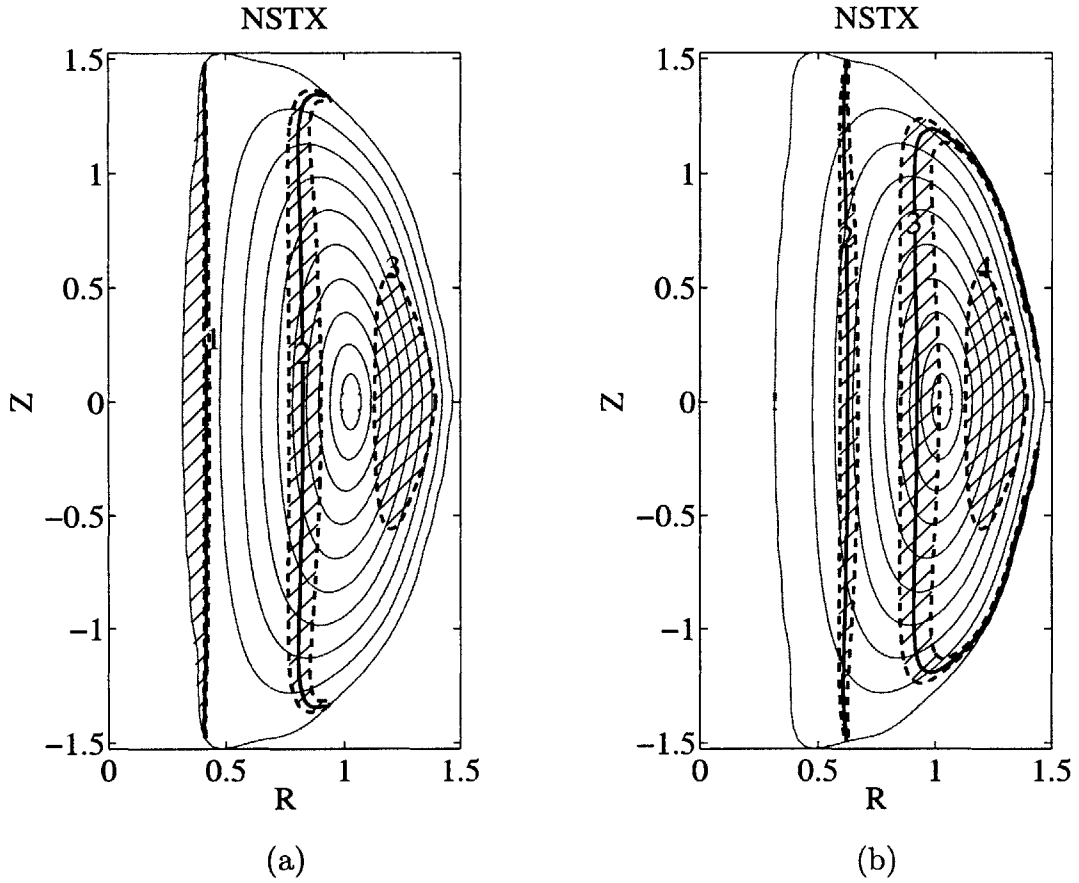


Figure 1-10: Same as Fig. 1-9 with $N_{\|} = 0.5$ but for different frequencies: (a) $f = 21$ GHz and (b) $f = 28$ GHz

third harmonic and LBF CD at second harmonic, while top (or bottom) launching would allow HBF CD at second harmonic and LBF CD at first harmonic. At $f = 28$ GHz, outboard launching is restricted to the midplane locations and therefore allows only HBF CD at fourth harmonic.

Comparing results obtained with three different frequencies (Figs. 1-9 and 1-10), we observe that at higher frequencies, the various cyclotron harmonics are closer to each other, which effectively restricts the accessible regions of the plasma. Therefore, for the sake of keeping a wide range of possible CD scenarios, low frequencies, typically favorable to X-B mode-conversion schemes[1], are better than high frequencies, usually favorable to O-X-B mode-conversion schemes. However, this fact is balanced by other

[1]See discussion in Section 1.2.1.

experimental constraints. For example, higher frequencies require smaller mirrors and therefore allow for a wider range of launching angles, which can be adjusted to control the location of CD. In addition, the mode-conversion process is subject to large density fluctuations close to the edge, which could decrease the MC efficiency.

### 1.3.4 Summary

A poloidal cross-section of accessible regions can be easily drawn for a given frequency and parallel wave number, as done in Figs. 1-9 and 1-10. Such maps are useful to determine schematically the location of EBWCD as well as possible scenarios - HBF or LBF CD.

High $B$-field CD appears to be possible at any harmonic $n \geq 2$ with launching near the midplane, and therefore seems to work for either low or high frequencies. In such CD scenario, wave-particle resonance occurs off axis on the outboard side and will likely involve strong magnetically trapped electron effects.

On the other side, the accessibility of LBF CD requires to use low frequencies - between first and second harmonic. In addition, the location of resonance is generally located in the core of the plasma, where magnetically trapped electrons are expected to play a lesser role.

# Chapter 2

# Description of Electron Bernstein Waves

In order to study EBWCD, it is necessary to calculate and describe the characteristics of EBWs. Indeed, the interaction between a given EBW mode and electrons depends on wave properties such as the frequency $\omega$, wave vector $\mathbf{k}$, polarization vector $\mathbf{e_k}$ and electric field amplitude $\|\mathbf{E_k}\|$. In a plasma where inhomogeneities occur on a scale-length much larger than the wavelength, the wave properties can be approximately calculated using the model of linear waves in a uniform plasma, and assuming thereafter that the plasma characteristics $\mathbf{k}$, $\mathbf{e_k}$ and $\|\mathbf{E_k}\|$ are slowly varying functions of space. This is known as the WKB approximation.

The basic concepts of the linear kinetic theory of plasma waves are reviewed in Section 2.1, where we focus in particular on the dispersion relation and on the energy equation, which relates in steady state the wave energy flow density and power dissipated and is the basis for the calculation of EBW power deposition. The non-relativistic kinetic susceptibility tensor is derived in many textbooks on kinetic waves, for example [58] [59] [60], and is recalled here.

In Section 2.2, the dispersion relation is solved analytically in the electrostatic approximation for EBWs propagating perpendicularly to the magnetic field, and the initial description of EBWs [1] is retrieved. This approximate description provides a useful insight into the behavior of EBW. In particular, characteristics of EBWs in the

vicinity of cyclotron harmonic resonances are very different depending on whether the resonance is approached from a low $B$-field (LBF) or a high $B$-field (HBF) region.

The kinetic linear dispersion relation and wave equation are solved exactly in Section 2.3, using the numerical solver *R2D2* [13]. Particular attention is given to the wave properties which enter the calculation of the quasilinear diffusion coefficient (3.192). In this work, vectors are written in bold characters, like $\mathbf{v}$, and unit vectors are covered with a hat, like $\widehat{\mathbf{v}}$. Tensors are written in blackboard characters, such as $\mathbb{T}$.

## 2.1 High-Frequency Linear Waves in a Hot Uniform Plasma

### 2.1.1 Linear wave equation and dispersion relation

Detailed and consistent derivations of linear wave theory can be found in [61], [59] and [58]. Elements of the theory relevant to the study of wave-particle resonance are presented here.

#### Maxwell's equations

Electromagnetic fields are generated by charge and current densities, according to Maxwell's equations

$$\begin{aligned} &\nabla \cdot \mathbf{E} = \frac{\rho}{\varepsilon_0} && \text{(a)} \\ &\nabla \cdot \mathbf{B} = 0 && \text{(b)} \\ &\nabla \times \mathbf{B} = \mu_0 \mathbf{J} + \mu_0 \varepsilon_0 \frac{\partial \mathbf{E}}{\partial t} && \text{(c)} \\ &\nabla \times \mathbf{E} = -\frac{\partial \mathbf{B}}{\partial t} && \text{(d)} \end{aligned} \tag{2.1}$$

where $\mathbf{E}(\mathbf{r}, t)$ and $\mathbf{B}(\mathbf{r}, t)$ are the electric and magnetic (induction) fields, and $\rho(\mathbf{r}, t)$ and $\mathbf{J}(\mathbf{r}, t)$ are the charge and current densities, respectively. The conservation of

charge density leads to the continuity equation

$$\frac{\partial \rho}{\partial t} + \nabla \cdot \mathbf{J} = 0 \tag{2.2}$$

In the absence of static fields, equation (2.1-b) can be derived by taking the divergence of Faraday's equation (2.1-d), and Gauss' law (2.1-a) can be derived by taking the divergence of Ampere's law (2.1-c) and using the continuity equation (2.2). In order to obtain a complete set of equations, we need an expression for $\rho(\mathbf{r}, t)$ and $\mathbf{J}(\mathbf{r}, t)$ as a function of $\mathbf{E}(\mathbf{r}, t)$ and $\mathbf{B}(\mathbf{r}, t)$.

### Linear wave equation

Under some conditions - which generally include sufficiently small-amplitude electromagnetic fields - non-linear effects, such as particle trapping in waves or non-linear coupling of waves, can be neglected. Then, the current density has a linear dependence on the electric field, and can in general be expressed as a convolution

$$\mathbf{J}(\mathbf{r}, t) = \iiint d^3r' \int dt' \, \mathbb{S}(\mathbf{r}, \mathbf{r}', t, t') \cdot \mathbf{E}(\mathbf{r}', t') \tag{2.3}$$

where $\mathbb{S}$ is the *conductivity tensor*, which depends on the equilibrium properties of the medium. In an infinite plasma with a homogeneous, constant equilibrium, which is invariant by translation in space and time, the conductivity tensor is only a function of the relative distance in space and time, and we can rewrite (2.3) as

$$\mathbf{J}(\mathbf{r}, t) = \iiint d^3r' \int dt' \, \mathbb{S}(\mathbf{r} - \mathbf{r}', t - t') \cdot \mathbf{E}(\mathbf{r}', t') \tag{2.4}$$

If we take a Fourier transform of this equation, defined for a field $F(\mathbf{r}, t)$ as

$$F_{\mathbf{k}}(\mathbf{k}, \omega) = \iiint d^3r \int dt \, e^{i\mathbf{k}\cdot\mathbf{r} - i\omega t} F(\mathbf{r}, t) \tag{2.5}$$

we obtain

$$\mathbf{J}_{\mathbf{k}}(\mathbf{k}, \omega) = \mathbb{S}(\mathbf{k}, \omega) \cdot \mathbf{E}_{\mathbf{k}}(\mathbf{k}, \omega) \tag{2.6}$$

In addition, the Fourier transform of Maxwell's equations (2.1) gives

$$\begin{aligned} i\mathbf{k}\cdot\mathbf{E}_\mathbf{k} &= \frac{\rho_\mathbf{k}}{\varepsilon_0} && \text{(a)} \\ i\mathbf{k}\cdot\mathbf{B}_\mathbf{k} &= 0 && \text{(b)} \\ i\mathbf{k}\times\mathbf{B}_\mathbf{k} &= \mu_0\mathbf{J}_\mathbf{k} - \mu_0\varepsilon_0 i\omega\mathbf{E}_\mathbf{k} && \text{(c)} \\ i\mathbf{k}\times\mathbf{E}_\mathbf{k} &= i\omega\mathbf{B}_\mathbf{k} && \text{(d)} \end{aligned} \tag{2.7}$$

Combining the two last equations, and using (2.6), we find the linear wave equation

$$\begin{aligned} \mathbf{k}\times\mathbf{k}\times\mathbf{E}_\mathbf{k} &= -i\mu_0\omega\mathbb{S}\cdot\mathbf{E}_\mathbf{k} - \mu_0\varepsilon_0\omega^2\mathbf{E}_\mathbf{k} \\ &= -\frac{\omega^2}{c^2}\left(\mathbb{I}+\mathbb{X}\right)\cdot\mathbf{E}_\mathbf{k} \\ &= -\frac{\omega^2}{c^2}\mathbb{K}\cdot\mathbf{E}_\mathbf{k} \end{aligned} \tag{2.8}$$

where we defined the *susceptibility tensor*

$$\mathbb{X} \equiv \frac{i}{\omega\varepsilon_0}\mathbb{S} \tag{2.9}$$

and the *permitivity tensor*

$$\mathbb{K} \equiv \mathbb{I} + \mathbb{X} \tag{2.10}$$

Introducing the normalized wave vector, or index of refraction

$$\mathbf{N} \equiv \frac{c}{\omega}\mathbf{k} \tag{2.11}$$

the wave equation (2.8) becomes

$$\mathbf{N}\times\mathbf{N}\times\mathbf{E}_\mathbf{k} + \mathbb{K}\cdot\mathbf{E}_\mathbf{k} = 0 \tag{2.12}$$

and hence

$$\left(\mathbf{NN} - N^2\mathbb{I} + \mathbb{K}\right)\cdot\mathbf{E}_\mathbf{k} = 0 \tag{2.13}$$

which is rewritten as

$$\mathbb{D} \cdot \mathbf{E}_{\mathbf{k}} = 0 \tag{2.14}$$

where

$$\mathbb{D} \equiv \mathbf{NN} - N^2\mathbb{I} + \mathbb{K} \tag{2.15}$$

is called the *dispersion tensor.*

### Dispersion relation

In order to find a non-trivial solution to the wave equation (2.14), the determinant of the dispersion tensor must be zero

$$D(\mathbf{k}, \omega) \equiv |\mathbb{D}| = 0 \tag{2.16}$$

This equation is called the *dispersion relation*, and can solved for either $\omega(\mathbf{k})$ or $k_i(\omega, k_j, k_k)$ where $i, j, k$ is a permutation of coordinates of $\mathbf{k}$. This relation gives the natural electromagnetic modes that can be independently excited in the homogeneous plasma. We also define a wave *phase velocity* and *group velocity*, respectively given by

$$\begin{aligned} \mathbf{v}_p &= \left.\frac{\omega}{k}\widehat{\mathbf{k}}\right|_{D(\mathbf{k},\omega)=0} \\ \mathbf{v}_g &= \left.\frac{\partial\omega}{\partial\mathbf{k}}\right|_{D(\mathbf{k},\omega)=0} \end{aligned} \tag{2.17}$$

where $k = \|\mathbf{k}\|$ and $\widehat{\mathbf{k}} = \mathbf{k}/k$ is the unit vector in the direction of the wave vector. Note that in a dispersive medium, $\omega$ and $k$ are not proportional in general, and thus we can have $v_p \neq v_g$. In addition, if the medium is anisotropic (for example, in the presence of a strong magnetic field), the group velocity $\mathbf{v}_g$ is not necessarily in the direction of the wave vector $\mathbf{k}$.

### Uniform plasma with static magnetic field

For a uniform plasma in a externally applied static magnetic field

$$\overline{\mathbf{B}} = \overline{B}\widehat{\mathbf{b}} \tag{2.18}$$

with $\overline{B} = \left\|\overline{\mathbf{B}}\right\|$ and where the bar refers to the static nature of the field, the cylindrical symmetry around the magnetic field direction $\widehat{\mathbf{b}}$ imposes that the dispersion relation be only a function of $k_\parallel$ and $k_\perp$, with

$$\begin{aligned} k_\parallel &= \mathbf{k} \cdot \widehat{\mathbf{b}} \\ k_\perp &= \left\| \mathbf{k} - k_\parallel \widehat{\mathbf{b}} \right\| \end{aligned} \tag{2.19}$$

and therefore the dispersion relation (2.16) can be written as

$$D\left(k_\parallel, k_\perp, \omega\right) = 0 \tag{2.20}$$

The cylindrical symmetry also imposes that the group velocity $\mathbf{v}_g$ be in the $\left(\widehat{\mathbf{k}}, \widehat{\mathbf{b}}\right)$ plane.

## 2.1.2 Energy equation for linear waves

In a uniform, weakly dissipative plasma, the conservation of energy for the linear mode $\mathbf{E}_\mathbf{k}$ is given by [61]

$$\frac{\partial w_\mathbf{k}}{\partial t} + \nabla \cdot \mathbf{s}_\mathbf{k} = -P_\mathbf{k}^{\text{lin}} \tag{2.21}$$

where $w_\mathbf{k}$ is the time-averaged energy density, $\mathbf{s}_\mathbf{k}$ is the time-averaged energy density flow, and $P_\mathbf{k}^{\text{lin}}$ is the density of power dissipated. This equation is function of the real parts of $\omega$ and $\mathbf{k}$, which will be implicit in this Subsection.

Note that any tensor $\mathbb{T} = \mathbb{T}^H + \mathbb{T}^A$ can be decomposed into hermitian $\mathbb{T}^H$ and

antihermitian $\mathbb{T}^A$ parts, which are given respectively by

$$\begin{aligned} \mathbb{T}^H &= \frac{1}{2}\left[\mathbb{T} + \mathbb{T}^\dagger\right] \\ \mathbb{T}^A &= \frac{1}{2}\left[\mathbb{T} - \mathbb{T}^\dagger\right] \end{aligned} \tag{2.22}$$

where the operator $\dagger = t*$ is the combination of a transposition and a complex conjugation.

### Wave energy density

The time-averaged energy density $w_{\mathbf{k}}$

$$w_{\mathbf{k}} = w_{\mathbf{k}P} + w_{\mathbf{k}T} \tag{2.23}$$

includes the electromagnetic energy density $w_{\mathbf{k}P}$ and the kinetic energy associated with the coherent motion of charged particles in the field $w_{\mathbf{k}T}$. These are given by

$$\begin{aligned} w_{\mathbf{k}P} &= \frac{\varepsilon_0}{4}\left\|\mathbf{E}_{\mathbf{k}}\right\|^2 + \frac{1}{4\mu_0}\left\|\mathbf{B}_{\mathbf{k}}\right\|^2 \\ w_{\mathbf{k}T} &= \frac{\varepsilon_0}{4}\mathbf{E}_{\mathbf{k}}^* \cdot \frac{\partial\left(\omega\mathbb{X}^H\right)}{\partial\omega} \cdot \mathbf{E}_{\mathbf{k}} \end{aligned} \tag{2.24}$$

Using Faraday's equation (2.7-d), we normalize the energy density $w_{\mathbf{k}}$ as

$$w_{\mathbf{k}} = \frac{\varepsilon_0}{2}\left\|\mathbf{E}_{\mathbf{k}}\right\|^2 \Sigma_{\mathbf{k}} \tag{2.25}$$

where the normalized energy density $\Sigma_{\mathbf{k}}$ thus decomposes as

$$\Sigma_{\mathbf{k}} = \Sigma_{\mathbf{k}P} + \Sigma_{\mathbf{k}T} \tag{2.26}$$

with the definitions

$$\begin{aligned}\Sigma_{\mathbf{k}P} &= \frac{1}{2}\left[1 + \|\mathbf{N}\times\mathbf{e}_{\mathbf{k}}\|^2\right] \\ \Sigma_{\mathbf{k}T} &= \frac{1}{2}\mathbf{e}_{\mathbf{k}}^* \cdot \frac{\partial\left(\omega\mathbb{X}^H\right)}{\partial\omega}\cdot\mathbf{e}_{\mathbf{k}}\end{aligned} \tag{2.27}$$

where $\mathbf{e}_{\mathbf{k}} = \mathbf{E}_{\mathbf{k}}/\|\mathbf{E}_{\mathbf{k}}\|$ is the polarization vector. The normalized energy density (2.26) can be rewritten as

$$\Sigma_{\mathbf{k}} = \frac{1}{2}\mathbf{e}_{\mathbf{k}}^* \cdot \left[\frac{\partial\left(\omega\mathbb{K}^H\right)}{\partial\omega} - \left(\mathbf{NN} - N^2\mathbb{I}\right)\right]\cdot\mathbf{e}_{\mathbf{k}} \tag{2.28}$$

where we used the identity

$$\|\mathbf{N}\times\mathbf{e}_{\mathbf{k}}\|^2 = \mathbf{e}_{\mathbf{k}}^*\cdot\left(N^2\mathbb{I} - \mathbf{NN}\right)\cdot\mathbf{e}_{\mathbf{k}} \tag{2.29}$$

With $\mathbf{N} = \mathbf{k}c/\omega$ we have at constant $\mathbf{k}$

$$\frac{\partial}{\partial\omega}\left[\omega^2\left(\mathbf{NN} - N^2\mathbb{I}\right)\right] = 0 \tag{2.30}$$

so that

$$\frac{\partial}{\partial\omega}\left[\omega\left(\mathbf{NN} - N^2\mathbb{I}\right)\right] = -\left(\mathbf{NN} - N^2\mathbb{I}\right) \tag{2.31}$$

and we can rewrite, using the expression (2.15) for the dispersion tensor

$$\Sigma_{\mathbf{k}} = \frac{\omega}{2}\frac{\partial}{\partial\omega}\left(\mathbf{e}_{\mathbf{k}}^*\cdot\mathbb{D}^H\cdot\mathbf{e}_{\mathbf{k}}\right) \tag{2.32}$$

where we used the wave equation (2.14) so that

$$\begin{aligned}\mathbb{D}^H\cdot\mathbf{e}_{\mathbf{k}} &= 0 \\ \mathbf{e}_{\mathbf{k}}^*\cdot\mathbb{D}^H &= 0\end{aligned} \tag{2.33}$$

in the limit of weak dissipation.

### Wave energy density flow

The time-averaged energy flow density $\mathbf{s}_\mathbf{k}$

$$\mathbf{s}_\mathbf{k} = \mathbf{s}_{\mathbf{k}P} + \mathbf{s}_{\mathbf{k}T} \tag{2.34}$$

includes both the electromagnetic Poynting flow $\mathbf{s}_P$ and the flow associated with the coherent motion of charged particles in the field $\mathbf{s}_T$, which are expressed as

$$\begin{aligned} \mathbf{s}_{\mathbf{k}P} &= \frac{1}{2\mu_0} \mathrm{Re}\left[\mathbf{E}_\mathbf{k}^* \times \mathbf{B}_\mathbf{k}\right] \\ \mathbf{s}_{\mathbf{k}T} &= -\frac{\varepsilon_0 \omega}{4} \mathbf{E}_\mathbf{k}^* \cdot \frac{\partial \mathbb{X}^H}{\partial \mathbf{k}} \cdot \mathbf{E}_\mathbf{k} \end{aligned} \tag{2.35}$$

Using Faraday's equation (2.7-d), we normalize the energy flow density $\mathbf{s}$ (2.34) as

$$\mathbf{s}_\mathbf{k} = \frac{\varepsilon_0 c}{2} \left\| \mathbf{E}_\mathbf{k} \right\|^2 \mathbf{\Phi}_\mathbf{k} \tag{2.36}$$

where the normalized energy flow density $\mathbf{\Phi}_\mathbf{k}$ thus decomposes as

$$\mathbf{\Phi}_\mathbf{k} = \mathbf{\Phi}_{\mathbf{k}P} + \mathbf{\Phi}_{\mathbf{k}T} \tag{2.37}$$

with the definitions

$$\begin{aligned} \mathbf{\Phi}_{\mathbf{k}P} &= \mathrm{Re}\left[\mathbf{e}_\mathbf{k}^* \times \mathbf{N} \times \mathbf{e}_\mathbf{k}\right] = \mathbf{N} - \mathrm{Re}\left[\left(\mathbf{e}_\mathbf{k}^* \cdot \mathbf{N}\right) \mathbf{e}_\mathbf{k}\right] \\ \mathbf{\Phi}_{\mathbf{k}T} &= -\frac{1}{2} \mathbf{e}_\mathbf{k}^* \cdot \frac{\partial \mathbb{X}^H}{\partial \mathbf{N}} \cdot \mathbf{e}_\mathbf{k} \end{aligned} \tag{2.38}$$

Using (2.77), the normalized energy flow density (2.37) can be rewritten as

$$\mathbf{\Phi}_\mathbf{k} = -\frac{1}{2} \frac{\partial}{\partial \mathbf{N}} \left( \mathbf{e}_\mathbf{k}^* \cdot \mathbb{D}^H \cdot \mathbf{e}_\mathbf{k} \right) \tag{2.39}$$

where we used the identity

$$\mathbf{N} - \mathrm{Re}\left[\left(\mathbf{e}_\mathbf{k}^* \cdot \mathbf{N}\right) \mathbf{e}_\mathbf{k}\right] = -\frac{1}{2} \mathbf{e}_\mathbf{k} \cdot \frac{\partial \left(\mathbf{N}\mathbf{N} - N^2 \mathbb{I}\right)}{\partial \mathbf{N}} \cdot \mathbf{e}_\mathbf{k}^* \tag{2.40}$$

and the expression (2.15) for the dispersion tensor.

### Relation between power flow and group velocity

In the limit of weak dissipation, we have (2.77)

$$D_{\mathbf{k}}^{H}(\mathbf{k},\omega) = \mathbf{e}_{\mathbf{k}}^{*} \cdot \mathbb{D}^{H} \cdot \mathbf{e}_{\mathbf{k}} = 0 \tag{2.41}$$

which can be viewed as a dispersion relation for the mode $\mathbf{e}_{\mathbf{k}}$. Using (2.17) we can rewrite the group velocity as

$$\mathbf{v}_g = -\frac{\partial D_{\mathbf{k}}^{H}(\mathbf{k},\omega)/\partial \mathbf{k}}{\partial D_{\mathbf{k}}^{H}(\mathbf{k},\omega)/\partial \omega} \tag{2.42}$$

and, with (2.32) and (2.39), we obtain the useful relation

$$\mathbf{\Phi}_{\mathbf{k}} = \Sigma_{\mathbf{k}} \frac{\mathbf{v}_g}{c} \tag{2.43}$$

or equivalently

$$\mathbf{s}_{\mathbf{k}} = \mathbf{v}_g w_{\mathbf{k}} \tag{2.44}$$

which states that the wave energy flows at the group velocity. Like the group velocity, the energy flow density $\mathbf{\Phi}_{\mathbf{k}}$ must be contained in the $\left(\widehat{\mathbf{k}}, \widehat{\mathbf{b}}\right)$ plane.

### Density of power dissipated

For weakly damped linear waves in an infinite homogeneous plasma, the time-averaged density of power dissipated $P_{\mathbf{k}}^{\text{lin}}$ associated with the Fourier mode $\mathbf{E}_{\mathbf{k}}$ is given by

$$P_{\mathbf{k}}^{\text{lin}} = \frac{1}{2}\mathbf{E}_{\mathbf{k}}^{*} \cdot \mathbb{S}^{H}(\mathbf{k},\omega) \cdot \mathbf{E}_{\mathbf{k}} \tag{2.45}$$

where $\mathbb{S}^{H}$ is the hermitian part of the conductivity tensor.

The relation between the conductivity and susceptibility tensors (2.9) is

$$\mathbb{S} = -\varepsilon_0 \omega i \mathbb{X} \tag{2.46}$$

so that the hermitian part of the conductivity tensor is

$$\mathbb{S}^H = \frac{\mathbb{S} + \mathbb{S}^\dagger}{2} = -i\varepsilon_0 \omega \mathbb{X}^A \tag{2.47}$$

where $\mathbb{X}^A$ is the anti-hermitian part of the susceptibility tensor (2.22). The density of power absorbed (2.45) becomes

$$\begin{aligned} P_{\mathbf{k}}^{\text{lin}} &= -i\frac{\varepsilon_0 \omega}{2} \mathbf{E}_{\mathbf{k}}^* \cdot \mathbb{X}^A \cdot \mathbf{E}_{\mathbf{k}} \\ &= -i\frac{\varepsilon_0 c}{2} \|\mathbf{E}_{\mathbf{k}}\|^2 \frac{\omega}{c} \mathbf{e}_{\mathbf{k}}^* \cdot \mathbb{X}^A \cdot \mathbf{e}_{\mathbf{k}} \end{aligned} \tag{2.48}$$

where $\mathbf{e}_{\mathbf{k}}$ is the polarization vector.

#### Absorption coefficient

With the normalization (2.36) of the time-averaged energy density flow $\mathbf{s}_{\mathbf{k}}$, (2.48) becomes

$$P_{\mathbf{k}}^{\text{lin}} = -i\frac{\|\mathbf{s}_{\mathbf{k}}\|}{\|\mathbf{\Phi}_{\mathbf{k}}\|} \frac{\omega}{c} \mathbf{e}_{\mathbf{k}}^* \cdot \mathbb{X}^A \cdot \mathbf{e}_{\mathbf{k}} \tag{2.49}$$

The absorption coefficient is by definition

$$\alpha_{\mathbf{k}}^{\text{lin}} = \frac{P_{\mathbf{k}}^{\text{lin}}}{\|\mathbf{s}_{\mathbf{k}}\|} \tag{2.50}$$

and therefore we obtain an expression for the absorption coefficient

$$\alpha_{\mathbf{k}}^{\text{lin}} = -i\frac{1}{\|\mathbf{\Phi}_{\mathbf{k}}\|} \frac{\omega}{c} \mathbf{e}_{\mathbf{k}}^* \cdot \mathbb{X}^A \cdot \mathbf{e}_{\mathbf{k}} \tag{2.51}$$

### 2.1.3 Plasma description and Vlasov equation

In a plasma, the charge and current densities depend on electromagnetic field through the motion of charge particles. The $j^{\text{th}}$ charged particle, of mass $m_j$, charge $q_j$, position $\mathbf{r}_j$ and momentum $\mathbf{p}_j$, is accelerated by electromagnetic fields according to Lorentz' force

$$\mathbf{F}\left(\mathbf{p}_j, \mathbf{r}_j, t\right) = q_j \left[\mathbf{E}\left(\mathbf{r}_j, t\right) + \mathbf{v}_j \times \mathbf{B}_j\left(\mathbf{r}_j, t\right)\right] \tag{2.52}$$

The equations of motion are

$$\begin{aligned} m_j \frac{d\mathbf{p}_j}{dt} &= \mathbf{F}_j \\ \frac{d\mathbf{r}_j}{dt} &= \mathbf{v}_j \end{aligned} \tag{2.53}$$

where the velocity is given by

$$\mathbf{v}_j = \frac{\mathbf{p}_j}{\gamma_j} \tag{2.54}$$

where $\gamma_j$ is the relativistic factor

$$\gamma_j = \sqrt{1 + \frac{p_j^2}{m_j^2 c^2}} \tag{2.55}$$

The charge and current densities are then obtained by adding the contribution of all $N$ charged particles

$$\begin{aligned} \rho(\mathbf{r}, t) &= \sum_{j=1}^{N} q_j \delta[\mathbf{r} - \mathbf{r}_j(t)] \\ \mathbf{J}(\mathbf{r}, t) &= \sum_{j=1}^{N} q_j \mathbf{v}_j \delta[\mathbf{r} - \mathbf{r}_j(t)] \end{aligned} \tag{2.56}$$

This is overall a closed system of equations, but with a very large number of unknown (of order $N$), and it cannot be solved for a typical fusion plasma. Therefore, a statistical approach is generally used, in order to solve for a hierarchy of probability functions. For plasmas with $n_e \lambda_e^3 \gg 1$ - where $\lambda_e = \sqrt{\varepsilon_0 T_e / (e^2 n_e)}$ is the Debye length - it suffices to consider only the "one-particle" distribution function $f_s(\mathbf{p}, \mathbf{r}, t)$ for each type $s$ of particles, and account for correlations by a binary "collision integral" among the $f_s$. In general, collisions between particles can be neglected for the calculation of electromagnetic waves in plasmas, provided that the wavelength of the wave is much longer that the Debye length, since the fluctuating Coulomb fields associated with discrete particles occur on distances smaller than $\lambda_e$. In a typical NSTX plasma ($T_e \simeq 1.3$ keV, $n_e \simeq 3 \times 10^{19}$ m$^{-3}$), the Debye length is $\lambda_e \simeq 50$ $\mu$m, while the wavelength of EBWs in such plasma is of the order or larger than a millimeter.

In collisionless dynamics, the evolution equation for the distribution function

$f_s(\mathbf{p}, \mathbf{r}, t)$ is the Vlasov equation

$$\frac{\partial f_s}{\partial t} + \mathbf{v} \cdot \nabla_{\mathbf{r}} f_s + \mathbf{F}(\mathbf{p}, \mathbf{r}, t) \cdot \nabla_{\mathbf{p}} f_s = 0 \tag{2.57}$$

where $\mathbf{p}$, $\mathbf{r}$ and $t$ are independent, continuous phase space variables, and $\mathbf{F}(\mathbf{p}, \mathbf{r}, t)$ is given by (2.52). When the plasma thermal effects on the characteristics of electromagnetic fields are small, it is possible to consider only a few moments of the Vlasov equation, which form a set of hydrodynamic - or fluid - equations and are much easier to solve than the full Vlasov equation. However, electron Bernstein waves (EBWs) are *kinetic plasma waves*, meaning that their characteristics depend of the velocity distribution of the plasma particles. Indeed, EBWs are waves in the electron cyclotron range of frequencies and may have a short wavelength comparable to the Larmor radius of electrons, and thus interact differently with particles depending on their velocity.

### 2.1.4 Hot plasma dielectric tensor

The linearized motion of charged particles in electromagnetic fields, in an infinite plasma with a homogeneous, constant equilibrium, leads to the existence of a susceptibility tensor such as (2.9). Such a tensor is derived from the Vlasov equation (2.57) after linearization and Fourier transformation. In addition, the plasma is assumed to be immersed in a uniform constant magnetic field, which generates anisotropy in the conductivity tensor. Retaining all thermal effects - by solving the Vlasov equation - and including a constant magnetic field, this susceptibility tensor is then appropriate to describe EBWs. An analytical expression for the susceptibility tensor can be obtained in the non-relativistic limit, when the zero-order, equilibrium distribution function for each species $s$ is a non-relativistic Maxwellian

$$f_{0s}(\mathbf{v}) = f_{\mathrm{M}s}^{\mathrm{nr}}(\mathbf{v}) \equiv \frac{n_s}{(2\pi T_s/m_s)^{3/2}} \exp\left[-\frac{m_s v^2}{2T_s}\right] \tag{2.58}$$

where $n_s$ and $T_s$ are the density and temperatures for the species $s$. The non-relativistic Vlasov equation

$$\frac{\partial f_s}{\partial t} + \mathbf{v} \cdot \nabla_{\mathbf{r}} f_s + \frac{q_s}{m_s} \left[ \mathbf{E}(\mathbf{r}, t) + \mathbf{v} \times \mathbf{B}(\mathbf{r}, t) \right] \cdot \nabla_{\mathbf{v}} f_s = 0 \tag{2.59}$$

is then linearized and used to derive the conductivity tensor.

### Non-relativistic hot plasma susceptibility tensor

The hot plasma susceptibility tensor $\mathbb{X}_{\mathrm{M}}(\mathbf{k}, \omega)$ for a non-relativistic plasma has been derived for example in [58] and [60] and is recalled here. The plasma frequency for the species $s$ is given by

$$\omega_{ps} = \sqrt{\frac{q_s^2 n_s}{\varepsilon_0 m_s}} \tag{2.60}$$

The particle thermal velocity is

$$v_{ts} = \sqrt{2} v_{Ts} \text{ with } v_{Ts} = \sqrt{k T_s / m_s} \tag{2.61}$$

The constant uniform magnetic field is assumed to be in the $\widehat{z}$ direction

$$\overline{\mathbf{B}} = \overline{B} \widehat{z} \tag{2.62}$$

and we define the rest mass cyclotron frequency for the species $s$:

$$\omega_{cs} = \frac{|q_s| \overline{B}}{m_s} \tag{2.63}$$

where $\overline{B}$ is the magnitude of the static magnetic field. The $\widehat{x}$ direction is chosen such that the $\mathbf{k}$ vector lies in the $(\widehat{x}, \widehat{z})$ plane

$$\mathbf{k} = k_{\perp} \widehat{x} + k_{\parallel} \widehat{z} \tag{2.64}$$

The susceptibility tensor is then the sum over the contribution of all species $s$

$$\mathbb{X}_{\mathrm{M}}(\mathbf{k},\omega) = \sum_{s} \mathbb{X}_{\mathrm{M}}^{s}(\mathbf{k},\omega) \tag{2.65}$$

where the susceptibility tensor $\mathbb{X}_{\mathrm{M}}^{s}(\mathbf{k},\omega)$ associated with a given species $s$ is the sum over contributions from all harmonic numbers $n$

$$\mathbb{X}_{\mathrm{M}}^{s}(\mathbf{k},\omega) = \frac{\omega_{ps}^{2}}{\omega^{2}}\zeta_{0s} \sum_{n=-\infty}^{\infty} \mathbb{Y}_{\mathrm{M}}^{s,n} \tag{2.66}$$

which decompose as

$$\begin{aligned}
Y_{\mathrm{M}xx}^{s,n} &= \frac{n^{2}}{\lambda_{s}}\Gamma_{ns}Z_{ns} \\
Y_{\mathrm{M}yy}^{s,n} &= \left(\frac{n^{2}}{\lambda_{s}}\Gamma_{ns} - 2\lambda_{s}\Gamma'_{ns}\right) Z_{ns} \\
Y_{\mathrm{M}zz}^{s,n} &= -\Gamma_{ns}\zeta_{ns}Z'_{ns} \\
Y_{\mathrm{M}xy}^{s,n} &= i\sigma_{s}n\Gamma'_{ns}Z_{ns} \\
Y_{\mathrm{M}yx}^{s,n} &= -Y_{\mathrm{M}xy}^{s,n} \\
Y_{\mathrm{M}xz}^{s,n} &= -\sigma_{\parallel}\frac{n}{\sqrt{2\lambda_{s}}}\Gamma_{ns}Z'_{ns} \\
Y_{\mathrm{M}zx}^{s,n} &= Y_{\mathrm{M}xz}^{s,n} \\
Y_{\mathrm{M}yz}^{s,n} &= i\sigma_{s}\sigma_{\parallel}\sqrt{\frac{\lambda_{s}}{2}}\Gamma'_{ns}Z'_{ns} \\
Y_{\mathrm{M}zy}^{s,n} &= -Y_{\mathrm{M}zy}^{s,n}
\end{aligned} \tag{2.67}$$

with

$$\begin{aligned}
\Gamma_{ns} &= e^{-\lambda_{s}} I_{n}(\lambda_{s}) && \text{(a)} \\
Z_{ns} &= Z(\zeta_{ns}) && \text{(b)} \\
\lambda_{s} &= \left(\frac{k_{\perp}v_{Ts}}{\omega_{cs}}\right)^{2} = (k_{\perp}\rho_{Ts})^{2} && \text{(c)} \\
\zeta_{ns} &= \frac{\omega - n\omega_{cs}}{|k_{\parallel}|\, v_{ts}} && \text{(d)} \\
\sigma_{\parallel} &= \operatorname{sign}(k_{\parallel}) && \text{(e)} \\
\sigma_{s} &= \operatorname{sign}(q_{s}) && \text{(f)}
\end{aligned} \tag{2.68}$$

where $I_n$ is the modified Bessel function of the first kind, $Z$ is the plasma dispersion function, and $\rho_{Ts}$ is the thermal Larmor radius for the species $s$.

### Hermitian part of the susceptibility tensor

In a non-relativistic hot plasma, the susceptibility tensor is given by (2.66). The hermitian part of $\mathbb{X}_{\mathrm{M}}^{s}(\mathbf{k}_r, \omega_r)$, which is used to calculate energy flow density through expressions (2.39) (2.15) and (2.10), is expressed as

$$\mathbb{X}_{\mathrm{M}}^{H,s}(\mathbf{k}, \omega) = \frac{\omega_{ps}^2}{\omega^2}\zeta_{0s} \sum_{n=-\infty}^{\infty} \mathbb{Y}_{\mathrm{M}}^{H,s,n} \tag{2.69}$$

where $\mathbb{Y}_{\mathrm{M}}^{H,s,n}$ is the hermitian part of $\mathbb{Y}_{\mathrm{M}}^{s,n}$ (2.67) and decomposes as

$$\begin{aligned}
Y_{\mathrm{M}xx}^{H,s,n} &= \frac{n^2}{\lambda_s}\Gamma_{ns}\,\mathrm{Re}\,(Z_{ns}) \\
Y_{\mathrm{M}yy}^{H,s,n} &= \left(\frac{n^2}{\lambda_s}\Gamma_{ns} - 2\lambda_s\Gamma'_{ns}\right)\mathrm{Re}\,(Z_{ns}) \\
Y_{\mathrm{M}zz}^{H,s,n} &= -\Gamma_{ns}\zeta_{ns}\,\mathrm{Re}\,(Z'_{ns}) \\
Y_{\mathrm{M}xy}^{H,s,n} &= i\sigma_s n\Gamma'_{ns}\,\mathrm{Re}\,(Z_{ns}) \\
Y_{\mathrm{M}yx}^{H,s,n} &= \left(Y_{\mathrm{M}xy}^{H,s,n}\right)^* = -Y_{\mathrm{M}xy}^{H,s,n} \\
Y_{\mathrm{M}xz}^{H,s,n} &= -\sigma_{\parallel}\frac{n}{\sqrt{2\lambda_s}}\Gamma_{ns}\,\mathrm{Re}\,(Z'_{ns}) \\
Y_{\mathrm{M}zx}^{H,s,n} &= \left(Y_{\mathrm{M}xz}^{H,s,n}\right)^* = Y_{\mathrm{M}xz}^{H,s,n} \\
Y_{\mathrm{M}yz}^{H,s,n} &= i\sigma_s\sigma_{\parallel}\sqrt{\frac{\lambda_s}{2}}\Gamma'_{ns}\,\mathrm{Re}\,(Z'_{ns}) \\
Y_{\mathrm{M}zy}^{H,s,n} &= \left(Y_{\mathrm{M}yz}^{H,s,n}\right)^* = -Y_{\mathrm{M}yz}^{H,s,n}
\end{aligned} \tag{2.70}$$

### Antihermitian part of the susceptibility tensor

In a non-relativistic hot plasma, the susceptibility tensor is given by (2.66). The anti-hermitian part of $\mathbb{X}_{\mathrm{M}}^{s}(\mathbf{k}_r, \omega_r)$, which is used to calculate damping through expression (2.51), is expressed as

$$\mathbb{X}_{\mathrm{M}}^{A,s}(\mathbf{k}, \omega) = \frac{\omega_{ps}^2}{\omega^2}\zeta_{0s} \sum_{n=-\infty}^{\infty} \mathbb{Y}_{\mathrm{M}}^{A,s,n} \tag{2.71}$$

where $\mathbb{Y}_{\mathrm{M}}^{A,s,n}$ is the antihermitian part of $\mathbb{Y}_{\mathrm{M}}^{s,n}$ (2.67) and decomposes as

$$
\begin{aligned}
Y_{\mathrm{M}xx}^{A,s,n} &= i\frac{n^2}{\lambda_s}\Gamma_{ns}\,\mathrm{Im}\,(Z_{ns}) \\
Y_{\mathrm{M}yy}^{A,s,n} &= i\left(\frac{n^2}{\lambda_s}\Gamma_{ns} - 2\lambda_s\Gamma'_{ns}\right)\mathrm{Im}\,(Z_{ns}) \\
Y_{\mathrm{M}zz}^{A,s,n} &= -i\Gamma_{ns}\zeta_{ns}\,\mathrm{Im}\,(Z'_{ns}) \\
Y_{\mathrm{M}xy}^{A,s,n} &= -\sigma_s n\Gamma'_{ns}\,\mathrm{Im}\,(Z_{ns}) \\
Y_{\mathrm{M}yx}^{A,s,n} &= -\left(Y_{\mathrm{M}xy}^{A,s,n}\right)^* = -Y_{\mathrm{M}xy}^{A,s,n} \\
Y_{\mathrm{M}xz}^{A,s,n} &= -i\sigma_{\parallel}\frac{n}{\sqrt{2\lambda_s}}\Gamma_{ns}\,\mathrm{Im}\,(Z'_{ns}) \\
Y_{\mathrm{M}zx}^{A,s,n} &= -\left(Y_{\mathrm{M}xz}^{A,s,n}\right)^* = Y_{\mathrm{M}xz}^{A,s,n} \\
Y_{\mathrm{M}yz}^{A,s,n} &= -\sigma_s\sigma_{\parallel}\sqrt{\frac{\lambda_s}{2}}\Gamma'_{ns}\,\mathrm{Im}\,(Z'_{ns}) \\
Y_{\mathrm{M}zy}^{A,s,n} &= -\left(Y_{\mathrm{M}yz}^{A,s,n}\right)^* = -Y_{\mathrm{M}yz}^{A,s,n}
\end{aligned}
\tag{2.72}
$$

We have the following properties of the plasma dispersion function [62] for real arguments

$$
\begin{aligned}
\mathrm{Im}\,(Z_{ns}) &= \sqrt{\pi}e^{-\zeta_{ne}^2} \\
\mathrm{Im}\,(Z'_{ns}) &= -2\zeta_{ns}\sqrt{\pi}e^{-\zeta_{ne}^2}
\end{aligned}
\tag{2.73}
$$

so that $\mathbb{Y}_{\mathrm{M}}^{A,s,n}$ can be rewritten as

$$
\mathbb{Y}_{\mathrm{M}}^{A,s,n} = \widetilde{\mathbb{Y}}_{\mathrm{M}}^{A,s,n}\sqrt{\pi}e^{-\zeta_{ne}^2} \tag{2.74}
$$

where $\widetilde{\mathbb{Y}}_{\mathrm{M}}^{A,s,n}$ decomposes as

$$
\begin{aligned}
\widetilde{Y}_{\mathrm{M}xx}^{A,s,n} &= i\frac{n^2}{\lambda_s}\Gamma_{ns} \\
\widetilde{Y}_{\mathrm{M}yy}^{A,s,n} &= i\left(\frac{n^2}{\lambda_s}\Gamma_{ns} - 2\lambda_s\Gamma'_{ns}\right) \\
\widetilde{Y}_{\mathrm{M}zz}^{A,s,n} &= 2i\Gamma_{ns}\zeta_{ns}^2 \\
\widetilde{Y}_{\mathrm{M}xy}^{A,s,n} &= -\sigma_s n\Gamma'_{ns} \\
\widetilde{Y}_{\mathrm{M}yx}^{A,s,n} &= -\left(\widetilde{Y}_{\mathrm{M}xy}^{A,s,n}\right)^* = -\widetilde{Y}_{\mathrm{M}xy}^{A,s,n} \\
\widetilde{Y}_{\mathrm{M}xz}^{A,s,n} &= 2i\sigma_{\parallel}\zeta_{ns}\frac{n}{\sqrt{2\lambda_s}}\Gamma_{ns} \\
\widetilde{Y}_{\mathrm{M}zx}^{A,s,n} &= -\left(\widetilde{Y}_{\mathrm{M}xz}^{A,s,n}\right)^* = \widetilde{Y}_{\mathrm{M}xz}^{A,s,n} \\
\widetilde{Y}_{\mathrm{M}yz}^{A,s,n} &= 2\sigma_s\sigma_{\parallel}\zeta_{ns}\sqrt{\frac{\lambda_s}{2}}\Gamma'_{ns} \\
\widetilde{Y}_{\mathrm{M}zy}^{A,s,n} &= -\left(\widetilde{Y}_{\mathrm{M}yz}^{A,s,n}\right)^* = -\widetilde{Y}_{\mathrm{M}yz}^{A,s,n}
\end{aligned}
\tag{2.75}
$$

## 2.2 Electrostatic Description of EBWs

The theory of linear plasma waves in a kinetic plasma described in Section 2.1 is used to calculate analytically the EBW characteristics in the electrostatic approximation, which gives an insight in the behavior of EBWs.

In general, for a kinetic plasma, the resolution of the dispersion relation (2.16) involves root finding techniques and requires one to have a good guess for $k_\perp$. It is possible to obtain a good guess for the EBW $k_\perp$ root by solving an approximate dispersion relation, in the electrostatic limit.

Moreover, it is possible to calculate the absorption coefficient and the normalized energy flow density for EBWs in the electrostatic approximations. These calculations will be used to characterize EBW damping in Chapter 5.

### 2.2.1 Electrostatic approximation

In all generality, we can decompose the electric field into its longitudinal $E_{\mathbf{k}L}$ and transverse $\mathbf{E}_{\mathbf{k}T}$ components with respect to the wave vector direction $\widehat{N} \equiv \mathbf{N}/N$

$$\mathbf{E_k} = E_{\mathbf{k}L}\widehat{N} + \mathbf{E}_{\mathbf{k}T} \tag{2.76}$$

Inserting this decomposition in the wave equation (2.13) leads to

$$\left(\mathbb{K} - N^2\mathbb{I}\right) \cdot \mathbf{E}_{\mathbf{k}T} + E_{\mathbf{k}L}\mathbb{K} \cdot \widehat{N} = 0 \tag{2.77}$$

If the following relation is verified for all components of the dielectric tensor

$$N^2 \gg |K_{ij}| \tag{2.78}$$

then the wave equation (2.77) is approximately

$$-N^2\mathbf{E}_{\mathbf{k}T} + E_{\mathbf{k}L}\mathbb{K} \cdot \widehat{N} \simeq 0 \tag{2.79}$$

and, projected on the wave vector direction, leads to an equation for $E_{\mathbf{k}L}$

$$\left(\mathbf{N} \cdot \mathbb{K} \cdot \mathbf{N}\right) E_{\mathbf{k}L} \simeq 0 \tag{2.80}$$

while the equation (2.79) then gives an expression for the transverse field

$$\mathbf{E}_{\mathbf{k}T} \simeq \frac{E_{\mathbf{k}L}}{N^2}\mathbb{K} \cdot \widehat{\mathbf{N}} \tag{2.81}$$

The equation (2.81) with the relation (2.78) leads to $\|\mathbf{E}_{\mathbf{k}T}\| \ll |E_{\mathbf{k}L}|$, and therefore

$$\mathbf{e_k} \simeq \widehat{\mathbf{N}} \tag{2.82}$$

which means that the electric field is mostly longitudinal, or electrostatic. This justifies the names *electrostatic approximation* for the relation (2.78) and *electrostatic wave equation* for (2.80).

### Electrostatic dispersion relation

In order to have a non-trivial solution to the electrostatic wave equation (2.80), it is therefore required that the following relation, called *electrostatic dispersion relation*, be satisfied.

$$D_L(\mathbf{k},\omega) \equiv \mathbf{N}\cdot\mathbb{K}\cdot\mathbf{N} = 0 \tag{2.83}$$

With the normalized wave vector (2.11) and the decomposition (2.64), the electrostatic dispersion relation (2.83) gives

$$N_\perp^2 K_{xx} + N_\perp N_\parallel \left(K_{xz} + K_{zx}\right) + N_\parallel^2 K_{zz} = 0 \tag{2.84}$$

### Energy flow density

In the electrostatic limit for the polarization (2.82), the energy flow density (2.51) becomes

$$\mathbf{\Phi}_\mathbf{k}^{\mathrm{ES}} = -\frac{1}{2}\frac{\partial}{\partial \mathbf{N}}\left(\widehat{\mathbf{N}}\cdot\mathbb{K}^H\cdot\widehat{\mathbf{N}}\right) \tag{2.85}$$

where we used

$$\widehat{\mathbf{N}}\cdot\left(\mathbf{NN} - N^2\mathbb{I}\right)\cdot\widehat{\mathbf{N}} = 0 \tag{2.86}$$

and we obtain

$$\mathbf{\Phi}_\mathbf{k}^{\mathrm{ES}} = -\frac{1}{2}\frac{\partial}{\partial \mathbf{N}}\left(\frac{1}{N^2}\left[N_\perp^2 X_{xx}^H + N_\perp N_\parallel\left(X_{xz}^H + X_{zx}^H\right) + N_\parallel^2 X_{zz}^H\right]\right) \tag{2.87}$$

### Absorption coefficient

In the electrostatic limit for the polarization (2.82), the absorption coefficient (2.51) becomes

$$\alpha_\mathbf{k}^{\mathrm{lin,ES}} = \frac{1}{\|\mathbf{\Phi}_\mathbf{k}\|}\frac{\omega}{cN^2}\left[N_\perp^2 X_{xx}^A + N_\perp N_\parallel\left(X_{xz}^A + X_{zx}^A\right) + N_\parallel^2 X_{zz}^A\right] \tag{2.88}$$

### 2.2.2 High frequency waves

#### Electrostatic dispersion relation for perpendicular propagation

In the case of perpendicular propagation, $N_{\parallel} = 0$ and the dispersion relation reduces to

$$K_{xx} = 0 \tag{2.89}$$

If we consider only high frequencies, in the electron cyclotron range such that $\omega \gg \omega_{pi}, \omega_{ci}$, the ion dynamics can be neglected and (2.89) becomes, using (2.10)

$$1 + X^e_{xx}(\mathbf{k}_{\perp}, \omega) = 0 \tag{2.90}$$

where $\mathbb{X}^e(\mathbf{k}, \omega)$ is the electron contribution to the susceptibility tensor.

#### Energy flow density

Neglecting the ion dynamics, the energy flow density (2.87) becomes

$$\mathbf{\Phi}^{\mathrm{ES}}_{\mathbf{k}} = -\frac{1}{2}\frac{\partial}{\partial \mathbf{N}}\left(\frac{1}{N^2}\left[N_{\perp}^2 X^{H,e}_{xx} + N_{\perp}N_{\parallel}\left(X^{H,e}_{xz} + X^{H,e}_{zx}\right) + N_{\parallel}^2 X^{H,e}_{zz}\right]\right) \tag{2.91}$$

where $\mathbb{X}^{H,e}$ is its antihermitian part of $\mathbb{X}^e$.

#### Absorption coefficient

Neglecting the ion dynamics, the absorption coefficient (2.88) becomes

$$\alpha^{\mathrm{lin,ES}}_{\mathbf{k}} = -i\frac{1}{\|\mathbf{\Phi}_{\mathbf{k}}\|}\frac{\omega}{cN^2}\left[N_{\perp}^2 X^{A,e}_{xx} + N_{\perp}N_{\parallel}\left(X^{A,e}_{xz} + X^{A,e}_{zx}\right) + N_{\parallel}^2 X^{A,e}_{zz}\right] \tag{2.92}$$

where $\mathbb{X}^{A,e}$ is the antihermitian part of $\mathbb{X}^e$.

### 2.2.3 Non-relativistic kinetic plasma

#### Dispersion relation

In a non-relativistic kinetic plasma, the susceptibility tensor is given by (2.66). The $X^e_{\mathrm{M}xx}(\mathbf{k},\omega)$ component is, using (2.67) and (2.68-a)

$$\begin{aligned} X^e_{\mathrm{M}xx}(\mathbf{k},\omega) &= \frac{\omega_{pe}^2}{\omega^2}\zeta_{0e}\sum_{n=-\infty}^{\infty} Y^{e,n}_{\mathrm{M}xx} \\ &= \frac{\omega_{pe}^2}{\omega^2}\zeta_{0e}\sum_{n=-\infty}^{\infty}\frac{n^2}{\lambda_e}e^{-\lambda_e}I_n(\lambda_e)\,Z(\zeta_{ne}) \end{aligned} \tag{2.93}$$

with

$$\begin{aligned} \lambda_e &= \left(\frac{k_\perp v_{Te}}{\omega_{ce}}\right)^2 \\ \zeta_{ne} &= \frac{\omega - n\omega_{ce}}{|k_\parallel|\,v_{te}} \end{aligned} \tag{2.94}$$

In the limit of perpendicular propagation, $k_\parallel \to 0$ and the factor $\zeta_{ne}$ diverges unless the wave frequency is exactly at a cyclotron harmonic resonance, in which case relativistic effects must be included. It is thus necessary to do an asymptotic expansion of the plasma dispersion function $Z(\zeta_{ne})$ for large arguments. This expansion gives for $|\zeta_{ne}| \gg 1$ [62]

$$Z(\zeta_{ne}) = -\frac{1}{\zeta_{ne}}\left[1+\frac{1}{2\zeta_{ne}^2}+\mathcal{O}\left(\frac{1}{\zeta_{ne}^4}\right)\right] \tag{2.95}$$

so that, in the limit $k_\parallel \to 0$, the electrostatic dispersion relation (2.90) becomes

$$1-\frac{\omega_{pe}^2}{\omega^2}\frac{e^{-\lambda_e}}{\lambda_e}\sum_{n=-\infty}^{\infty} I_n(\lambda_e)\frac{n^2\omega}{\omega-n\omega_{ce}} = 0 \tag{2.96}$$

Defining the normalized quantities

$$\begin{aligned} \Psi &= \frac{\omega_{pe}^2}{\omega_{ce}^2} \\ q &= \frac{\omega}{\omega_{ce}} \end{aligned} \tag{2.97}$$

we obtain

$$1 = \Psi \frac{e^{-\lambda_e}}{\lambda_e} \sum_{n=-\infty}^{\infty} I_n(\lambda_e) \frac{1}{q} \frac{n^2}{q-n} \tag{2.98}$$

which becomes

$$1 = 2\Psi \frac{e^{-\lambda_e}}{\lambda_e} \sum_{n=1}^{\infty} I_n(\lambda_e) \frac{n^2}{q^2 - n^2} \tag{2.99}$$

where we used the following property of the Bessel functions

$$I_{-n}(z) = I_n(z) \tag{2.100}$$

Equation (2.99) is the electrostatic EBW dispersion relation, which can solve for $q^2(\lambda_e)$ to give $\omega(k_\perp)$. It has an infinite number of roots. However, if we consider only the $N$ first harmonics, the equation (2.99) is a $N^{\text{th}}$ order polynomial for $q^2(\lambda_e)$, which has therefore $N$ roots. Polynomial equations are easily solved by standard numerical routines, and our polynomial was implemented in a numerical code to solve the electrostatic dispersion relation. We found that a $N^{\text{th}}$ order polynomial is sufficient to accurately solve for the $N-1$ first roots, while the correct determination of the $N^{\text{th}}$ root requires at least the $(N+1)^{\text{th}}$ order polynomial.

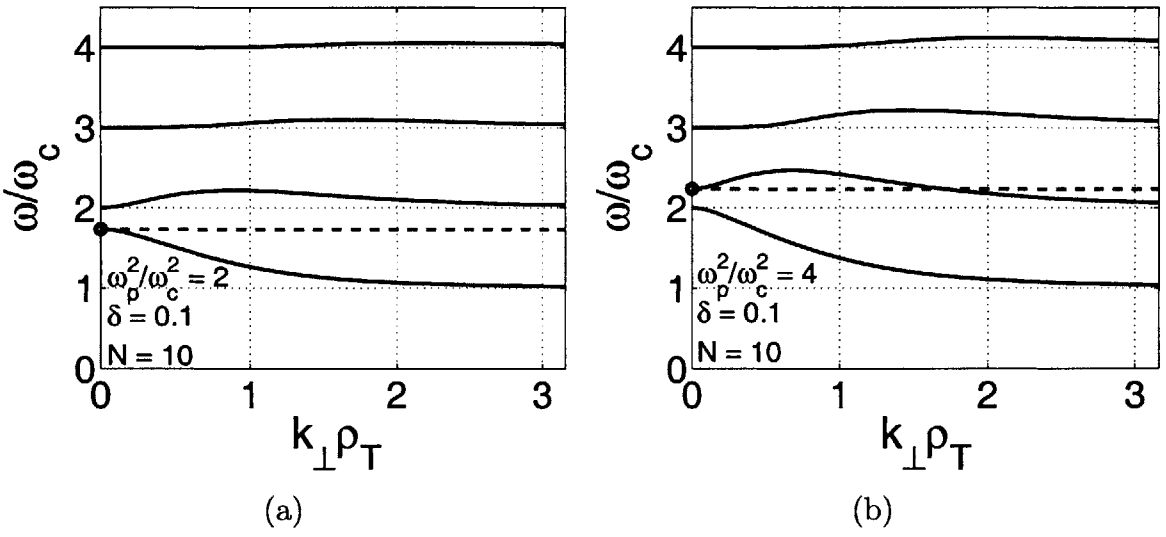


Figure 2-1: Electrostatic EBW roots calculated with $N = 10$ for (a) $\omega_{pe}^2 = 2\omega_{ce}^2$ and (b) $\omega_{pe}^2 = 4\omega_{ce}^2$. The thermal velocity is expressed as $v_{Te} = \delta c$, where we assumed $\delta = 0.1$.

On Figure 2-1 we show the four first electrostatic EBW roots calculated using $N = 10$ and $\Psi = 2$ (graph a) and $\Psi = 4$ (graph b) respectively. The dashed red line corresponds to the location of the upper-hybrid resonance (UHR) where EBWs can be mode-converted from electromagnetic EC waves. We see a structural difference for the EBW root issued at the UHR between the two graphs, depending on whether the UHR is below the second harmonic (a) where the root remains below the UHR frequency towards the first cyclotron harmonic ($q = 1$), or above the second harmonic (b) where the root starts above the UHR frequency and then crosses this frequency towards the second cyclotron harmonic ($q = 2$). The transition occurs for $q_{\text{UHR}} = 2$, which means for $\omega_{\text{UHR}} = 2\omega_{ce}$ or for $\Psi = 3$ since the UHR frequency is given by

$$\omega_{\text{UHR}}^2 = \omega_{pe}^2 + \omega_{ce}^2 \tag{2.101}$$

Because this dispersion relation was derived in the electrostatic approximation, the solution fails when electromagnetic effects becomes important. Clearly, we do not expect the electrostatic approximation to be valid when the phase velocity of the wave becomes of the order of the speed of light, that is, for $\omega \gtrsim k_\perp c$. Equivalently, it means that our solution fails for

$$k_\perp \rho_{Te} \lesssim \beta_{Te} q \tag{2.102}$$

where

$$\beta_{Te} = \frac{v_{Te}}{c} \tag{2.103}$$

In particular, it is not valid near the MCR. In Section 2.3, the full electromagnetic dispersion relation (2.16) will be solved for the non-relativistic hot plasma electron susceptibility tensor (2.66), and we will investigate the validity of the electrostatic root when compared to the exact solution of the dispersion relation.

### Energy flow density

The high-frequency electrostatic energy flow density (2.91) becomes, in a non-relativistic kinetic plasma (2.69)

$$\mathbf{\Phi}_{\mathbf{k}}^{\mathrm{ES}} = \sum_{n=-\infty}^{\infty} \mathbf{\Phi}_{\mathbf{k},n}^{\mathrm{ES}} \tag{2.104}$$

where the contribution of the harmonic $n$ is

$$\mathbf{\Phi}_{\mathbf{k},n}^{\mathrm{ES}} = -\frac{1}{2}\frac{\omega_{pe}^2}{\omega^2}\frac{\partial}{\partial \mathbf{N}}\left(\frac{\zeta_{0e}}{N^2}\left[N_\perp^2 Y_{xx}^{H,e} + N_\perp N_\parallel \left(Y_{xz}^{H,e} + Y_{zx}^{H,e}\right) + N_\parallel^2 Y_{zz}^{H,e}\right]\right) \tag{2.105}$$

which, using (2.70), is explicitly expressed as

$$\mathbf{\Phi}_{\mathbf{k},n}^{\mathrm{ES}} = -\frac{1}{2}\frac{\omega_{pe}^2}{\omega^2}\frac{\partial}{\partial \mathbf{N}}\left(\frac{n^2 N_\perp^2 \Gamma_{ne}}{\sqrt{2}\left|N_\parallel\right|\beta_{Te} N^2 \lambda_e}\left[\mathrm{Re}\left(Z_{ne}\right) - \left|N_\parallel\right|\beta_{Te}\frac{(1+y_n)}{\sqrt{2}y_n^2}\,\mathrm{Re}\left(Z'_{ne}\right)\right]\right) \tag{2.106}$$

where we used the definitions (2.94) rewritten as

$$\begin{aligned} \lambda_e &= N_\perp^2 \frac{\omega^2}{\omega_{ce}^2}\beta_{Te}^2 \\ \zeta_{ne} &= \frac{1 - \dfrac{n\omega_{ce}}{\omega}}{\sqrt{2}\left|N_\parallel\right|\beta_{Te}} \\ \beta_{Te} &= \frac{v_{Te}}{c} \end{aligned} \tag{2.107}$$

and the definition

$$y_n = \frac{n\omega_{ce}}{\omega} \tag{2.108}$$

Using the following differential property of the plasma dispersion function

$$Z'_{ne}\left(\zeta_{ne}\right) = -2\left[1 + \zeta_{ne} Z\left(\zeta_{ne}\right)\right] \tag{2.109}$$

the expression (2.106) simplifies to

$$\mathbf{\Phi}_{\mathbf{k},n}^{\mathrm{ES}} = -\frac{1}{2}\frac{\omega_{pe}^2}{\omega^2}\frac{\partial}{\partial \mathbf{N}}\left(\frac{n^2 N_\perp^2 \Gamma_{ne}}{N^2 \lambda_e y_n^2}\left[\frac{\mathrm{Re}\left(Z_{ne}\right)}{\sqrt{2}\left|N_\parallel\right|\beta_{Te}} + (1+y_n)\right]\right) \tag{2.110}$$

Away from the resonance, we have $|\zeta_{ne}| \gg 1$ and we can use the expansion (2.95) for the plasma dispersion function, which gives $\mathrm{Re}\,(Z_{ne}) \simeq -1/\zeta_{ne}$ so that, using $N_\perp \simeq N$, we find

$$\mathbf{\Phi}^{\mathrm{ES}}_{\mathbf{k},n} \simeq \frac{1}{2}\frac{\omega_{pe}^2}{\omega^2}\frac{\partial}{\partial \mathbf{N}}\left(\frac{n^2}{(1-y_n)}\frac{\Gamma_{ne}}{\lambda_e}\right) \tag{2.111}$$

Adding all harmonic contributions, the total energy flow density can be written as (2.104)

$$\mathbf{\Phi}^{\mathrm{ES}}_{\mathbf{k},n} \simeq -\frac{1}{2}\frac{\partial}{\partial \mathbf{N}}\left(1 - \frac{\omega_{pe}^2}{\omega^2}\frac{e^{-\lambda_e}}{\lambda_e}\sum_{n=-\infty}^{\infty} I_n(\lambda_e)\frac{n^2\omega}{(\omega - n\omega)}\right) \tag{2.112}$$

and we find that in the limit $|\zeta_{ne}| \gg 1$, the normalized energy flow density (2.112) is related to the electrostatic dispersion relation (2.96) in accordance with the relation (2.39).

In the non-relativistic electrostatic limit, far from resonances, there is no flow in the parallel direction, since $\Gamma_{ne}/\lambda_e$ is independent of $N_\parallel$. The perpendicular component of the energy flow density becomes

$$\mathbf{\Phi}^{\mathrm{ES}}_{\mathbf{k}\perp} = \frac{1}{2}\frac{\omega_{pe}^2}{\omega^2}\sum_{n=-\infty}^{\infty}\frac{n^2}{(1-y_n)}\frac{\partial}{\partial N_\perp}\left(\frac{\Gamma_{ne}}{\lambda_e}\right) \tag{2.113}$$

which can be rewritten as

$$\mathbf{\Phi}^{\mathrm{ES}}_{\mathbf{k}\perp} = \frac{\omega_{pe}^2}{\omega_{ce}^2}\beta_{Te}\widetilde{\Phi}(q,\lambda_e) \tag{2.114}$$

with

$$\begin{aligned}\widetilde{\Phi}(q,\lambda_e) &= \sum_{n=-\infty}^{\infty}\frac{n^2\sqrt{\lambda_e}}{q-n}\frac{\partial}{\partial\lambda_e}\left(\frac{\Gamma_{ne}}{\lambda_e}\right) \\ &= 2\sum_{n=1}^{\infty}\frac{n^2 q\sqrt{\lambda_e}}{q^2-n^2}\frac{\partial}{\partial\lambda_e}\left(\frac{\Gamma_{ne}}{\lambda_e}\right)\end{aligned} \tag{2.115}$$

We will show in Section 2.3 that $\lambda_e = (k_\perp\rho_{Te})^2$ is rather insensitive to variations in the temperature and density (except near the MCR). Therefore, the perpendicular power flow of EBWs is roughly proportional to the density and the thermal velocity of electrons (2.114). The density dependence can be understood in the sense that a higher density means that there are more electrons to coherently transport energy

with the wave.

### Absorption coefficient

The high-frequency electrostatic absorption coefficient (2.92) becomes, in a non-relativistic kinetic plasma (2.71)

$$\alpha_{\mathbf{k}}^{\text{lin,ES}} = \sum_{n=-\infty}^{\infty} \alpha_{\mathbf{k},n}^{\text{lin,ES}} \tag{2.116}$$

where the contribution of the harmonic $n$ is, using (2.74)

$$\alpha_{\mathbf{k},n}^{\text{lin,ES}} = -i \frac{1}{\|\mathbf{\Phi}_{\mathbf{k}}\|} \frac{\omega}{cN^2} \frac{\omega_{pe}^2}{\omega^2} \zeta_{0e} \sqrt{\pi} e^{-\zeta_{ne}^2} \left[ N_\perp^2 \widetilde{Y}_{\text{M}xx}^{A,e,n} + N_\perp N_\parallel \left( \widetilde{Y}_{\text{M}xz}^{A,e,n} + \widetilde{Y}_{\text{M}zx}^{A,e,n} \right) + N_\parallel^2 \widetilde{Y}_{\text{M}zz}^{A,e,n} \right] \tag{2.117}$$

which, using (2.75), is explicitly expressed as

$$\alpha_{\mathbf{k},n}^{\text{lin,ES}} = \frac{1}{\|\mathbf{\Phi}_{\mathbf{k}}\|} \frac{\omega}{cN^2} \frac{\omega_{pe}^2}{\omega^2} \zeta_{0e} \sqrt{\pi} e^{-\zeta_{ne}^2} \frac{\Gamma_{ne}}{2\lambda_e} \left[ \sqrt{2} N_\perp n + 2\sqrt{\lambda_e} \left| N_\parallel \right| \zeta_{ne} \right]^2 \tag{2.118}$$

With the definitions (2.107) and (2.108), we find

$$\sqrt{2} N_\perp n + 2\sqrt{\lambda_e} \left| N_\parallel \right| \zeta_{ne} = \sqrt{2} N_\perp \frac{\omega}{\omega_{ce}} \tag{2.119}$$

so that we obtain

$$\alpha_{\mathbf{k},n}^{\text{lin,ES}} = \sqrt{\frac{\pi}{2}} \frac{1}{\|\mathbf{\Phi}_{\mathbf{k}}\|} \frac{\omega}{c} \frac{\omega_{pe}^2}{\omega_{ce}^2} \frac{1}{\left| N_\parallel \right| \beta_{Te}} \frac{\Gamma_{ne}}{\lambda_e} \exp \left[ -\frac{(1 - y_n)^2}{2 N_\parallel^2 \beta_{Te}^2} \right] \tag{2.120}$$

where we used $N_\perp \simeq N$.

We see that the $n^{\text{th}}$ harmonic contribution of the absorption coefficient includes a Gaussian term that peaks at the resonance ($y_n = 1$) and is dominated by magnetic field variations.

The expression (2.114) for the power flow is valid only far from resonances, where $|\zeta_{ne}| \gg 1$. However, more detailed studies of the plasma dispersion function show that the the expansion for large arguments remains valid down to $|\zeta_{ne}| \gtrsim 3$. In that

case, inserting (2.114) in (2.120) gives (since there is no parallel energy flow in that limit)

$$\alpha_{\mathbf{k},n}^{\text{lin,ES}} = \sqrt{\frac{\pi}{2}} \frac{\omega}{c} \frac{1}{|N_\parallel| \beta_{Te}^2} \frac{\Gamma_{ne}}{\lambda_e \widetilde{\Phi}(q, \lambda_e)} \exp\left[ -\frac{(1-y_n)^2}{2N_\parallel^2 \beta_{Te}^2} \right] \tag{2.121}$$

and we see that unlike ECWs, the absorption of EBWs does not depend upon the density.

### Optical depth and EBW absorption

We assume that the plasma is in a slab geometry, and that the inhomogeneity scale length is much larger than the wavelength, such that the results from this section are valid in the WKB approximation. The magnetic field, in the uniform $\widehat{\mathbf{z}}$ direction, is a slowly varying (and monotonically increasing) function of $x$. All other plasma parameters are assumed to be constant.

The optical depth defined as the integral of the absorption coefficient along the propagation path of the wave across the resonance. For a given mode $(\omega, \mathbf{k})$ and a given cylotron resonance harmonic $n$, it is defined as

$$\tau_{\mathbf{k},n} = \int_{-\infty}^{\infty} ds\ \alpha_{\mathbf{k},n} \tag{2.122}$$

where $s$ is the distance along the propagation path, in the direction of the group velocity and the power flow $\mathbf{\Phi}_\mathbf{k}$. Because of the slab symmetry, the power flow is in the $(\widehat{\mathbf{x}}, \widehat{\mathbf{z}})$ plane and thus

$$\frac{dx}{ds} = \frac{|\Phi_{\mathbf{k}\perp}|}{\|\mathbf{\Phi}_\mathbf{k}\|} \tag{2.123}$$

From the definition of $y_n$ (2.108), we find, using $y_n \simeq 1$

$$\frac{dy_n}{dx} \simeq \frac{1}{L_B} \tag{2.124}$$

where $L_B$ is the magnetic field variation scalelength. We obtain

$$\tau_{\mathbf{k},n} = \int_{-\infty}^{\infty} dy_n \frac{\|\mathbf{\Phi}_\mathbf{k}\|}{|\Phi_{\mathbf{k}\perp}|} L_B \alpha_{\mathbf{k},n} \tag{2.125}$$

We also define the parameter

$$p_n = \frac{1 - y_n}{\beta_{Te} N_{\|}} \tag{2.126}$$

which measures the distance from resonance ($y_n = 1$) in terms of magnetic field variation, and accounts for the Doppler shift effect through the term $\beta_{Te} N_{\|}$. We can rewrite (2.125) as

$$\tau_{\mathbf{k},n} = \int_{-\infty}^{\infty} dp_n \, \beta_{Te} \left| N_{\|} \right| \frac{\|\mathbf{\Phi}_{\mathbf{k}}\|}{|\Phi_{\mathbf{k}\perp}|} L_B \alpha_{\mathbf{k},n} \tag{2.127}$$

Because $\lambda_e$ is very different for HBF and LBF approaches to the resonance, we calculate the two contribution to $\tau_{\mathbf{k},n}$ separately and define the optical half-depth

$$\begin{aligned} \tau_{\mathbf{k},n}^{\mathrm{LBF}} &= \textstyle\int_0^{\infty} dp_n \, \beta_{Te} \left| N_{\|} \right| \frac{\|\mathbf{\Phi}_{\mathbf{k}}\|}{|\Phi_{\mathbf{k}\perp}|} L_B \alpha_{\mathbf{k},n} && \text{for LBF approach } (y_n < 1) \\ \tau_{\mathbf{k},n}^{\mathrm{HBF}} &= \textstyle\int_{-\infty}^{0} dp_n \, \beta_{Te} \left| N_{\|} \right| \frac{\|\mathbf{\Phi}_{\mathbf{k}}\|}{|\Phi_{\mathbf{k}\perp}|} L_B \alpha_{\mathbf{k},n} && \text{for HBF approach } (y_n > 1) \end{aligned} \tag{2.128}$$

On each side, the values for $\lambda_e$ and $|\Phi_{\mathbf{k}\perp}|$ can be considered as being approximately constant, and the variations of the other factors outside the exponential in (2.128) can be neglected compared to the strong variations of the Gaussian term, such that we can approximately integrate (2.128) using the expression (2.120) and find

$$\begin{aligned} \tau_{\mathbf{k},n}^{\mathrm{LBF}} &= \frac{\pi}{2} \frac{\omega}{c} \frac{\omega_{pe}^2}{\omega_{ce}^2} \frac{L_B}{|\Phi_{\mathbf{k}\perp}|_{\mathrm{LBF}}} \left[ \frac{\Gamma_{ne}}{\lambda_e} \right]_{\mathrm{LBF}} && \text{for LBF approach } (y_n < 1) \\ \tau_{\mathbf{k},n}^{\mathrm{HBF}} &= \frac{\pi}{2} \frac{\omega}{c} \frac{\omega_{pe}^2}{\omega_{ce}^2} \frac{L_B}{|\Phi_{\mathbf{k}\perp}|_{\mathrm{HBF}}} \left[ \frac{\Gamma_{ne}}{\lambda_e} \right]_{\mathrm{HBF}} && \text{for HBF approach } (y_n > 1) \end{aligned} \tag{2.129}$$

The optical half-depth $\tau_{\mathbf{k},n}$ will be evaluated in Section 5.1.6, where we will show that $\tau_{\mathbf{k},n}^{\mathrm{LBF}} \gg 1$, which means that EBWs are completely absorbed at harmonics of the cyclotron frequency.

## 2.3 Characteristics of Electron Bernstein Waves

In this section, we calculate the wave characteristics using the full electromagnetic kinetic plasma susceptibility tensor (2.66) for electrons $\mathbb{X}_{\mathrm{M}}^{e}(\mathbf{k},\omega)$ in (2.10) and (2.15). The solution is obtained numerically using the code *R2D2* [13]. The guess for finding the appropriate root of the dispersion relation is provided by the electrostatic root (2.99) for EBWs. Once the appropriate $k_\perp$ roots of the dispersion relation (2.16) have been found, the polarization vector $\mathbf{e_k} = \mathbf{E_k}/\left\|\mathbf{E_k}\right\|$ can be obtained by calculating the normalized eigenvectors of the wave equation (2.14) for the mode $(\omega,\mathbf{k})$. The power flow density $\mathbf{s_k}$ and the density of power dissipated $P_\mathbf{k}$ are obtained using the expressions (2.34) and (2.45) respectively.

In this section, we focus in particular on the wave characteristics that enter the RF quasilinear diffusion coefficient (3.192) and thus determine the wave-particle interaction. These are the normalized components of the wave vector $N_\parallel$ and $k_\perp\rho_{Te}$, the polarization vector $\mathbf{e_k}$, and the normalied perpendicular power flow $\Phi_{\mathbf{k}\perp} = \left\|\mathbf{\Phi_k}\right\|$, which is also a measure of the electric field amplitude for a given incident power density, since $\Phi_{\mathbf{k}\perp}^{-1} \propto \left\|\mathbf{E_k}\right\|^2 / \left\|\mathbf{s}_{\mathbf{k}\perp}\right\|$ (2.36). For comparison, electromagnetic waves in vacuum have $\Phi_\mathbf{k}^{-1} = 1$.

We calculate the EBW characteristics assuming a fixed frequency $\omega_0/(2\pi) = 14$ GHz, as a function of $N_\parallel$ and the equilibrium properties of the plasma, namely the density $n_e$, the temperature $T_e$ and the static magnetic field $B$ or, equivalently, the following normalized parameters:

- the squared ratio of the plasma frequency to the wave frequency, proportional to $n_e$

$$\alpha^2 = \frac{\omega_{pe}^2}{\omega^2} \propto n_e \tag{2.130}$$

- the ratio of the cyclotron frequency to the wave frequency, proportional to $B$

$$b = \frac{\omega_{ce}}{\omega} \propto B \tag{2.131}$$

- the ratio of the thermal velocity to the speed of light, proportional to $\sqrt{T_e}$

$$\beta_{Te} = \frac{v_{Te}}{c} \propto \sqrt{T_e} \tag{2.132}$$

Our nominal parameters are $\alpha_0^2 = 10$, $b_0 = 0.6$ and $\beta_{Te0} = 0.05$. For the frequency $\omega_0$, these parameters correspond to $n_{e0} = 2.4 \times 10^{19}$ m$^{-3}$, $T_{e0} = 1.3$ keV, and $B = 0.3$ T. They are typical of core parameters in a NSTX-type plasma. Note that the value $b_0 = 0.6$ means that the closest cyclotron harmonic is $n = 2$ (which occurs at $b = 0.5$).

Results from *R2D2* will be compared to those obtained within the electrostatic approximation in Section 2.2 with $N_\parallel = 0$. In the electrostatic approximation, the electric field is assumed to be longitudinal, and therefore the polarization vector $\mathbf{e}^{\mathrm{ES}}$ is simply (2.82)

$$\mathbf{e}_{\mathbf{k}}^{\mathrm{ES}} = \widehat{\mathbf{N}} \tag{2.133}$$

The polarization plays an important role in the wave-particle interaction, where the diffusion coefficient depends on the rotating field and parallel components of the polarization vector, defined as

$$\begin{aligned} e_{\mathbf{k},+,} &= \frac{e_{\mathbf{k},x} + i e_{\mathbf{k},y}}{\sqrt{2}} \\ e_{\mathbf{k},-} &= \frac{e_{\mathbf{k},x} - i e_{\mathbf{k},y}}{\sqrt{2}} \\ e_{\mathbf{k},\parallel} &= e_{\mathbf{k},z} \end{aligned} \tag{2.134}$$

In the electrostatic approximation, the components of $\mathbf{e}_{\mathbf{k}}^{\mathrm{ES}}$ (2.133) are then

$$\begin{aligned} e_{\mathbf{k},+}^{\mathrm{ES}} &= \frac{N_\perp}{\sqrt{2}N} \\ e_{\mathbf{k},-}^{\mathrm{ES}} &= \frac{N_\perp}{\sqrt{2}N} \\ e_{\mathbf{k},\parallel}^{\mathrm{ES}} &= \frac{N_\parallel}{N} \end{aligned} \tag{2.135}$$

We anticipate that our analytic description in the electrostatic approximation is expected to fail when the large argument expansion (2.95) of the plasma dispersion function becomes invalid. In fact, a detailed study of the dispersion function shows

that the expansion fails completely for $|\zeta_{ne}| \lesssim 1$, that is,

$$\frac{|1 - nb|}{|N_{\|}|\,\beta_{Te}} \lesssim \sqrt{2} \tag{2.136}$$

In that case, the imaginary part of the plasma dispersion function, which goes like $\exp[-\zeta_{ne}^2]$ [62], is expected to become significant, and therefore strong damping of the EBWs should occur. This occurs near cyclotron resonances where $b \simeq 1/n$. The presence of $|N_{\|}|$ and $\beta_{Te}$ in the denominator is a signature of the Doppler-shift effect.

### 2.3.1 Effect of $N_{\|}$ on EBW characteristics

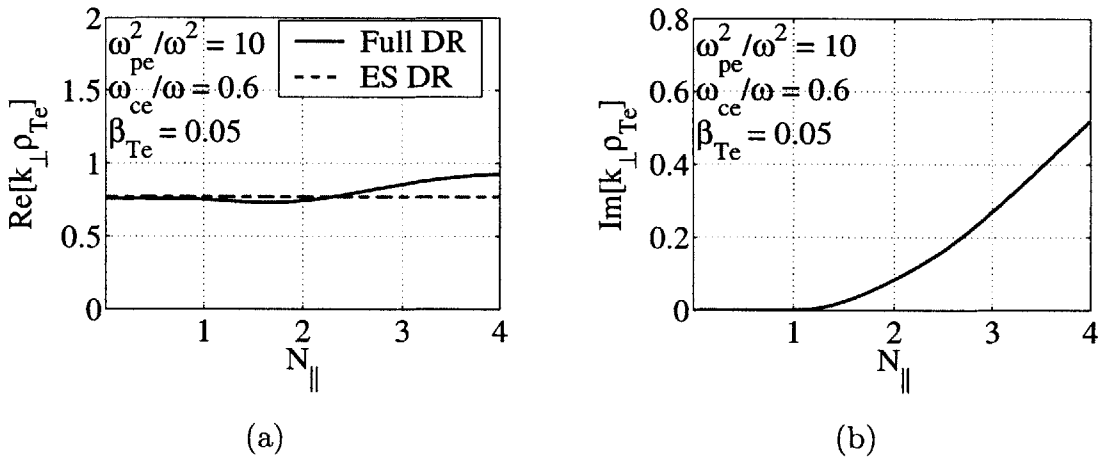


Figure 2-2: Real part (a) and imaginary part (b) of the EBW root $N_{\perp}$ as a function of $N_{\|}$, showed as blue solid lines. On graph (a), the electrostatic EBW root is also shown, as a dashed red line.

The EBW root $k_{\perp}\rho_{Te}$ is calculated as a function of $N_{\|}$ keeping all plasma parameters constant, and displayed as a blue solid line on Fig. 2-2, with the real part on graph (a) and the imaginary part on graph (b). On graph (a), the electrostatic root calculated using (2.99) is shown for comparison, as a red dashed line; it does not vary with $N_{\|}$ since it was derived for $N_{\|} = 0$. We see that the real part of the root calculated from the full dispersion relation does not differ much from the electrostatic root up to $N_{\|} \simeq 1$, and that differences remain small for $N_{\|} \lesssim 3$. We observe that the electrostatic approximation is very good for calculating the real part $k_{\perp}\rho_{Te}$ for

EBWs, since we can hardly distinguish between the roots for $N_\parallel = 0$. For large parallel wave numbers, $N_\parallel > 3$, two approximations made in deriving (2.99) become questionable: (1) the two first terms in (2.84), which are neglected in the $N_\parallel \to 0$ limit, may now have a significant contribution, and (2) the inequality (2.136), which with our parameters gives $|N_\parallel| \gtrsim 3$, is a condition for the failure of our analytical description. In addition, the Doppler broadening of the cyclotron resonance appears as the imaginary part of $N_\perp$ increases, according to (2.136). A significant imaginary part ($\mathrm{Im}\,[k_\perp \rho_{Te}] \sim \mathrm{Re}\,[k_\perp \rho_{Te}]$) means that there is strong resonant damping on electrons, which may also generate current. The role of $N_\parallel$ on EBWCD will be investigated in Chapter 5.

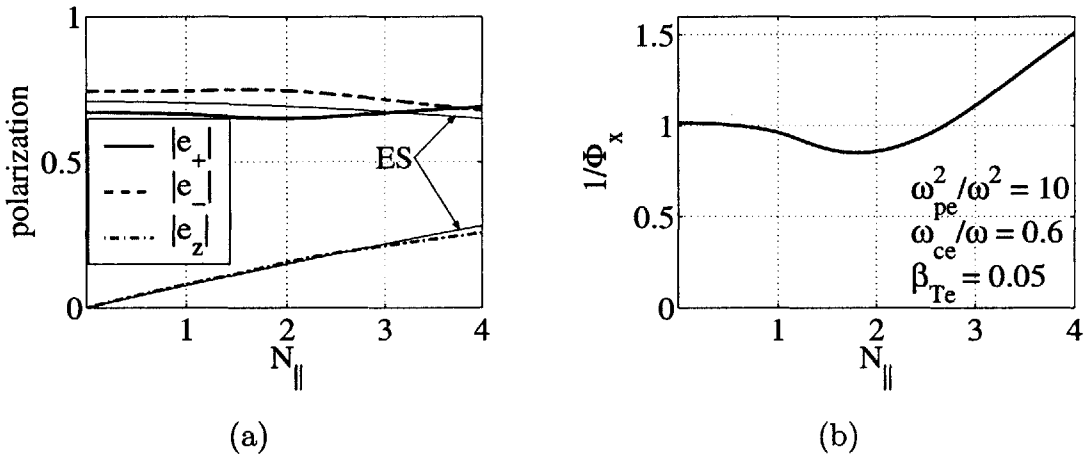


Figure 2-3: Graph (a): components of the polarization vector $\mathbf{e_k}$ as a function of $N_\parallel$. The electrostatic (ES) polarization is shown for comparison. Graph (b): normalized electric field amplitude, $\Phi_{\mathbf{k}\perp}^{-1} \propto \|\mathbf{E}_0\|^2 / \|\mathbf{s}_{\mathbf{k}\perp}\|$, as a function of $N_\parallel$.

The components of the polarization vector are shown on Fig. 2-3 as a function $N_\parallel$ (graph (a)) and we see that the parallel component of the polarization increases linearly with $N_\parallel$ as predicted in the electrostatic limit (2.135), which is a good approximation for the polarization. On graph (b) we show that the normalized energy flow $\Phi_{\mathbf{k}\perp} = \Phi_{\mathbf{k}x}$ does not vary much with $N_\parallel$ for $N_\parallel \lesssim 3$. This is in accordance with the expression (2.114) obtained for $\Phi_{\mathbf{k}\perp}$ in the electrostatic limit. For $N_\parallel > 3$, the weak dissipation limit used in deriving the expression (2.39) for $\Phi_{\mathbf{k}}$ is no longer valid.

To summarize, the EBW root $\mathrm{Re}\,[k_\perp \rho_{Te}]$, polarization $\mathbf{e_k}$ and perpendicular power

flow $\Phi_{\mathbf{k}\perp}$ do not vary much with the parallel wave number $N_\parallel$, except for the parallel component of the polarization which varies as $e_{\mathbf{k},\parallel} \simeq N_\parallel/N$. In the remaining of this section, we will consider a fixed value $N_\parallel = N_{\parallel 0} \equiv (1 + 1/b_0)^{-1/2} \simeq 0.61$ for which the O- and L- cut-offs coincide, and therefore where O-X-B mode conversion is favored.

### 2.3.2 Effect of the magnetic field on EBW characteristics

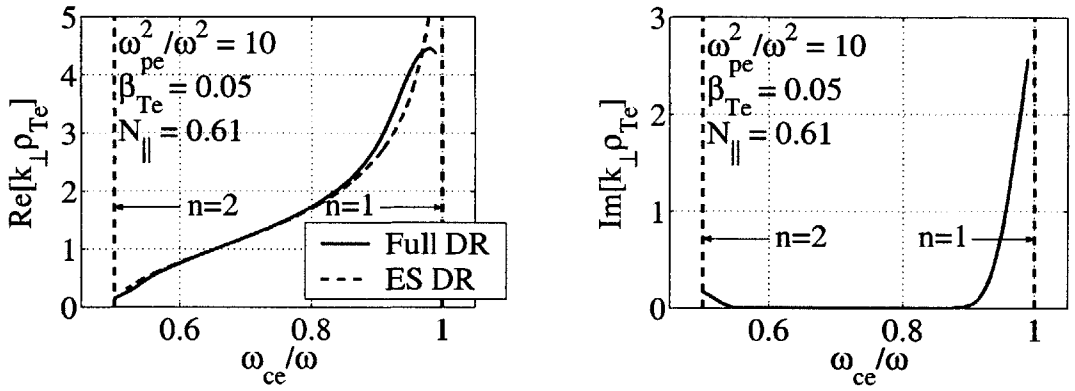


Figure 2-4: Real (a) and imaginary (b) parts of the EBW root $N_\perp$ as a function of $b = \omega_{ce}/\omega$ for $N_\parallel = N_{\parallel 0}$, calculated using the full non-relativistic dispersion relation (blue solid line) and, on graph (a), the electrostatic dispersion relation (red dashed line). The dashed vertical lines show to the location of cyclotron resonances.

We calculate the variations of the EBW characteristics as a function of the magnetic field ratio $b = \omega_{ce}/\omega$, between the second ($b = 1/2$) and first harmonic ($b = 1$). All other plasma parameters are kept constant and we take $N_\parallel = N_{\parallel 0} = 0.61$.

The real part of the EBW root $k_\perp \rho_{Te}$ is shown on Fig. 2-4, graph (a). We observe strong variations of $\mathrm{Re}\,[k_\perp \rho_{Te}]$ are a function of $\omega_{ce}/\omega$, from low values ($\mathrm{Re}\,[k_\perp \rho_{Te}] \lesssim 0.5$ corresponding to $N_\perp \lesssim 5$) near second harmonic, to very high values ($\mathrm{Re}\,[k_\perp \rho_{Te}] \gtrsim 3$ corresponding to $N_\perp \gtrsim 50$) near the first harmonic (the dashed vertical lines show to the location of cyclotron harmonic resonances). The electrostatic root, shown as a red dashed line, seems a good approximation to the exact root (blue solid line) except near the resonances. In fact, this graph is an inverted representation of graph (b) in Fig. 2-1, for values $1 < q < 2$.

The condition (2.136), which sets a limit on the validity of our analytical description in the electrostatic approximation (failure of our $Z(\zeta_{ne})$ function expansion (2.95)), gives $b \gtrsim 0.95$ near first harmonic and $b \lesssim 0.52$ near second harmonic. The region where the expansion is invalid is therefore twice as wide on the $n = 1$ side, which explains why the approximate description fails "earlier" on that side. The condition (2.136) also explains why $\mathrm{Im}[N_\perp]$, shown on graph (b), picks up further from resonance on the $n = 1$ side. The imaginary part of the wave vector characterizes damping near the Doppler-shifted resonances.

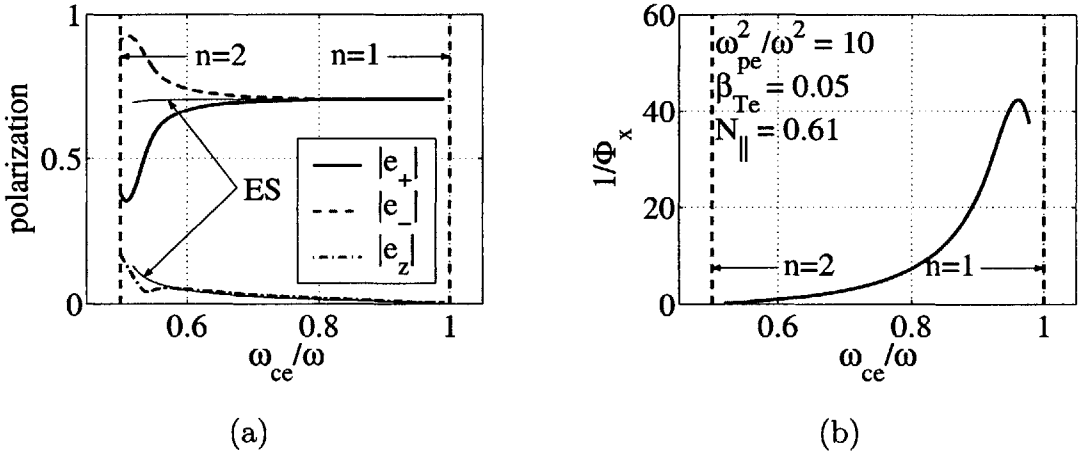


Figure 2-5: Graph (a): components of the polarization vector $\mathbf{e_k}$ as a function of $b = \omega_{ce}/\omega$. The electrostatic (ES) polarization is shown for comparison. Graph (b): normalized electric field amplitude, $\Phi_{\mathbf{k}\perp}^{-1} \propto \|\mathbf{E}_0\|^2 / \|\mathbf{s}_{\mathbf{k}\perp}\|$, as a function of $b$.

The components of the polarization vector are shown on Fig. 2-5 as a function $\omega_{ce}/\omega$ (graph (a)). Near the $n = 1$ resonance, where $k_\perp \rho_{Te}$ - and therefore $N$ - is very large, the parallel component of the polarization is very small, in accordance with (2.135), and the polarization is basically electrostatic. On the opposite side, towards the $n = 2$ resonance, the wave number $N$ is much smaller and the contribution of $e_{\mathbf{k},\|}$ more significant. In addition, the polarization becomes very different from the electrostatic limit (2.133) near the second harmonic, a sign that electromagnetic effect are important. In graph (b) we see that the normalized power flow $\Phi_{\mathbf{k}\perp} = \Phi_{\mathbf{k}x}$ varies significantly with $b$, and $\Phi_{\mathbf{k}\perp}^{-1} \propto \|\mathbf{E}_0\|^2 / \|\mathbf{s}_{\mathbf{k}\perp}\|$ follows essentially the profile of $\mathrm{Re}[k_\perp \rho_{Te}]$ (Fig. 2-4). When $\mathrm{Re}[k_\perp \rho_{Te}]$ becomes large (near $n = 1$ resonance), the

wave becomes electrostatic and, for a given incident power density $s_{\mathbf{k}\perp}$, the electric field amplitude is very large ($\Phi_{\mathbf{k}\perp}^{-1} > 30$). However, when $\mathrm{Re}\,[k_\perp \rho_{Te}]$ is low (near $n = 2$ resonance), the wave has strong electromagnetic features and the electric field amplitude is small ($\Phi_{\mathbf{k}\perp}^{-1} < 1$).

### 2.3.3 Effect of the temperature on EBW characteristics

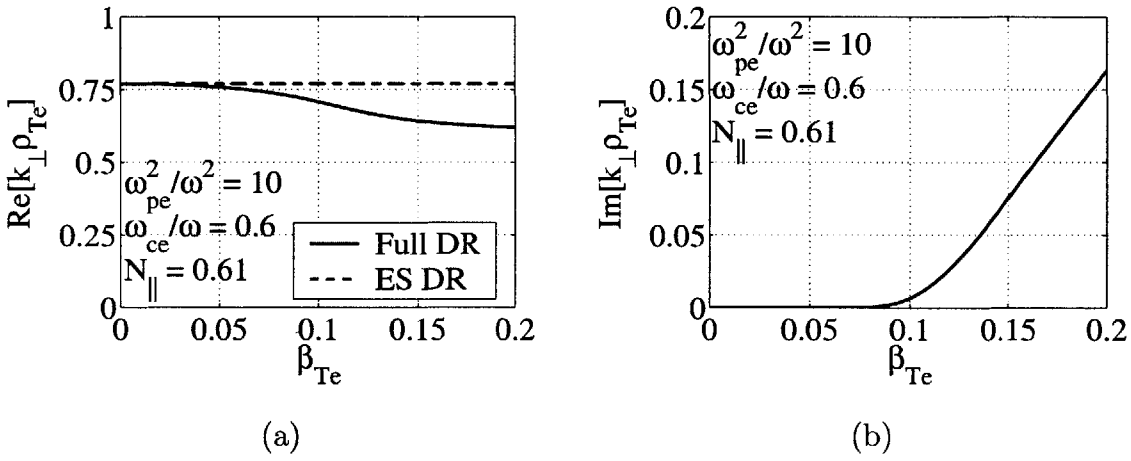


Figure 2-6: Real (a) and imaginary (b) parts of the EBW root $N_\perp$ as a function of $\beta_{Te} = v_{Te}/c$ for $N_\parallel = N_{\parallel 0}$, calculated using the full non-relativistic dispersion relation (blue solid line) and, on graph (a), the electrostatic dispersion relation (red dashed line).

The EBW characteristics are calculated as a function of $\beta_{Te} = \sqrt{T_e/mc^2}$ keeping all other plasma parameters constant and taking $N_\parallel = N_{\parallel 0} = 0.61$. The real part of the EBW root $k_\perp \rho_{Te}$ is shown on Fig. 2-6, graph (a), where the solid blue line represents the exact root and the dashed red line is the approximate root in the electrostatic limit. The electrostatic root does not depend on $\beta_{Te}$, which was expected since there is no temperature dependence in the electrostatic dispersion relation (2.99) solved for $\omega(\lambda_e)$ where $\lambda_e = (k_\perp \rho_{Te})^2$. The exact root does not vary much with the temperature, and is very close to the electrostatic root for $\beta_{Te} \lesssim 0.05$. The approximate form is expected to fail completely when the condition (2.136) is satisfied for $n = 2$ (the nearest harmonic), which gives $\beta_{Te} \gtrsim 0.2$ with our parameters. As expected from (2.136), increasing $\beta_{Te}$ lead to larger Doppler-shift and therefore

increasing imaginary part of the root, as seen on graph (b), which means increasing damping.

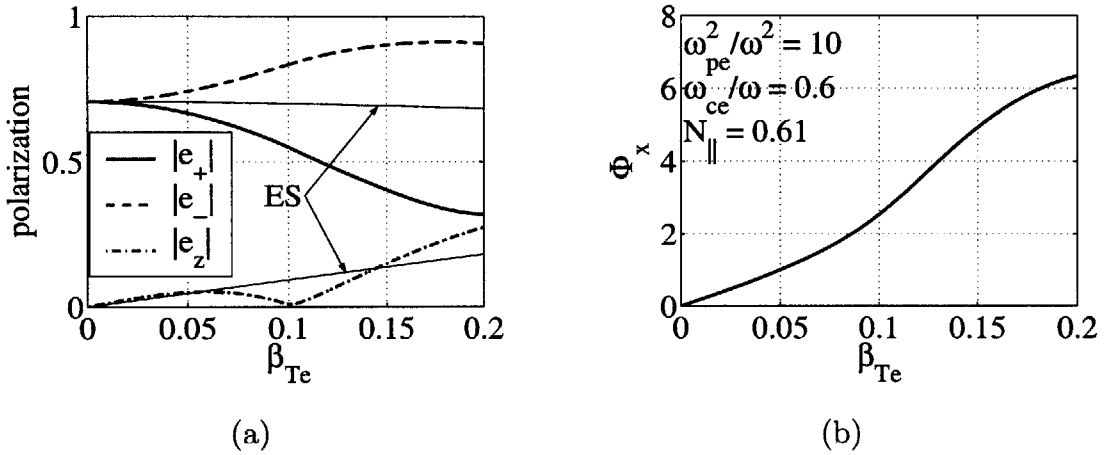


Figure 2-7: Graph (a): components of the polarization vector $\mathbf{e_k}$ as a function of $\beta_{Te} = v_{Te}/c$ for $N_\parallel = N_{\parallel 0}$. The electrostatic (ES) polarization is shown for comparison. Graph (b): normalized inverse electric field amplitude, $\Phi_{\mathbf{k}\perp} \propto \left(\|\mathbf{E}_0\|^2 / \|\mathbf{s}_{\mathbf{k}\perp}\|\right)^{-1}$, as a function of $\beta_{Te}$.

The components of the polarization vector are shown on Fig. 2-7 as a function of $\beta_{Te}$ (graph (a)) and we see that the polarization differs significantly from the electrostatic limit (2.135) for $\beta_{Te} \gtrsim 0.05$. The temperature also has an important effect on the normalized power flow, as shown on graph (b) where $\Phi_{\mathbf{k}\perp} = \Phi_{\mathbf{k}x}$ increases linearly with $\beta_{Te}$ for small $\beta_{Te}$, in accordance with the expression (2.114) obtained for $\Phi_{\mathbf{k}\perp}$ in the electrostatic limit.

### 2.3.4 Effect of the density on EBW characteristics

The EBW characteristics are calculated as a function of the normalized density $\alpha^2 = \omega_{pe}^2/\omega^2$ keeping all other plasma parameters constant and taking $N_\parallel = N_{\parallel 0} = 0.61$. The real part of the EBW root $k_\perp \rho_{Te}$ is shown on Fig. 2-6, graph (a), where the solid blue line represents the exact root and the dashed red line is the approximate root in the electrostatic limit. We see that the EBW root does not depend much upon the density as long as it is far from the upper-hybrid resonance, which is located at

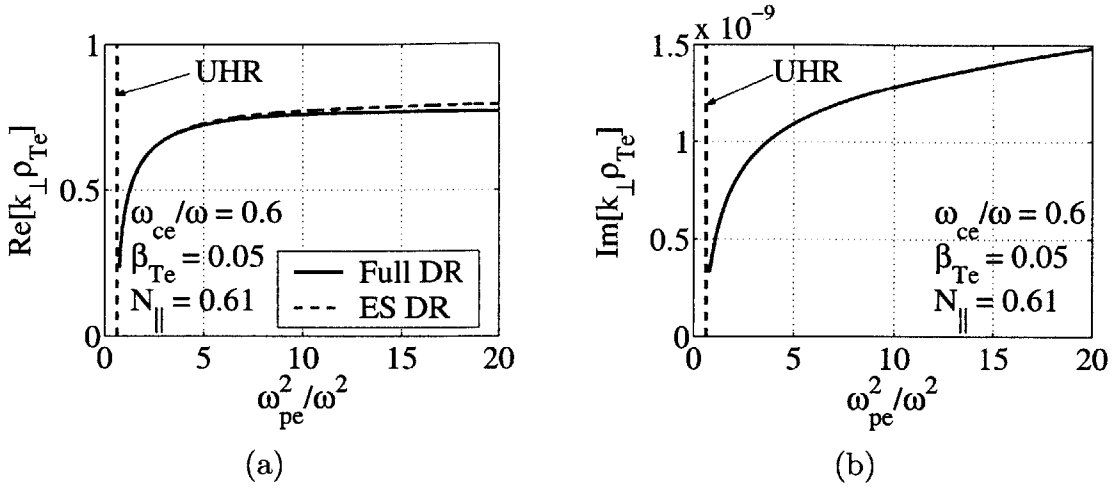


Figure 2-8: Real (a) and imaginary (b) parts of the EBW root $N_\perp$ as a function of $\alpha = \omega_{pe}^2/\omega^2$ for $N_\parallel = N_{\parallel 0}$, calculated using the full non-relativistic dispersion relation (blue solid line) and, on graph (a), the electrostatic dispersion relation (red dashed line).

very low densities (typically near the plasma edge) and shown as a vertical dashed line. We also notice that the exact root is very close the electrostatic approximation, although the difference increases slightly with increasing density. The imaginary part is shown on graph (b) and has a similar dependence as the real part.

The components of the polarization vector are shown on Fig. 2-7 as a function of $\alpha^2$ (graph (a)) and we see that the polarization also diverges steadily from the electrostatic limit (2.135) as $\omega_{pe}^2/\omega^2$ increases. The density also has an important effect on the normalized power flow, as shown on graph (b) where $\Phi_{\mathbf{k}\perp} = \Phi_{\mathbf{k}x}$ increases linearly with $\alpha^2$, which agrees with the expression (2.114) obtained for $\Phi_{\mathbf{k}\perp}$ in the electrostatic limit.

### 2.3.5 Conclusions

When the results obtained in this section are considered in perspective of a EBW heating or current drive experimental situation, they lead to the following qualitative observations:

- EBWs are kinetic waves that are found to be well described in the electrostatic

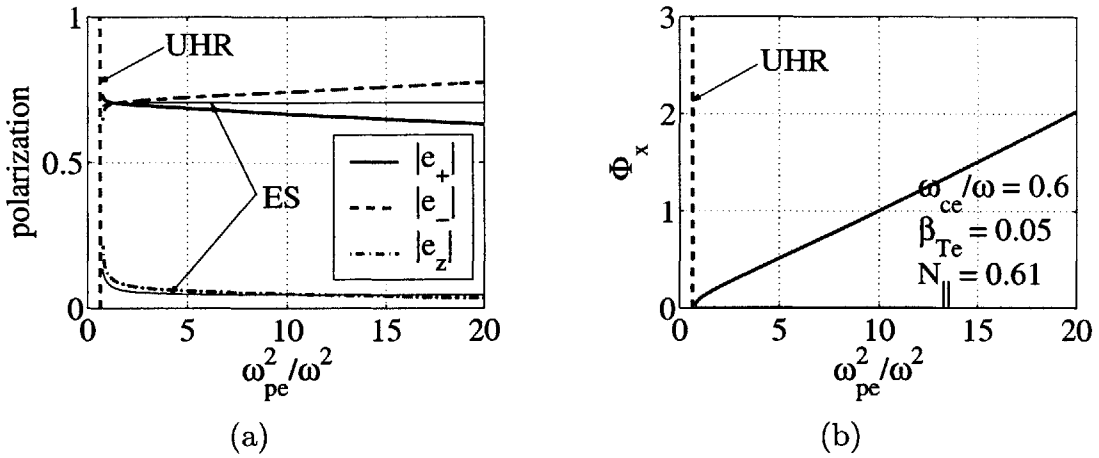


Figure 2-9: Graph (a): components of the polarization vector $\mathbf{e_k}$ as a function of $\alpha = \omega_{pe}^2/\omega^2$ for $N_\parallel = N_{\parallel 0}$. The electrostatic (ES) polarization is shown for comparison. Graph (b): normalized inverse electric field amplitude, $\Phi_{\mathbf{k}\perp} \propto \left(\|\mathbf{E}_0\|^2 / \|\mathbf{s}_{\mathbf{k}\perp}\|\right)^{-1}$, as a function of $\alpha$.

approximation away from the resonances. The approximate analytical results (2.99) and (2.114), obtained in the electrostatic limit, are generally valid as long as the expansion (2.95) of the plasma dispersion function remains valid, which breaks down when the condition (2.136) is satisfied.

- EBWs are propagating waves between two harmonics of the cyclotron frequency. However, they are completely absorbed at the Doppler-shifted harmonic resonances. The wave absorption coefficient is independent of the plasma density, a property of waves for which the energy flow is mostly carried by electrons coherently moving with the wave.

- In accordance with the electrostatic dispersion relation (2.99), the root of the dispersion relation, or normalized perpendicular wave vector $\mathrm{Re}\,[k_\perp \rho_{Te}]$, does not vary much as a function of $N_\parallel$ and the temperature, and is rather insensitive to density variations away from the MCR.

- After the EBWs are generated at the MCR (Description in Section 1.2.1), they propagate towards the central, high density ($\alpha^2 \gg 1$) and temperature ($\beta_{Te} \gtrsim 0.05$) region until they eventually approach an electron cyclotron har-

monic resonance, where they are damped. There is also a possibility that the wave encounters no resonance along the propagation and reaches the edge again, where it can be reflected or mode-converted to EC modes. Therefore, inside the plasma, the behaviour of EBWs is dominated by magnetic field variations. We have shown on Fig. 2-4 and Fig. 2-5 that the EBW characteristics depend very much on whether a harmonic is approached from the lower $B$-field (LBF) region, where $\omega_{ce} < \omega$, or a higher $B$-field (HBF) region where $\omega_{ce} > \omega$. A comparative summary of these two scenarios is given in Table 2.1.

- The polarization is mostly electrostatic - along the wave vector - except near the HBF harmonic where $\mathrm{Re}\,[k_\perp \rho_{Te}]$ is small and electromagnetic effects on the polarization are important.

- The condition (2.136), which is a measure of the proximity to cyclotron resonances and includes (temperature and $N_\parallel$-dependent) Doppler shift effects, also characterizes the strong damping condition measured by $\mathrm{Im}\,[k_\perp \rho_{Te}]$.

- The normalized electric field amplitude $\Phi_{\mathbf{k}\perp}^{-1} \propto \|\mathbf{E}_0\|^2 / \|\mathbf{s}_{\mathbf{k}\perp}\|$ has a strong dependence upon density and temperature. It typically evolves as $\Phi_{\mathbf{k}\perp} \propto n_e \beta_{Te}$, meaning that for a given incident power flow, the electric field amplitude is larger in low density and low temperature regions. When the electric field amplitude becomes too large, non-linear effects, such as trapping in wave, can take place. The onset of these effects will therefore depend upon density and temperature - as well as the average power density carried by the wave. These effects are considered in Section 3.5.3.

The calculations presented in this chapter are obtained for an infinite homogeneous plasma. Going from an infinite to a bounded plasma, such as in a torus, does not change fundamentally the equations - we should consider discrete Fourier modes rather than continuous ones -, and these equations remain valid in such continuous form when the wavelength $\lambda$ is much smaller than the plasma size, which is a good approximation.

| Scenario | LBF Approach | HBF Approach |
|---|---|---|
| EBW root | Large $\mathrm{Re}\,[k_\perp \rho_{Te}] \gtrsim 3$ | Small $\mathrm{Re}\,[k_\perp \rho_{Te}] \lesssim 0.5$ |
| Polarization | Basically electrostatic | Strong electromagnetic effects |
| Normalized **E**-field | Very large $\Phi_{\mathbf{k}\perp}^{-1} > 30$ | Small $\Phi_{\mathbf{k}\perp}^{-1} < 1$ |

Table 2.1: Comparative table of EBW characteristics depending of damping scenario: low-$B$ field (LBF) approach versus high-$B$ field (HBF) approach

However, these calculations do not strictly apply to an inhomogeneous plasma. Still, in the regions of the plasma where the equilibrium inhomogeneity scale length is much larger than the wavelength, it has been shown that the dispersion relation is satisfied locally, which is known as the WKB approximation. Therefore, the calculations presented in this section can be used to understand the evolution of the wave characteristics along the propagation through a plasma with a slowly varying inhomogeneous equilibrium. In the regions where the equilibrium inhomogeneity scale length becomes comparable or shorter than the wavelength, notably in the MCR where $k_\perp \rightarrow 0$ at cut-offs, this description fails.

# Chapter 3

# Kinetic Description of Toroidal Plasmas with Non-circular Cross-sections

## 3.1 Introduction

In this chapter, a kinetic description of axisymmetric toroidal plasmas is given for the general case of closed nested flux-surfaces with arbitrary geometry. After defining the equilibrium magnetic field in appropriate coordinates systems, we describe in Section 3.2 the motion of a single electron in this magnetic field, which is characterized by a constants of the motion, the energy - since magnetic forces do no work - and an adiabatic invariant, the magnetic moment, which results from the fast gyromotion. The inhomogeneity of the magnetic field is unavoidable in a torus, and results in the trapping of a fraction of electrons in the low magnetic field regions. Another effect of the magnetic field inhomogeneity is to generate particle drifts. The drift across flux-surfaces, associated with temperature and density radial gradients in the plasma, is responsible for the bootstrap current. However, the orbit deviation from a flux-surface is very small compared to the size of the plasma and the poloidal orbit length, and it is a good approximation, for electrons, to assume that the particle is exactly

on the flux-surface when integrating along the particle orbit.

The drift-kinetic equation, which accounts for this drift, is derived in Section 3.3 from the Boltzmann equation with Fokker-Planck collisions. The effect of RF fields - such as Electron Bernstein Waves - on the plasma is described by a quasilinear operator that is added ad-hoc to the drift-kinetic equation. This 4-D equation (2-D in axisymmetric configuration space, 2-D in gyroaveraged momentum space) is reduced to a set of two 3-D equations by applying the small drift approximation, which accounts for the fact that the drift velocity is much smaller than the parallel velocity of electrons. This approximation effectively decouples the flux-surfaces. These 3-D equations are further reduced to a set of 2-D bounce-averaged equations (in momentum space) using the low-collisionality approximation, under which the motion of a given electron is not altered much by collisions or quasilinear diffusion over the course of one poloidal transit time (for passing electrons) or bounce time (for trapped electrons). The differential operators in the kinetic equation are expressed in a conservative form as the divergence of momentum-space fluxes with diffusive and convective parts. The bounce-averaging of these operators is expressed analytically and for the general case, using the symmetry properties of the distribution functions, and leads to an expression for bounce-averaged diffusion tensor and convection vectors, which must be specified for each operator (collisions and quasilinear diffusion).

The Fokker-Planck collisions operator is linearized and bounce-averaged in Section 3.4. The quasilinear operator is derived in Appendix B for a Gaussian beam in a uniform plasma. Its application to a toroidal plasma is discussed and justified in Section 3.5, where it is transformed to enter the bounce-averaged kinetic equation. The validity of the quasilinear operator with respect to non-linear effects is also discussed.

Finally, the calculation of moments of the distribution function is presented in Section 3.6, after introducing the flux-surface averaging operation. It allows us to evaluate the flux-surface averaged density, plasma current, and collisional or RF power dissipated, from the bounce-averaged distribution function. The stream function, which gives a useful mapping of steady-state fluxes, is also calculated.

## 3.2 Electron Dynamics in an Axisymmetric Torus

In this section, we first introduce the axisymmetric toroidal magnetic equilibrium applicable to tokamaks and STs. The particle motion in this magnetic field is described and the drift across magnetic flux surfaces is calculated. In addition, the bounce-averaging operation is defined in the zero-banana width limit, when the drifts can be neglected in first approximation. The results presented here are not derived from first principles, although this has been done in previous works refered to in this section. The properties of the equilibrium magnetic field are obtained from ideal MHD equations [63] [64]. The motion of particles in a non-uniform magnetic field has been derived by expanding the equation of motion to orders of $\rho_L/L_B \ll 1$ where $\rho_L$ is the Larmor radius and $L_B$ is the scale length of magnetic field variations [65] [66]. Equivalently, these equation have been derived using an Hamiltonian approach [67].

### 3.2.1 Toroidal plasma field geometry and configuration space coordinates systems

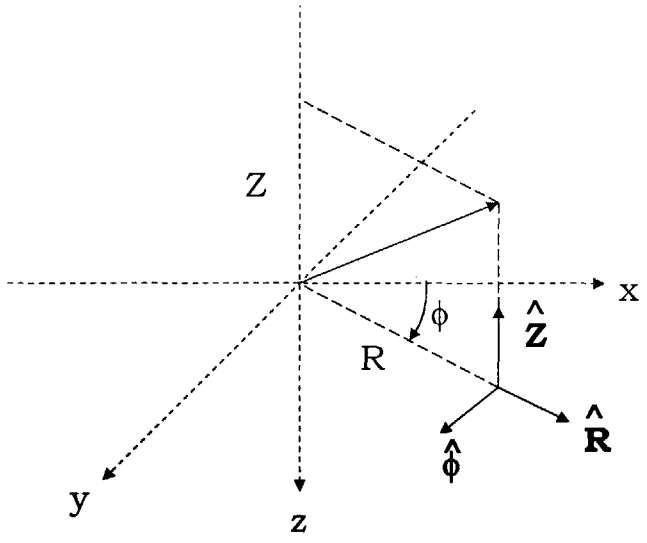


Figure 3-1: Cylindrical coordinate system $(R, Z, \phi)$ for axisymmetric toroidal plasmas.

A natural coordinates system for an axisymmetric toroidal plasma is the cylindrical system $(R, Z, \phi)$, defined in (A.46) and shown in Fig. 3-1, where $R$ is the distance from the torus axis of symmetry, $Z$ is the (generally vertical) position along this axis, and $\phi$ is the angle in the toroidal direction. The system $(R, Z, \phi)$ is oriented such that the toroidal magnetic field be positive $\mathbf{B} \cdot \nabla\phi > 0$. In other words, if the toroidal field is directed clockwise from a top view, then $\nabla Z$ is oriented towards the top of the torus. Otherwise, it is oriented towards the bottom of the torus. The corresponding local direct orthonormal vector basis is $\left(\widehat{\mathbf{R}}, \widehat{\mathbf{Z}}, \widehat{\phi}\right)$, defined in (A.49), with (A.51)

$$\begin{aligned} \widehat{\mathbf{R}} &= \nabla R \\ \widehat{\mathbf{Z}} &= \nabla Z \\ \widehat{\phi} &= R\nabla\phi \end{aligned} \tag{3.1}$$

Many useful geometrical and differential properties of this system are derived in Appendix A. Note that with our definitions, the angle $\phi$ is oriented in the opposite direction from the one used generally in ideal MHD, where the direct orthonormal vector basis is $\left(\widehat{\mathbf{R}}, \widehat{\phi}, \widehat{\mathbf{Z}}\right)$. The present prescription allows us to use the same toroidal coordinate $\phi$ throughout various coordinate systems defined below.

In a toroidal axisymmetric geometry, the equilibrium magnetic field can be expressed generally as [64]

$$\mathbf{B} = I(\psi)\nabla\phi + \nabla\phi \times \nabla\psi \tag{3.2}$$

where $\psi$ is called the *magnetic flux function* and $I(\psi)$ is a free function related to the toroidal magnetic field, and which accounts for the plasma dia- or paramagnetism. In an axisymmetric system, $\psi$ is independent of $\phi$ and therefore $\nabla\psi \cdot \nabla\phi = 0$ and we get from (3.2) that $\mathbf{B} \cdot \nabla\psi = 0$. The magnetic field is therefore included in nested surfaces of constant $\psi$, called *flux surfaces.*

A consequence of the axisymmetric magnetic equilibrium is the existence of a magnetic axis in the toroidal direction, located at the fixed position $(R_p, Z_p)$ ,which corresponds to the innermost flux-surface. The magnetic axis is an extremum of the magnetic flux function $\psi$. The value of $\psi$ on axis can be arbitrarily chosen as $\psi = 0$.

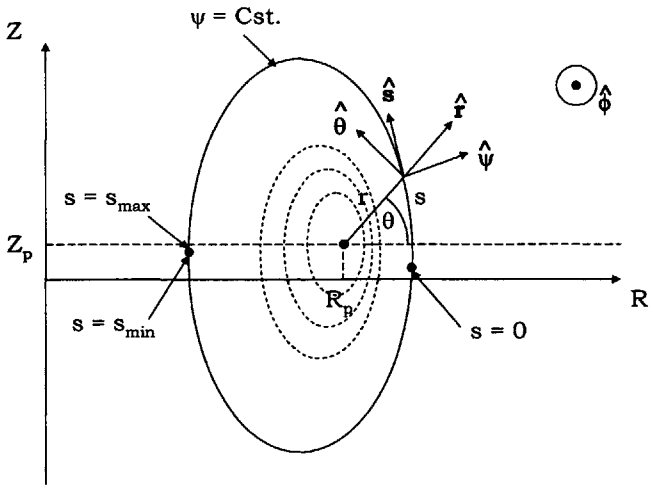


Figure 3-2: Flux coordinates system $(\psi, s, \phi)$ for axisymmetric toroidal plasmas with closed nested flux-surfaces.

Using this axis as a reference, we define the coordinate system $(\psi, s, \phi)$, shown in Fig. 3-2, where the distance $s$ is the curvilinear length along the poloidal magnetic field lines (A.72). In this study, we assume that the magnetic field amplitude has only one maximum and one minimum on the flux-surface, which is generally the case for tokamaks and STs

$$\begin{aligned} B_{\max}(\psi) &\equiv \max_{s} \{B(\psi, s)\} \\ B_0(\psi) &\equiv \min_{s} \{B(\psi, s)\} \end{aligned} \tag{3.3}$$

and we choose the origin of $s$ to be at the position of minimum $B$-field amplitude within a flux-surface.

$$B(\psi, s \equiv 0) = B_0(\psi) \tag{3.4}$$

Note that from now on, and all along this thesis, the subscript 0 refers to quantities evaluated at the position of minimum $B$-field on a given flux-surface. The range of $s$ on a given flux-surface is limited by $s_{\min}(\psi)$ and $s_{\max}(\psi)$ which are set at the position of maximum magnetic field, such that

$$\begin{aligned} B(\psi, s \equiv s_{\min} < 0) &= B_{\max}(\psi) \\ B(\psi, s \equiv s_{\max} > 0) &= B_{\max}(\psi) \end{aligned} \tag{3.5}$$

The local direct orthogonal vector basis corresponding to the system $(\psi, s, \phi)$ is $\left(\widehat{\psi}, \widehat{\mathbf{s}}, \widehat{\phi}\right)$, defined in (A.74), with (A.78)

$$\begin{aligned} \widehat{\psi} &= \frac{\nabla\psi}{\|\nabla\psi\|} \\ \widehat{\mathbf{s}} &= \nabla s = \widehat{\phi} \times \widehat{\psi} \end{aligned} \tag{3.6}$$

The toroidal magnetic field is

$$\mathbf{B}_T = I(\psi)\nabla\phi = B_\phi \widehat{\phi} \tag{3.7}$$

with $B_\phi = I(\psi)\|\nabla\phi\|$. With our prescription that $\mathbf{B} \cdot \nabla\phi > 0$, we have that $B_\phi > 0$ and $I(\psi) > 0$, and therefore the (positive definite) toroidal component of the field is

$$B_T \equiv \|\mathbf{B}_T\| = B_\phi = \frac{I(\psi)}{R} \tag{3.8}$$

If the plasma current is in the same direction as the magnetic field, $I_\phi > 0$, the poloidal field is directed counter-clockwise in the poloidal plane, as shown by $\widehat{\mathbf{s}}$ on Fig. 3-2, and the flux function $\psi$ increases in the radial direction. Then, the magnetic axis is a minimum of $\psi$. If $I_\phi < 0$, $\psi$ decreases in the radial direction and the magnetic axis is a maximum of $\psi$. The poloidal magnetic field is

$$\mathbf{B}_P = \nabla\phi \times \nabla\psi = B_s \widehat{\mathbf{s}} \tag{3.9}$$

with $B_s = \|\nabla\psi\|\,\|\nabla\phi\|$. Therefore, the (definite positive) poloidal component of the field is

$$B_P \equiv \|\mathbf{B}_P\| = B_s = \frac{\|\nabla\psi\|}{R} \tag{3.10}$$

The total magnetic field magnitude is simply

$$B \equiv \|\mathbf{B}\| = \sqrt{B_T^2 + B_P^2} \tag{3.11}$$

The magnetic flux function $\psi$ is related to the poloidal flux of $\mathbf{B}$. Indeed, let's

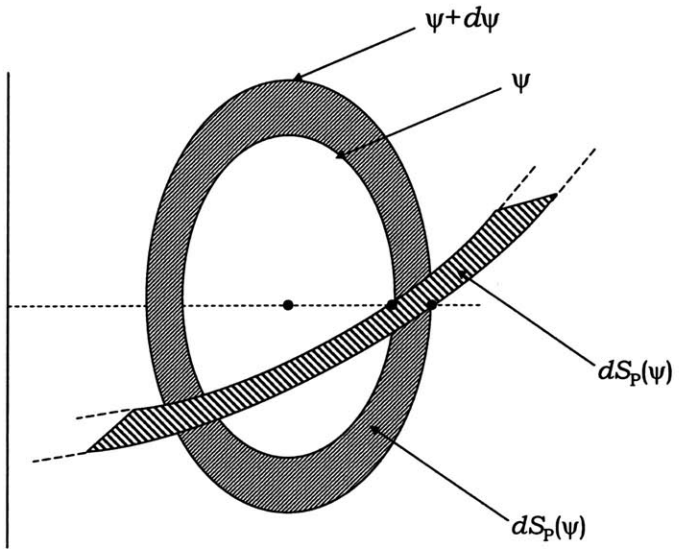


Figure 3-3: Elementary toroidal surface $dS_T(\psi)$ and poloidal surface $dS_P(\psi)$ for the calculation of flux of magnetic field $\mathbf{B}$ within a given flux-surface $\psi$.

consider the flux of $\mathbf{B}_P$ across a toroidal surface $S_T(\psi)$ as shown on Fig. 3-3. Because the magnetic flux is a conserved quantity, the surface $S_T(\psi)$ can be taken at any poloidal location. We choose arbitrarily the $s = 0$ surface. Using axisymmetry, (3.10) and the expression (A.81) for elementary surfaces of constant $s$, we find

$$\begin{aligned}\psi_P(\psi) &= \iint_{S_P(\psi)} d\mathbf{S} \cdot \mathbf{B}_P \\ &= 2\pi \int_0^{\psi} \frac{R d\psi}{\|\nabla\psi\|} B_P \\ &= 2\pi\psi \end{aligned} \tag{3.12}$$

and we see that $\psi$ is the poloidal flux per radian.

Because the range of $s$ depends on $\psi$ (3.5), it is often more convenient to work with the coordinate system $(\psi, \theta, \phi)$, where $\theta$ is the poloidal angle measured from the magnetic axis. The $\theta$ range $(-\pi, \pi)$ is now independent of $\psi$, which simplifies numerical calculations. On the other hand, the contravariant vectors $\nabla\psi$ and $\nabla\theta$ (A.91) are not orthogonal. This coordinate system, also shown on Fig. 3-2, is a blend

of $(\psi, s, \phi)$ and $(r, \theta, \phi)$, which is defined in (A.59) with the basis (A.64)

$$\begin{aligned} \widehat{\mathbf{r}} &= \nabla r \\ \widehat{\theta} &= r\nabla\theta \end{aligned} \tag{3.13}$$

The properties of this curvilinear system are detailed in Appendix A. We also define, for geometrical purposes, a flux-function $\rho(\psi)$ which coincides with the normalized radius on the horizontal outboard mid-plane. Indeed, in an axisymmetric system, using the functions $R(\psi, \theta)$ and $Z(\psi, \theta)$, we define $\rho(\psi)$ as

$$\rho(\psi) = \frac{R(\psi, 0) - R_p}{R_a - R_p} \tag{3.14}$$

where $R_p = R(0, 0)$ is the location of magnetic axis and $R_a \equiv R(\psi_a, 0)$ is the value of $R$ on the separatrix ($\psi = \psi_a$) as it crosses the horizontal mid-plane ($\theta = 0$). We have by construction $0 \leq \rho \leq 1$ in the plasma. Here $a_p = R_a - R_p$ is defined arbitrarily as the plasma minor radius, since this definition merges $a_p$ for circular concentric flux-surfaces. We also define the position $\theta_0(\psi)$ corresponding to the (unique) location of minimum $B$-field on the flux-surface

$$\theta_0(\psi) \equiv \theta|_{B(\psi,\theta)=B_0(\psi)} \tag{3.15}$$

When the plasma is up-down symmetric, we have $\theta_0 = 0$. The system $(\psi, \theta, \phi)$ will be used from now on and through this thesis.

### Safety Factor $q(\psi)$

The safety factor $q(\psi)$ is a measure of the average number of toroidal rotations completed while following a field line for one entire poloidal rotation. It is precisely defined as

$$q(\psi) \equiv \frac{d\psi_T}{d\psi_P} \tag{3.16}$$

where $\psi_T$ is the toroidal flux and $\psi_P$ in the poloidal flux. The toroidal flux is the flux of $\mathbf{B}_T$ through the poloidal surface $S_P(\psi)$ as shown on Fig. 3-3. Using axisymmetry,

(3.8) and the expression (A.94) for elementary surfaces with constant $\phi$, we find, using (A.90),

$$\begin{aligned}\psi_T(\psi) &= \iint_{S_T(\psi)} d\mathbf{S}\cdot\mathbf{B}_T \\ &= \int_0^{\psi} d\psi \int_{-\pi}^{\pi} d\theta \frac{r}{\left|\widehat{\psi}\cdot\widehat{\mathbf{r}}\right| \|\nabla\psi\|} B_T \end{aligned} \tag{3.17}$$

We recall (3.12)

$$\psi_P(\psi) = 2\pi\psi \tag{3.18}$$

so that, using (3.17) and (3.10), the safety factor (3.16) becomes

$$q(\psi) = \int_0^{2\pi} \frac{d\theta}{2\pi} \frac{1}{\left|\widehat{\psi}\cdot\widehat{\mathbf{r}}\right|} \frac{r}{R} \frac{B_T}{B_P} \tag{3.19}$$

### 3.2.2 Particle motion in a magnetic field and momentum space coordinates systems

Because of the fast gyromotion of particles in the magnetic field, we use momentum space coordinates systems with rotational symmetry in order to reduce the dimensionality of the problem. Two different momentum space coordinates system are considered through this work:

- First, the cylindrical coordinate system $(p_\parallel, p_\perp, \varphi)$, where $p_\parallel$ is the component of the momentum along the magnetic field, $p_\perp$ is the component perpendicular to the field, and $\varphi$ is the gyro-angle. This system is defined in (A.100). The cylindrical momentum-space coordinate system has the natural symmetry of wave-particle interaction.

- Second, the spherical coordinate system $(p, \xi, \varphi)$, defined in (A.113), where $p$ is the magnitude of the momentum, and $\xi$ is the cosine of the pitch-angle. The spherical momentum-space coordinate system has the natural symmetry of collisions. It is the primary system, used in the *DKE* code, for an accurate

description of collisions.

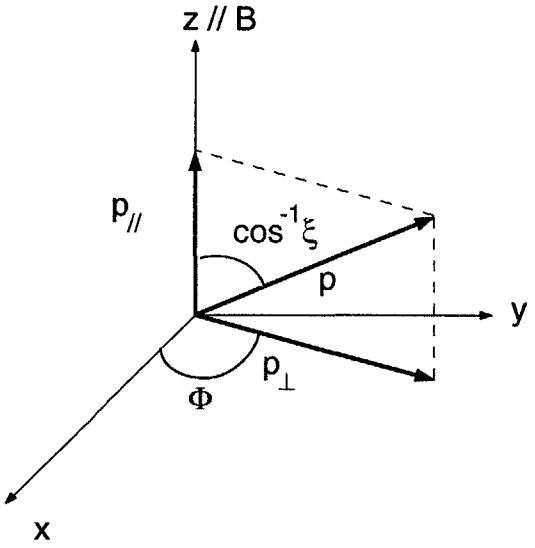


Figure 3-4: Momentum space coordinates systems $(p_\parallel, p_\perp, \varphi)$ and $(p, \xi, \varphi)$.

The momentum space and the two systems are shown on Fig. 3-4. In a relativistic plasma, the velocity is related to the momentum by (2.54)

$$\mathbf{v} = \frac{\mathbf{p}}{\gamma m_e} \tag{3.20}$$

where (2.55)

$$\gamma\left(\|\mathbf{p}\|\right) = \sqrt{1 + \frac{p_\parallel^2 + p_\perp^2}{m_e^2 c^2}} = \sqrt{1 + \frac{p^2}{m_e^2 c^2}} \tag{3.21}$$

is the relativistic factor.

The motion of an electron in a uniform magnetic field is decomposed into a gyration in the plane perpendicular to the field line and a free streaming along the field line [64]. The radius of the gyration, also called electron Larmor radius or gyroradius, is

$$\rho_L = \frac{p_\perp}{m_e \omega_{ce}} \tag{3.22}$$

where

$$\omega_{ce} = \frac{eB}{m_e} \tag{3.23}$$

is the rest mass gyrofrequency. When the magnetic field is non-uniform and when its variations, both in amplitude and directions, occur on a scale length much larger than the Larmor radius, then the modifications to the particle motion can be viewed as a perturbation to the gyromotion, and consists of relatively slow particle drifts. When averaged over the fast gyro-motion, the resulting velocity - called guiding center velocity - is then the sum of the fast streaming along field lines and a slow drift

$$\mathbf{v}_{\rm gc} = v_{\parallel}\widehat{\mathbf{b}} + \mathbf{v}_D \tag{3.24}$$

where $\widehat{b} = \mathbf{B}/B$ is the unit vector in the magnetic field direction.

In a constant equilibrium and the absence of equilibrium electric field, the drift velocity $\mathbf{v}_D$ is the sum of the $\nabla B$ drift, due to changes in the magnitude of $\mathbf{B}$, and the curvature drift, due to changes in the direction of $\mathbf{B}$. It is given by [64]

$$\mathbf{v}_D = \frac{1}{\Omega_e}\left(v_{\parallel}^2 + \frac{v_{\perp}^2}{2}\right)\frac{\mathbf{B}\times\nabla B}{B^2} \tag{3.25}$$

where $\Omega_e$ is the relativistic cyclotron frequency

$$\Omega_e = \frac{q_e B}{\gamma m_e} = -\frac{\omega_{ce}}{\gamma} \tag{3.26}$$

### 3.2.3 Constants of the motion and particle motion along the field lines

Because magnetic fields cannot do any work on charged particles, the electron's kinetic energy $\mathcal{E}$ is a constant of the motion

$$\frac{d\mathcal{E}}{dt} = 0 \tag{3.27}$$

where $\mathcal{E}$ is expressed relativistically as

$$\mathcal{E} = (\gamma - 1)\, mc^2 \tag{3.28}$$

In addition, the fast gyromotion results in the existence of an adiabatic invariant [64],

$$\frac{d\mu}{dt} \simeq 0 \tag{3.29}$$

where $\mu$ is the magnetic moment

$$\mu = \frac{p_\perp^2}{2\gamma m_e B} = \frac{q_e v_\perp^2}{2\Omega_e} \tag{3.30}$$

Because of the conservation of energy and magnetic moment, the parallel velocity of the electron decreases as it moves towards regions of higher magnetic field amplitude. This effective force in the parallel direction is called mirror force, as it is the principal longitudinal confining effect in a mirror machine. In a toroidal plasma, the parallel velocity of an electron moving towards higher field regions can sometimes vanish before the electrons reaches the location of maximum magnetic field $B_{\max}(\psi)$. In that case, the electron bounces back towards lower field regions, and is called a trapped electron, as it is confined in a region of low magnetic field. All electrons confined on a given flux surface $\psi$ will pass by the point of lowest magnetic field $B_0(\psi)$ on that flux-surface. In an axisymmetric plasma, it is therefore possible to identify electrons by the value of their momentum components $p_{\|0}$ and $p_{\perp 0}$ as they reach the point where $B(\psi, \theta) = B_0(\psi)$.

The turning points $\theta_T$ in the bounce motion are then determined by the location where $v_\|$ vanishes. The conservation of energy (3.28) leads to the conservation of $\gamma$ and therefore, using (3.21)

$$p_{\|0}^2 + p_{\perp 0}^2 = p_\|^2 + p_\perp^2 \tag{3.31}$$

while the conservation of magnetic moment (3.30) gives

$$\frac{p_{\perp 0}^2}{B_0(\psi)} = \frac{p_\perp^2}{B(\psi, \theta_T)} \tag{3.32}$$

We define the ratio $\Psi(\psi,\theta)$, on a given flux surface, between the magnetic field and its minimum value $B_0(\psi)$ on that flux-surface.

$$\Psi(\psi,\theta) \equiv \frac{B(\psi,\theta)}{B_0(\psi)} \tag{3.33}$$

so that, at the turning point where $p_\parallel = 0$, (3.32) with (3.31) gives

$$\Psi(\psi,\theta_T) = 1 + \frac{p_{\parallel 0}^2}{p_{\perp 0}^2} \tag{3.34}$$

Trapped electrons are such that there exists such poloidal location $\theta_T$ and therefore

$$1 + \frac{p_{\parallel 0}^2}{p_{\perp 0}^2} < \Psi_{\max}(\psi) \tag{3.35}$$

where $\Psi_{\max}(\psi) \equiv B_{\max}(\psi)/B_0(\psi)$. The two turning points are

$$\begin{aligned}
\theta_{T\min}\left(p_{\parallel 0}, p_{\perp 0}, \psi\right) &\equiv \min\left\{\theta \left| B(\psi,\theta_T) \le \left(1 + \frac{p_{\parallel 0}^2}{p_{\perp 0}^2}\right) B_0(\psi)\right.\right\} \\
\theta_{T\max}\left(p_{\parallel 0}, p_{\perp 0}, \psi\right) &\equiv \max\left\{\theta \left| B(\psi,\theta_T) \le \left(1 + \frac{p_{\parallel 0}^2}{p_{\perp 0}^2}\right) B_0(\psi)\right.\right\}
\end{aligned} \tag{3.36}$$

and we have $\theta_{T\min} = -\theta_{T\max}$ in an up-down symmetric plasma.

In spherical momentum coordinates $(p,\xi)$, the conservation of energy (3.28) gives

$$p_0 = p \tag{3.37}$$

meaning that the magnitude of the particle momentum is conserved, while the conservation of magnetic moment (3.32) leads to

$$\frac{1-\xi_0^2}{B_0(\psi)} = \frac{1-\xi^2}{B(\psi,\theta)} \tag{3.38}$$

so that, at the turning point where $\xi = 0$,

$$\Psi(\psi, \theta_T) = \frac{1}{1 - \xi_0^2} \tag{3.39}$$

Trapped electrons on a given flux-surface are therefore such that

$$\xi_0^2 < \xi_{0T}^2(\psi) \tag{3.40}$$

where we defined

$$\xi_{0T}(\psi) \equiv \sqrt{1 - \frac{1}{\Psi_{\max}(\psi)}} \tag{3.41}$$

In spherical coordinates, electrons are therefore identified by their momentum $p$, which is a constant of the motion, and by the value $\xi_0$ of their pitch-angle as they cross the point of minimum $B$-field on the flux-surface. The turning points (3.36) of an electron $(p, \xi_0)$ can also be defined in $(p, \xi)$ coordinates, using (3.39)

$$\begin{aligned} \theta_{T\min}(\xi_0, \psi) &\equiv \min\left\{\theta \,\middle|\, B(\psi, \theta_T) \leq \frac{B_0(\psi)}{1 - \xi_0^2}\right\} \\ \theta_{T\max}(\xi_0, \psi) &\equiv \max\left\{\theta \,\middle|\, B(\psi, \theta_T) \leq \frac{B_0(\psi)}{1 - \xi_0^2}\right\} \end{aligned} \tag{3.42}$$

The pitch-angle of an electron varies along the flux-surface according to (3.38)

$$\xi = \sigma\sqrt{1 - \Psi(\psi, \theta)(1 - \xi_0^2)} \tag{3.43}$$

where $\sigma$ =sign($\xi_0$). We can also derive the condition for an electron with pitch-angle $\xi$ at the poloidal location $\theta$ to be trapped. From (3.38) and (3.41) the condition is

$$\xi < \xi_T(\psi, \theta) = \sqrt{1 - \frac{\Psi(\psi, \theta)}{\Psi_{\max}(\psi)}} \tag{3.44}$$

We define the limits $\theta_{\min}$ and $\theta_{\max}$ as

$$\begin{aligned}\theta_{\min}(\psi,\xi_0) &= \begin{cases} -\pi & \text{for passing particles} \\ \theta_{T\min} & \text{for trapped particles} \end{cases} \\ \theta_{\max}(\psi,\xi_0) &= \begin{cases} \pi & \text{for passing particles} \\ \theta_{T\max} & \text{for trapped particles} \end{cases}\end{aligned} \tag{3.45}$$

where $\theta_{T\min}$ and $\theta_{T\max}$ were defined in (3.42). The conditions for an electron $(p,\xi_0)$ to be able to reach a given poloidal location $\theta$ is then

$$\theta_{\min}(\psi,\xi_0) \leq \theta \leq \theta_{\max}(\psi,\xi_0) \tag{3.46}$$

which, using (3.34), can also be written as

$$\Psi(\psi,\theta) \leq \frac{1}{1-\xi_0^2} \tag{3.47}$$

or equivalently

$$|\xi_0| \geq \sqrt{1-\frac{1}{\Psi(\psi,\theta)}} \tag{3.48}$$

### 3.2.4 Particle drift in an axisymmetric toroidal plasma

In an axisymmetric toroidal plasma, the equilibrium magnetic field is given by (3.2), which is rewritten in $(\psi,s,\phi)$ coordinates as

$$\mathbf{B} = \frac{I(\psi)}{R}\widehat{\phi} + \frac{\|\nabla\psi\|}{R}\widehat{s} \tag{3.49}$$

and is necessarily non-uniform. In that case, particles are subject to drifts both within and across the flux-surfaces. We are particularly interested in drifts across the flux-surfaces as they are essentially responsible for the existence of the bootstrap current.

### Drift Velocity from the Expression of Single Particle Drift

The guiding-center drift velocity due to the magnetic field gradient and curvature is given by (3.25) and its component perpendicular to the flux-surface can be written as

$$\mathbf{v}_D \cdot \nabla\psi = \frac{1}{\Omega_e}\left(v_\parallel^2 + \frac{v_\perp^2}{2}\right)\frac{1}{B^2}\nabla\psi \times \mathbf{B} \cdot \nabla B \tag{3.50}$$

Inserting the expression (3.49) of the magnetic field, we find

$$\mathbf{v}_D \cdot \nabla\psi = \frac{1}{\Omega_e}\left(v_\parallel^2 + \frac{v_\perp^2}{2}\right)\frac{\|\nabla\psi\|}{B^2 R}\left[\|\nabla\psi\|\,\widehat{\phi} - I(\psi)\,\widehat{s}\right] \cdot \nabla B \tag{3.51}$$

Using axisymmetry and the expression (A.83) for the gradient in $(\psi, s, \phi)$ coordinates, the equation (3.51) becomes

$$\mathbf{v}_D \cdot \nabla\psi = -\frac{1}{\Omega_e}\left(v_\parallel^2 + \frac{v_\perp^2}{2}\right)\frac{\|\nabla\psi\|\, I(\psi)}{B^2 R}\frac{\partial B}{\partial s} \tag{3.52}$$

With the definition (3.30) of the magnetic moment $\mu$, we rewrite

$$\mathbf{v}_D \cdot \nabla\psi = -\frac{1}{\Omega_e}\frac{\|\nabla\psi\|\, I(\psi)}{B^2 R}\left(v_\parallel^2 + \frac{\mu\Omega_e}{q_e}\right)\frac{\partial B}{\partial s} \tag{3.53}$$

Using the conservation of magnetic moment (3.29) along the particle motion

$$\frac{\mu\Omega_e}{q_e}\frac{\partial B}{\partial s} = \Omega_e \frac{\partial}{\partial s}\left(\frac{\mu B}{q_e}\right) \tag{3.54}$$

and using the conservation of energy (3.28) and the identity

$$\frac{v_\parallel^2}{B}\frac{\partial B}{\partial s} = \frac{\partial}{\partial s}\left(\frac{v_\parallel^2}{2}\right) - v_\parallel B \frac{\partial}{\partial s}\left(\frac{v_\parallel}{B}\right) \tag{3.55}$$

we get

$$\frac{1}{B}\left(v_\parallel^2 + \frac{\mu\Omega_e}{q_e}\right)\frac{\partial B}{\partial s} = -v_\parallel B \frac{\partial}{\partial s}\left(\frac{v_\parallel}{B}\right) \tag{3.56}$$

and finally, the equation (3.53) becomes

$$\mathbf{v}_D \cdot \nabla\psi = \frac{v_\parallel}{\Omega_e} I(\psi) \frac{\|\nabla\psi\|}{R} \frac{\partial}{\partial s}\left(\frac{v_\parallel}{B}\right) \tag{3.57}$$

In addition, using (3.49) and axisymmetry,

$$\mathbf{B} \cdot \nabla = \frac{\|\nabla\psi\|}{R} \frac{\partial}{\partial s} \tag{3.58}$$

so that we can rewrite (3.57) as

$$\mathbf{v}_D \cdot \nabla\psi = \frac{v_\parallel}{\Omega_e} I(\psi)\, \mathbf{B} \cdot \nabla\left(\frac{v_\parallel}{B}\right) \tag{3.59}$$

**Drift velocity from the conservation of canonical momentum**

The drift velocity (3.59) was obtained based on the expression (3.25), which was not derived from first principles. Note that we can also derive the drift velocity using the conservation of canonical momentum, which is also a constant of the motion because of axisymmetry. It is expressed as

$$P_\phi = R\left[\gamma m_e v_\phi + q_e A_\phi\right] \tag{3.60}$$

where $A_\phi$ is the toroidal component of the vector potential.

From the relation

$$\mathbf{B} = \nabla \times \mathbf{A} \tag{3.61}$$

with the expression (A.85) of a curl in $(\psi, s, \phi)$ coordinates, we have

$$B_s = \frac{1}{R}\frac{\partial}{\partial\phi}(A_\psi) - \frac{\|\nabla\psi\|}{R}\frac{\partial}{\partial\psi}(RA_\phi) \tag{3.62}$$

Then, using axisymmetry and the expression (3.10) for the poloidal field, we get

$$RA_\phi = -\psi \tag{3.63}$$

where we chose arbitrarily $A_\phi(\psi = 0) = 0$.

Because the toroidal canonical momentum is a constant of the motion, we have

$$\mathbf{v}_{\mathrm{gc}} \cdot \nabla P_\phi = 0 \tag{3.64}$$

which becomes, using (3.24), (3.63) and the conservation of energy so that $\mathbf{v}_{\mathrm{gc}} \cdot \nabla \gamma = 0$,

$$\mathbf{v}_D \cdot \nabla \psi = \frac{\gamma m_e}{q_e} \mathbf{v}_{\mathrm{gc}} \cdot \nabla (R v_\phi) \tag{3.65}$$

Assuming a priori that $|v_\parallel| \gg |\mathbf{v}_D|$, a condition that is well verified consistent with the conservation of magnetic moment, this equation reduces to

$$\mathbf{v}_D \cdot \nabla \psi = \frac{\gamma m_e}{q_e B} v_\parallel \mathbf{B} \cdot \nabla (R v_\phi) = \frac{v_\parallel}{\Omega_e} \mathbf{B} \cdot \nabla (R v_\phi) \tag{3.66}$$

The toroidal velocity is related to the parallel velocity by

$$v_\phi = \frac{B_\phi}{B} v_\parallel = \frac{I(\psi)}{RB} v_\parallel \tag{3.67}$$

Since $I(\psi)$ is a flux function, it can be taken out of the gradient, so that

$$\mathbf{v}_D \cdot \nabla \psi = \frac{v_\parallel}{\Omega_e} I(\psi) \mathbf{B} \cdot \nabla \left( \frac{v_\parallel}{B} \right) \tag{3.68}$$

an expression which is the same as (3.59).

### Deviation of particle orbits from the flux-surface

Because of the drift across flux-surfaces, particles are not strictly confined to a given flux-surface. Considering that the gradient of magnetic field amplitude is globally in the inward direction ($\nabla B \simeq -\widehat{\mathbf{R}} B/R$), the drift velocity in the poloidal plane (3.25) is arroximately

$$v_{DP} \simeq -\frac{1}{\Omega_e} \left( v_\parallel^2 + \frac{v_\perp^2}{2} \right) \frac{B_T}{RB} \widehat{\mathbf{Z}} \tag{3.69}$$

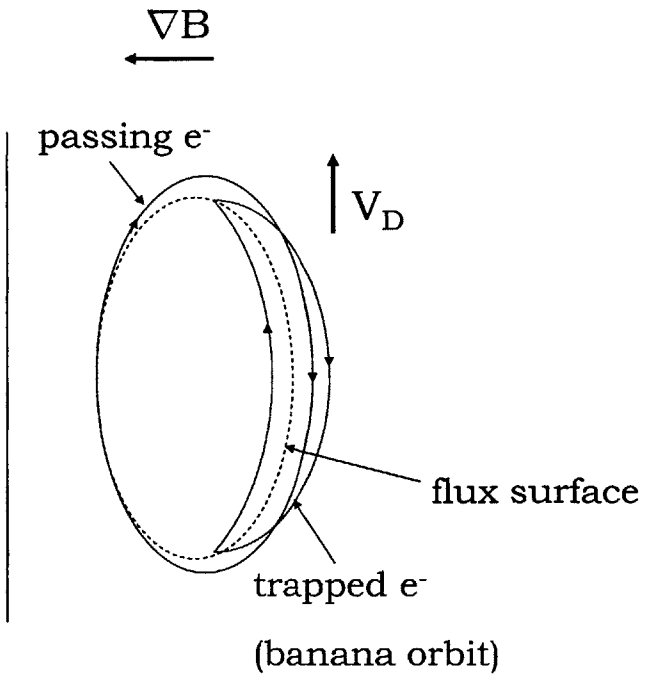


Figure 3-5: Poloidal projection of particle orbits in a toroidal plasma.

and is therefore directed in the vertical direction. Because ions and electrons drift in opposite direction, this drift could generate a vertical electric field that would lead to a loss of confinement due to resulting $\mathbf{E} \times \mathbf{B}$ drift in the outboard direction. However, along the poloidal motion of particles, this drift is directed alternatively towards the core and toward the edge of the plasma, such that it cancels exactly over the course of one transit or bounce period. This explains why a poloidal field is necessary to confine a ST or tokamak plasma. Although the cumulative drift vanishes over one poloidal motion, particles drift across the flux-surfaces along their orbit, as illustrated on figure 3-5, which results of the characteristic shape for trapped electrons, called *banana orbits*. The maximum deviation off the flux-surface can be estimated by calculating the accumulated drift over half a bounce or transit time $\tau_b$. From (3.69), we get

$$\Delta r_D \simeq v_{DP}\frac{\tau_b}{2} \simeq \begin{cases} \rho_{Te}\pi q & \text{for passing electrons} \\ \rho_{Te}\dfrac{\pi q}{\xi_{0T}} & \text{for trapped electrons} \end{cases} \tag{3.70}$$

where we used the estimation (3.103) for the bounce time and where we used $q \simeq \widetilde{q}B_T/B$. We see that the particle deviation from the flux-surface is not more than a few Larmor radii, and that it is larger for trapped electrons, because their parallel velocity is smaller.

### 3.2.5 Bounce time and bounce averaging operation

#### Transit or Bounce Time

Because the orbit deviation from a flux-surface is very small compared to the size of the plasma and the poloidal orbit length, it is a good approximation, for electrons, to assume that the particle is exactly on the flux-surface when integrating along the particle orbit. In this limit of zero-banana width, the forward and backward motion of trapped electrons follow the same trajectory. In that case, we can define the bounce time as the time for a trapped electron to complete half a bounce period. The poloidal transit time for a passing electron is defined as the time to complete a full orbit in the poloidal plane. We define then, for any electron

$$\tau_b(\psi) = \int_{s_{\min}}^{s_{\max}} \frac{ds}{|v_s|} = \int_{s_{\min}}^{s_{\max}} \frac{ds}{|v_\parallel|} \frac{B}{B_P} \tag{3.71}$$

where $v_s$ is the guiding center velocity along the poloidal field lines, and $v_\parallel$ is its velocity parallel to the magnetic field. The limits $s_{\min}$ and $s_{\max}$ are defined in (3.5) for passing electrons, and are the positions, along the field lines, of turning points for trapped electrons.

The differential arc length $ds$ along the poloidal field line is generally expressed in curvilinear coordinates $(u^1, u^2, u^3)$ as (A.11)

$$ds = \sqrt{g_{ij} du^i du^j} \tag{3.72}$$

where the $g_{ij}$ are the metric coefficients, defined in (A.10). In the $(\psi, \theta, \phi)$ coordinates system, the variations $d\psi$ and $d\phi$ are essentially zero along the poloidal field line. As

a consequence, (3.72) reduces to

$$ds = \sqrt{g_{22}} d\theta \tag{3.73}$$

where the metric factor $\sqrt{g_{22}}$ represent the poloidal distance per radian along the field lines. The bounce time (3.71) becomes

$$\tau_b(\psi) = \int_{\theta_{\min}}^{\theta_{\max}} d\theta \frac{\sqrt{g_{22}}}{|v_\parallel|} \frac{B}{B_P} \tag{3.74}$$

where the limits $\theta_{\min}$ and $\theta_{\max}$ are defined in (3.45).

In spherical momentum coordinates, we have (A.113)

$$\frac{v_\parallel}{v} = \frac{p_\parallel}{p} = \xi \tag{3.75}$$

so that

$$\tau_b(\psi) = \frac{2\pi}{v|\xi_0|} \int_{\theta_{\min}}^{\theta_{\max}} \frac{d\theta}{2\pi} \sqrt{g_{22}} \frac{\xi_0}{\xi} \frac{B}{B_P} \tag{3.76}$$

The bounce time can then be normalized as

$$\tau_b(\psi, \xi_0) = \frac{2\pi R_p \widetilde{q}(\psi)}{v|\xi_0|} \lambda(\psi, \xi_0) \tag{3.77}$$

where

$$\lambda(\psi, \xi_0) = \frac{1}{\widetilde{q}(\psi)} \int_{\theta_{\min}}^{\theta_{\max}} \frac{d\theta}{2\pi} \frac{\sqrt{g_{22}}}{R_p} \frac{\xi_0}{\xi} \frac{B}{B_P} \tag{3.78}$$

and

$$\widetilde{q}(\psi) \equiv \int_0^{2\pi} \frac{d\theta}{2\pi} \frac{\sqrt{g_{22}}}{R_p} \frac{B}{B_P} \tag{3.79}$$

The bounce time is in fact normalized to the transit time of particles with parallel momentum only, since $\lambda(\psi, \pm 1) = 1$. The factor $\widetilde{q}(\psi)$ represents the length of field lines within one poloidal rotation, normalized by $2\pi R_p$.

The covariant metric element $g_{22}$ is given by (A.8)-(A.10), which in the $(\psi, \theta, \phi)$

system becomes (A.89)

$$g_{22} = \frac{r}{\left|\widehat{\psi} \cdot \widehat{\mathbf{r}}\right|} \tag{3.80}$$

Consequently, the normalized bounce time takes the form

$$\lambda(\psi, \xi_0) = \frac{1}{\widetilde{q}(\psi)} \int_{\theta_{\min}}^{\theta_{\max}} \frac{d\theta}{2\pi} \frac{1}{\left|\widehat{\psi} \cdot \widehat{\mathbf{r}}\right|} \frac{r}{R_p} \frac{B}{B_P} \frac{\xi_0}{\xi} \tag{3.81}$$

with

$$\widetilde{q}(\psi) = \int_0^{2\pi} \frac{d\theta}{2\pi} \frac{1}{\left|\widehat{\psi} \cdot \widehat{r}\right|} \frac{r}{R_p} \frac{B}{B_P} \tag{3.82}$$

### Bounce Averaging

Anticipating that the kinetic equation will be reduced based on the fast streaming motion along the field lines, we define an average over the poloidal motion, which accounts for changes in the particle velocity, including trapping, and effectively annihilates any term of the type $\mathbf{v}_s \cdot \partial/\partial s$ in the zero banana-width limit. This is called the bounce-averaging operation

$$\begin{aligned} \{\mathcal{A}\} &= \frac{1}{\tau_b} \left[\frac{1}{2} \sum_{\sigma}\right]_T \int_{s_{\min}}^{s_{\max}} \frac{ds}{|v_s|} \mathcal{A} \\ &= \frac{1}{\tau_b} \left[\frac{1}{2} \sum_{\sigma}\right]_T \int_{s_{\min}}^{s_{\max}} \frac{ds}{|v_\parallel|} \frac{B}{B_P} \mathcal{A} \end{aligned} \tag{3.83}$$

where the sum over $\sigma = \text{sign}(v_\parallel)$ applies to trapped particles only. This is an average over a poloidal rotation for passing electrons, and over both the forward and backward motion for trapped electrons. It can be rewritten in $(\psi, \theta, \phi)$ coordinates using (3.73)

$$\{\mathcal{A}\} = \frac{1}{\tau_b} \left[\frac{1}{2} \sum_{\sigma}\right]_T \int_{\theta_{\min}}^{\theta_{\max}} d\theta \frac{\sqrt{g_{22}}}{|v_\parallel|} \frac{B}{B_P} \mathcal{A} \tag{3.84}$$

and in terms of the normalized bounce time $\lambda$ using expression (3.78)

$$\{\mathcal{A}\} = \frac{1}{\lambda \widetilde{q}} \left[\frac{1}{2}\sum_{\sigma}\right]_T \int_{\theta_{\min}}^{\theta_{\max}} \frac{d\theta}{2\pi} \frac{\sqrt{g_{22}}}{R_p} \frac{B}{B_P} \frac{\xi_0}{\xi} \mathcal{A} \tag{3.85}$$

or, inserting the expression (3.80) for $\sqrt{g_{22}}$

$$\{\mathcal{A}\} = \frac{1}{\lambda \widetilde{q}} \left[\frac{1}{2}\sum_{\sigma}\right]_T \int_{\theta_{\min}}^{\theta_{\max}} \frac{d\theta}{2\pi} \frac{1}{\left|\widehat{\psi} \cdot \widehat{\mathbf{r}}\right|} \frac{r}{R_p} \frac{B}{B_P} \frac{\xi_0}{\xi} \mathcal{A} \tag{3.86}$$

We anticipate that bounce averaging the momentum-space operators in the kinetic equations leads to a set of coefficients that all have a similar structure, denoted $\lambda_{k,l,m}$ and $\overline{\lambda}_{k,l,m}$, which are define as

$$\left\{ \left( \frac{\xi(\psi,\theta,\xi_0)}{\xi_0} \right)^k \Psi^l(\psi,\theta) \left( \frac{R_0(\psi)}{R(\psi,\theta)} \right)^m \right\} \equiv \frac{\lambda_{k,l,m}(\psi,\xi_0)}{\lambda(\psi,\xi_0)} \tag{3.87}$$

and

$$\sigma \left\{ \sigma \left( \frac{\xi(\psi,\theta,\xi_0)}{\xi_0} \right)^k \Psi^l(\psi,\theta) \left( \frac{R_0(\psi)}{R(\psi,\theta)} \right)^m \right\} \equiv \frac{\overline{\lambda}_{k,l,m}(\psi,\xi_0)}{\lambda(\psi,\xi_0)} \tag{3.88}$$

where

$$R_0(\psi) \equiv R(\psi,\theta_0) \tag{3.89}$$

Note that by definition, $\lambda_{0,0,0} = \lambda$. In addition,

$$\overline{\lambda}_{k,l,m} = \begin{cases} \lambda_{k,l,m} & \text{for passing particles} \\ 0 & \text{for trapped particles} \end{cases} \tag{3.90}$$

## 3.3 Drift-Kinetic Equation

In this work, we do not undertake the derivation of a consistent drift-kinetic formulation in the presence of RF fields. Rather, we derive the drift-kinetic equation independently from the presence of RF fields, and assume that the cumulative effect of the wave particle interaction on a slow time scale (of the order of the collision time) is approximately described by the quasilinear operator derived by Kennel &

Engelmann [41] and Lerche [42] for a uniform plasma.

This approach, first followed by S. Schultz [32], is justified by assuming that the inhomogeneity in the plasma - which is responsible for the mirror force and the drifts of the flux-surface - does not significantly affect wave-particle interaction. For this assumption to be valid, it is required that (1) the extent of particle orbits off the flux-surface is small as compared to the variation of RF wave characteristics, and (2) the changes in the particle velocity due to the equilibrium inhomogeneities do not affect the particle resonance. The condition (1) is easily satisfied for electrons, because the radial shift of their orbits is small (of the order of a few Larmor radii), which is consistent with the zero-banana width limit in the bounce-averaging operation. However, the condition (2) is more restrictive, and imposes limits on the spatial extent of RF beams, which we will investigate in section 3.5.2.

We point out that the derivation of a quasilinear operator consistent with toroidal geometry has been undertaken in previous works, either by direct averaging techniques [44] or from a Hamiltonian approach [68]. However, this operators have been derived for mirror machines and space plasmas, respectively, and consider only the motion of trapped electrons. They do not directly apply to the tokamak plasma where both passing and trapped electrons must be considered. It can be readily shown, however, that the operator derived in [44] reduces to the operators from [41] and [42] in first approximation for equilibria with large inhomogeneity space scale.

### 3.3.1 Boltzmann equation

In kinetic theory, electrons are described statistically by a distribution function $f(\mathbf{r}, \mathbf{p}, t)$, which represent the phase-space density of particles with momentum $\mathbf{p}$ at the position $\mathbf{r}$ and time $t$. The evolution of the distribution function is governed by the Boltzmann equation

$$\frac{\partial f}{\partial t} + \mathbf{v} \cdot \nabla_{\mathbf{r}} f + \mathbf{F}(\mathbf{r}, \mathbf{p}, t) \cdot \nabla_{\mathbf{p}} f = \mathcal{C}(f) \tag{3.91}$$

where $\mathbf{v}$ is the velocity the particles (2.54)

$$\mathbf{v} = \frac{\mathbf{p}}{m_e \gamma} \tag{3.92}$$

and $\mathbf{F}(\mathbf{r}, \mathbf{p}, t)$ is the electromagnetic force acting on electrons, called Lorentz force

$$\mathbf{F}(\mathbf{r}, \mathbf{p}, t) = q_e \left[\mathbf{E}(\mathbf{r}, t) + \mathbf{v} \times \mathbf{B}(\mathbf{r}, t)\right] \tag{3.93}$$

where $\mathbf{E}(\mathbf{r}, t)$ and $\mathbf{B}(\mathbf{r}, t)$ are the electric and magnetic field, respectively. The operator $C(f)$ describes the effect of collisions with both like and unlike particles.

In the derivation of the drift-kinetic equation, we consider only the equilibrium field $\mathbf{B}(\mathbf{r})$, and ignore the perturbation field (typically generated by RF sources). The Boltzmann equation (3.91) can then be rewritten as

$$\frac{\partial f}{\partial t} + \mathbf{v} \cdot \nabla_{\mathbf{r}} f - \frac{q_e B}{m_e \gamma} \frac{\partial f}{\partial \varphi} = C(f) \tag{3.94}$$

where we used the following identity, based on (3.92), (A.102) and the expression (A.110) for the gradient in cylindrical momentum coordinates

$$q_e \mathbf{v} \times \mathbf{B}(\mathbf{r}) \cdot \nabla_{\mathbf{p}} f = -\frac{q_e B}{m_e \gamma} \frac{\partial f}{\partial \varphi} \tag{3.95}$$

where $B = \|\mathbf{B}\|$. With the definition (3.26) for the gyrofrequency, we get

$$\frac{\partial f}{\partial t} + \mathbf{v} \cdot \nabla_{\mathbf{r}} f - \Omega_e(\mathbf{r}) \frac{\partial f}{\partial \varphi} = C(f) \tag{3.96}$$

### 3.3.2 Drift-Kinetic Equation

In tokamaks, the gyro-frequency is typically much larger than the collision frequency and the bounce frequency, such that, to leading order, the equation (3.96) reduces to $\partial f / \partial \varphi = 0$ and $f$ is gyro-independent. Gyro-averaging equation (3.96) gives then

the *drift-kinetic equation* (DKE) [69]

$$\frac{\partial f}{\partial t} + \mathbf{v}_{\mathrm{gc}} \cdot \nabla_{\mathbf{r}} f = \mathcal{C}(f) \tag{3.97}$$

where $\mathbf{v}_{\mathrm{gc}}$ is the guiding center velocity, obtained after gyro-averaging the particle velocity, and $f = f(\mathbf{r}, p, \xi, t)$. At this stage, we introduce the quasilinear operator, which describes the diffusive effects of RF fields on the macroscopic, gyro-independent distribution function. We obtain the DKE with RF diffusion

$$\frac{\partial f}{\partial t} + \mathbf{v}_{\mathrm{gc}} \cdot \nabla_{\mathbf{r}} f = \mathcal{C}(f) + \mathcal{Q}(f) \tag{3.98}$$

The guiding center velocity is decomposed into the fast motion along the field lines, and a drift velocity. It is expressed as (3.24)

$$\mathbf{v}_{\mathrm{gc}} = v_{\parallel} \widehat{b} + \mathbf{v}_D \tag{3.99}$$

The drifts within the flux-surface are neglected compared to the fast parallel streaming, and we retain only the drift across flux-surfaces, which is responsible for the existence of the bootstrap current and is given by (3.59)

$$\mathbf{v}_D \cdot \nabla \psi = \frac{v_{\parallel}}{\Omega_e} I(\psi)\, \mathbf{B} \cdot \nabla_{\mathbf{r}} \left( \frac{v_{\parallel}}{B} \right) \tag{3.100}$$

Using the expression for the gradient in $(\psi, s, \phi)$ corrdinates (A.83), we rewrite the DKE (3.98) in steady-state form as

$$v_s \frac{\partial f}{\partial s} + \frac{v_{\parallel}}{\Omega_e} I(\psi) \frac{\|\nabla \psi\|}{R} \frac{\partial}{\partial s} \left( \frac{v_{\parallel}}{B} \right) \frac{\partial f}{\partial \psi} = \mathcal{C}(f) + \mathcal{Q}(f) \tag{3.101}$$

### 3.3.3 Time scales in the DKE

The DKE (3.101) is a linear partial integro-differential equation for the steady-state distribution $f = f(\psi, s, p, \xi)$ in axisymmetric plasmas. However, it is possible to reduce this equation to a set of 2D momentum-space equations by ordering the different

time scales in this equation. This reduction is important not only with respect to the challenge of multidimensional numerical calculations, but also in order to extract the relevant physics of particle motion and wave-particle interaction. The physical interpretation and corresponding time scales of the terms in equation (3.101) are respectively

1. Parallel motion along magnetic field lines

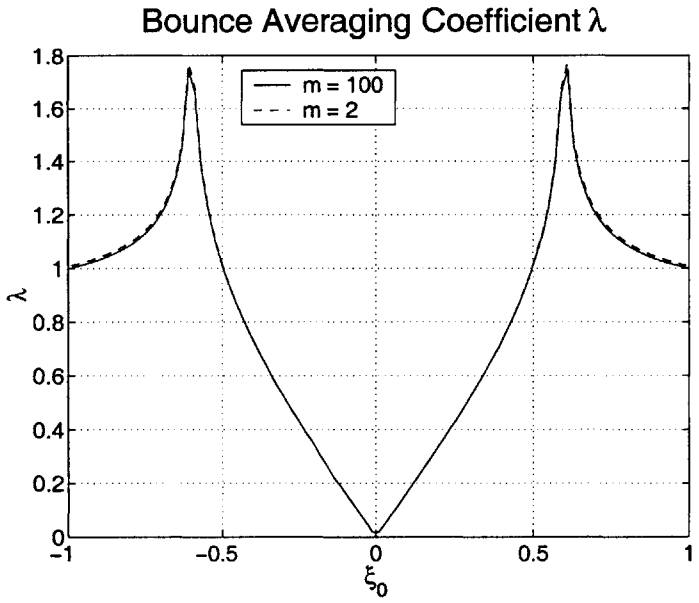


Figure 3-6: Normalized bounce time $\lambda(\psi, \xi_0)$ as a function of the pitch angle coordinate $\xi_0$ for $\xi_{0T} \simeq 0.6$.

The characteristic time scale of the parallel streaming along field lines is $\tau_b$, the bounce or transit time for trapped or passing electrons respectively. It is given by (3.77)

$$\tau_b(\psi, \xi_0) = \frac{2\pi R_p \widetilde{q}(\psi)}{v|\xi_0|} \lambda(\psi, \xi_0) \tag{3.102}$$

A detailed study of $\lambda(\psi, \xi_0)$, plotted in Fig. 3-6, shows that for passing electrons we have typically $\lambda(\psi, \xi_0)/|\xi_0| \simeq 1$, while for trapped electrons we have $\lambda(\psi, \xi_0)/|\xi_0| \simeq 1/\xi_{0T}$. Therefore, the typical bounce or transit time of electrons

is of the order of

$$\begin{cases} \overline{\tau}_{bP} \simeq \dfrac{2\pi R_p \widetilde{q}}{v_{Te}} & \text{for passing electrons} \\ \\ \overline{\tau}_{bT} \simeq \dfrac{2\pi R_p \widetilde{q}}{\xi_{0T} v_{Te}} & \text{for trapped electrons} \end{cases} \tag{3.103}$$

2. Drift across flux-surfaces

The drift time scale is defined as the time for an electron to drift on a cumulative distance of the order of the plasma radial size $a_p$, and can be derived from (3.101)

$$\tau_d \simeq \frac{2\pi R_p a_p}{v_{Te}\rho_{Te}} \frac{B}{B_T} \tag{3.104}$$

where we define the thermal Larmor radius

$$\rho_{Te} = \frac{v_{Te}}{\omega_{ce}} \tag{3.105}$$

3. Collisions

Collisions are described by a Fokker-Planck operator (Section 3.4), which accounts for the cumulative effect of many small-angle collisions. The collision time $\tau_c$ represents the time-scale for a diffusive deflection of the order of $\pi/2$ and is given by [56]

$$\tau_c = \nu_c^{-1} = \frac{4\pi\varepsilon_0^2 m_e^2 v_{Te}^3}{q_e^4 n_e \ln\Lambda} \tag{3.106}$$

where $\ln\Lambda$ is the well known Coulomb logarithm, a slowly varying function of the plasma temperature and density. A characteristic collisional time scale for trapped electrons is the detrapping time, defined as the typical time for a trapped electron to be detrapped due to collisional pitch-angle scattering. The typical detrapping deflection for trapped electrons is smaller than $\pi/2$ by a factor $\xi_{0T}$. Because pitch-angle scattering is a diffusive process, the average deflection increases like the square root of time, $\Delta\xi \sim \sqrt{\Delta t}$. Therefore, the detrapping time is shorter than the $\pi/2$ collisional time by a factor $\xi_{0T}^2$ and we

have

$$\tau_{dt} \simeq \xi_{0T}^2 \tau_c \tag{3.107}$$

4. Quasilinear diffusion

   In quasilinear theory, the cumulative effect of RF fields on the macroscopic distribution function is a momentum space diffusion characterized by a diffusion coefficient $D_{\mathrm{QL}}$, which will be determined in Section 3.5. The corresponding diffusive time scale can be expressed as

$$\tau_{\mathrm{QL}} \simeq \frac{p_{Te}^2}{D_{\mathrm{QL}}} \tag{3.108}$$

### 3.3.4 Small drift expansion

In tokamaks and STs, the drift time scale, as defined in (3.104), is typically much longer than the bounce, collisional and quasilinear time scales, and we define the small drift parameter as being the ratio

$$\delta \equiv \frac{\tau_{bP}}{\tau_d} \simeq \frac{\rho_{Te}}{a_p} \frac{\widetilde{q} B_T}{B} \simeq q \frac{\rho_{Te}}{a_p} \tag{3.109}$$

where we used $q \simeq \widetilde{q} B_T / B$ based on (3.19) and (3.82). The small parameter $\delta$ can also be viewed as the ratio of the banana radial deviation from the flux-surface $\Delta r_D$ (3.70) to the plasma size $a_p$.

In a typical NSTX plasma ($q \simeq 3$, $a_p \simeq 0.9$ m, $T_e = 1.3$ keV, $B = 0.3$ T), we find $\delta \simeq 10^{-3}$ , which indicates that the small drift approximation is well validated.

Ordering equation (3.101) in powers of $\delta \ll 1$ after expanding $f = f_0 + f_1 + \cdots$, we get

- At zero order

$$v_s \frac{\partial f_0}{\partial s} = \mathcal{C}(f_0) + \mathcal{Q}(f_0) \tag{3.110}$$

  which is the usual Fokker-Planck equation, obtained when the effects of radial drifts is neglected.

- At first order

$$v_s \frac{\partial f_1}{\partial s} + \frac{v_\parallel}{\Omega_e} I(\psi) B_P \frac{\partial}{\partial s}\left(\frac{v_\parallel}{B}\right) \frac{\partial f_0}{\partial \psi} = \mathcal{C}(f_1) + \mathcal{Q}(f_1) \tag{3.111}$$

which we will refer to as the drift-kinetic equation, since the effects of radial drifts are included.

### 3.3.5 Low collisionality ordering

In the low collisionality, so-called banana regime, the collisional detrapping time $\tau_{dt}$ is much longer than the bounce time of trapped particles $\tau_{bP}$, meaning that trapped electrons typically bounce back and forth many times before their orbit is affected by collisions. The collisionality is measured by the parameter

$$\nu^* = \frac{\tau_{bP}}{\tau_{dt}} \simeq \frac{2\pi R_p \widetilde{q}}{\tau_c v_{Te} \xi_{0T}^3} \tag{3.112}$$

In a typical NSTX plasma, the collisionality parameter is very small, except very near the magnetic axis, where the trapped particle fraction vanishes, and near the edge, where typically $\tau_c v_{Te} \to 0$. The profile of $\nu^*$ is shown on Fig. 3-7 for a typical NSTX plasma with the profiles of Fig. 1-8. Note that near the magnetic axis, the fraction of trapped particles vanishes and therefore $\nu^*$ becomes irrelevant. Then, the collisionality parameter for passing particles $\nu = \tau_{bT}/\tau_{dt}$, which typically remains very small, should be considered instead.

In the case where $\nu^* \ll 1$, the collisionless approach to particle motion done in section 3.2 is essentially valid. If in addition we assume that the effect of RF fields is small in the course of one bounce-period, meaning $\tau_{\mathrm{QL}} \geq \tau_{bT}/\nu^*$, we can (sub)order the equations (3.110) and (3.111) with respect to $\nu^*$, in the so-called *banana regime* $\delta \ll \nu^* \ll 1$, which gives at leading order:

- For the Fokker-Planck equation (3.110)

$$\frac{\partial f_0}{\partial s} = 0 \tag{3.113}$$

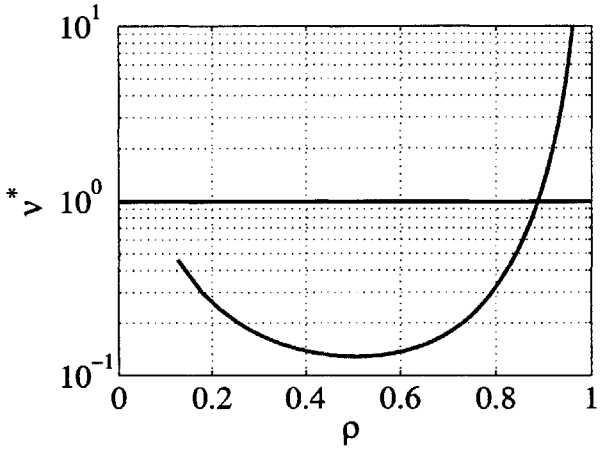


Figure 3-7: Collisionality parameter $\nu^*$ for a typical NSTX plasma.

which means that $f_0$ is constant along the field lines, and therefore symmetric in $\xi$ in the trapped region.

- For the Drift-kinetic equation (3.111)

$$v_s \frac{\partial f_1}{\partial s} + v_{\|} \frac{I(\psi) B_P}{\Omega_e} \frac{\partial}{\partial s} \left( \frac{v_{\|}}{B} \right) \frac{\partial f_0}{\partial \psi} = 0 \tag{3.114}$$

which integrates as

$$f_1 = \widetilde{f} + g \tag{3.115}$$

where, using $v_s = v_{\|} B_P / B$ and the fact that $f_0$ is constant along field lines,

$$\begin{aligned} \widetilde{f} &= -\int^s \frac{I(\psi) B}{\Omega_e} \frac{\partial}{\partial s} \left( \frac{v_{\|}}{B} \right) \frac{\partial f_0}{\partial \psi} \\ &= -\frac{I(\psi) v_{\|}}{\Omega_e} \frac{\partial f_0}{\partial \psi} \end{aligned} \tag{3.116}$$

and $g$ is an integration function of $(\mathbf{p}, \psi)$ but constant in $s$, and therefore is also symmetric in the trapped region. We determined in Section 3.2.1 that with our expression (3.2) for the magnetic field, the flux function $\psi$ increases in the radial direction if the plasma current is in the same direction as the magnetic

field ($I_\phi > 0$). In that case, $\partial f_0/\partial\psi < 0$ and with $\Omega_e < 0$ we see that $\widetilde{f}$ is of the opposite sign to $v_\parallel$. Because electrons carry a negative current, we find that the drifts generate a current in the direction of the magnetic field, and therefore the bootstrap current is in the same direction as the plasma current.

### 3.3.6 Bounce averaging and steady-state equations

- The evolution equation for $f_0$ can now be obtained by bounce-averaging the equation (3.110), which annihilates the motion along the fields lines, since using (3.83), $v_s = \sigma |v_s|$ and the fact that $f_0$ is constant along field lines.

$$\left\{ v_s \frac{\partial f_0}{\partial s} \right\} = \frac{1}{\tau_b} \left[ \frac{1}{2} \sum_\sigma \right]_T \sigma \left[ f_0 \right]_{s_{\min}}^{s_{\max}} = 0 \tag{3.117}$$

We obtain the steady-state bounced-averaged Fokker-Planck equation

$$\{\mathcal{C}(f_0)\} + \{\mathcal{Q}(f_0)\} = 0 \tag{3.118}$$

- The evolution equation for $f_1$ is obtained by bounce-averaging the equation (3.111). Because $g$ is constant along field lines, $\{v_s \partial g/\partial s\} = 0$ using (3.117). We also have that

$$\left\{ v_s \frac{\partial \widetilde{f}}{\partial s} \right\} = \frac{1}{\tau_b} \left[ \frac{1}{2} \sum_\sigma \right]_T \sigma \left[ \widetilde{f} \right]_{s_{\min}}^{s_{\max}} = 0 \tag{3.119}$$

since $s_{\min}$ and $s_{\max}$ coincide for passing electrons, and $\widetilde{f}(s_{\min}) = \widetilde{f}(s_{\max}) = 0$ for trapped electrons since $v_\parallel$ vanishes at these points (3.116). In addition, we have

$$\left\{ \frac{v_\parallel}{\Omega_e} I(\psi) B_P \frac{\partial}{\partial s} \left( \frac{v_\parallel}{B} \right) \frac{\partial f_0}{\partial \psi} \right\} = \frac{BI(\psi)}{\Omega_e \tau_b} \frac{\partial f_0}{\partial \psi} \left[ \frac{1}{2} \sum_\sigma \right]_T \sigma \left[ \frac{v_\parallel}{B} \right]_{s_{\min}}^{s_{\max}} = 0 \tag{3.120}$$

since $s_{\min}$ and $s_{\max}$ coincide for passing electrons, and $v_\parallel$ vanishes at the turning

points. We obtain the steady-state bounced-averaged DKE

$$\{\mathcal{C}(f_1)\} + \{\mathcal{Q}(f_1)\} = 0 \tag{3.121}$$

and therefore, for linearized collision and RF diffusion operators,

$$\{\mathcal{C}(g)\} + \{\mathcal{Q}(g)\} = -\left\{\mathcal{C}\left(\widetilde{f}\right)\right\} - \left\{\mathcal{Q}\left(\widetilde{f}\right)\right\} \tag{3.122}$$

Note that $f_0$ is a solution of the homogeneous part of the linear equation (3.122), and therefore any solution of the type

$$g' = g + c_g f_0 \tag{3.123}$$

is also solution of (3.122). We choose to solve (3.122) for the solution $g$ that is identically zero in the trapped region, and then solve (3.123) for $c_g$ by using the conservation of the flux-surface averaged density.

### 3.3.7 Conservative formulation of the kinetic equation

#### Operator expressed as the divergence of a flux

As we will show in Section 3.4 and 3.5, the quasilinear diffusion operator and the differential part of the collision operator can be expressed in a conservative form as the divergence of a flux. Therefore, we write formally

$$\begin{aligned} \mathcal{C}(f) &= -\nabla_{\mathbf{p}} \cdot \mathbf{S}^{\mathrm{C}} + \mathcal{I}(f) \\ \mathcal{Q}(f) &= -\nabla_{\mathbf{p}} \cdot \mathbf{S}^{\mathrm{RF}} \end{aligned} \tag{3.124}$$

where $\mathcal{I}(f)$ is an integral contribution to the collision operator, which ensures momentum conservation. The kinetic equations (3.118) and (3.122) can therefore be

rewritten respectively as

$$\begin{aligned} &\nabla_{\mathbf{p}} \cdot \mathbf{S}(f_0) = \mathcal{I}(f_0) && \text{(a)} \\ &\nabla_{\mathbf{p}} \cdot \mathbf{S}(g) + \nabla_{\mathbf{p}} \cdot \mathbf{S}\left(\widetilde{f}\right) = \mathcal{I}(g) + \mathcal{I}\left(\widetilde{f}\right) && \text{(b)} \end{aligned} \tag{3.125}$$

where $\mathbf{S} = \mathbf{S}^{\mathrm{C}} + \mathbf{S}^{\mathrm{RF}}$ is the total momentum-space flux. For these gyro-averaged kinetic equations, the divergence is $(p, \xi)$ coordinates is given by (A.124)

$$\nabla_{\mathbf{p}} \cdot \mathbf{S}(f) = \frac{1}{p^2}\frac{\partial}{\partial p}\left[p^2 S_p(f)\right] - \frac{1}{p}\frac{\partial}{\partial \xi}\left[\sqrt{1-\xi^2}\, S_\xi(f)\right] \tag{3.126}$$

with the definitions

$$\begin{aligned} S_p(f) &= \mathbf{S}(f) \cdot \widehat{\mathbf{p}} \\ S_\xi(f) &= \mathbf{S}(f) \cdot \widehat{\xi} \end{aligned} \tag{3.127}$$

**Bounce-averaged divergence operator**

The bounce averaging of the divergence operator (3.126) gives

$$\{\nabla_{\mathbf{p}} \cdot \mathbf{S}\} = \left\{\frac{1}{p^2}\frac{\partial}{\partial p}\left(p^2 S_p\right)\right\} - \left\{\frac{1}{p}\frac{\partial}{\partial \xi}\left(\sqrt{1-\xi^2}\, S_\xi\right)\right\} \tag{3.128}$$

where the bounce averaging operation is defined in (3.86)

$$\{\mathcal{A}\} = \frac{1}{\lambda \widetilde{q}}\left[\frac{1}{2}\sum_{\sigma}\right]_T \int_{\theta_{\min}}^{\theta_{\max}} \frac{d\theta}{2\pi} \frac{1}{\left|\widehat{\psi} \cdot \widehat{\mathbf{r}}\right|} \frac{r}{R_p}\frac{B}{B_P}\frac{\xi_0}{\xi}\mathcal{A} \tag{3.129}$$

and $\xi$ is given along the trajectory by (3.43)

$$\xi(\psi, \theta, \xi_0) = \sigma\sqrt{1 - \Psi(\psi, \theta)\left(1 - \xi_0^2\right)} \tag{3.130}$$

with (3.33)

$$\Psi(\psi, \theta) = \frac{B(\psi, \theta)}{B_0(\psi)} \tag{3.131}$$

From (3.130) we derive the identities

$$\begin{aligned} \xi d\xi &= \Psi \xi_0 d\xi_0 \\ (1-\xi^2) &= \Psi\,(1-\xi_0^2) \end{aligned} \tag{3.132}$$

Then, using (3.132) and keeping in mind that $|\xi_0| = \sigma\xi_0$ is independent of $\sigma$, we can transform as follows,

$$\begin{aligned} &\left\{\frac{1}{p}\frac{\partial}{\partial\xi}\left(\sqrt{1-\xi^2}S_\xi\right)\right\} \\ &= \frac{1}{\lambda\widetilde{q}}\left[\frac{1}{2}\sum_\sigma\right]_T\int_{\theta_{\min}}^{\theta_{\max}}\frac{d\theta}{2\pi}\frac{1}{\left|\widehat{\psi}\cdot\widehat{r}\right|}\frac{r}{R_p}\frac{B}{B_P}\frac{\xi_0}{\xi}\frac{1}{p}\frac{\partial}{\partial\xi}\left(\sqrt{1-\xi^2}S_\xi\right) \\ &= \frac{1}{\lambda p}\frac{\partial}{\partial\sigma\xi_0}\frac{1}{\widetilde{q}}\left[\frac{1}{2}\sum_\sigma\right]_T\int_{\theta_{\min}}^{\theta_{\max}}\frac{d\theta}{2\pi}\frac{1}{\left|\widehat{\psi}\cdot\widehat{r}\right|}\frac{r}{R_p}\frac{B}{B_P}\frac{\sigma}{\Psi}\sqrt{1-\xi^2}S_\xi \\ &= \frac{1}{\lambda p}\frac{\partial}{\partial\xi_0}\sqrt{1-\xi_0^2}\sigma\frac{1}{\widetilde{q}}\left[\frac{1}{2}\sum_\sigma\right]_T\int_{\theta_{\min}}^{\theta_{\max}}\frac{d\theta}{2\pi}\frac{1}{\left|\widehat{\psi}\cdot\widehat{r}\right|}\frac{r}{R_p}\frac{B}{B_P}\frac{\sigma}{\sqrt{\Psi}}S_\xi \\ &= \frac{1}{\lambda p}\frac{\partial}{\partial\xi_0}\sqrt{1-\xi_0^2}\lambda\sigma\left\{\frac{\sigma\xi}{\sqrt{\Psi}\xi_0}S_\xi\right\} \end{aligned} \tag{3.133}$$

Consequently, we can rewrite the bounce-averaged divergence operator (3.128) as

$$\{\nabla_{\mathbf{p}}\cdot\mathbf{S}\} = \frac{1}{p^2}\frac{\partial}{\partial p}\left(p^2 S_p^{(0)}\right) - \frac{1}{\lambda p}\frac{\partial}{\partial\xi_0}\left(\sqrt{1-\xi_0^2}\lambda S_{\xi_0}^{(0)}\right) \tag{3.134}$$

where we defined

$$\begin{aligned} S_p^{(0)} &= \{S_p\} \\ S_{\xi_0}^{(0)} &= \sigma\left\{\frac{\sigma\xi}{\sqrt{\Psi}\xi_0}S_\xi\right\} \end{aligned} \tag{3.135}$$

We must check the conservative nature of the equation (3.134). The integral of $\{\nabla_{\mathbf{p}}\cdot\mathbf{S}\}$ over the $(p,\xi)$ momentum space (Jacobian (A.119) $J_{\mathbf{p}} = p^2$) and over the incremental volume of a flux-surface (Jacobian (A.92) $J_{\mathbf{r}} = Rr/\left\|\nabla\psi\right\|\left|\widehat{\psi}\cdot\widehat{\mathbf{r}}\right|$) is given

by

$$\begin{aligned}\frac{d\mathcal{K}}{d\psi} &= 4\pi^2 \int_0^{2\pi} d\theta J_{\mathbf{r}} \int_0^{\infty} dp \int_{-1}^{1} d\xi J_{\mathbf{p}} \left\{\nabla_{\mathbf{p}} \cdot \mathbf{S}\right\} \\ &= 4\pi^2 \int_0^{2\pi} d\theta J_{\mathbf{r}} \int_{-1}^{1} d\xi \left[p^2 S_p^{(0)}\right]_{p=0}^{p=\infty} \\ &\qquad - 4\pi^2 \frac{2\pi R_p \widetilde{q}\,(\psi)}{B_0} \int_0^{\infty} p dp \left[\sqrt{1-\xi_0^2}\lambda S_{\xi_0}^{(0)}\right]_{-1}^{1} \\ &= 0 \end{aligned} \tag{3.136}$$

and therefore the operator (3.134) conserves particles on a given flux-surface.

### 3.3.8 Decomposition of bounce-averaged fluxes

As we will determine is Section 3.4 and 3.5, the total momentum-space flux has both a convective part (collisional drag) and a diffusive part (collisional momentum diffusion and pitch-angle scattering, RF diffusion), so that it can be decomposed as

$$\mathbf{S}_{\mathbf{p}}(f) = -\mathbb{D}_{\mathbf{p}} \cdot \nabla_{\mathbf{p}} f + \mathbf{F}_{\mathbf{p}} f \tag{3.137}$$

where $\mathbb{D}$ is the diffusion tensor and $\mathbf{F}$ is the convection vector. The gradient vector $\nabla_{\mathbf{p}}$ in $(p, \xi)$ coordinates system in given by (A.123)

$$\nabla_{\mathbf{p}} = \begin{pmatrix} \dfrac{\partial}{\partial p} \\ \\ -\dfrac{\sqrt{1-\xi^2}}{p}\dfrac{\partial}{\partial \xi} \end{pmatrix} \tag{3.138}$$

so that

$$\begin{aligned} S_p &= -D_{pp}\frac{\partial f}{\partial p} + \frac{\sqrt{1-\xi^2}}{p} D_{p\xi}\frac{\partial f}{\partial \xi} + F_p f \\ S_\xi &= -D_{\xi p}\frac{\partial f}{\partial p} + \frac{\sqrt{1-\xi^2}}{p} D_{\xi\xi}\frac{\partial f}{\partial \xi} + F_\xi f \end{aligned} \tag{3.139}$$

In order to evaluate the bounce-averaged fluxes (3.135) as a function of the bounce-averaged distribution functions, we must treat separately the cases of $f_0$ and $g$ from the case of $\widetilde{f}$.

### Distribution functions $f_0$ and $g$

The distribution functions $f_0$ and $g$ are independent of $\theta$ and they are also symmetric in the trapped region. We denote such function as $f$ and evaluate the bounce-averaging terms in the decomposition (3.139) from (3.135). We have $f(p,\xi) = f^{(0)}(p,\xi_0)$ which is independent of $\theta$ and also of $\sigma$ in the trapped region. Using (3.132) and keeping in mind that $|\xi_0| = \sigma\xi_0$ is independent of $\sigma$, we get

$$
\begin{aligned}
&\bullet\ -\left\{D_{pp}\frac{\partial f}{\partial p}\right\} = -\left\{D_{pp}\right\}\frac{\partial f^{(0)}}{\partial p} \\
&\bullet\ \left\{D_{p\xi}\frac{\sqrt{1-\xi^2}}{p}\frac{\partial f}{\partial \xi}\right\} = \frac{\sqrt{1-\xi_0^2}}{p}\sigma\left\{\frac{\sigma\xi}{\sqrt{\Psi}\xi_0}D_{p\xi}\right\}\frac{\partial f^{(0)}}{\partial \xi_0} \\
&\bullet\ \left\{F_p f\right\} = \left\{F_p\right\} f^{(0)} \\
&\bullet\ -\sigma\left\{\frac{\sigma\xi}{\sqrt{\Psi}\xi_0}D_{\xi p}\frac{\partial f}{\partial p}\right\} = -\sigma\left\{\frac{\sigma\xi}{\sqrt{\Psi}\xi_0}D_{\xi p}\right\}\frac{\partial f^{(0)}}{\partial p} \\
&\bullet\ \sigma\left\{\frac{\sigma\xi}{\sqrt{\Psi}\xi_0}D_{\xi\xi}\frac{\sqrt{1-\xi^2}}{p}\frac{\partial f}{\partial \xi}\right\} = \frac{\sqrt{1-\xi_0^2}}{p}\left\{\frac{\xi^2}{\Psi\xi_0^2}D_{\xi\xi}\right\}\frac{\partial f^{(0)}}{\partial \xi_0} \\
&\bullet\ \sigma\left\{\frac{\sigma\xi}{\sqrt{\Psi}\xi_0}F_\xi f_0\right\} = \sigma\left\{\frac{\sigma\xi}{\sqrt{\Psi}\xi_0}F_\xi\right\} f^{(0)}
\end{aligned}
\tag{3.140}
$$

and we can rewrite

$$
\mathbf{S}_{\mathbf{p}}^{(0)}(f) = -\mathbb{D}_{\mathbf{p}}^{(0)}\cdot\nabla_{\mathbf{p}_0} f^{(0)} + \mathbf{F}_{\mathbf{p}}^{(0)} f^{(0)} \tag{3.141}
$$

where the bounce averaged flux is decomposed into

$$\mathbf{S}_{\mathbf{p}}^{(0)}(f) = \begin{pmatrix} S_p^{(0)}\left(f^{(0)}\right) \\ S_{\xi_0}^{(0)}\left(f^{(0)}\right) \end{pmatrix} \tag{3.142}$$

with

$$\begin{aligned} S_p^{(0)}\left(f^{(0)}\right) &= -D_{pp}^{(0)}\frac{\partial f^{(0)}}{\partial p} + \frac{\sqrt{1-\xi_0^2}}{p}D_{p\xi}^{(0)}\frac{\partial f^{(0)}}{\partial \xi_0} + F_p^{(0)}f^{(0)} \\ S_{\xi_0}^{(0)}\left(f^{(0)}\right) &= -D_{\xi p}^{(0)}\frac{\partial f^{(0)}}{\partial p} + \frac{\sqrt{1-\xi_0^2}}{p}D_{\xi\xi}^{(0)}\frac{\partial f^{(0)}}{\partial \xi_0} + F_\xi^{(0)}f^{(0)} \end{aligned} \tag{3.143}$$

by defining the diffusion components

$$\begin{aligned} D_{pp}^{(0)} &= \{D_{pp}\} \\ D_{p\xi}^{(0)} &= \sigma\left\{\frac{\sigma\xi}{\sqrt{\Psi}\xi_0}D_{p\xi}\right\} \\ D_{\xi p}^{(0)} &= \sigma\left\{\frac{\sigma\xi}{\sqrt{\Psi}\xi_0}D_{\xi p}\right\} \\ D_{\xi\xi}^{(0)} &= \left\{\frac{\xi^2}{\Psi\xi_0^2}D_{\xi\xi}\right\} \end{aligned} \tag{3.144}$$

and the convection components

$$\begin{aligned} F_p^{(0)} &= \{F_p\} \\ F_\xi^{(0)} &= \sigma\left\{\frac{\sigma\xi}{\sqrt{\Psi}\xi_0}F_\xi\right\} \end{aligned} \tag{3.145}$$

where the gradient vector in the reduced $(p, \xi_0)$ momentum space is

$$\nabla_{\mathbf{p_0}} = \begin{pmatrix} \dfrac{\partial}{\partial p} \\ \\ \dfrac{-\sqrt{1-\xi_0^2}}{p}\dfrac{\partial}{\partial \xi_0} \end{pmatrix} \tag{3.146}$$

**Distribution function $\widetilde{f}$**

The distribution function $\widetilde{f}$ (3.116)

$$\widetilde{f} = -\frac{I(\psi)\, v_{\parallel}}{\Omega_e} \frac{\partial f_0}{\partial \psi} \tag{3.147}$$

depends explicitly upon the parallel velocity and the magnetic field, and therefore upon the poloidal angle $\theta$. It can be rewritten as

$$\widetilde{f} = \frac{\xi}{\Psi \xi_0} \widetilde{f}^{(0)} \tag{3.148}$$

where

$$\widetilde{f}^{(0)} = \frac{I(\psi)\, p \xi_0}{e B_0(\psi)} \frac{\partial f_0^{(0)}}{\partial \psi} \tag{3.149}$$

is independent of $\theta$ and is antisymmetric in the trapped region, since $f_0^{(0)}$ is symmetric and $\xi_0$ is antisymmetric. As a result, only $\sigma \widetilde{f}^{(0)}$ can be taken out of the bounce

averaging operator. Taking the bounce-average of each term in (3.139), we find

$$
\begin{aligned}
&\bullet \quad \left\{-D_{pp}\frac{\partial \widetilde{f}}{\partial p}\right\} = -\sigma\left\{\sigma\frac{\xi}{\Psi\xi_0}D_{pp}\right\}\frac{\partial \widetilde{f}^{(0)}}{\partial p} \\
&\bullet \quad \left\{D_{p\xi}\frac{\sqrt{1-\xi^2}}{p}\frac{\partial \widetilde{f}}{\partial \xi}\right\} \\
&\qquad = \frac{\sqrt{1-\xi_0^2}}{p}\left[\left\{\frac{\xi^2}{\Psi^{3/2}\xi_0^2}D_{p\xi}\right\}\frac{\partial \widetilde{f}^{(0)}}{\partial \xi_0} + \sigma\left\{\sigma\frac{\Psi-1}{\Psi^{3/2}\xi_0^3}D_{p\xi}\right\}\widetilde{f}^{(0)}\right] \\
&\bullet \quad \left\{F_p\widetilde{f}\right\} = \sigma\left\{\sigma\frac{\xi}{\Psi\xi_0}F_p\right\}\widetilde{f}^{(0)} \\
&\bullet \quad -\sigma\left\{\frac{\sigma\xi}{\sqrt{\Psi}\xi_0}D_{\xi p}\frac{\partial \widetilde{f}}{\partial p}\right\} = -\left\{\frac{\xi^2}{\Psi^{3/2}\xi_0^2}D_{\xi p}\right\}\frac{\partial \widetilde{f}^{(0)}}{\partial p} \\
&\bullet \quad \sigma\left\{\frac{\sigma\xi}{\sqrt{\Psi}\xi_0}D_{\xi\xi}\frac{\sqrt{1-\xi^2}}{p}\frac{\partial \widetilde{f}}{\partial \xi}\right\} \\
&\qquad = \frac{\sqrt{1-\xi_0^2}}{p}\left[\sigma\left\{\frac{\sigma\xi^3}{\Psi^2\xi_0^3}D_{\xi\xi}\right\}\frac{\partial \widetilde{f}^{(0)}}{\partial \xi_0} + \left\{\frac{\xi\left(\Psi-1\right)}{\Psi^2\xi_0^4}D_{\xi\xi}\right\}\widetilde{f}^{(0)}\right] \\
&\bullet \quad \sigma\left\{\frac{\sigma\xi}{\sqrt{\Psi}\xi_0}F_\xi\widetilde{f}\right\} = \left\{\frac{\xi^2}{\Psi^{3/2}\xi_0^2}F_\xi\right\}\widetilde{f}^{(0)}
\end{aligned}
\tag{3.150}
$$

where the following relation was used

$$
\frac{\partial}{\partial\xi_0}\frac{\xi}{\xi_0} = \sigma\frac{\Psi-1}{|\xi|\,\xi_0^2} \tag{3.151}
$$

We can therefore rewrite

$$
\mathbf{S}_{\mathbf{p}}^{(0)}\left(\widetilde{f}\right) = -\widetilde{\mathbb{D}}_{\mathbf{p}}^{(0)}\cdot\nabla_{p,\xi_0}\widetilde{f}^{(0)} + \widetilde{\mathbf{F}}_{\mathbf{p}}^{(0)}\widetilde{f}^{(0)}
$$

where the bounce averaged flux is decomposed into

$$\mathbf{S}_{\mathbf{p}}^{(0)}\left(\widetilde{f}\right)=\left(\begin{array}{c}\widetilde{S}_{p}^{(0)}\left(\widetilde{f}^{(0)}\right)\\ \widetilde{S}_{\xi_0}^{(0)}\left(\widetilde{f}^{(0)}\right)\end{array}\right) \tag{3.152}$$

with

$$\begin{aligned}\widetilde{S}_{p}^{(0)}\left(\widetilde{f}^{(0)}\right)&=-\widetilde{D}_{pp}^{(0)}\frac{\partial\widetilde{f}^{(0)}}{\partial p}+\frac{\sqrt{1-\xi_0^2}}{p}\widetilde{D}_{p\xi}^{(0)}\frac{\partial\widetilde{f}^{(0)}}{\partial\xi_0}+\widetilde{F}_{p}^{(0)}\widetilde{f}^{(0)}\\ \widetilde{S}_{\xi_0}^{(0)}\left(\widetilde{f}^{(0)}\right)&=-\widetilde{D}_{\xi p}^{(0)}\frac{\partial\widetilde{f}^{(0)}}{\partial p}+\frac{\sqrt{1-\xi_0^2}}{p}\widetilde{D}_{\xi\xi}^{(0)}\frac{\partial\widetilde{f}^{(0)}}{\partial\xi_0}+\widetilde{F}_{\xi}^{(0)}\widetilde{f}^{(0)}\end{aligned} \tag{3.153}$$

by defining the diffusion components

$$\begin{aligned}\widetilde{D}_{pp}^{(0)}&=\sigma\left\{\sigma\frac{\xi}{\Psi\xi_0}D_{pp}\right\}\\ \widetilde{D}_{p\xi}^{(0)}&=\left\{\frac{\xi^2}{\Psi^{3/2}\xi_0^2}D_{p\xi}\right\}\\ \widetilde{D}_{\xi p}^{(0)}&=\left\{\frac{\xi^2}{\Psi^{3/2}\xi_0^2}D_{\xi p}\right\}\\ \widetilde{D}_{\xi\xi}^{(0)}&=\sigma\left\{\frac{\sigma\xi^3}{\Psi^2\xi_0^3}D_{\xi\xi}\right\}\end{aligned} \tag{3.154}$$

and the convection components

$$\begin{aligned}\widetilde{F}_{p}^{(0)}&=\sigma\left\{\sigma\frac{\xi}{\Psi\xi_0}F_p\right\}+\frac{\sqrt{1-\xi_0^2}}{p\xi_0^3}\left\{\frac{(\Psi-1)}{\Psi^{3/2}}D_{p\xi}\right\}\\ \widetilde{F}_{\xi}^{(0)}&=\left\{\frac{\xi^2}{\Psi^{3/2}\xi_0^2}F_\xi\right\}+\frac{\sqrt{1-\xi_0^2}}{p\xi_0^3}\sigma\left\{\frac{\sigma\xi\,(\Psi-1)}{\xi_0\Psi^2}D_{\xi\xi}\right\}\end{aligned} \tag{3.155}$$

where we use the fact that $\sigma\xi_0^3$ may be taken out of the bounce averaged operator, since $\xi_0^3$ is an odd function of $\xi_0$.

## 3.4 Linearized Fokker-Planck Collisions Operator

### 3.4.1 Linearized collision operator

The collision operator results from interactions between electrons with themselves and with all ion species $s$

$$\mathcal{C}(f) = \mathcal{C}(f,f) + \sum_s \mathcal{C}(f, f_{Ms}) \tag{3.156}$$

where $f_{Ms}$ is the distribution function for ions of species $s$ and is assumed to be a Maxwellian with Temperature $T_s$ and density $n_s$. The term $\mathcal{C}(f,f)$ is bilinear, but can be linearized under the assumption that collisions dominate the bulk electrons, such that the distribution function $f$ may be expanded as

$$f \simeq f_{Me} + \delta f \tag{3.157}$$

where $f_{Me}$ is the Maxwellian electron distribution function, and $\delta f$ is the perturbation due to RF-electron interaction, which is assumed to be globally small compared to $f_{Me}$. The non-linear term $\mathcal{C}(\delta f, \delta f)$ is neglected, and $\mathcal{C}(f_{Me}, f_{Me}) = 0$ since the Maxwellian is the equilibrium distribution in the absence of perturbations. Therefore, we approximate

$$\mathcal{C}(f,f) \simeq \mathcal{C}(f, f_{Me}) + \mathcal{C}(f_{Me}, f) \tag{3.158}$$

The operator $\mathcal{C}(f, f_{Me})$ and the electron-ion collision operators $\mathcal{C}(f, f_{Ms})$ are differential operators which can be put in the conservative form

$$\mathcal{C}(f, f_M) = -\nabla_{\mathbf{p}} \cdot \mathbf{S}^{\mathrm{C}}_{\mathbf{p}}(f) \tag{3.159}$$

where the flux vector $\mathbf{S}^{\mathrm{C}}_{\mathbf{p}}$ is decomposed into a diffusive part and a convective part as

$$\mathbf{S}^{\mathrm{C}}_{\mathbf{p}}(f) = -\mathbb{D}^{\mathrm{C}}_{\mathbf{p}} \cdot \nabla_{\mathbf{p}} f + \mathbf{F}^{\mathrm{C}}_{\mathbf{p}} f \tag{3.160}$$

Because of the symmetry of the collisional process, the collisional diffusion tensor components

$$\begin{aligned} D_{pp}^{\mathrm{C}} &= A(\psi, p) \\ D_{p\xi}^{\mathrm{C}} &= 0 \\ D_{\xi p}^{\mathrm{C}} &= 0 \\ D_{\xi\xi}^{\mathrm{C}} &= B_t(\psi, p) \end{aligned} \tag{3.161}$$

and the collisional convection vector components

$$\begin{aligned} F_{p}^{\mathrm{C}} &= -F(\psi, p) \\ F_{\xi}^{\mathrm{C}} &= 0 \end{aligned} \tag{3.162}$$

are only function of the magnitude $p$ of the electron momentum. The coefficient $A(\psi, p)$ corresponds to the momentum diffusion while $B_t(\psi, p)$ describes pitch-angle scattering. The convection factor $F(\psi, p)$ describes the collisional drag. The collision coefficients are independent of $\xi$ and the (numerically challenging) cross terms $D_{p\xi}^{\mathrm{C}}$ and $D_{\xi p}^{\mathrm{C}}$ are identically zero, which makes the spherical coordinate system $(p, \xi)$ the natural system to describe collisions, and the system chosen for the numerical resolution of the kinetic equation.

The term $\mathcal{C}(f_M, f)$ in an integral term which describe the effect on the bulk due to collisions with the perturbed distribution function. While taking into account the exact form of this correction term $\mathcal{C}(f_M, f)$ is not necessary, it is important to use an approximate form that conserves momentum, in order to obtain a correct calculation of the current. This can be done by expanding the gyro-averaged distribution $f$ as a sum of Legendre harmonics according to the relation

$$f(t, \mathbf{r}, p, \xi) = \sum_{m=0}^{\infty} (m + 1/2)\, f_m(t, \mathbf{r}, p)\, P_m(\xi) \tag{3.163}$$

where $P_m(\xi)$ are the Legendre polynomials and the Legendre coefficients are

$$f_m(t, \mathbf{r}, p) = \int_{-1}^{+1} f(t, \mathbf{r}, p, \xi)\, P_m(\xi)\, d\xi \tag{3.164}$$

The linear operator $\mathcal{C}(f_M, f)$ becomes

$$\mathcal{C}(f_M, f) = \sum_{m=0}^{\infty} (m + 1/2)\, \mathcal{C}(f_M, f_m(t, \mathbf{r}, p)\, P_m(\xi)) \tag{3.165}$$

The zero-order term is a isotropic distribution $f_0(t, \mathbf{r}, p) \simeq f_M$, which does not exchange parallel momentum with the Maxwellian; therefore, its effect of the Maxwellian is neglected. Since $P_0(\xi) = 1$,

$$\mathcal{C}(f_M, f_m(t, \mathbf{X}, p)\, P_0(\xi)) \simeq \mathcal{C}(f_M, f_M) = 0,$$

The operator $\mathcal{C}(f_M, f)$ is then approximated to

$$\mathcal{C}(f_M, f) \simeq \mathcal{C}\left(f_M, \frac{3}{2}\xi f_1(t, \mathbf{r}, p)\right) \tag{3.166}$$

since $P_1(\xi) = \xi$, where terms $m \geq 2$ are neglected. We use the notations in Ref. [54]

$$\mathcal{C}(f_M, f) = -\frac{3}{2}\xi \mathcal{I}[f_M, f_1(t, \mathbf{r}, p)] \tag{3.167}$$

where $\mathcal{I}$ is an integral operator over $p$. Because $\mathcal{C}(f_M, f)$ is a corrective term, it can be treated explicitly in the numerical resolution of the kinetic equation. The total collision operator (3.156) can be rewritten as

$$\mathcal{C}(f) = \sum_{s=e,i} \mathcal{C}(f, f_{Ms}) - \frac{3}{2}\xi \mathcal{I}[f_M, f_1(t, \mathbf{r}, p)] \tag{3.168}$$

By construction, the linearized electron-electron collision operator conserves momentum, but not energy, so there is no need to introduce an energy loss term in the kinetic equation (to compensate for the RF power deposition) in order to converge to a steady-state. The coefficients $A(\psi, p)$, $B_t(\psi, p)$, $F(\psi, p)$ and the operator $\mathcal{I}[f_M, f_1(t, \mathbf{r}, p)]$ have been explicitly evaluated in Ref. [54], following the work done in Ref. [37]. We refer to these papers for detailed expressions.

### 3.4.2 Bounce-averaged differential collisional operator

According to the results of Section 3.3.8, the bounce averaging of an operator of the form (3.159) requires to evaluate the bounce-averaged diffusion tensor $\mathbb{D}_{\mathbf{p}}^{(0)}$ and convection vector $\mathbf{F}_{\mathbf{p}}^{(0)}$ defined by (3.144), (3.145) for the contributions of the $\theta$-independent functions $f_0$ and $g$, as well as the diffusion tensor $\widetilde{\mathbb{D}}_{\mathbf{p}}^{(0)}$ and convection vector $\widetilde{\mathbf{F}}_{\mathbf{p}}^{(0)}$ defined by (3.154) and (3.155) for the $\theta$-dependent functions $\widetilde{f}$.

#### Flux coefficients for the distribution functions $f_0$ and $g$

Applying (3.144) and (3.145) to (3.161) and (3.162), and using (3.132), we find

$$\begin{aligned} D_{pp}^{\mathrm{C}(0)} &= A(\psi, p) \\ D_{p\xi}^{\mathrm{C}(0)} &= 0 \\ D_{\xi p}^{\mathrm{C}(0)} &= 0 \\ D_{\xi\xi}^{\mathrm{C}(0)} &= \frac{\lambda_{2,-1,0}}{\lambda} B_t(\psi, p) \end{aligned} \tag{3.169}$$

and

$$\begin{aligned} F_{p}^{\mathrm{C}(0)} &= -F(\psi, p) \\ F_{\xi}^{\mathrm{C}(0)} &= 0 \end{aligned} \tag{3.170}$$

where we used

$$\left\{ \frac{\xi^2}{\Psi \xi_0^2} \right\} = \frac{\lambda_{2,-1,0}}{\lambda} \tag{3.171}$$

according to the definition (3.87).

#### Flux coefficients for the distribution function $\widetilde{f}$

Applying (3.154) and (3.155) to (3.161) and (3.162), and using (3.132), we find

$$\begin{aligned} \widetilde{D}_{pp}^{\mathrm{C}(0)} &= \frac{\overline{\lambda}_{1,-1,0}}{\lambda} A(\psi, p) \\ \widetilde{D}_{p\xi}^{\mathrm{C}(0)} &= 0 \\ \widetilde{D}_{\xi p}^{\mathrm{C}(0)} &= 0 \\ \widetilde{D}_{\xi\xi}^{\mathrm{C}(0)} &= \frac{\overline{\lambda}_{3,-2,0}}{\lambda} B_t(\psi, p) \end{aligned} \tag{3.172}$$

and the convection components

$$\begin{aligned}\widetilde{F}_p^{C(0)} &= -\frac{\overline{\lambda}_{1,-1,0}}{\lambda} F(\psi, p) \\ \widetilde{F}_\xi^{C(0)} &= \frac{\left(\overline{\lambda}_{1,-1,0} - \overline{\lambda}_{1,-2,0}\right)}{\lambda} \frac{\sqrt{1-\xi_0^2}}{p\xi_0^3} B_t(\psi, p)\end{aligned} \tag{3.173}$$

where the following bounce-average coefficients were determined in accordance with the definition (3.88)

$$\begin{aligned}\sigma\left\{\frac{\sigma\xi}{\Psi\xi_0}\right\} &= \frac{\overline{\lambda}_{1,-1,0}}{\lambda} \\ \sigma\left\{\frac{\sigma\xi^3}{\Psi^2\xi_0^3}\right\} &= \frac{\overline{\lambda}_{3,-2,0}}{\lambda} \\ \sigma\left\{\frac{\sigma\xi(\Psi-1)}{\xi_0\Psi^2}\right\} &= \frac{\overline{\lambda}_{1,-1,0}}{\lambda} - \frac{\overline{\lambda}_{1,-2,0}}{\lambda}\end{aligned} \tag{3.174}$$

### 3.4.3 Bounce-averaged integral collisional operator

The integral term (3.167) must also be bounce-averaged. Applying the bounce operation (3.86) gives

$$\{C(f_M, f)\} = -\frac{3}{2}\sigma\xi_0\left\{\sigma\frac{\xi}{\xi_0}\mathcal{I}[f_M, f_1]\right\} \tag{3.175}$$

#### Flux coefficients for the distribution functions $f_0$ and $g$

For the $\theta$-independent functions $f_0$ and $g$, whichsatisfy $f(p,\xi) = f^{(0)}(p,\xi_0)$, the integral (3.164) for $m = 1$ can be transformed according to (3.132) $\xi d\xi = \Psi\xi_0 d\xi_0$ and the condition (3.48) such that an electron $\xi_0$ reaches the poloidal location $\theta$ if

$$|\xi_0| \geq \sqrt{1 - \frac{1}{\Psi(\psi,\theta)}} \tag{3.176}$$

We get

$$f_1(p,\xi) = \Psi\int_{-1}^{+1} d\xi_0\, \xi_0 f H\left(|\xi_0| - \sqrt{1-\frac{1}{\Psi(\psi,\theta)}}\right) = \Psi f_1^{(0)} \tag{3.177}$$

with $f_1^{(0)}$ being a $\theta$-independent function

$$f_1^{(0)} \equiv \int_{-1}^{+1} d\xi_0 \, \xi_0 f^{(0)} H\left(|\xi_0| - \sqrt{1 - \frac{1}{\Psi(\psi,\theta)}}\right)$$
$$= \int_{-1}^{+1} d\xi_0 \, \xi_0 f^{(0)} \tag{3.178}$$

where the symmetry of $f^{(0)}$ in the trapped region cancels the trapped particle contribution. With the definition (3.88)

$$\sigma\left\{\frac{\sigma\xi\Psi}{\xi_0}\right\} = \frac{\overline{\lambda}_{1,1,0}}{\lambda} \tag{3.179}$$

the integral collisional term (3.175) becomes, using (3.177)

$$\{C(f_M, f)\} = -\frac{\overline{\lambda}_{1,-1,0}}{\lambda}\frac{3}{2}\xi_0 \mathcal{I}\left[f_M, f_1^{(0)}\right] \tag{3.180}$$

**Flux coefficients for the distribution function $\widetilde{f}$**

The distribution function $\widetilde{f}$ (3.116) can be rewritten as (3.148)

$$\widetilde{f} = \frac{\xi}{\Psi\xi_0}\widetilde{f}^{(0)} \tag{3.181}$$

where $\widetilde{f}^{(0)}$is independent of $\theta$ and is antisymmetric in the trapped region. With the integral (3.164) for $m = 1$, the integral collisional term (3.175) transforms according to (3.132) $\xi d\xi = \Psi\xi_0 d\xi_0$ and the condition (3.176) as

$$\left\{C\left(f_M, \widetilde{f}\right)\right\} = -\frac{3}{2}\xi_0 \mathcal{I}\left[f_M, \widetilde{f}_1^{(0)}\right] \tag{3.182}$$

with the definition

$$\widetilde{f}_1^{(0)} \equiv \sigma\left\{\sigma\frac{\xi}{\xi_0}\int_{-1}^{+1} d\xi_0 \xi \widetilde{f}^{(0)} H\left(|\xi_0| - \sqrt{1 - \frac{1}{\Psi(\psi,\theta)}}\right)\right\} \tag{3.183}$$

since $\mathcal{I}$ is a linear integral operator over $p$ and therefore permutes with the bounce-averaging operation. We can permute the integrals over $\theta$ and $\xi_0$, using the equivalence (3.46)-(3.48) and (3.86), and obtain

$$\widetilde{f}_1^{(0)} = \frac{1}{\lambda} \int_{-1}^{+1} d\xi_0 \, \xi_0 \widetilde{f}^{(0)} \overline{\lambda}_{2,0,0} \tag{3.184}$$

where we used the definition (3.88)

$$\lambda \sigma \left\{ \sigma \frac{\xi^2}{\xi_0^2} \right\} = \overline{\lambda}_{2,0,0} \tag{3.185}$$

## 3.5 RF Quasilinear Diffusion

### 3.5.1 Quasilinear operator in a uniform plasma

#### Quasilinear operator in conservative form

The quasilinear operator describing the slow evolution of the macroscopic distribution function $f$ under the effect of the fields has been derived by Kennel & Engelmann [41] and extended by Lerche [42] to relativistic plasmas. The conservative form of this quasilinear operator was derived in Appendix B.2 for an electric field of the form (B.26)

$$\mathbf{E}(\mathbf{r}, t) = \sum_b \mathrm{Re}\left[\mathbf{E}_b(\mathbf{r}) \, e^{-i\omega_b t}\right] \tag{3.186}$$

and gives an expression as the divergence of a flux (B.11-A.124)

$$\mathcal{Q}(f) = -\nabla_{\mathbf{p}} \cdot \mathbf{S}^{\mathrm{RF}} = -\frac{\partial}{\partial p}\left(p^2 S_p^{\mathrm{RF}}\right) + \frac{1}{p}\frac{\partial}{\partial \xi}\left(\sqrt{1-\xi^2} S_\xi^{\mathrm{RF}}\right) \tag{3.187}$$

where the flux is the sum over contributions from all RF frequencies present in the plasma, which are assumed to constitute a discrete set of monochromatic waves (B.21)

$$\mathbf{S}^{\mathrm{RF}} = \sum_b \mathbf{S}_b^{\mathrm{RF}}(\omega_b, \mathbf{E}_b) \tag{3.188}$$

The momentum-space flux associated with a wave $(\omega_b, \mathbf{E}_b)$ is purely diffusive

$$\mathbf{S}_b^{\mathrm{RF}}(\omega_b, \mathbf{E}_b) = -\mathbb{D}_b^{\mathrm{RF}}(\omega_b, \mathbf{E}_b) \cdot \nabla_{\mathbf{p}} f \tag{3.189}$$

The RF diffusion tensor elements, given in $(p, \xi)$ coordinates by (B.44), contain the contribution of all harmonics. Because electrons have a negative charge $q_e = -e$, it is convenient to transform $n \to -n$ in order to work with positive harmonic numbers. In that case, the diffusion tensor elements become

$$\begin{aligned}
D_{b,pp}^{\mathrm{RF}} &= \sum_{n=-\infty}^{+\infty} (1-\xi^2)\, D_n^{\mathrm{RF}}(\mathbf{p}, \omega_b, \mathbf{E}_b) \\
D_{b,p\xi}^{\mathrm{RF}} &= \sum_{n=-\infty}^{+\infty} -\frac{\sqrt{1-\xi^2}}{\xi}\left(1-\xi^2-\frac{n\omega_{ce}}{\gamma\omega_b}\right) D_n^{\mathrm{RF}}(\mathbf{p}, \omega_b, \mathbf{E}_b) \\
D_{b,\xi p}^{\mathrm{RF}} &= \sum_{n=-\infty}^{+\infty} -\frac{\sqrt{1-\xi^2}}{\xi}\left(1-\xi^2-\frac{n\omega_{ce}}{\gamma\omega_b}\right) D_n^{\mathrm{RF}}(\mathbf{p}, \omega_b, \mathbf{E}_b) \\
D_{b,\xi\xi}^{\mathrm{RF}} &= \sum_{n=-\infty}^{+\infty} \frac{1}{\xi^2}\left(1-\xi^2-\frac{n\omega_{ce}}{\gamma\omega_b}\right)^2 D_n^{\mathrm{RF}}(\mathbf{p}, \omega_b, \mathbf{E}_b)
\end{aligned} \tag{3.190}$$

where we used

$$\omega_{ce} = \frac{eB}{m_e} = -\gamma\Omega \tag{3.191}$$

and where $D_n^{\mathrm{RF}}(\mathbf{p}, \omega_b, \mathbf{E}_b)$ is the diffusion coefficient associated with the wave $(\omega_b, \mathbf{E}_b)$ at the $n$'s harmonic cyclotron resonance (B.41). It is given here in $(p, \xi)$ coordinates and after the $n \to -n$ transformation

$$D_n^{\mathrm{RF}}(\mathbf{p}, \omega_b, \mathbf{E}_b) = \lim_{V\to\infty} \frac{\pi e^2}{2V} \iiint \frac{d^3k}{(2\pi)^3} \|\mathbf{E}_{\mathbf{k},b}\|^2 \left|\Theta_{\mathbf{k}}^{(n)}(\mathbf{p}, \mathbf{k}, \mathbf{e}_{\mathbf{k},b})\right|^2 \delta\left(\omega_b - k_\parallel \frac{p\xi}{\gamma m_e} - \frac{n\omega_{ce}}{\gamma}\right) \tag{3.192}$$

where $\mathbf{E}_{\mathbf{k},b}$ are the Fourier components of $\mathbf{E}_b$ (B.3)

$$\mathbf{E}_{\mathbf{k},b}(\mathbf{k}) = \iiint d^3r\, \mathbf{E}_b(\mathbf{r})\, e^{-i\mathbf{k}\cdot\mathbf{r}} \tag{3.193}$$

and $\mathbf{e}_{\mathbf{k},b} = |\mathbf{E}_{\mathbf{k},b}| / \|\mathbf{E}_{\mathbf{k},b}\|$ is the corresponding polarization vector. $\Theta_{\mathbf{k}}^{(n)}$ is the polarization term (B.25) and is given here after the $n \rightarrow -n$ transformation

$$\Theta_{\mathbf{k}}^{(n)} = \frac{1}{\sqrt{2}} e_{\mathbf{k},b,+} e^{-i\alpha} J_{n+1}(z) + \frac{1}{\sqrt{2}} e_{\mathbf{k},b,-} e^{+i\alpha} J_{n-1}(z) + \frac{p_{\parallel}}{p_{\perp}} e_{\mathbf{k},b,\parallel} J_n(z) \tag{3.194}$$

where we used $J_{-n}(z) = (-1)^n J_{-n}(z)$ and $J_n(-z) = (-1)^n J_n(z)$, and with the definition

$$z \equiv \frac{k_{\perp}}{\omega_{ce}} \frac{p\sqrt{1-\xi^2}}{m_e} \tag{3.195}$$

### Diffusion coefficient for a Gaussian beam

The diffusion coefficient (3.192) was evaluated in Appendix B.3 for the case of a localized wave with Gaussian transverse amplitude profile in a uniform plasma. The Gaussian beam is initially characterized by the frequency $\omega_b$, the central parallel wave vector $k_{b\parallel}$, the beam size $d_b$, and the total power $P_b$ in the beam. The central perpendicular wave number is then determined from the dispersion relation $D(\omega_b, k_{b\parallel}, k_{b\perp}) = 0$ (2.16). The energy is propagating in the direction of the group velocity $\mathbf{v}_{g,b} = \partial\omega_b/\partial\mathbf{k}_b$ (2.17). The polarization $\mathbf{e}_b$ is defined by $\mathbf{e}_b = |\mathbf{E}_b| / \|\mathbf{E}_b\|$ where $\mathbf{E}_b$ is determined from (2.14) for the mode $(\mathbf{k}_b, \omega_b)$, and the normalized power flow $\mathbf{\Phi}_b$ is obtained from (2.39). The beam size $d_b$ is defined such that the beam intensity is down by a factor $e$ from the maximum intensity at a distance $d_b$ from the beam central line of propagation. It is assumed that the beam size is much larger than the wavelength $d_b \gg \lambda_b = 2\pi/k_b$, such that diffraction can be neglected. A corollary to this condition is that the spectral width (B.59) of the beam $\Delta k_b = 1/d_b$, is much smaller than the wave vector $k_b$, which justifies to solve the dispersion relation only for the central $\mathbf{k}_b$. Then, the diffusion coefficient (3.192) becomes (B.93)

$$D_n^{\mathrm{RF}}(\mathbf{p}) = \lim_{V\rightarrow\infty} \frac{P_b L_b}{V} \frac{e^2\pi}{\varepsilon_0 c |\Phi_b|} \frac{\gamma m_e}{p|\xi|} \left|\Theta_b^{(n)}\right|^2 \frac{1}{\sqrt{\pi}\Delta k_{b\parallel}} \exp\left[-\frac{\left(k_{\parallel\mathrm{res}} - k_{b\parallel}\right)^2}{\Delta k_{b\parallel}^2}\right] \tag{3.196}$$

where $L_b$ is the beam path length in the plasma volume $V$, and where we defined $\Theta_b^{(n)} = \Theta_{\mathbf{k}}^{(n)}(\mathbf{p}, \mathbf{k}_b, \mathbf{e}_b)$,

$$k_{\parallel \mathrm{res}} = \frac{m_e}{p\xi}(\gamma\omega_b - n\omega_{ce}) \tag{3.197}$$

and

$$\Delta k_{b\parallel} = \frac{|\Phi_{b\perp}|}{\Phi_b}\Delta k_b \tag{3.198}$$

where $\Phi_{b\perp}$ is the component of $\mathbf{\Phi}_b$ perpendicular to the magnetic field.

### 3.5.2 Application to toroidal plasmas

#### Approximations and validity of the operator (3.187) in toroidal plasmas

In a torus, the plasma is bounded and non-uniform. In order for the operator (3.187) to apply to a toroidal plasma, several approximations must be made and justified.

- First, in a bounded plasma, the Fourier space is discrete rather than continuous as in (3.192). The continuous description is a good approximation if $\lambda \ll L$, where $\lambda = 2\pi/k$ is the wavelength and $L$ is the size of the plasma. This condition is well satisfied for EBWs in typical tokamaks and STs; for example, in NSTX with $L \sim 1$ m, $\omega/2\pi \sim 14$ GHz, and $N \geq 4$, we have $\lambda/L \leq 0.005$.

- The motion of electrons is in first approximation confined to a flux-surface, and equilibrium properties such as the density and the temperature are uniform within this flux-surface. Because the equilibrium non-uniformity across flux-surfaces occurs on a scale $L$ much larger than the typical lengths involved in wave propagation and wave-particle interaction ($\lambda, \rho_{Te}$), the wave properties $\mathbf{k}_b$, $P_b$, $\mathbf{e}_b$ and $\mathbf{\Phi}_b$ can be considered to be slowly varying functions of space, and the derivations of Appendix B are a good approximation, such that we can use the operator (3.192) for wave-particle interaction, with the volume $V$ being the incremental volume of the flux-surface under consideration.

- However, the magnetic field amplitude $B$ - and therefore the gyrofrequency $\Omega$ - are not uniform within a flux-surface. In addition, this non-uniformity leads to

changes in the parallel and perpendicular velocities of electrons. The changes in $\Omega$ and $v_{\|}$ along the propagation within the wavepacket may lead to dephasing in the wave-particle interaction. Indeed, resonant interaction between electrons and the wave occurs when the phase $\nu = \left(\omega_b - k_{\|} v_{\|} - n\Omega\right) t$ is constant across the wavepacket [44]. The time for an electron to cross the wavepacket is $d_{b\|} / \left|v_{\|}\right|$, where $d_{b\|}$ is the projection of the wavepacket on the field line within the flux-surface. Assuming that the condition $\omega_b - k_{\|} v_{\|} - n\Omega = 0$ is satified in the center of the wavepacket, the dephasing $\delta\nu$ accumulated during the electron transit across the wavepacket is bounded by

$$\delta\nu = \left(\delta k_{\|} \left|v_{\|}\right| + \left|k_{b\|}\right| \delta v_{\|} + n\delta\Omega\right) \frac{d_{b\|}}{\left|v_{\|}\right|} \tag{3.199}$$

In order for the wave-particle resonance to be maintained across the wavepacket, it is required that $\delta\nu < 2\pi$. We assume that the wavepacket crosses the flux-surface under consideration around the poloidal location $\theta_b$.

- The changes in the $k_{\|}$ spectrum are essentially $\delta k_{b\|} = \Delta k_{b\|}$, where $\Delta k_{b\|}$ is the width in $k$ spectrum and $\Delta k_{b\|} = 1/d_{b\|}$. Therefore, the dephasing due to $\delta k_{\|}$ is typically of order $\Delta k_{\|} d_{b\|} = 1$ and is independent of the beam size. It simply derives from the spectral properties of wavepackets and reflects the uncertainty principle.
- The changes in the cyclotron frequency are typically of order

$$\delta\Omega \simeq \Omega \frac{dR}{R} \simeq \Omega \frac{d_{b\|}}{R} \sin\theta_b \frac{B_P}{B} \tag{3.200}$$

since $R$ is the scalelength of $B$-field variations and the projection $dR$ of the field line element $d_{b\|}$ on the direction of inhomogeneity is of the order of $dR \simeq B_P \sin\theta_b / B$. The condition $\delta\nu < 2\pi$ therefore imposes a limit on the beam size

$$d_{b\|}^2 < \frac{4\pi}{n\Omega} \frac{v_{Te} R}{\sin\theta_b} \frac{B}{B_P} \tag{3.201}$$

where we used that $v_{\|} > 2v_{Te}$ for typical electron-EBW interaction. In a

typical ST such as NSTX, we typically have $n\Omega/2\pi \simeq \omega/2\pi \sim 14$ GHz, $B_P \sim B$, $R \sim 1$ m, $v_{Te} \sim 0.05c$, which leads to $d_{b\|} < 0.05/\sqrt{\sin\theta_b}$ m. This condition is well satisfied near the outboard or inboard horizontal midplane where $\theta_b \to 0, \pi$, but becomes restrictive near $\theta_b = \pm 90°$.

- The changes in the parallel velocity are related to the changes in the magnetic field according to the conservation of energy (3.28) and magnetic moment (3.29), which give $\delta v_\| / \left|v_\|\right| \sim \delta\Omega/2\Omega$ so that, using (3.200)

$$\delta v_\| \simeq \frac{\left|v_\|\right|}{2}\frac{d_{b\|}}{R}\sin\theta_b\frac{B_P}{B} \tag{3.202}$$

and the condition $\delta\nu < 2\pi$ imposes a second limit on the beam size

$$d_{b\|}^2 < \frac{4\pi}{\left|k_\|\right|}\frac{R}{\sin\theta_b}\frac{B}{B_P} \tag{3.203}$$

In a typical ST such as NSTX, this condition leads to $d_{b\|} < 0.2/\sqrt{\left|N_\|\right|\sin\theta_b}$ m, which is less restrictive than the condition (3.201) for relevant $\left|N_\|\right|$.

In conclusion, applying the operator (3.187) for a spatially localized beam in a toroidal plasma is valid as long as the condition (3.201), which is a measure of the dephasing that results from magnetic field variations, is satisfied. Otherwise, it is required to use different methods to calculate the diffusion coefficient, for example by studying the motion of electrons through a wavepacket, as in Ref. [70], but in a non-uniform magnetic field, which would likely require numerical calculations. Another option is to develop and use an orbit code which numerically integrates the wave-particle interaction over the particle orbit [71]. It can be expected, however, that the non-uniformity of $B$ and therefore $v_\|$ would lead to a reduction of the diffusion coefficient along with a broadening of the resonance region in momentum space. The conditions of applicability of the operator (3.187) with the diffusion coefficient (3.192) will be assumed to be satisfied from now on. Consequently, the inhomogeneity across the region of wave-particle interaction is neglected within a given flux-surface, such that any $\theta$-dependent quantity - such as the magnetic field $B$ and the parallel velocity

$v_{\|}$ - is evaluated at $\theta = \theta_b$ in the quasilinear operator (3.187) and diffusion coefficient (3.192). This operation can be mathematically imposed by transforming the diffusion coefficient (3.192) according to

$$D_n^{\mathrm{RF}}(\mathbf{p}) \rightarrow D_n^{\mathrm{RF}}(\mathbf{p})\, 2\pi\delta(\theta - \theta_b) \tag{3.204}$$

which will be integrated with the bounce-averaging operation.

### Diffusion Coefficient for a Gaussian beam in toroidal plasmas

Within the approximations of Subsection 3.5.2, we derive the diffusion coefficient for a Gaussian beam in toroidal plasma. The beam is characterized by the frequency $\omega_b$, the central parallel wave vector $k_{b\|}$, the beam size $d_b$, and the total power $P_b$ in the beam. Considering a given flux surface $\psi$ crossed by the beam at the poloidal location $\theta_b$, we rewrite (3.196) with the transformation (3.204) as

$$D_n^{\mathrm{RF}}(\mathbf{p}_b) = 2\pi\delta(\theta - \theta_b)\, D_b^{\mathrm{RF}} \frac{\gamma m_e}{p\,|\xi_b|} \left|\Theta_b^{(n)}\right|^2 \frac{1}{\sqrt{\pi}\Delta N_{b\|}} \exp\left[-\frac{\left(N_{\|\mathrm{res}b} - N_{b\|}\right)^2}{\Delta N_{b\|}^2}\right] \tag{3.205}$$

where we make use of the condition $\theta = \theta_b$ to define $\Theta_b^{(n)} = \Theta_{\mathbf{k}}^{(n)}(\mathbf{p}_b, \mathbf{k}_b, \mathbf{e}_b)$,

$$N_{\|\mathrm{res}b} = \frac{m_e c}{p\xi_b}\left(\gamma - \frac{n\omega_{ce,b}}{\omega_b}\right) \tag{3.206}$$

and

$$\Delta N_{b\|} = \frac{c}{\omega_b d_{b\|}} = \frac{c}{\omega_b d_b}\frac{|\Phi_{b\perp}|}{\Phi_b} \tag{3.207}$$

with $\mathbf{p}_b(p, \xi_b)$ being the momentum of a given electron $(p, \xi_0)$ at the poloidal location $\theta_b$ where the gyrofrequency is $\omega_{ce,b}$. The constant factor $D_b^{\mathrm{RF}}$ in the diffusion coefficient (3.205) is calculated for the infinitesimal volume $dV(\psi)$ of the flux-surface $\psi$.

$$D_b^{\mathrm{RF}} = \frac{dL_b(\psi, \theta_b)}{dV(\psi)} \frac{P_b e^2 \pi}{\varepsilon_0 \omega_b |\Phi_b|} \tag{3.208}$$

where $dL_b(\psi, \theta_b)$ is the beam infinitesimal path length within the flux-surface.

The beam trajectory $\mathbf{r}_b$ and the evolution of wave vector $\mathbf{k}_b$ require propagation calculations, such as ray-tracing techniques. In this work, these calculations are not undertaken, and therefore we do not intend to solve the full current-drive problem, from excitation to propagation and damping of EBWs. Rather, we consider only the vicinity of the damping region, near a cyclotron resonance, and this region is assumed to be sufficiently narrow such that the parallel wave number $N_{b\|}$ is approximately constant across the damping region. In this work, we assume in addition that the beam propagates near the horizontal mid-plane ($\theta = 0, \pi$) in a up-down symmetric plasma, and that the beam poloidal extent be small, meaning $d \ll 2\pi r$. This assumptions allow us to study EBWCD without solving the beam propagation problem, and is motivated by the following considerations:

- Near the horizontal midplane, and for sufficiently narrow beams ($d \ll 2\pi r$), the tokamak geometry is close to a slab geometry. In that case, the components of the wave vector perpendicular to the direction of inhomogeneity are conserved.

- Consequently, and as shown in works on EBW ray-tracing [8], the evolution of $N_{b\|}$ is much slower near the horizontal midplane than above or below that midplane. Therefore, our approach that $N_{b\|}$ be considered constant in the vicinity of the damping region is more valid near the mid-plane. Note that we do not require that the beam propagates strictly on the midplane, so that $N_{b\|}$ may have experienced some cumulative upshift or downshift before reaching the damping region. This gives us all latitude to consider a wide range of values for $N_{b\|}$.

- In the slab geometry, the component of the wave vector that is perpendicular to both the direction of inhomogeneity and the direction of the magnetic field is also conserved. In the meanwhile, $k_{b\perp}$ experiences a significant upshift, from 0 at the L cut-off in the MCR, to very large values for EBW in the WKB region. Consequently, the perpendicular wave vector is mostly in the direction of inhomogeneity, $\mathbf{k}_{b\perp} \| \widehat{\psi}$. Because the power flow $\mathbf{\Phi}_b$ - which is in the direction of the ray propagation - lies in the $\left(\mathbf{k}, \widehat{\mathbf{b}}\right)$ plane, its perpendicular component

must also be in the direction of inhomogeneity. Therefore, the path length in the flux-surface is $dL_b(\psi,\theta_b) = dl(\psi,\theta_b)\,\Phi_b/|\Phi_{b\perp}|$ where $dl(\psi,\theta_b)$ is the width of the flux-surface at the poloidal location $\theta_b$. The constant factor in the diffusion coefficient (3.208) can then be rewritten as

$$D_b^{\mathrm{RF}} = \frac{dl(\psi,\theta_b)}{dV(\psi)}\frac{P_b e^2 \pi}{\varepsilon_0 \omega_b |\Phi_{b\perp}|} \tag{3.209}$$

- In the quasi-slab geometry near the horizontal midplane, and for sufficiently narrow beams, the magnetic field $B$ is approximately uniform in magnitude and direction within a flux-surface, and therefore the parallel velocity $v_\parallel$ of a given electron is approximately constant. In that case, the condition (3.201) is well satisfied ($\sin\theta_b \to 0$) and our quasi-linear operator is more valid.

- We can expect that trapped particle will play an important role in off-axis EBWCD, because the trapped particle fraction is significant in small aspect ratio STs, and because the EBW-induced diffusion is mostly perpendicular in momentum space. As a consequence, by calculating EBWCD near horizontal mid-plane ($\theta = 0, \pi$), where the trapped particle fraction is respectively maximum (outboard side) and minimum (inboard side), we expect to encompass most of the important physics of EBWCD.

To summarize, restricting our study to the horizontal midplane allows us to work in a quasi-slab geometry, in which electrons see a locally quasi-uniform plasma and our quasilinear operator (3.187) is valid. In addition, with the symmetry of the slab geometry, it is sufficient to calculate the local dispersion relation and corresponding wave characteristics to provide all necessary information for the RF diffusion coefficient. This is not true is general toroidal geometry, in which the direction of the power flow, for example, in not determined with respect to the flux-surfaces by solving the dispersion relation only.

For an infinitesimal surface, the width of the flux-surface at the poloidal location

$\theta_b$ is given by (A.93)

$$\frac{dl\left(\psi,\theta_b\right)}{d\psi}=\frac{1}{\left\|\nabla\psi\right\|\left|\widehat{\psi}\cdot\widehat{\mathbf{r}}\right|}=\frac{1}{B_P R\left|\widehat{\psi}\cdot\widehat{\mathbf{r}}\right|} \tag{3.210}$$

and the infinitesimal volume of the flux-surface is (A.95)

$$\frac{dV\left(\psi\right)}{d\psi}=\int_0^{2\pi}d\theta\int_0^{2\pi}d\phi\frac{Rr}{\left\|\nabla\psi\right\|\left|\widehat{\psi}\cdot\widehat{\mathbf{r}}\right|} \tag{3.211}$$

which can be rewritten for an axisymmetric plasma as

$$\frac{dV\left(\psi\right)}{d\psi}=\frac{4\pi^2 R_p\widehat{q}\left(\psi\right)}{B_0\left(\psi\right)} \tag{3.212}$$

where we defined the pseudo safety factor $\widehat{q}$ as

$$\widehat{q}\left(\psi\right)\equiv\int_0^{2\pi}\frac{d\theta}{2\pi}\frac{1}{\left|\widehat{\psi}\cdot\widehat{\mathbf{r}}\right|}\frac{r}{R_p}\frac{B_0\left(\psi\right)}{B_P} \tag{3.213}$$

The diffusion factor (3.209) becomes

$$D_b^{\mathrm{RF}}=\frac{e^2\pi}{\varepsilon_0\omega_b\left|\Phi_{b\perp}\right|}\frac{P_b}{4\pi^2 r\left(\psi,\theta_b\right)R_p}\widehat{F}_g\left(\psi,\theta_b\right) \tag{3.214}$$

where we introduce the factor

$$\widehat{F}_g\left(\psi,\theta\right)\equiv\frac{rB_0}{\widehat{q}RB_P\left|\widehat{\psi}\cdot\widehat{\mathbf{r}}\right|} \tag{3.215}$$

which accounts for the geometry of the flux surfaces. Note that for circular concentric flux-surfaces, $\widehat{F}_g\left(\psi,\theta_b\right)=1$.

### 3.5.3 Estimate of non-linear electron trapping effects

It has been shown [72] [59] that electrons resonating with finite-amplitude electrostatic waves propagating obliquely with respect to the magnetic field - such as EBWs - have

finite-amplitude oscillations in the wave frame, characterized by a bounce frequency

$$\omega_T = \left[\frac{eV_b k_\parallel^2}{m_e} J_n\left(\frac{k_{b\perp} v_\perp}{\Omega}\right)\right]^{1/2} \tag{3.216}$$

where $V_b$ is the electrostatic potential and $n$ is the harmonic number of the resonance, characterized by $\omega_b = k_{b\parallel} v_\parallel + n\Omega$. The amplitude of the oscillation in $p_\parallel$ is given by

$$\Delta p_{\parallel T} = \frac{2m\omega_T}{k_{b\parallel}} \tag{3.217}$$

The importance of these non-linear effects can be measured by the ratio of the trapping time $\tau_T = 2\pi/\omega_T$ to the transit time - or autocorrelation time - $\tau_{RF} = d_{b\parallel}/v_\parallel$ of an electron through the RF beam, which is characterized by a width $d_{b\parallel}$ along the magnetic field. Indeed, if $\tau_T \gg \tau_{RF}$, trapping is not able to affect the wave particle resonance during the interaction time. On the other limit, when $\tau_T \ll \tau_{RF}$, the electron has bounced many times in the wave frame during the interaction period, which basically cancels any energy of momentum transfer from the wave to the particle. In other words, we can take the condition $\tau_T > \tau_{RF}$ as a limit of validity for the quasilinear approach. In addition, note that the ratio of the trapping width $\Delta p_{\parallel T}$ to the spectral width of the wave (in momentum space) $\Delta p_\parallel \approx p_\parallel \Delta k_{b\parallel}/k_{b\parallel}$ gives approximately the ratio $\tau_{RF}/\tau_T$

$$\frac{\Delta p_{\parallel T}}{\Delta p_\parallel} \approx \frac{2m\omega_T}{k_{b\parallel}} \frac{k_{b\parallel}}{p_\parallel \Delta k_{b\parallel}} \approx 2\pi \frac{\tau_{RF}}{\tau_T} \tag{3.218}$$

which means that requiring that the trapping time be longer than the interaction time is equivalent to requiring that the trapping width be small compared to the interaction width in momentum space.

For $k_{b\perp} \gg k_{b\parallel}$, the electrostatic potential is related to the electric field amplitude through

$$E_b = \|\nabla V_b\| \approx k_{b\perp} V_b \tag{3.219}$$

and the power density in the beam is related to the electric field by (B.71)

$$P_b = \pi d_b^2 \frac{\varepsilon_0 c}{2} \Phi_b E_b^2 \tag{3.220}$$

Approximating the power density in the beam to be uniform within an area of radius $d_b$ corresponding to the beam size, we have

$$E_b = \left( \frac{2}{\varepsilon_0 c \Phi_b} \frac{P_b}{\pi d_b^2} \right)^{1/2} \tag{3.221}$$

and the bounce frequency in the wave (3.216) becomes

$$\omega_T = \left[ \frac{e k_{b\|}^2}{m_e k_{b\perp}} \left( \frac{2}{\varepsilon_0 c \Phi_b} \frac{P_b}{\pi d_b^2} \right)^{1/2} J_n \left( \frac{k_{b\perp} v_\perp}{\Omega} \right) \right]^{1/2} \tag{3.222}$$

so that the ratio of the transit time to the bounce time is

$$\frac{\tau_{RF}}{\tau_T} = \frac{d_{b\|}}{2\pi v_\|} \left[ \frac{e k_{b\|}^2}{m_e k_{b\perp}} \left( \frac{2}{\varepsilon_0 c \Phi_b} \frac{P_b}{\pi d_b^2} \right)^{1/2} J_n \left( \frac{k_{b\perp} v_\perp}{\Omega} \right) \right]^{1/2} \tag{3.223}$$

which gives numerically

$$\frac{\tau_{RF}}{\tau_T} = K \frac{N_\| f_{b[\mathrm{GHz}]}^{1/2} d_{b[\mathrm{m}]}^{1/2} P_{b[\mathrm{MW}]}^{1/4}}{|\sin \beta_b| \left( v_\| / v_{Te} \right) \beta_{Te} N_{b\perp}^{1/2} \Phi^{1/4}} J_n^{1/2} \left( \frac{k_{b\perp} v_\perp}{\Omega} \right) \tag{3.224}$$

where $|\sin \beta_b| = d_b / d_{b\|} = |\Phi_{b\perp}| / \Phi_b$ is a measure of the incidence of the power flow with respect to the magnetic field line. The numerical coefficient is

$$K = \frac{e^{1/2} 10^6}{2^{1/4} \pi^{3/4} c^{7/4} m_e^{1/2} \varepsilon_0^{1/4}} \simeq 0.13 \tag{3.225}$$

Taking typical NSTX EBWCD parameters $N_\| \simeq 1$, $f \simeq 14$ GHz, $d \simeq 0.1$ m, $P \simeq 2$ MW, $v_\| \simeq 3.5 v_{Te}$, $J_n \left( k_\perp v_\perp / \Omega \right) \simeq 1$, $\beta_{Te} \simeq 0.05$, $|\sin \beta_b| \simeq 0.5$, we get, for typical LBF cases ($N_\perp \simeq 50, \Phi \simeq 0.05$), and also typical HBF cases ($N_\perp \simeq 5, \Phi \simeq 5$) that $\tau_{RF} / \tau_T \simeq 0.5$. This means that for EBWCD in typical STs such as NSTX, trapping effects are expected to play a role and need to be investigated in more detail; they

may lead to some decrease in the energy and momentum transfer between EBWs and electrons. A systematic study of interaction between particles and a wavepacket, such as the one done in Ref. [70], should be done for the case of a plasma in a magnetic field in order to quantify the effect of particle trapping when $\tau_T \lesssim \tau_{RF}$. This is beyond the scope of this work, where we restrict ourselves to cases where $\tau_T > \tau_{RF}$.

### 3.5.4 Bounce-averaging of the quasilinear operator

According to the results of Section 3.3.8, the bounce averaging of an operator of the form (3.187) requires to evaluate the bounce-averaged diffusion tensors $\mathbb{D}_{\mathbf{p}}^{(0)}$ and convection vector $\mathbf{F}_{\mathbf{p}}^{(0)}$defined by (3.144) and (3.145) for the contributions of the $\theta$-independent functions $f_0$ and $g$, as well as the diffusion tensors $\widetilde{\mathbb{D}}_{\mathbf{p}}^{(0)}$ and convection vector $\widetilde{\mathbf{F}}_{\mathbf{p}}^{(0)}$ defined by (3.154) and (3.155) for the $\theta$-dependent functions $\widetilde{f}$.

#### Flux coefficients for the distribution functions $f_0$ and $g$

Since RF fluxes are purely diffusive, we have $\mathbf{F}_{\mathbf{p}}^{\mathrm{RF}(0)} = 0$ (3.145). Applying (3.144) to (3.190) and using (3.132) as well as $\omega_{ce} = \Psi\omega_{ce,0}$ with

$$\omega_{ce,0} = \frac{eB_0}{m_e} \tag{3.226}$$

we find

$$\begin{aligned}
D_{b,pp}^{\mathrm{RF}(0)} &= \sum_{n=-\infty}^{+\infty} \left(1-\xi_0^2\right) D_n^{\mathrm{RF}(0)}\left(p,\xi_0\right) \\
D_{b,p\xi}^{\mathrm{RF}(0)} &= \sum_{n=-\infty}^{+\infty} -\frac{\sqrt{1-\xi_0^2}}{\xi_0}\left(1-\xi_0^2-\frac{n\omega_{ce,0}}{\gamma\omega_b}\right) D_n^{\mathrm{RF}(0)}\left(p,\xi_0\right) \\
D_{b,\xi p}^{\mathrm{RF}(0)} &= \sum_{n=-\infty}^{+\infty} -\frac{\sqrt{1-\xi_0^2}}{\xi_0}\left(1-\xi_0^2-\frac{n\omega_{ce,0}}{\gamma\omega_b}\right) D_n^{\mathrm{RF}(0)}\left(p,\xi_0\right) \\
D_{b,\xi\xi}^{\mathrm{RF}(0)} &= \sum_{n=-\infty}^{+\infty} \frac{1}{\xi_0^2}\left(1-\xi_0^2-\frac{n\omega_{ce,0}}{\gamma\omega_b}\right)^2 D_n^{\mathrm{RF}(0)}\left(p,\xi_0\right)
\end{aligned} \tag{3.227}$$

where we defined

$$D_n^{\mathrm{RF}(0)}\left(p,\xi_0\right) = \left\{\Psi D_n^{\mathrm{RF}}\left(p,\xi\right)\right\} \tag{3.228}$$

We note that the bounce-averaging operation (3.144) on the diffusion tensor (3.190) gives a diffusion tensor (3.227) that is function of a bounce-averaged diffusion coefficient $D_n^{\mathrm{RF}(0)}$ common to all tensor elements. Applying the bounce-averaging operation to (3.205) gives

$$D_n^{\mathrm{RF}(0)}(p,\xi_0) = \left[\frac{1}{2}\sum_{\sigma}\right]_T H\left[|\xi_0| - \sqrt{1-\frac{1}{\Psi(\psi,\theta_b)}}\right] \times D_b^{\mathrm{RF}(0)} \frac{\gamma m_e}{p|\xi_b|}\left|\Theta_b^{(n)}\right|^2 \frac{1}{\sqrt{\pi}\Delta N_{b\|}} \exp\left[-\frac{\left(N_{\|\mathrm{res}b} - N_{b\|}\right)^2}{\Delta N_{b\|}^2}\right] \tag{3.229}$$

where we defined

$$D_b^{\mathrm{RF}(0)} = \frac{e^2\pi}{\varepsilon_0\omega_b|\Phi_{b\perp}|}\frac{P_b}{4\pi^2 r(\psi,\theta_b)R_p}\widehat{F}_g(\psi,\theta_b)\widetilde{F}_g(\psi,\theta_b)\frac{\Psi_b}{\lambda}\frac{\xi_0}{\xi_b} \tag{3.230}$$

and introduced the factor

$$\widetilde{F}_g(\psi,\theta) \equiv \frac{rB}{\widetilde{q}R_pB_P\left|\widehat{\psi}\cdot\widehat{r}\right|} \tag{3.231}$$

Note that for circular concentric flux-surfaces, $\widetilde{F}_g(\psi,\theta) = 1$. The equivalence (3.46-3.48) gives the Heaviside function in (3.229), which ensures that only trapped electrons that reach the poloidal location $\theta_b$ do interact with the wave.

**Flux coefficients for the distribution function $\widetilde{f}$**

Applying (3.154) and (3.155) to (3.190) and using (3.132) as well as $\omega_{ce} = \Psi\omega_{ce,0}$ with (3.226), we find

$$\begin{aligned}
\widetilde{D}_{b,pp}^{\mathrm{RF}(0)} &= \sum_{n=-\infty}^{+\infty} \left(1-\xi_0^2\right) \widetilde{D}_n^{\mathrm{RF}(0)\mathrm{D}}\left(p,\xi_0\right) \\
\widetilde{D}_{b,p\xi}^{\mathrm{RF}(0)} &= \sum_{n=-\infty}^{+\infty} -\frac{\sqrt{1-\xi_0^2}}{\xi_0}\left(1-\xi_0^2-\frac{n\omega_{ce,0}}{\gamma\omega_b}\right) \widetilde{D}_n^{\mathrm{RF}(0)\mathrm{D}}\left(p,\xi_0\right) \\
\widetilde{D}_{b,\xi p}^{\mathrm{RF}(0)} &= \sum_{n=-\infty}^{+\infty} -\frac{\sqrt{1-\xi_0^2}}{\xi_0}\left(1-\xi_0^2-\frac{n\omega_{ce,0}}{\gamma\omega_b}\right) \widetilde{D}_n^{\mathrm{RF}(0)\mathrm{D}}\left(p,\xi_0\right) \\
\widetilde{D}_{b,\xi\xi}^{\mathrm{RF}(0)} &= \sum_{n=-\infty}^{+\infty} \frac{1}{\xi_0^2}\left(1-\xi_0^2-\frac{n\omega_{ce,0}}{\gamma\omega_b}\right)^2 \widetilde{D}_n^{\mathrm{RF}(0)\mathrm{D}}\left(p,\xi_0\right)
\end{aligned} \tag{3.232}$$

and

$$\begin{aligned}
\widetilde{F}_p^{\mathrm{RF}(0)} &= \frac{\sqrt{1-\xi_0^2}}{p\xi_0^3} \sum_{n=-\infty}^{+\infty} -\frac{\sqrt{1-\xi_0^2}}{\xi_0}\left(1-\xi_0^2-\frac{n\omega_{ce,0}}{\gamma\omega_b}\right) \widetilde{D}_n^{\mathrm{RF}(0)\mathrm{F}}(p,\xi_0) \\
\widetilde{F}_\xi^{\mathrm{RF}(0)} &= \frac{\sqrt{1-\xi_0^2}}{p\xi_0^3} \sum_{n=-\infty}^{+\infty} \frac{1}{\xi_0^2}\left(1-\xi_0^2-\frac{n\omega_{ce,0}}{\gamma\omega_b}\right)^2 \widetilde{D}_n^{\mathrm{RF}(0)\mathrm{F}}(p,\xi_0)
\end{aligned} \tag{3.233}$$

where

$$\begin{aligned}
\widetilde{D}_n^{\mathrm{RF}(0)\mathrm{D}}(p,\xi_0) &= \sigma\left\{\sigma\frac{\xi}{\xi_0}D_n^{\mathrm{RF}}(p,\xi)\right\} \\
\widetilde{D}_n^{\mathrm{RF}(0)\mathrm{F}}(p,\xi_0) &= \sigma\left\{\sigma\left(\Psi-1\right)\frac{\xi_0}{\xi}D_n^{\mathrm{RF}}(p,\xi)\right\}
\end{aligned}$$

Again, the bounce-averaging operations (3.154) and (3.155) on the diffusion tensor (3.190) give a diffusion tensor (3.232) and a convection vector (3.233) which elements are function of common bounce-averaged diffusion coefficients, respectively $\widetilde{D}_n^{\mathrm{RF}(0)\mathrm{D}}$ and $\widetilde{D}_n^{\mathrm{RF}(0)\mathrm{F}}$. We also note that the bounce-averaging of the RF quasilinear operator for the drift distribution function $\widetilde{f}$ also generates a convective term. Applying the

bounce-averaging operations to (3.205) gives

$$\begin{aligned}
\widetilde{D}_n^{\mathrm{RF(0)D}}(p,\xi_0) &= \sigma\left[\frac{1}{2}\sum_{\sigma}\right]_T \sigma H\left[|\xi_0| - \sqrt{1-\frac{1}{\Psi(\psi,\theta_b)}}\right] \\
&\times \widetilde{D}_b^{\mathrm{RF(0)D}} \frac{\gamma m_e}{p|\xi_b|}\left|\Theta_b^{(n)}\right|^2 \frac{1}{\sqrt{\pi}\Delta N_{b\|}} \exp\left[-\frac{\left(N_{\|\mathrm{res}b} - N_{b\|}\right)^2}{\Delta N_{b\|}^2}\right] \\
\widetilde{D}_n^{\mathrm{RF(0)F}}(p,\xi_0) &= \sigma\left[\frac{1}{2}\sum_{\sigma}\right]_T \sigma H\left[|\xi_0| - \sqrt{1-\frac{1}{\Psi(\psi,\theta_b)}}\right] \\
&\times \widetilde{D}_b^{\mathrm{RF(0)F}} \frac{\gamma m_e}{p|\xi_b|}\left|\Theta_b^{(n)}\right|^2 \frac{1}{\sqrt{\pi}\Delta N_{b\|}} \exp\left[-\frac{\left(N_{\|\mathrm{res}b} - N_{b\|}\right)^2}{\Delta N_{b\|}^2}\right]
\end{aligned} \tag{3.234}$$

where we defined

$$\begin{aligned}
\widetilde{D}_b^{\mathrm{RF(0)D}} &= \frac{e^2\pi}{\varepsilon_0\omega_b|\Phi_{b\perp}|}\frac{P_b}{4\pi^2 r(\psi,\theta_b)R_p}\widehat{F}_g(\psi,\theta_b)\widetilde{F}_g(\psi,\theta_b)\frac{1}{\lambda} \\
\widetilde{D}_b^{\mathrm{RF(0)F}} &= \frac{e^2\pi}{\varepsilon_0\omega_b|\Phi_{b\perp}|}\frac{P_b}{4\pi^2 r(\psi,\theta_b)R_p}\widehat{F}_g(\psi,\theta_b)\widetilde{F}_g(\psi,\theta_b)\frac{(\Psi_b-1)}{\lambda}\frac{\xi_0^2}{\xi_b^2}
\end{aligned} \tag{3.235}$$

and used the equivalence (3.46-3.48).

## 3.6 Moments of the Distribution Function

Once the steady-state distribution function is calculated from solving the drift-kinetic equation, it is possible to take moments of the distribution function. Because of the fast parallel motion of particles, only the moments that are averaged over a flux surface are of physical relevance. These moments can be expressed as a function of the $\theta$-independent distribution functions $f_0^{(0)}$, $\widetilde{f}^{(0)}$ and $g^{(0)}$. In this section, we introduce the flux-surface averaging of both flux and volumic quantities, and apply this operation to the density, the toroidal current density, and the power density associated with a given momentum-space flux, such as quasilinear RF-induced fluxes or collisional fluxes.

### 3.6.1 Flux-surface averaging

#### Toroidal flux quantities

We consider the flux-surface averaging of a flux quantity through a poloidal surface, generally noted $\mathbf{\Gamma}(\psi,\theta)$. An example of such flow is the toroidal plasma current. We calculate the averaged flux of $\mathbf{\Gamma}$ through the infinitesimal poloidal surface $dS_P(\psi)$

$$\langle\Gamma\rangle_S(\psi) = \frac{\int_{dS_P(\psi)} \mathbf{dS}_\phi \cdot \mathbf{\Gamma}(\psi,\theta)}{\int_{dS_P(\psi)} dS_\phi} \tag{3.236}$$

In the $(\psi,\theta,\phi)$ system, the differential poloidal surface element is given by (A.94)

$$\mathbf{dS}_\phi = \frac{r}{\|\nabla\psi\| \left|\widehat{\psi}\cdot\widehat{\mathbf{r}}\right|} d\psi d\theta \widehat{\phi} \tag{3.237}$$

so that the infinitesimal poloidal surface element $dS_p(\psi)$ of radial extent $d\psi$ is

$$dS_P(\psi) = \int_{dS_P(\psi)} dS_\phi = d\psi \int_0^{2\pi} d\theta \frac{r}{\|\nabla\psi\| \left|\widehat{\psi}\cdot\widehat{\mathbf{r}}\right|} = \frac{2\pi\overline{q}(\psi)}{B_0(\psi)} d\psi \tag{3.238}$$

where we used (3.10) and defined the pseudo safety factor $\overline{q}$ as

$$\overline{q}(\psi) \equiv \int_0^{2\pi} \frac{d\theta}{2\pi} \frac{1}{\left|\widehat{\psi}\cdot\widehat{\mathbf{r}}\right|} \frac{r}{R} \frac{B_0(\psi)}{B_P} \tag{3.239}$$

The flux-surface averaged flux in the toroidal direction becomes

$$\langle\Gamma\rangle_\phi(\psi) = \left(\frac{dS_p}{d\psi}\right)^{-1} \int_0^{2\pi} d\theta \frac{r}{\|\nabla\psi\| \left|\widehat{\psi}\cdot\widehat{\mathbf{r}}\right|} \left[\widehat{\phi}\cdot\mathbf{\Gamma}(\psi,\theta)\right] \tag{3.240}$$

which gives, using (3.238)

$$\langle\Gamma\rangle_\phi(\psi) = \frac{1}{\overline{q}(\psi)} \int_0^{2\pi} \frac{d\theta}{2\pi} \frac{1}{\left|\widehat{\psi}\cdot\widehat{\mathbf{r}}\right|} \frac{r}{R} \frac{B_0(\psi)}{B_P} \left[\widehat{\phi}\cdot\mathbf{\Gamma}(\psi,\theta)\right] \tag{3.241}$$

### Volumic quantities

We consider the flux-surface averaging of a volumic quantity, such as the density or a dissipated power density, generally noted $\mathbf{\Phi}(\psi,\theta)$. It is defined as the average value of $\mathbf{\Phi}$ within the infinitesimal volume $dV(\psi)$

$$\langle \mathbf{\Phi} \rangle_V (\psi) = \frac{\iint_{dV(\psi)} \mathbf{\Phi}(\psi,\theta)\, dV}{\iint_{dV(\psi)} dV} \tag{3.242}$$

In the $(\psi,\theta,\phi)$ system, the differential volume elements is given by (A.95)

$$dV = \frac{Rr}{\|\nabla\psi\| \left|\widehat{\psi}\cdot\widehat{\mathbf{r}}\right|} d\psi d\theta d\phi \tag{3.243}$$

and the infinitesimal volume element $dV(\psi)$ of a flux-surface was previously calculated (3.212)

$$dV = \frac{4\pi^2 R_p \widehat{q}(\psi)}{B_0(\psi)} d\psi \tag{3.244}$$

so that the flux-surface averaged quantity in the toroidal direction becomes

$$\langle \mathbf{\Phi} \rangle_V (\psi) = \frac{1}{\widehat{q}(\psi)} \int_0^{2\pi} \frac{d\theta}{2\pi} \frac{1}{\left|\widehat{\psi}\cdot\widehat{\mathbf{r}}\right|} \frac{r}{R_p} \frac{B_0(\psi)}{B_P} \mathbf{\Phi}(\psi,\theta) \tag{3.245}$$

## 3.6.2 Plasma density

### Definition

The electron density $n_e(\psi,\theta)$ is given by the relation

$$n_e(\psi,\theta) = 2\pi \int_{-1}^{+1} d\xi \int_0^{\infty} p^2 dp\; f(p,\xi,\psi,\theta) \tag{3.246}$$

**Flux-surface averaging**

Using the general expression (3.245) of the flux-surface averaging of a volumic quantity, we transform

$$\begin{aligned}\langle n_e\rangle_V(\psi) &= \frac{1}{\widehat{q}}\int_0^{2\pi}\frac{d\theta}{2\pi}\frac{1}{\left|\widehat{\psi}\cdot\widehat{\mathbf{r}}\right|}\frac{r}{R_p}\frac{B_0}{B_P}n_e(\psi,\theta)\\ &= \frac{2\pi}{\widehat{q}}\int_0^{\infty}p^2dp\int_0^{2\pi}\frac{d\theta}{2\pi}\frac{1}{\left|\widehat{\psi}\cdot\widehat{\mathbf{r}}\right|}\frac{r}{R_p}\frac{B_0}{B_P}\int_{-1}^{+1}d\xi\, f(\psi,\theta,p,\xi)\\ &= \frac{2\pi}{\widehat{q}}\int_0^{\infty}p^2dp\int_0^{2\pi}\frac{d\theta}{2\pi}\frac{1}{\left|\widehat{\psi}\cdot\widehat{\mathbf{r}}\right|}\frac{r}{R_p}\frac{B_0}{B_P}\int_{-1}^{+1}\left[\frac{1}{2}\sum_{\sigma=\pm1}\right]_T d\xi\, f(\psi,\theta,p,\xi)\end{aligned} \tag{3.247}$$

where the sum over $\sigma$ for trapped electrons can be introduced because of the integral over $\xi$. Using (3.132) $\xi d\xi = \Psi\xi_0 d\xi_0$ with the condition (3.48) such that an electron $\xi_0$ reaches the poloidal location $\theta$

$$|\xi_0| \geq \sqrt{1-\frac{1}{\Psi(\psi,\theta)}} \tag{3.248}$$

we get

$$\int_{-1}^{+1}\left[\frac{1}{2}\sum_{\sigma=\pm1}\right]_T d\xi = \int_{-1}^{+1}\left[\frac{1}{2}\sum_{\sigma=\pm1}\right]_T \Psi(\psi,\theta)\frac{\xi_0}{\xi}H\left(|\xi_0|-\sqrt{1-\frac{1}{\Psi(\psi,\theta)}}\right)d\xi_0 \tag{3.249}$$

where $H$ is the usual Heaviside function which is defined as $H(x)=1$ for $x>0$ and $H(x)=0$ otherwise.

Note that the condition (3.248) is equivalent to (3.46)

$$\theta_{\min}(\psi,\xi_0) \leq \theta \leq \theta_{\max}(\psi,\xi_0) \tag{3.250}$$

so that, after permuting the integrals over $\theta$ and $\xi_0$, we get

$$\langle n_e \rangle_V (\psi) = \frac{2\pi}{\widehat{q}} \int_0^\infty p^2 dp \int_{-1}^{+1} d\xi_0 \times \left[ \frac{1}{2} \sum_{\sigma=\pm 1} \right]_T \int_{\theta_{\min}}^{\theta_{\max}} \frac{d\theta}{2\pi} \frac{1}{\left| \widehat{\psi} \cdot \widehat{r} \right|} \frac{r}{R_p} \frac{B}{B_P} \frac{\xi_0}{\xi} f(\psi, \theta, p, \xi_0) \tag{3.251}$$

where the bounce-averaging of the distribution (3.86) appears naturally. Therefore, the expression (3.251) can be rewritten in the simple form

$$\langle n_e \rangle_V (\psi) = 2\pi \frac{\widetilde{q}}{\widehat{q}} \int_0^\infty p^2 dp \int_{-1}^{+1} d\xi_0 \, \lambda \{ f(\psi, \theta, p, \xi_0) \} \tag{3.252}$$

where $f = f_0 + \widetilde{f} + g$.

### Distribution functions $f_0$ and $g$

The distribution functions $f_0$ and $g$ are constant along a field line, and for such $\theta$-independent distribution function $f$, we have $f(\psi, \theta, p, \xi) = f^{(0)}(\psi, p, \xi_0)$ such that we obtain

$$\langle n_e \rangle_V \left( \psi, f^{(0)} \right) = 2\pi \frac{\widetilde{q}}{\widehat{q}} \int_0^\infty p^2 dp \int_{-1}^{+1} d\xi_0 \, \lambda f^{(0)} \tag{3.253}$$

### Distribution function $\widetilde{f}$

The distribution function $\widetilde{f}$ (3.116) depends explicitly upon the poloidal angle $\theta$, but can be rewritten as (3.148) $\widetilde{f} = \xi / (\Psi \xi_0) \widetilde{f}^{(0)}$ where $\widetilde{f}^{(0)}$ is independent of $\theta$ but is antisymmetric in the trapped region.

Therefore, the flux-surface averaged density contribution of $\widetilde{f}$ becomes

$$\langle \widetilde{n}_e \rangle_V \left( \psi, \widetilde{f}^{(0)} \right) = 2\pi \frac{\widetilde{q}}{\widehat{q}} \int_0^\infty p^2 dp \int_{-1}^{+1} d\xi_0 \, \overline{\lambda}_{1,-1,0} \widetilde{f}^{(0)} \tag{3.254}$$

where

$$\overline{\lambda}_{1,-1,0} = \sigma \left\{ \sigma \frac{\xi}{\Psi(\psi, \theta) \xi_0} \right\} \lambda \tag{3.255}$$

is defined according to (3.88).

### Total distribution function

The total flux-surface averaged density for the total distribution function $f = f_0 + \widetilde{f} + g$ becomes

$$\langle n_e \rangle_V (\psi) = \langle n_e \rangle_V \left( \psi, f_0^{(0)} \right) + \langle n_e \rangle_V \left( \psi, g^{(0)} \right) + \langle \widetilde{n}_e \rangle_V \left( \psi, \widetilde{f}^{(0)} \right) \tag{3.256}$$

## 3.6.3 Current Density

### Definition

The density of current carried by electrons is given by

$$\mathbf{J}(\mathbf{r}) = q_e \iiint d^3p \, \mathbf{v} f(\mathbf{r}, \mathbf{p}) \tag{3.257}$$

so that the parallel current density is

$$J_\parallel (\mathbf{r}) = q_e \iiint d^3p \, v_\parallel f(\mathbf{r}, \mathbf{p}) \tag{3.258}$$

which becomes in $(\psi, \theta, p, \xi)$ phase space

$$J_\parallel (\psi, \theta) = 2\pi q_e \int_0^\infty p^2 dp \int_{-1}^1 d\xi \, \frac{p\xi}{\gamma m_e} f(\psi, \theta, p, \xi) \tag{3.259}$$

### Flux-Surface Averaged toroidal current

The flux-surface averaged current density in the toroidal direction is given by (3.241)

$$\begin{aligned} \left\langle J_\parallel \right\rangle_\phi (\psi) &= \frac{1}{\overline{q}} \int_0^{2\pi} \frac{d\theta}{2\pi} \frac{1}{\left| \widehat{\psi} \cdot \widehat{\mathbf{r}} \right|} \frac{r}{R} \frac{B_0}{B_P} J_\parallel (\psi, \theta) \left[ \widehat{\phi} \cdot \widehat{\mathbf{b}} \right] \\ &= \frac{1}{\overline{q}} \int_0^{2\pi} \frac{d\theta}{2\pi} \frac{1}{\left| \widehat{\psi} \cdot \widehat{\mathbf{r}} \right|} \frac{r}{R} \frac{B_T}{B_P} \frac{J_\parallel (\psi, \theta)}{\Psi (\psi, \theta)} \end{aligned} \tag{3.260}$$

where we used (3.39). Using (3.132) and (3.48), and inserting (3.259), we find

$$\left\langle J_{\parallel}\right\rangle_{\phi}(\psi)=\frac{2\pi q_e}{m_e}\frac{1}{\overline{q}}\int_0^{\infty}\frac{p^3}{\gamma}dp\int_{-1}^{1}d\xi_0\,\sigma\xi_0\widetilde{q}\lambda\left\{\frac{\xi}{\xi_0}\frac{R_p}{R}\frac{B_T}{B}\sigma f\left(\psi,\theta,p,\xi\right)\right\} \tag{3.261}$$

### Distribution functions $f_0$ and $g$

The distribution functions $f_0$ and $g$ are constant along a field line and symmetric in the trapped region, and for such $\theta$-independent distribution function $f$, we have $f\left(\psi,\theta,p,\xi\right)=f^{(0)}\left(\psi,p,\xi_0\right)$ such that we can define

$$\left\langle J_{\parallel}\right\rangle_{\phi}\left(\psi,f^{(0)}\right)=\frac{2\pi q_e}{m_e}\frac{q}{\overline{q}}\int_0^{\infty}\frac{p^3}{\gamma}dp\int_{-1}^{1}d\xi_0\,H\left(|\xi_0|-\xi_{0T}\right)\xi_0 f^{(0)} \tag{3.262}$$

since $\left[\frac{1}{2}\sum_{\sigma=\pm1}\right]_T\sigma=0$ for trapped electrons and, according to (3.19)

$$\widetilde{q}\lambda\left\{\frac{\xi}{\xi_0}\frac{R_p}{R}\frac{B_T}{B}\right\}=\int_0^{2\pi}\frac{d\theta}{2\pi}\frac{1}{\left|\widehat{\psi}\cdot\widehat{\mathbf{r}}\right|}\frac{r}{R}\frac{B_T}{B_P}=q\left(\psi\right) \tag{3.263}$$

### Distribution function $\widetilde{f}$

The distribution function $\widetilde{f}$ (3.116) depends explicitly upon the poloidal angle $\theta$, but can be rewritten as (3.148) $\widetilde{f}=\xi/\left(\Psi\xi_0\right)\widetilde{f}^{(0)}$ where $\widetilde{f}^{(0)}$ is independent of $\theta$ but is antisymmetric in the trapped region, such that only $\sigma\widetilde{f}^{(0)}$ can be taken out from the bounce averaging.

Therefore, the flux-surface averaged toroidal current density contribution of $\widetilde{f}$ becomes

$$\left\langle \widetilde{J}_{\parallel}\right\rangle_{\phi}\left(\psi,\widetilde{f}^{(0)}\right)=\frac{2\pi q_e}{m_e}\frac{\widetilde{q}}{\overline{q}}\frac{B_{T0}}{B_0}\frac{R_p}{R_0}\int_0^{\infty}\frac{p^3}{\gamma}dp\int_{-1}^{1}d\xi_0\,\lambda_{2,-2,2}\xi_0\widetilde{f}^{(0)} \tag{3.264}$$

since

$$\lambda\left\{\frac{\xi^2}{\Psi\xi_0^2}\frac{R_p}{R}\frac{B_T}{B}\right\}=\lambda\frac{B_{T0}}{B_0}\frac{R_p}{R_0}\left\{\frac{\xi^2}{\xi_0^2}\frac{1}{\Psi^2}\frac{R_0}{R}\frac{B_T}{B_{T0}}\right\}=\frac{B_{T0}}{B_0}\frac{R_p}{R_0}\lambda_{2,-2,2} \tag{3.265}$$

where we used $RB_T = I(\psi) = R_0 B_{T0}$ and where

$$\lambda_{2,-2,2} = \left\{ \left( \frac{\xi^2}{\xi_0^2} \right)^2 \Psi^{-2} \left( \frac{R_0}{R} \right)^2 \right\} \lambda \tag{3.266}$$

is defined according to (3.87).

### Total distribution function

The total flux-surface averaged toroidal current density for the total distribution function $f = f_0 + \widetilde{f} + g$ becomes

$$\langle J_\parallel \rangle_\phi (\psi) = \langle J_\parallel \rangle_\phi \left( \psi, f_0^{(0)} \right) + \langle J_\parallel \rangle_\phi \left( \psi, g^{(0)} \right) + \left\langle \widetilde{J}_\parallel \right\rangle_\phi \left( \psi, \widetilde{f}^{(0)} \right) \tag{3.267}$$

## 3.6.4 Power Density Associated with a Flux

### Definition

The kinetic energy associated with a relativistic electron of momentum $p$ is

$$E_c = m_e c^2 (\gamma - 1) \tag{3.268}$$

Then, the local energy density of electrons is

$$\varepsilon(\mathbf{r}) = \int d^3p \; m_e c^2 (\gamma - 1) f(\mathbf{r}, \mathbf{p}) \tag{3.269}$$

The density of power absorbed through the process $\mathcal{O}$, $P_{abs}^{\mathcal{O}}$, is

$$P_{abs}^{\mathcal{O}}(\mathbf{r}) = \left. \frac{\partial \varepsilon}{\partial t} \right|_{\mathcal{O}} = \int d^3p \; m_e c^2 (\gamma - 1) \left. \frac{\partial f(\mathbf{r}, \mathbf{p})}{\partial t} \right|_{\mathcal{O}} \tag{3.270}$$

When the operator is described in conservative form, as the divergence of a flux

$$\left. \frac{\partial f}{\partial t} \right|_{\mathcal{O}} = -\nabla_{\mathbf{p}} \cdot \mathbf{S}_{\mathbf{p}}^{\mathcal{O}} = -\frac{1}{p^2} \frac{\partial}{\partial p} \left( p^2 S_p^{\mathcal{O}} \right) + \frac{1}{p} \frac{\partial}{\partial \xi} \left( \sqrt{1 - \xi^2} S_\xi^{\mathcal{O}} \right) \tag{3.271}$$

then the power density becomes

$$P_{\text{abs}}^{\mathcal{O}} = -2\pi m_e c^2 \int_0^{\infty} p^2 dp \; (\gamma - 1) \int_{-1}^{+1} d\xi \left[ \frac{1}{p^2} \frac{\partial}{\partial p} \left( p^2 S_p^{\mathcal{O}} \right) - \frac{1}{p} \frac{\partial}{\partial \xi} \left( \sqrt{1-\xi^2} S_\xi^{\mathcal{O}} \right) \right] \tag{3.272}$$

The integration of the $S_\xi^{\mathcal{O}}$ term gives no contribution, since the particle energy is function of $p$ only

$$\int_{-1}^{+1} d\xi \, \frac{\partial}{\partial \xi} \left( \sqrt{1-\xi^2} S_\xi^{\mathcal{O}} \right) = \left[ \sqrt{1-\xi^2} S_\xi^{\mathcal{O}} \right]_{-1}^{+1} = 0 \tag{3.273}$$

and the equation (3.272) reduces to

$$P_{\text{abs}}^{\mathcal{O}} = -2\pi m_e c^2 \int_{-1}^{+1} d\xi \int_0^{\infty} (\gamma - 1) \frac{\partial}{\partial p} \left( p^2 S_p^{\mathcal{O}} \right) dp \tag{3.274}$$

Integrating by parts, we get

$$P_{\text{abs}}^{\mathcal{O}} = -2\pi m_e c^2 \int_{-1}^{+1} d\xi \left( \left[ (\gamma - 1) p^2 S_p^{\mathcal{O}} \right]_0^{\infty} - \int_0^{\infty} \frac{d\gamma}{dp} p^2 S_p^{\mathcal{O}} dp \right) \tag{3.275}$$

Assuming that $\lim_{p \to \infty} p^2 S_p^{\mathcal{O}} = 0$, and using

$$\frac{d\gamma}{dp} = \frac{p}{\gamma m_e^2 c^2} \tag{3.276}$$

the equation (3.275) reduces to

$$P_{\text{abs}}^{\mathcal{O}}(\psi, \theta) = 2\pi \int_{-1}^{+1} d\xi \int_0^{\infty} dp \, \frac{p^3}{\gamma m_e} S_p^{\mathcal{O}} \tag{3.277}$$

### Flux-Surface Averaging

Starting from the general expression of the flux-surface averaging of a volume quantity (3.245), the flux-surface averaged power density $\left\langle P_{abs}^{\mathcal{O}} \right\rangle_V (\psi)$ is

$$\left\langle P_{abs}^{\mathcal{O}} \right\rangle_V (\psi) = \frac{1}{\widehat{q}} \int_0^{2\pi} \frac{d\theta}{2\pi} \frac{1}{\left| \widehat{\psi} \cdot \widehat{r} \right|} \frac{r}{R_p} \frac{B_0}{B_P} P_{abs}^{\mathcal{O}}(\psi, \theta) \tag{3.278}$$

which becomes

$$\left\langle P_{abs}^{\mathcal{O}}\right\rangle_V(\psi) = 2\pi\int_0^\infty dp\,\frac{p^3}{\gamma m_e}\frac{1}{\widehat{q}}\int_0^{2\pi}\frac{d\theta}{2\pi}\frac{1}{\left|\widehat{\psi}\cdot\widehat{r}\right|}\frac{r}{R_p}\frac{B_0}{B_P}\int_{-1}^{+1}d\xi\,\left[\frac{1}{2}\sum_{\sigma=\pm1}\right]_T S_p^{\mathcal{O}} \quad (3.279)$$

where the sum over $\sigma$ for trapped electrons can be added in the integral over $\xi$. Using $\xi d\xi = \Psi\xi_0 d\xi_0$ with the condition (3.48) on $\xi_0$ we permute the integrals over $\theta$ and $\xi_0$ and find

$$\left\langle P_{abs}^{\mathcal{O}}\right\rangle_V(\psi) = 2\pi\frac{\widetilde{q}}{\widehat{q}}\int_0^\infty dp\,\frac{p^3}{\gamma m_e}\int_{-1}^{+1}d\xi_0\lambda\left\{S_p^{\mathcal{O}}\right\} \quad (3.280)$$

Using the definition (3.135), we observe that the flux-surface averaged power density is calculated using the momentum flux component of the bounce-averaged kinetic equation:

$$\left\langle P_{abs}^{\mathcal{O}}\right\rangle_V(\psi) = 2\pi\frac{\widetilde{q}}{\widehat{q}}\int_0^\infty dp\,\frac{p^3}{\gamma m_e}\int_{-1}^{+1}d\xi_0\lambda S_p^{(0)\mathcal{O}} \quad (3.281)$$

where $S_p^{(0)\mathcal{O}}$ was evaluated for each operator in the kinetic equation.

### 3.6.5 Stream Function for Momentum Space fluxes

When the integral term in the collision operator is neglected, the Fokker-Planck equation (3.125) reduces to

$$\nabla_{\mathbf{p}}\cdot\mathbf{S}_{\mathbf{p}}(f_0) = 0 \quad (3.282)$$

where $f_0 = f_0(p,\xi,\psi)$. Because $\mathbf{S_p}$ is a divergence-free field vector, it can be expressed as the curl of a stream function

$$\mathbf{S_p} = \nabla\times\mathbf{T_p} \quad (3.283)$$

The expression of a curl in momentum space $(p, \xi, \varphi)$ is given by relation (A.125) in Appendix A

$$S_p = \frac{1}{p}\frac{\partial}{\partial \xi}\left(\sqrt{1-\xi^2}T_\varphi\right) + \frac{1}{p\sqrt{1-\xi^2}}\frac{\partial T_\xi}{\partial \varphi}$$

$$S_\xi = \frac{1}{p}\frac{\partial}{\partial p}\left(pT_\varphi\right) - \frac{1}{p\sqrt{1-\xi^2}}\frac{\partial T_p}{\partial \varphi} \tag{3.284}$$

$$S_\varphi = -\frac{1}{p}\frac{\partial}{\partial p}\left(pT_\xi\right) - \frac{\sqrt{1-\xi^2}}{p}\frac{\partial T_p}{\partial \xi}$$

Because $S_\varphi = 0$, we can choose $T_\xi = T_p = 0$, which leads to

$$\begin{aligned} S_p &= \frac{1}{p}\frac{\partial}{\partial \xi}\left(\sqrt{1-\xi^2}T_\varphi\right) \\ S_\xi &= \frac{1}{p}\frac{\partial}{\partial p}\left(pT_\varphi\right) \end{aligned} \tag{3.285}$$

and we can rewrite

$$\mathbf{S_p} = \nabla \times T_\varphi \widehat{\varphi} \tag{3.286}$$

In order to give a physical meaning to $T_\varphi(p, \xi, \psi)$, we define formally

$$T_\varphi(\psi, p, \xi) = K(\psi, p, \xi)\, A(\psi, p, \xi) \tag{3.287}$$

where the function $A(p, \xi)$ is such that the flux of electrons between two contours $A_1$ and $A_2$ is equal to $n_e(\psi)\,(A_2 - A_1)$. Lets consider a path $\gamma_{12}$ between the contours $A_1$ and $A_2$. The total flux of electrons through this path, which is in fact a surface, given the rotational symmetry in $\varphi$, is given by

$$\begin{aligned} \Gamma_{12} &= \iint_{S_{12}} dS\, \mathbf{S_p} \cdot \widehat{n} \\ &= \iint_{S_{12}} d\mathbf{S} \cdot \nabla \times T_\varphi \widehat{\varphi} \\ &= \oint_{C_{12}} T_\varphi\, d\mathbf{l} \cdot \widehat{\varphi} \end{aligned} \tag{3.288}$$

By rotational symmetry in $\varphi$, and using (A.120), we get

$$\Gamma_{12} = 2\pi p_2 \sqrt{1-\xi_2^2} T_{\varphi 2} \; - 2\pi p_1 \sqrt{1-\xi_1^2} T_{\varphi 1} \tag{3.289}$$

If we define

$$K(\psi, p, \xi) \equiv \frac{n_e(\psi)}{2\pi p \sqrt{1-\xi^2}} \tag{3.290}$$

we obtain

$$\Gamma_{12} = n_e(\psi)(A_2 \; - A_1) \tag{3.291}$$

and therefore the total flux between the contours $A_1$ and $A_2$ is equal to $n_e(\psi)$ $(A_2 - A_1)$. We call $A(\psi, p, \xi)$ the stream function, and we get finally

$$S_p = \frac{n_e(\psi)}{2\pi p^2} \frac{\partial A}{\partial \xi} \tag{3.292}$$

$$S_\xi = \frac{n_e(\psi)}{2\pi p \sqrt{1-\xi^2}} \frac{\partial A}{\partial p} \tag{3.293}$$

Since there are no fluxes across the internal boundaries in the momentum space, this boundary coincide with a contour $A$, and therefore we can arbitrarily set this value to 0:

$$A(0, \xi) = A(p, \pm 1) = 0 \tag{3.294}$$

Then $A$ can be calculated by any of the integrals

$$A(\psi, p, \xi) = \frac{2\pi p^2}{n_e(\psi)} \int_{-1}^{\xi} d\xi \; S_p = \frac{2\pi p^2}{n_e(\psi)} \int_{1}^{\xi} d\xi' \; S_p \tag{3.295}$$

or

$$A(\psi, p, \xi) = \frac{2\pi \sqrt{1-\xi^2}}{n_e(\psi)} \int_0^p p' dp' \; S_\xi \tag{3.296}$$

However, $A(\psi, p, \xi)$ remains a function of $\xi$, which depends upon $\theta$. Starting from the bounce-averaged fluxes, it is interesting to compute a function $A^{(0)}(\psi, p, \xi_0)$, such

that

$$
\begin{aligned}
A^{(0)}\left(0,\xi_0\right) &= \overline{A}\left(p,\pm 1\right) = 0 \\
S_p^{(0)} &= \frac{n_e\left(\psi\right)}{2\pi p^2}\frac{\partial A^{(0)}}{\partial \xi_0} \\
S_\xi^{(0)} &= \frac{n_e\left(\psi\right)}{2\pi p\sqrt{1-\xi_0^2}}\frac{\partial A^{(0)}}{\partial p}
\end{aligned}
\tag{3.297}
$$

We first need to demonstrate the existence of such a function. Starting from $S_p^{(0)}$,

$$
\begin{aligned}
A^{(0)}\left(\psi,p,\xi_0\right) &= \frac{2\pi p^2}{n_e\left(\psi\right)}\int_{-1}^{\xi_0} d\xi_0' \ \left\{S_p\right\} \\
&= \frac{2\pi p^2}{n_e\left(\psi\right)}\int_{-1}^{\xi_0} d\xi_0' \ \frac{1}{\lambda\widetilde{q}}\left[\frac{1}{2}\sum_\sigma\right]_T \int_{\theta_{\min}}^{\theta_{\max}} \frac{d\theta}{2\pi}\frac{1}{\left|\widehat{\psi}\cdot\widehat{r}\right|}\frac{r}{R_p}\frac{B}{B_P}\frac{\xi_0'}{\xi'}S_p \\
&= \int_{-1}^{\xi_0} d\xi_0' \ \frac{1}{\lambda\widetilde{q}}\left[\frac{1}{2}\sum_\sigma\right]_T \int_0^{2\pi} \frac{d\theta}{2\pi}H\left(B_b-B\right)\frac{1}{\left|\widehat{\psi}\cdot\widehat{r}\right|}\frac{r}{R_p}\frac{B}{B_P}\frac{\xi_0'}{\xi'}\frac{\partial A}{\partial \xi'} \\
&= \frac{\sigma}{\lambda\widetilde{q}}\left[\frac{1}{2}\sum_\sigma\right]_T \int_0^{2\pi} \frac{d\theta}{2\pi}\frac{1}{\left|\widehat{\psi}\cdot\widehat{r}\right|}\frac{r}{R_p}\frac{B}{B_P} \\
&\qquad \int_{-1}^{\xi_0} d\xi_0' H\left(\left|\xi_0\right|-\sqrt{1-\frac{1}{\Psi}}\right)\sigma\frac{\xi_0'}{\xi'}\frac{\partial A}{\partial \xi'} \\
&= \frac{\sigma}{\lambda\widetilde{q}}\left[\frac{1}{2}\sum_\sigma\right]_T \int_0^{2\pi} \frac{d\theta}{2\pi}\frac{1}{\left|\widehat{\psi}\cdot\widehat{r}\right|}\frac{r}{R_p}\frac{B}{B_P}\frac{\sigma}{\Psi}\int_{-1}^{\xi} d\xi'\frac{\partial A}{\partial \xi'} \\
&= \frac{\sigma}{\lambda\widetilde{q}}\left[\frac{1}{2}\sum_\sigma\right]_T \int_0^{2\pi} \frac{d\theta}{2\pi}\frac{1}{\left|\widehat{\psi}\cdot\widehat{r}\right|}\frac{r}{R_p}\frac{B_0}{B_P}\sigma A \\
&= \sigma\frac{\widehat{q}}{\lambda\widetilde{q}}\left[\frac{1}{2}\sum_\sigma\right]_T \left\langle\sigma A\right\rangle_V
\end{aligned}
\tag{3.298}
$$

where we used

$$
\theta_{\min}\le\theta\le\theta_{\max} \Leftrightarrow B\le B_b \Leftrightarrow \sqrt{1-\frac{1}{\Psi}}\le\left|\xi_0\right| \tag{3.299}
$$

Now, starting from $S_\xi^{(0)}$, we have

$$
\begin{aligned}
A^{(0)}(\psi,p,\xi_0) &= \frac{2\pi\sqrt{1-\xi_0^2}}{n_e(\psi)}\int_0^p p'dp'\,\sigma\left\{\frac{\sigma\xi}{\sqrt{\Psi}\xi_0}S_\xi\right\} \\
&= \frac{2\pi\sqrt{1-\xi_0^2}}{n_e(\psi)}\int_0^p p'dp'\,\sigma\frac{1}{\lambda\widetilde{q}}\left[\frac{1}{2}\sum_\sigma\right]_T\int_{\theta_{\min}}^{\theta_{\max}}\frac{d\theta}{2\pi}\frac{1}{\left|\widehat{\psi}\cdot\widehat{r}\right|}\frac{r}{R_p}\frac{B}{B_P}\frac{\sigma}{\sqrt{\Psi}}S_\xi \\
&= \int_0^p dp'\,\sigma\frac{1}{\lambda\widetilde{q}}\left[\frac{1}{2}\sum_\sigma\right]_T\int_{\theta_{\min}}^{\theta_{\max}}\frac{d\theta}{2\pi}\frac{1}{\left|\widehat{\psi}\cdot\widehat{r}\right|}\frac{r}{R_p}\frac{B}{B_P}\frac{\sigma}{\sqrt{\Psi}}\frac{\sqrt{1-\xi_0^2}}{\sqrt{1-\xi^2}}\frac{\partial A}{\partial p'} \\
&= \frac{\sigma}{\lambda\widetilde{q}}\left[\frac{1}{2}\sum_\sigma\right]_T\int_{\theta_{\min}}^{\theta_{\max}}\frac{d\theta}{2\pi}\frac{1}{\left|\widehat{\psi}\cdot\widehat{r}\right|}\frac{r}{R_p}\frac{B}{B_P}\frac{\sigma}{\Psi}\int_0^p dp'\frac{\partial A}{\partial p'} \\
&= \frac{\sigma}{\lambda\widetilde{q}}\left[\frac{1}{2}\sum_\sigma\right]_T\int_{\theta_{\min}}^{\theta_{\max}}\frac{d\theta}{2\pi}\frac{1}{\left|\widehat{\psi}\cdot\widehat{r}\right|}\frac{r}{R_p}\frac{B_0}{B_P}\sigma A \\
&= \sigma\frac{\widehat{q}}{\lambda\widetilde{q}}\left[\frac{1}{2}\sum_\sigma\right]_T\langle\sigma A\rangle_V
\end{aligned}
\tag{3.300}
$$

and we find the same function $A^{(0)}$. The existence of a function $A^{(0)}$ verifying (3.297) is therefore demonstrated. We need now to demonstrate that $A^{(0)}$ verifying (3.297) leads to the bounce-averaged Fokker-Planck equation (3.134):

$$
\begin{aligned}
\{\nabla_{\mathbf{p}}\cdot\mathbf{S}_{\mathbf{p}}\} &= \frac{1}{p^2}\frac{\partial}{\partial p}\left(p^2S_p^{(0)}\right)-\frac{1}{\lambda p}\frac{\partial}{\partial\xi_0}\left(\sqrt{1-\xi_0^2}\lambda S_{\xi_0}^{(0)}\right) \\
&= \frac{1}{p^2}\frac{\partial}{\partial p}\left(p^2\frac{n_e(\psi)}{2\pi p^2}\frac{\partial A^{(0)}}{\partial\xi_0}\right)-\frac{1}{\lambda p}\frac{\partial}{\partial\xi_0}\left(\sqrt{1-\xi_0^2}\lambda\frac{n_e(\psi)}{2\pi p\sqrt{1-\xi_0^2}}\frac{\partial A^{(0)}}{\partial p}\right) \\
&= \frac{1}{\lambda p^2}\frac{\partial^2}{\partial p\xi_0}\left[\frac{\lambda n_e(\psi)A^{(0)}}{2\pi}\right]-\frac{1}{\lambda p^2}\frac{\partial^2}{\partial\xi_0\partial p}\left[\frac{\lambda n_e(\psi)A^{(0)}}{2\pi}\right] \\
&= 0
\end{aligned}
\tag{3.301}
$$

In conclusion, a stream function verifying

$$
A^{(0)}(0,\xi_0) = \overline{A}(p,\pm1) = 0 \tag{3.302}
$$

has been found which leads to the bounce-averaged Fokker-Planck equation and which

can be calculated from the bounce-averaged fluxes by either

$$A^{(0)}\left(\psi,p,\xi_0\right)=\frac{2\pi p^2}{n_e\left(\psi\right)}\int_{-1}^{\xi_0}d\xi_0'\;S_p^{(0)}=\frac{2\pi p^2}{n_e\left(\psi\right)}\int_{1}^{\xi_0}d\xi_0'\;S_p^{(0)} \tag{3.303}$$

or

$$A^{(0)}\left(\psi,p,\xi_0\right)=\frac{2\pi\sqrt{1-\xi_0^2}}{n_e\left(\psi\right)}\int_0^p p'dp'\;S_\xi^{(0)} \tag{3.304}$$

relations.

# Chapter 4

# Numerical Solver for the Drift Kinetic Equation

In the presence of RF fields, the bounce-averaged drift kinetic equation cannot be solved analytically. Therefore, in collaboration with Yves Peysson from CEA-Cadarache, France, I have developped a numerical code that solves the steady-state DKE and calculates moments of the resulting distribution function such as the current density and the density of power absorbed. It should be pointed out that the code *DKE* presented in this section includes a novel, fast and consistent treatment of conservative radial dynamics, which is important for integrated current drive calculations because of the role of anomalous radial transport on current deposition and current drive efficiency, and also for studying any consistent coupling between radial and momentum-space dynamics, for example wave-induced transport or collisional transport. Such investigations are outside the scope of the present study, and therefore radial dynamics is ignored in the present work, meaning that any consistent, classical or neoclassical coupling between radial transport and momentum space dynamics, is neglected. For more details on the *DKE* code, including a description of the conservative formalism for 3D dynamics (radial and momentum-space), the reader is referred to Ref. [73].

## 4.1 Conservative Formalism in Momentum Space

### 4.1.1 Bounce-averaged kinetic equation

The appropriate kinetic equation for RFCD calculations was derived in Section 3.3.7. The small drift and low collisionality approximations led to a set of two 2-D bounce-averaged kinetic equations (3.125) for the distribution functions $f_0^{(0)}(p,\xi_0)$ and $g^{(0)}(p,\xi_0)$.

Since these equations are bounce-averaged, they are solved as a function of $(p,\xi_0)$, where the pitch-angle coordinate $\xi_0$ represents the value of $\xi$ as the electron passes through the point of minimum $B$-field on a given flux-surface. **For the sake of readability, we will omit the superscripts $^{(0)}$ and subscripts $_0$ refering to bounce-averaged quantities in the entire chapter, keeping in mind that all operators are assumed to apply to the $(p,\xi_0)$ space and all fields are bounce-averaged.** More explicitly, one can refer to the following equivalence in the notations

$$\begin{aligned}
\xi_0 &\longleftrightarrow \xi \\
f_0^{(0)} &\longleftrightarrow f_0 \\
g^{(0)} &\longleftrightarrow g \\
\widetilde{f}^{(0)} &\longleftrightarrow \widetilde{f} \\
\mathbf{S}_\mathbf{p}^{(0)} &\longleftrightarrow \mathbf{S}_\mathbf{p} \\
\mathbb{D}_\mathbf{p}^{(0)} &\longleftrightarrow \mathbb{D}_\mathbf{p} \\
\mathbf{F}_\mathbf{p}^{(0)} &\longleftrightarrow \mathbf{F}_\mathbf{p} \\
B_0(\psi) &\longleftrightarrow B(\psi)
\end{aligned} \tag{4.1}$$

The equations (3.125) are thus rewritten as

$$\begin{aligned}
&\nabla_\mathbf{p}\cdot\mathbf{S}_\mathbf{p}(f_0,\mathbb{D}_\mathbf{p},\mathbf{F}_\mathbf{p}) = \mathcal{I}(f_0) && \text{(a)} \\
&\nabla_\mathbf{p}\cdot\mathbf{S}_\mathbf{p}(g,\mathbb{D}_\mathbf{p},\mathbf{F}_\mathbf{p}) + \nabla_\mathbf{p}\cdot\mathbf{S}_\mathbf{p}\left(\widetilde{f},\widetilde{\mathbb{D}}_\mathbf{p},\widetilde{\mathbf{F}}_\mathbf{p}\right) = \mathcal{I}(g) + \widetilde{\mathcal{I}}\left(\widetilde{f}\right) && \text{(b)}
\end{aligned} \tag{4.2}$$

and the total distribution function is

$$f^{\text{tot}} = f_0 + \widetilde{f} + g \tag{4.3}$$

with (3.149)

$$\widetilde{f} = \frac{I(\psi)\, p\xi}{eB(\psi)} \frac{\partial f_0}{\partial \psi} \tag{4.4}$$

In addition, we must ensure that $f_0$ is symmetric in the trapped region and $g$ is identically zero in the trapped region. The bounce-averaged integral terms $\mathcal{I}$ and $\widetilde{\mathcal{I}}$ describe the effect of collisions on the bulk of electrons due to collisions with the perturbed distribution. They are given by (3.180) and (3.182) respectively. The divergence operator acting on the fluxes (3.134) is expressed as

$$\nabla_{\mathbf{p}} \cdot \mathbf{S}_{\mathbf{p}} = \frac{1}{p^2} \frac{\partial}{\partial p} \left(p^2 S_p\right) - \frac{1}{\lambda p} \frac{\partial}{\partial \xi} \left(\sqrt{1-\xi^2} \lambda S_\xi\right) \tag{4.5}$$

and the momentum-space fluxes (3.143) and (3.153) decompose as

$$\begin{aligned} S_p\left(f, \mathbb{D}_{\mathbf{p}}, \mathbf{F}_{\mathbf{p}}\right) &= -D_{pp} \frac{\partial f}{\partial p} + \frac{\sqrt{1-\xi^2}}{p} D_{p\xi} \frac{\partial f}{\partial \xi} + F_p f \\ S_\xi\left(f, \mathbb{D}_{\mathbf{p}}, \mathbf{F}_{\mathbf{p}}\right) &= -D_{\xi p} \frac{\partial f}{\partial p} + \frac{\sqrt{1-\xi^2}}{p} D_{\xi\xi} \frac{\partial f}{\partial \xi} + F_\xi f \end{aligned} \tag{4.6}$$

The momentum-space diffusion tensors $\mathbb{D}_{\mathbf{p}}$, $\widetilde{\mathbb{D}}_{\mathbf{p}}$ and convection vectors $\mathbf{F}_{\mathbf{p}}, \widetilde{\mathbf{F}}_{\mathbf{p}}$ describe the effect of collisions and RF quasilinear diffusion. We have thus

$$\begin{aligned} \mathbb{D}_{\mathbf{p}} &= \mathbb{D}_{\mathbf{p}}^{\mathrm{C}} + \mathbb{D}_{\mathbf{p}}^{\mathrm{RF}} \\ \widetilde{\mathbb{D}}_{\mathbf{p}} &= \widetilde{\mathbb{D}}_{\mathbf{p}}^{\mathrm{C}} + \widetilde{\mathbb{D}}_{\mathbf{p}}^{\mathrm{RF}} \\ \mathbf{F}_{\mathbf{p}} &= \mathbf{F}_{\mathbf{p}}^{\mathrm{C}} + \mathbf{F}_{\mathbf{p}}^{\mathrm{RF}} \\ \widetilde{\mathbf{F}}_{\mathbf{p}} &= \widetilde{\mathbf{F}}_{\mathbf{p}}^{\mathrm{C}} + \widetilde{\mathbf{F}}_{\mathbf{p}}^{\mathrm{RF}} \end{aligned} \tag{4.7}$$

where the respective coefficients are given by (3.169-3.170) and (3.172-3.173) for collisions, and (3.227) and (3.232-3.233) for RF quasilinear diffusion.

It must be pointed out that in this formalism, all momentum space fluxes are taken into account consistently at the same level, such that the collision and the quasilinear operator - for all RF waves - will be discretized in a uniform, consistent manner. This procedure is different from many other kinetic codes in which the divergence form

of operators is not used and each operator is discretized separately. In addition, the divergence form of the operator leads to the development of a discretization scheme that intrinsically conserve particles, such that unlike many other codes, there is no need for a numerical source of particle in *DKE*, which is an intrinsically conservative code.

### 4.1.2 Resolution of the drift kinetic equation

Using the structure of the system of equations (4.2-4.4), the process of solving the kinetic equation for $f^{\text{tot}}$ is divided into three steps:

- Solve the steady-state distribution function $f_0$ from (4.2-a)
- Calculate the distribution $\widetilde{f}$ by taking the radial derivative of $f_0$ according to (4.4)
- Solve the steady-state distribution function $g$ from (4.2-b) where the operators acting on $\widetilde{f}$ are considered as a source term.

The equations (4.2) are both of the form

$$\nabla_{\mathbf{p}} \cdot \mathbf{S}_{\mathbf{p}} \left( f, \mathbb{D}_{\mathbf{p}}, \mathbf{F}_{\mathbf{p}} \right) = \mathcal{I}\left( f \right) + \mathcal{S} \tag{4.8}$$

where $f$ represents $f_0$ or $g$, and the source term is

$$\mathcal{S} = \begin{cases} 0 & \text{in the equation for } f_0 \\ -\nabla_{\mathbf{p}} \cdot \mathbf{S}_{\mathbf{p}} \left( \widetilde{f}, \widetilde{\mathbb{D}}_{\mathbf{p}}, \widetilde{\mathbf{F}}_{\mathbf{p}} \right) + \widetilde{\mathcal{I}} \left( \widetilde{f} \right) & \text{in the equation for } g \end{cases} \tag{4.9}$$

It is worth noting that the differential and integral parts of the equations (4.2) for $f_0$ and $g$ are identical, which greatly simplifies the calculation and saves computational time. Note, however, that we must ensure that $f_0$ is symmetric in the trapped region while $g$ is identically zero in the trapped region. This symmetrization can be enforced implicitly in the equation (4.8) and results in specific boundary conditions (BC) at the trapped/passing boundary. These BC will be discussed in Section 4.3.

The algorithm to solve equation (4.8) will be described in Section 4.4. The steady-state distribution function results from a time-like relaxation of (4.8) starting from some initial distribution function (generally, but not necessarily, a Maxwellian). We rewrite equation (4.8) as

$$\frac{\partial f}{\partial t} + \nabla_{\mathbf{p}} \cdot \mathbf{S}_{\mathbf{p}} \left( f, \mathbb{D}_{\mathbf{p}}, \mathbf{F}_{\mathbf{p}} \right) = \mathcal{I}\left( f \right) + \mathcal{S} \tag{4.10}$$

where $t$ is a time-like parameter. In order to avoid singularities in the divergence operator (A.124) when solving this equation numerically, it is multiplied by the Jacobian of momentum space (A.119) $J_{\mathbf{p}} = p^2$. The actual form of equation (4.8) solved in the code is thus

$$\frac{\partial}{\partial t}\left( p^2 f \right) + p^2 \nabla_{\mathbf{p}} \cdot \mathbf{S}_{\mathbf{p}} \left( f, \mathbb{D}_{\mathbf{p}}, \mathbf{F}_{\mathbf{p}} \right) = p^2 \mathcal{I}\left( f \right) + p^2 \mathcal{S} \tag{4.11}$$

### 4.1.3 Normalizations

In order to ensure a good numerical precision in the resolution of the kinetic equation, this equation must be normalized. The distribution function must be evaluated at several radial positions, so that the radial derivative (4.4) can be evaluated. We define a reference temperature $T_e^\dagger$ and a reference density $n_e^\dagger$, which are arbitrarily defined, but are typically chosen as the maximum values for $T_e\left(\psi\right)$ and $n_e\left(\psi\right)$. We can then define the local normalized temperatures

$$\begin{aligned} \overline{T}_e\left(\psi\right) &\equiv \frac{T_e\left(\psi\right)}{T_e^\dagger} \\ \overline{n}_e\left(\psi\right) &\equiv \frac{n_e\left(\psi\right)}{n_e^\dagger} \end{aligned} \tag{4.12}$$

Because collisions are the dominant process in most of the momentum space, the equation is normalized to the momentum and time scales associated with collisions. The time is naturally normalized to the collision time $\tau_c^\dagger$ given by (3.106) $\tau_c^\dagger = \left(4\pi\varepsilon_0^2 m_e^2 v_{Te}^{\dagger 3}\right) / \left(q_e^4 n_e^\dagger \ln\Lambda^\dagger\right)$ where $v_{Te}^\dagger = \sqrt{T_e^\dagger / m_e}$ is the thermal velocity and $\ln\Lambda^\dagger = 25.2 - 0.5 \times \log\left(n_e^\dagger\right) + \log\left(T_e^\dagger\right)$ is the usual Coulomb logarithm. The momen-

tum is normalized to the thermal momentum $p_{Te}^{\dagger} = m_e v_{Te}^{\dagger}$. The flux-function $\psi$ was chosen to be zero on the magnetic axis. It is normalized according to its value at the edge $\psi_a$. We define the normalized variables

$$\overline{t} \equiv \frac{t}{\tau_c^{\dagger}}$$

$$\overline{p} \equiv \frac{p}{p_{Te}^{\dagger}} \tag{4.13}$$

$$\overline{\psi} \equiv \frac{\psi}{\psi_a}$$

and the normalized fields

$$\overline{f} = \frac{f}{n_e^{\dagger}/p_{Te}^{\dagger 3}}$$

$$\overline{\mathbf{S}}_{\mathbf{p}} = \frac{\mathbf{S}_{\mathbf{p}}}{n_e^{\dagger}/\left(\tau_c^{\dagger} p_{Te}^{\dagger 2}\right)}$$

$$\overline{\mathbb{D}}_{\mathbf{p}} = \frac{\mathbb{D}_{\mathbf{p}}}{p_{Te}^{\dagger 2}/\tau_c^{\dagger}} \tag{4.14}$$

$$\overline{\mathbf{F}}_{\mathbf{p}} = \frac{\mathbf{F}_{\mathbf{p}}}{p_{Te}^{\dagger}/\tau_c^{\dagger}}$$

$$\overline{\mathcal{I}} = \frac{\mathcal{I}}{n_e^{\dagger}/\left(\tau_c^{\dagger} p_{Te}^{\dagger 3}\right)}$$

so that the equation (4.11) remains structurally identical with the normalized fields and variables. The same is true for the flux divergence expression (4.5), the flux decomposition (4.6), and the source term (4.9). The equation (4.4) becomes

$$\overline{\widetilde{f}} = \overline{C}\,\overline{p}\,\xi \frac{\partial \overline{f}_0}{\partial \overline{\psi}} \tag{4.15}$$

where we define the following normalized variable

$$\overline{C} = \frac{I(\psi) p_{Te}^{\dagger}}{eB(\psi) \psi_a} \tag{4.16}$$

From here on, all variables and fields are assumed to be normalized, and the bars above the symbols is omitted for simplicity.

## 4.2 Discretization of the kinetic equation

### 4.2.1 Grid definitions

The kinetic equations (4.11-4.15) are discretized according to the finite difference scheme with non-uniform grids. The normalized variables in these equations and corresponding spaces are

$$\begin{aligned} 0 \leq p < \infty \\ -1 \leq \xi \leq 1 \\ 0 \leq t < \infty \\ 0 \leq \psi \leq 1 \end{aligned} \tag{4.17}$$

We define the grids

| | | | |
|---|---|---|---|
| $p_i$ | $i = 0, 1, \cdots N_p$ | $p_0 = 0$ | $p_{N_p} = p_{\max} > 0$ |
| $\xi_j$ | $j = 0, 1, \cdots N_\xi$ | $\xi_0 = -1$ | $\xi_{N_\xi} = 1$ |
| $t_k$ | $k = 0, 1, \cdots N_t$ | $t_0 = 0$ | $t_{N_t} = t_{\max} > 0$ |
| $\psi_l$ | $l = -, 0, +$ | | $0 \leq \psi_- < \psi_0 < \psi_+ \leq 1$ |

(4.18)

In momentum space, the existence of internal boundary conditions ($p = 0$, $\xi = \pm 1$) requires that the flux of momentum vanishes at the corresponding boundaries. It will be demonstrated in Section 4.3 that these boundary conditions are naturally satisfied if the momentum space grid is defined with respect to the flux discretization. The grid (4.18) will be referred to as the flux grid, or full grid.

In other words, the grid (4.18), which includes boundaries, defines cells that accupy

all of the momentum space (up to $p = p_{\max}$). Naturally, the flux in momentum space must be defined on the cell boundaries. Hence, for a proper discretization of the differential operators, the distribution functions must be discretized on a intermediate grid, or half-grid. This grid is defined according to the median positions of the full grid, or center of the cells:

$$\begin{array}{|llll|} \hline p_{i+1/2} & i = 0, 1, \cdots N_p - 1 & p_{i+1/2} = \dfrac{p_{i+1} + p_i}{2} \\ \hline \xi_{j+1/2} & j = 0, 1, \cdots N_\xi - 1 & \xi_{j+1/2} = \dfrac{\xi_{j+1} + \xi_j}{2} \\ \hline \end{array} \tag{4.19}$$

The momentum space grid is shown in Fig. 4-1 where a particular cell is considered. The flux components $S_p$ and $S_\xi$ are defined on the respective cell boundaries and the distribution function is defined at the center of the cell.

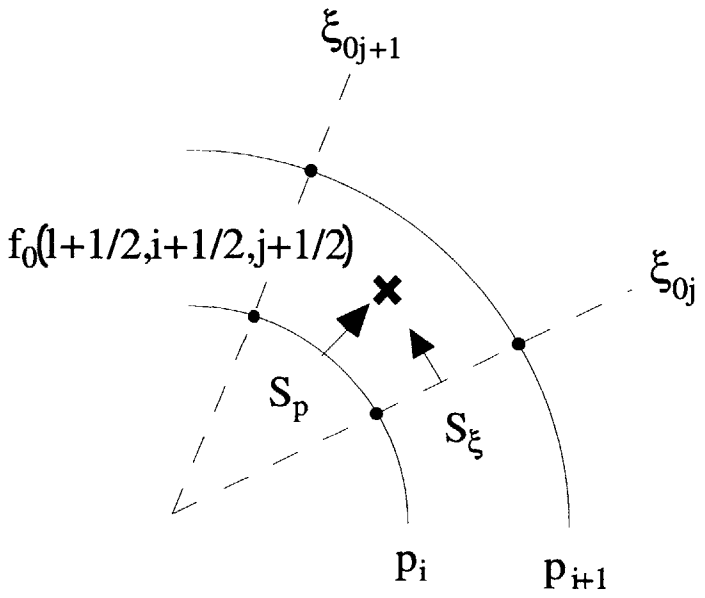


Figure 4-1: Momentum space full grid cell.

The choice of using non-uniform grids is motivated by several considerations:

- The radial and pitch-angle grids are linked through the trapped/passing boundary, which is defined by (3.41)

$$\xi_T(\psi) = \sqrt{1 - \frac{1}{\Psi_{\max}(\psi)}} \tag{4.20}$$

and the fluxes across this boundary $S_\xi$ must be defined at this location $\xi_T(\psi)$ in order to ensure the proper symmetrization (for $f_0$) or specification (for $g$) of the distribution function in the trapped region. The trapped/passing boundary is in fact another internal boundary. Therefore, all the points $\xi_{T,l} = \xi_T(\psi_l)$ must correspond to one $\xi_j$ grid point, since the fluxes are defined on the entire grid. This condition can be systematically satisfied only with a non-uniform $\xi_j$ grid.

- A better accuracy in the numerical solution of the kinetic equation can be achieved if a finer grid is used in the vicinity of internal boundaries ($p = 0$, $\xi = \pm 1$, $\xi = \xi_T(\psi)$). With non-uniform grids, a finer grid can prescribed in these vicinities while keeping a coarser grid elsewhere, such that the computing cost of improving accuracy is limited.

- Under some circumstances (for example, in LBF EBWCD), the region of momentum space where the wave-particle resonance is significant is very limited in one or both dimensions of momentum space. In that case, it is again possible to use finer grids in that region only, greatly improving accuracy while limiting the increase in computing costs.

The grid intervals associated with the half grid points are defined naturally as the full grid cell widths

$$\begin{aligned} \Delta p_{i+1/2} &= p_{i+1} - p_i \\ \Delta \xi_{j+1/2} &= \xi_{j+1} - \xi_j \end{aligned} \tag{4.21}$$

The grid intervals associated with the full grid are defined with respect to the half grid positions, such that

$$\begin{aligned} \Delta p_i &= p_{i+1/2} - p_{i-1/2} = \frac{\Delta p_{i+1/2} + \Delta p_{i-1/2}}{2} \\ \Delta \xi_j &= \xi_{j+1/2} - \xi_{j-1/2} = \frac{\Delta \xi_{j+1/2} + \Delta \xi_{j-1/2}}{2} \end{aligned} \tag{4.22}$$

### 4.2.2 Numerical differentiation in momentum space

*Divergence operator*: In the kinetic equation (4.11), the divergence operator $p^2\nabla_{\mathbf{p}}\cdot\mathbf{S_p}$ is defined on the same momentum grid as the distribution function, that is $(i+1/2, j+1/2)$. On a given flux-surface $\psi_l$ at time $t_k$ (the field dependence upon $l$ and $k$ will be kept implicit in this section) this operator is expressed as (4.5)

$$p^2\nabla_{\mathbf{p}}\cdot\mathbf{S_p}\big|_{i+1/2,j+1/2} = \left.\frac{\partial\left(p^2 S_p\right)}{\partial p}\right|_{i+1/2,j+1/2} - \frac{p_{i+1/2}}{\lambda_{j+1/2}}\left.\frac{\partial\left(\sqrt{1-\xi^2}\lambda S_\xi\right)}{\partial\xi}\right|_{i+1/2,j+1/2} \tag{4.23}$$

where the discretized differential terms naturally call for fluxes to be expressed on the full grid

$$\left.\frac{\partial}{\partial p}\left(p^2 S_p\right)\right|_{i+1/2,j+1/2} = \frac{p_{i+1}^2 S_{p,i+1,j+1/2} - p_i^2 S_{p,i,j+1/2}}{\Delta p_{i+1/2}}$$

$$\left.\frac{\partial}{\partial\xi}\left(\sqrt{1-\xi^2}\lambda S_\xi\right)\right|_{i+1/2,j+1/2} = \frac{\sqrt{1-\xi_{j+1}^2}\lambda_{j+1}S_{\xi,i+1/2,j+1} - \sqrt{1-\xi_j^2}\lambda_j S_{\xi,i+1/2,j}}{\Delta\xi_{j+1/2}} \tag{4.24}$$

*Momentum space fluxes*: They are decomposed according to (4.6). With $S_p$ defined on the full $p_i$ grid and $S_\xi$ defined on the full $\xi_j$ grid according to (4.24), we find that the flux $\mathbf{S_p}\left(f, \mathbb{D}_{\mathbf{p}}, \mathbf{F_p}\right)$ is discretized as

$$S_{p,i,j+1/2} = -D_{pp,i,j+1/2}\left.\frac{\partial f}{\partial p}\right|_{i,j+1/2} + \frac{\sqrt{1-\xi_{j+1/2}^2}}{p_i}D_{p\xi,i,j+1/2}\left.\frac{\partial f}{\partial\xi}\right|_{i,j+1/2} + F_{p,i,j+1/2}f_{i,j+1/2}$$

$$S_{\xi,i+1/2,j} = -D_{\xi p,i+1/2,j}\left.\frac{\partial f}{\partial p}\right|_{i+1/2,j} + \frac{\sqrt{1-\xi_j^2}}{p_{i+1/2}}D_{\xi\xi,i+1/2,j}\left.\frac{\partial f}{\partial\xi}\right|_{i+1/2,j} + F_{\xi,i+1/2,j}f_{i+1/2,j} \tag{4.25}$$

*Gradients*: Keeping in mind that the distribution function is defined on the half grid, the gradient terms associated with $D_{pp}$ and $D_{\xi\xi}$ are discretized in a straightfor-

ward manner

$$\left.\frac{\partial f}{\partial p}\right|_{i,j+1/2} = \frac{f_{i+1/2,j+1/2} - f_{i-1/2,j+1/2}}{\Delta p_i}$$
$$\left.\frac{\partial f}{\partial \xi}\right|_{i+1/2,j} = \frac{f_{i+1/2,j+1/2} - f_{i+1/2,j-1/2}}{\Delta \xi_j} \tag{4.26}$$

However, the discretization of $\left.\frac{\partial f}{\partial \xi}\right|_{i,j+1/2}$ and $\left.\frac{\partial f}{\partial p}\right|_{i+1/2,j}$, associated respectively with the cross terms $D_{p\xi}$ and $D_{\xi p}$, is not straightforward and has been the subject of many debates. There are at least three possible procedure.

- The first approach modifies the operator discretization (4.24) for the cross terms, by analytically differentiating the flux term, which gives

$$\left.\frac{\partial}{\partial p}\left(p\sqrt{1-\xi^2}D_{p\xi}\frac{\partial f}{\partial \xi}\right)\right|_{i+1/2,j+1/2} = \left.\frac{\partial}{\partial p}\left(p\sqrt{1-\xi^2}D_{p\xi}\right)\right|_{i+1/2,j+1/2}\left.\frac{\partial f}{\partial \xi}\right|_{i+1/2,j+1/2}$$
$$+p_{i+1/2}\sqrt{1-\xi^2_{j+1/2}}D_{p\xi,i+1/2,j+1/2}\left.\frac{\partial^2 f}{\partial p\partial \xi}\right|_{i+1/2,j+1/2}$$

$$\left.\frac{\partial\left(\sqrt{1-\xi^2}\lambda D_{\xi p}\frac{\partial f}{\partial p}\right)}{\partial \xi}\right|_{i+1/2,j+1/2} = \left.\frac{\partial\left(\sqrt{1-\xi^2}\lambda D_{\xi p}\right)}{\partial \xi}\right|_{i+1/2,j+1/2}\left.\frac{\partial f}{\partial p}\right|_{i+1/2,j+1/2}$$
$$+\sqrt{1-\xi^2_{j+1/2}}\lambda_{j+1/2}D_{\xi p,i+1/2,j+1/2}\left.\frac{\partial^2 f}{\partial p\partial \xi}\right|_{i+1/2,j+1/2} \tag{4.27}$$

  The advantage of this discretization scheme is that the cross-derivative terms $\left.\frac{\partial^2 f}{\partial p\partial \xi}\right|_{i+1/2,j+1/2}$ are all identical and defined at the center of the cell, and are thus evaluated in a completely symmetrical manner with respect to the neighboring points. The downside, however, is that the internal boundary conditions are no longer naturally satisfied for the cross terms and must be enforced.

- The second approach consists of discretizing the terms $\left.\frac{\partial f}{\partial \xi}\right|_{i,j+1/2}$ and $\left.\frac{\partial f}{\partial p}\right|_{i+1/2,j}$

according to

$$\left.\frac{\partial f}{\partial \xi}\right|_{i,j+1/2} = \frac{f_{i,j+1} - f_{i,j}}{\Delta \xi_{j+1/2}}$$
$$\left.\frac{\partial f}{\partial p}\right|_{i+1/2,j} = \frac{f_{i+1,j} - f_{i,j}}{\Delta p_{i+1/2}} \tag{4.28}$$

which has the advantage of exactly satisfying boundary conditions. However, the distribution functions are now defined at the cell corners $f_{i,j}$, and the interpolation to the neighboring half grid points is complicated and not very accurate.

- There is a third approach, which satisfies the internal boundary conditions and avoids the grid points at the cell corners. In this approach, the cross terms are discretized according to

$$\left.\frac{\partial f}{\partial \xi}\right|_{i,j+1/2} = \frac{f_{i,j+3/2} - f_{i,j-1/2}}{\Delta \xi_{j+1} + \Delta \xi_j}$$
$$\left.\frac{\partial f}{\partial p}\right|_{i+1/2,j} = \frac{f_{i+3/2,j} - f_{i-1/2,j}}{\Delta p_{i+1} + \Delta p_i} \tag{4.29}$$

With this scheme, which is chosen from now on in this work, the discretization of the operator (4.23) requires to calculate the following diffusion and convection tensors at all grid points

$$\mathbb{D}_{\mathbf{p}} : \begin{cases} D_{pp,i,j+1/2} \\ D_{p\xi,i,j+1/2} \\ D_{\xi p,i+1/2,j} \\ D_{\xi\xi,i+1/2,j} \end{cases} \qquad \mathbf{F}_{\mathbf{p}} : \begin{cases} F_{p,i,j+1/2} \\ F_{\xi,i+1/2,j} \end{cases} \tag{4.30}$$

and involves the distribution function at the half grid points and also at the following full grid points

$$\begin{cases} f_{i,j+1/2} \\ f_{i+1/2,j} \end{cases} \tag{4.31}$$

### 4.2.3 Interpolations of the distribution function

Regardless of which scheme is used for the discretization of the operator (4.23), the distribution function must be interpolated from the full grid points $(i, j+1/2)$ and $(i+1/2, j)$ to the neighboring half-grid points. An interpolation scheme for (4.31) is very generally defined in the form

$$\begin{aligned} f_{i,j+1/2} &= \left(1-\delta_{p,i,j+1/2}\right) f_{i+1/2,j+1/2} + \delta_{p,i,j+1/2} f_{i-1/2,j+1/2} \\ f_{i+1/2,j} &= \left(1-\delta_{\xi,i+1/2,j}\right) f_{i+1/2,j+1/2} + \delta_{\xi,i+1/2,j} f_{i+1/2,j-1/2} \end{aligned} \tag{4.32}$$

where the interpolation coefficients $\delta_{p,i,j+1/2}$ and $\delta_{\xi,i+1/2,j}$ are such that $0 < \delta < 1$ and must be specified.

#### Pitch-angle interpolations

The variations in the distribution as a function of the pitch-angle coordinate $\xi$ are usually relatively slow (they is no variation at all for a Maxwellian distribution) and they are locally well approximated by a linear dependence, such that the linear interpolation works well. It gives

$$\delta_{\xi,i+1/2,j} = \frac{\Delta\xi_{j+1/2}}{\Delta\xi_{j-1/2} + \Delta\xi_{j+1/2}} \tag{4.33}$$

which reduces to $\delta_{\xi,i+1/2,j} = 1/2$ for uniform $\xi$ grids.

#### Momentum interpolations

In kinetic calculations, the usual linear interpolation works very poorly in the momentum $p$ direction, because of the rapid, highly non-linear variations of the distribution function as a function of $p$ (typically close to a Maxwellian dependence $\exp\left[-p^2/2\right]$). The interpolation coefficients are indeed calculated such that the Maxwellian distribution function - which results from the effect of collisions - be the exact numerical solution in the absence of RF waves [74].

In steady-state, the operator (4.23) must vanish. In the absence of RF waves, only collisions come into play, and the solution of the equation must be isotropic by symmetry since collisions have spherical symmetry. In other words, the collisional diffusion $\mathbf{D}_{\mathbf{p}}^{\mathrm{C}}$ and convection $\mathbf{F}_{\mathbf{p}}^{\mathrm{C}}$ coefficients are independent of $\xi$. For an isotropic distribution function, the operator (4.23) reduces to $\frac{\partial}{\partial p}\left(p^2 S_p\right) = 0$ which integrates to $p^2 S_p = 0$. As it is intuitively expected for an isotropic distribution, there must be no steady state fluxes. In other words, the effects of collisional momentum drag $\mathbf{F}_{\mathbf{p}}^{\mathrm{C}}$ must compensate the effects of momentum diffusion $\mathbf{D}_{\mathbf{p}}^{\mathrm{C}}$, which gives (4.6)

$$D_{pp}^{\mathrm{C}} \frac{\partial f}{\partial p} = F_p^{\mathrm{C}} f \tag{4.34}$$

*Analytical solution*: Is easy to show that the solution of this equation is indeed a Maxwellian distribution. The collisional coefficients $D_{pp}^{\mathrm{C}}$ and $F_p^{\mathrm{C}}$ are easily related through [37]

$$D_{pp}^{\mathrm{C}} = -\frac{F_p^{\mathrm{C}}}{v} \tag{4.35}$$

so that, with $p = \gamma v$, (4.34) becomes

$$\frac{\partial f}{\partial p} = -\frac{p}{\gamma} f \tag{4.36}$$

which integrates to

$$f = f(0) \exp\left[-\int_0^p \frac{p}{\gamma} dp\right] \tag{4.37}$$

with $\gamma = \sqrt{1 + p^2 \beta_{Te}^2}$ so that the integral becomes explicitly $\int_0^p \frac{p}{\gamma} dp = \frac{(\gamma - 1)}{\beta_{Te}^2}$ so that

$$f_{\mathrm{M}}(p) = f(0) \exp\left[-\frac{(\gamma - 1)}{\beta_{Te}^2}\right] \tag{4.38}$$

and, multiplying by $(\gamma + 1)$ both the numerator and denominator

$$f_{\mathrm{M}}(p) = f(0) \exp\left[-\frac{p^2}{(\gamma + 1)}\right] \tag{4.39}$$

which is the relativistic Maxwellian distribution.

*Numerical solution*: In the following calculations, there is no dependence upon $\xi$ because the collision coefficients and the distribution function are isotropic. Therefore, the $j + 1/2$ index is kept implicit. Inserting the expressions (4.25) for the discretized fluxes and given that there is no cross term $D_{p\xi}$ for collisions, (4.34) becomes

$$D^{\mathrm{C}}_{pp,i} \left.\frac{\partial f}{\partial p}\right|_i = F^{\mathrm{C}}_{p,i} f_i \tag{4.40}$$

which reduces to

$$\gamma_i \left.\frac{\partial f}{\partial p}\right|_i = p_i f_i \tag{4.41}$$

when the relation (4.35) is used.

With the expression (4.26) for the momentum gradient and the expression (4.32) for the interpolation, this equation gives

$$-\frac{\gamma_i}{p_i}\frac{f_{i+1/2} - f_{i-1/2}}{\Delta p_i} = (1 - \delta_{p,i})\, f_{i+1/2} + \delta_{p,i} f_{i-1/2} \tag{4.42}$$

which is rewritten as

$$\delta_{p,i} = \frac{\gamma_i}{p_i \Delta p_i} - \frac{1}{\left(f_{i-1/2}/f_{i+1/2} - 1\right)} \tag{4.43}$$

Because the Maxwellian $f = f_{\mathrm{M}}$ is the exact solution of this equation, we can relate $f_{i+1/2} = f_{\mathrm{M}}\left(p_{i+1/2}\right)$ to $f_{i-1/2} = f_{\mathrm{M}}\left(p_{i-1/2}\right)$ using (4.38) as

$$f_{i+1/2} = f_{i-1/2} \exp\left[\frac{\gamma_{i-1/2} - \gamma_{i+1/2}}{\beta^2_{Te}}\right] \tag{4.44}$$

The relations (4.19) and (4.21) are combined so that

$$\begin{aligned} p_{i+1/2} &= p_i + \frac{\Delta p_{i+1/2}}{2} \\ p_{i-1/2} &= p_i - \frac{\Delta p_{i-1/2}}{2} \end{aligned} \tag{4.45}$$

and a Taylor expansion around $p = p_i$ of the gamma factors gives

$$\begin{aligned}\gamma_{i+1/2} &= \gamma_i \left[1 + \frac{p_i \Delta p_{i+1/2} \beta_{Te}^2}{2\gamma_i^2} + \frac{\left(\Delta p_{i+1/2}\right)^2 \beta_{Te}^2}{8\gamma_i^4} + \mathcal{O}\left[\left(\Delta p_{i+1/2}\right)^3 \beta_{Te}^4\right]\right] \\ \gamma_{i-1/2} &= \gamma_i \left[1 - \frac{p_i \Delta p_{i-1/2} \beta_{Te}^2}{2\gamma_i^2} + \frac{\left(\Delta p_{i-1/2}\right)^2 \beta_{Te}^2}{8\gamma_i^4} + \mathcal{O}\left[\left(\Delta p_{i-1/2}\right)^3 \beta_{Te}^4\right]\right]\end{aligned} \tag{4.46}$$

and we obtain

$$f_{i+1/2} \simeq f_{i-1/2} \exp\left[-\frac{p_i \Delta p_i}{\gamma_i} - \frac{\Delta p_i}{4\gamma_i^3}\left(\Delta p_{i+1/2} - \Delta p_{i-1/2}\right)\right] \tag{4.47}$$

Hence, the interpolation coefficient becomes

$$\delta_{p,i} = \frac{\gamma_i}{p_i \Delta p_i} - \frac{1}{\exp\left[\frac{p_i \Delta p_i}{\gamma_i} + \frac{\Delta p_i}{4\gamma_i^3}\left(\Delta p_{i+1/2} - \Delta p_{i-1/2}\right)\right] - 1} \tag{4.48}$$

$$= g\left(\frac{p_i \Delta p_i}{\gamma_i}, \frac{\Delta p_i}{4\gamma_i^3}\left(\Delta p_{i+1/2} - \Delta p_{i-1/2}\right)\right) \tag{4.49}$$

where we define the generalized Chang & Cooper interpolation function $g(x,y) = \frac{1}{x} - \frac{1}{\exp(x+y)-1}$ with the interpolation factors are $x = \frac{p_i \Delta p_i}{\gamma_i}$ and $y = \frac{\Delta p_i}{4\gamma_i^3}\left(\Delta p_{i+1/2} - \Delta p_{i-1/2}\right)$. As expected, if the intervals go to zero ($\Delta p_i \to 0$) or near the origin ($p_i \to 0$) where $\partial f_M / \partial p \to 0$, we find $\delta_{p,i} \to \frac{1}{2}$. The Chang & Cooper function $g(x,0)$ is plotted on Fig. 4-2, where we see that the interpolation can differ significantly from the value $g(0,0) = \frac{1}{2}$. For example, with a typical uniform momentum grid defined by ($p_{\max} = 20, n_p = 201$), we find $\Delta p_i = 0.1$ and therefore the maximum value for $x = \frac{p_i \Delta p_i}{\gamma_i}$ is $x_{\max} = 2$ is the non-relativistic limit, and $g(x_{\max}, 0) = 0.34$.

### 4.2.4 Discretized differential operator

With the differentiation and interpolation schemes developed in this section, the divergence operator $p^2 \nabla_{\mathbf{p}} \cdot \mathbf{S}_{\mathbf{p}}$, calculated at the half-grid point $(i+1/2, j+1/2)$ by (4.23), can be expressed as a function of $f_{i+1/2,j+1/2}$ and the eight neighboring points,

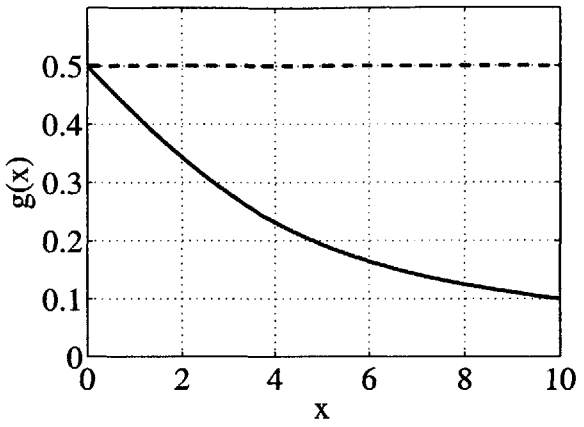


Figure 4-2: Chang & Cooper function $g(x)$.

such that we can define

$$p^2 \nabla_{\mathbf{p}} \cdot \mathbf{S}_{\mathbf{p}}\big|_{i+1/2,j+1/2} = \sum_{i'=i-1}^{i'=i+1} \sum_{j'=j-1}^{j'=j+1} M_{i'+1/2,j'+1/2} f_{i'+1/2,j'+1/2} \tag{4.50}$$

The coefficients $M_{i'+1/2,j'+1/2}$ are given in Appendix C.

Note that near the boundaries of momentum space, this differentiation scheme calls for the value of the distribution function that are outside the boundaries, for example at the point $(-1/2, j)$. Fortunately, the value of $f$ at these points is known by symmetry, which in fact leads to boundary conditions on the momentum flux such that the value of $f$ outside boundaries will not be used. More details are given in Section 4.3.

### 4.2.5 Radial differentiation

In order to calculate the distribution function $\widetilde{f}$ on the flux surface $\psi_0$, the distribution function $f_0$ is calculated at the position $\psi_0$ as well as on two neighboring flux-surfaces $\psi_-$ and $\psi_+$ with $\psi_- < \psi_0 < \psi_+$, such that $\widetilde{f}$ can be obtained from performing a

numerical radial derivative according to (4.4)

$$\widetilde{f}(\psi_0) = \frac{I(\psi_0)\, p\xi}{eB(\psi_0)} \left.\frac{\partial f_0}{\partial \psi}\right|_{\psi=\psi_0} \tag{4.51}$$

A parabolic interpolation of the form $y = a\psi^2 + b\psi + c$ is used to calculate the radial derivative $\dfrac{dy}{d\psi} = 2a\psi + b$. The coefficients $a, b$ and $c$ are determined from the values $y_-, y_0$ and $y_+$ at the respective radial grid points $\psi_-, \psi_0$ and $\psi_+$, which is written in matrix form as

$$\begin{pmatrix} y_- \\ y_0 \\ y_+ \end{pmatrix} = \mathbb{V} \cdot \begin{pmatrix} c \\ b \\ a \end{pmatrix} \tag{4.52}$$

where $\mathbb{V}$ is a Van der Monde matrix of order 3

$$\mathbb{V} = \begin{pmatrix} 1 & \psi_- & \psi_-^2 \\ 1 & \psi_0 & \psi_0^2 \\ 1 & \psi_+ & \psi_+^2 \end{pmatrix} \tag{4.53}$$

which can be inverted to

$$\mathbb{V}^{-1} = \frac{1}{\det(\mathbb{V})} \begin{pmatrix} \Delta\psi_+\psi_0\psi_+ & -\Delta\psi_0\psi_-\psi_+ & \Delta\psi_-\psi_0\psi_- \\ -\Delta\psi_+(\psi_0+\psi_+) & \Delta\psi_0(\psi_-+\psi_+) & -\Delta\psi_-(\psi_0+\psi_-) \\ \Delta\psi_+ & -\Delta\psi_0 & \Delta\psi_- \end{pmatrix} \tag{4.54}$$

where we defined

$$\begin{aligned} \Delta\psi_+ &= \psi_+ - \psi_0 \\ \Delta\psi_- &= \psi_0 - \psi_- \\ \Delta\psi_0 &= \psi_+ - \psi_- = \Delta\psi_+ - \Delta\psi_- \end{aligned} \tag{4.55}$$

Using $\left.\dfrac{dy}{d\psi}\right|_{\psi=\psi_0} = 2a\psi_0 + b$, one finds

$$\left.\frac{dy}{d\psi}\right|_{\psi=\psi_0} = \frac{1}{\det(\mathbb{V})}\left(-\Delta\psi_+^2 y_- + \Delta\psi_0(\Delta\psi_+ - \Delta\psi_-)\, y_0 + \Delta\psi_-^2 y_+\right) \tag{4.56}$$

with the determinant

$$\det(\mathbb{V}) = \Delta\psi_-\Delta\psi_0\Delta\psi_+ \tag{4.57}$$

This differentiation scheme is thus applied to (4.51) with

$$\left.\frac{\partial f_0}{\partial\psi}\right|_{\psi=\psi_0} = -\frac{\Delta\psi_+}{\Delta\psi_0\Delta\psi_-}f_0(\psi_-) + \frac{(\Delta\psi_+ - \Delta\psi_-)}{\Delta\psi_+\Delta\psi_-}f_0(\psi_0) + \frac{\Delta\psi_-}{\Delta\psi_0\Delta\psi_+}f_0(\psi_+) \tag{4.58}$$

For a uniform radial grid, $\Delta\psi_+ = \Delta\psi_-$ and this expression reduces to $\left.\frac{\partial f_0}{\partial\psi}\right|_{\psi=\psi_0} = \frac{f_0(\psi_+) - f_0(\psi_-)}{\psi_+ - \psi_-}$.

### 4.2.6 Numerical integration in momentum space

Numerical integration in momentum space is required in the calculation of:

- the discretized diffusion tensor and convection vector elements listed in (4.30), which enter the coefficients $M_{i'+1/2,j'+1/2}$,
- the operators $\mathcal{I}(f)$ and $\widetilde{\mathcal{I}}\left(\widetilde{f}\right)$ in (4.8-4.9),
- the moments of the distribution function such as the current and the density of power absorbed.

The calculation of these terms only involves algebraic expressions and numerical integrations. The corresponding discretized expressions are not reported in this thesis, but can be found in the extensive report [73] on the *DKE* code. However, the numerical integration in momentum space is described here for the general case.

For a given discretized momentum space variable $x_k$ - which represents either $p_i$ or $\xi_j$ - the integration domain can be bounded by full grid positions $(x_{k\,\min}, x_{k\,\max})$ - this includes integration over the entire spaces $(x_0, x_{n_x})$ and integration up to the trapped/passing boundary, which is a full grid position in pitch–angle - or by half grid positions $\left(x_{k\,\min+1/2}, x_{k\,\max+1/2}\right)$, or by a compination of the two. The integrals are evaluated numerically using the trapezoidal method, according to the following schemes:

- If $F$ is discretized on the half-grid $F_{k+1/2} = F\left(x_{k+1/2}\right)$

$$\begin{aligned}
&\int_{x_{k\,\min}}^{x_{k\,\max}} F(x)\ dx \Longrightarrow \sum_{k=k\,\min}^{k\,\max-1} F_{k+1/2}\Delta x_{k+1/2} \\
&\int_{x_k}^{x_{k+1/2}} F(x)\ dx \Longrightarrow \frac{\Delta x_{k+1/2}}{2} F_{k+1/2} \\
&\int_{x_{k-1/2}}^{x_k} F(x)\ dx \Longrightarrow \frac{\Delta x_{k-1/2}}{2} F_{k-1/2}
\end{aligned} \tag{4.59}$$

- If $F$ is discretized on the full grid $F_k = F(x_k)$

$$\begin{aligned}
&\int_{x_{k\,\min-1/2}}^{x_{k\,\max+1/2}} F(x)\ dx \Longrightarrow \sum_{k=k\,\min}^{k\,\max} F_k \Delta x_k \\
&\int_{x_k}^{x_{k+1/2}} F(x)\ dx \Longrightarrow \frac{\Delta x_{k+1/2}}{2} F_k \\
&\int_{x_{k-1/2}}^{x_k} F(x)\ dx \Longrightarrow \frac{\Delta x_{k-1/2}}{2} F_k
\end{aligned} \tag{4.60}$$

Note that when the expression for $F(x)$ is only an explicit function of $x$, the grid $x_k$ does not have to be any of the grids defined for the flux and distribution function in (4.18) and (4.19) respectively. Instead, a much finer grid can be used to calculate the integrals more accurately. This is the case for the collision integrals defined in (3.169-3.170). However, when $F(x)$ depends upon the distribution function - like in the moment integrals or the operators $\mathcal{I}(f)$ and $\widetilde{\mathcal{I}}\left(\vec{f}\right)$ - the grid (4.18) must be used.

## 4.3 Initial and Boundary Conditions

### 4.3.1 Initial conditions

The initial value for the zero-order distribution function $f_0$ is chosen to be the relativistic Maxwellian, which is the exact solution of the Fokker-Planck equation (4.2-a) in the absence of RF field. Using the expression (B.118), derived in Appendix B, and using the normalization procedure of Section 4.1.3, the relativistic Maxwellian is

expressed as

$$f_{\mathrm{M}}(p,\psi) = \frac{n_e(\psi)}{(2\pi)^{3/2} T_e^{3/2}(\psi)} R\left(T_e(\psi)\beta_{Te}^{\dagger 2}\right) \exp\left[-\frac{p^2}{(\gamma+1)T_e(\psi)}\right] \tag{4.61}$$

with

$$\begin{aligned} \beta_{Te}^{\dagger} &= \sqrt{\frac{T_e^{\dagger}}{m_e c^2}} \\ \gamma(p) &= \sqrt{1+p^2\beta_{Te}^{\dagger 2}} \end{aligned} \tag{4.62}$$

and where $R(x)$ is given by (B.119) with the approximate form (B.120) $R(x) = \left[1+\frac{15x}{8}+\frac{105}{128}x^2+\mathcal{O}(x^3)\right]$.

The initial value for the first-order distribution function $g$ can be chosen to be identically zero, since there is a driving source term in the drift-kinetic equation (4.2-b). However, the convergence to a steady-state can be greatly increased with using the approximate analytical solution obtained in the absence of RF waves and in the Lorentz limit $Z_i \gg 1$ where pitch-angle scattering with ions is the dominant collisional process. This solution is developed in Ref. [73].

### 4.3.2 Internal boundary conditions

The internal boundaries - apart from the trapped/passing boundary, which is treated separately in the next section - correspond to the axes or planes of symmetry of the system. In the gyro-averaged momentum space, the direction of the magnetic field is an axis of symmetry. In spherical coordinates, this axis is defined by the following position of momentum space (4.17): $p = 0$, $\xi = -1$ and $\xi = 1$. Therefore, by cylindrical symmetry of momentum space, there is no flux of momentum through this axis. This condition is intrinsically verified in the expression divergence (4.5) of the divergence operator

$$\nabla_{\mathbf{p}} \cdot \mathbf{S}_{\mathbf{p}} = \frac{1}{p^2}\frac{\partial}{\partial p}\left(p^2 S_p\right) - \frac{1}{\lambda p}\frac{\partial}{\partial \xi}\left(\sqrt{1-\xi^2}\lambda S_\xi\right) \tag{4.63}$$

since $p^2 S_p$ and $\sqrt{1-\xi^2}\lambda S_\xi$ naturally vanish at $p = 0$ and $|\xi| = 1$ respectively. In order to ensure that the internal boundary conditions are numerically satisfied, it was chosen to discretize the flux on the full grid - which includes these boundaries. Indeed, the discretization of the divergence operator (4.23) using (4.24) at the internal limits of momentum space $i = 0$, $j = 0$, $j = n_\xi$ - corresponding to $p = 0$, $\xi = -1$ and $\xi = 1$ - respectively involves the following flux contributions on the internal boundaries

$$\begin{aligned} & p_0^2 S_{p,0,j+1/2} = 0 \\ & \sqrt{1-\xi_0^2}\lambda_0 S_{\xi,i+1/2,0} = 0 \\ & \sqrt{1-\xi_{n_\xi}^2}\lambda_{n_\xi} S_{\xi,i+1/2,n_\xi} = 0 \end{aligned} \tag{4.64}$$

which vanish because $p_0 = 0$, $\xi_0 = -1$ and $\xi_{n_\xi} = 1$. The internal boundary conditions are thus intrinsically satisfied with this discretization scheme. Consequently, in the discretization (4.50) of the differential operator at the limits $i = 0$, $j = 0$, $j = n_\xi$, it is not necessary to evaluate the distribution function at the neighboring points outside the boundaries, because the identities (4.64) cancel their contribution. It is easy to verify from the expressions developed in Appendix C that the elements $\left(M_{-1/2,j-1/2}, M_{-1/2,j+1/2}, M_{-1/2,j+3/2}\right)$, $\left(M_{i-1/2,-1/2}, M_{i+1/2,-1/2}, M_{i+3/2,-1/2}\right)$, and $\left(M_{i-1/2,n_\xi+1/2}, M_{i+1/2,n_\xi+1/2}, M_{i+1/2,n_\xi+1/2}\right)$ are identically zero.

Note that in other schemes used in kinetic theory, where the distribution function is specified on the full grid rather than the fluxes, extra points must be added outside the boundaries to numerically satisfied the boundary conditions.

### 4.3.3 Trapped/passing boundary

#### Distribution function $f_0$

In the low collisionality regime, which is assumed through this work, the bounce time of trapped electrons is much shorter than the collisions and RF diffusion times. Therefore, a trapped electron with momentum $(p, \xi)$ (with $|\xi| < \xi_T$) - as it crosses the outboard horizontal midplane - bounces back before undergoing any significant change of momentum due to collisions or RF diffusion, such that after one bounce time, it

crosses the same midplane with momentum $(p, -\xi)$. As a consequence, trapped electrons with $(p, \xi)$ and $(p, -\xi)$ are completely equivalent, and the distribution function $f_0$ is symmetric in the trapped region, which is also obtained from equation (3.113).

When solving the bounce-averaged Fokker-Planck equation (4.2-a), it must be ensured that $f_0$ is symmetric in the trapped region. This condition can in fact be systematically satisfied implicitly in the differential operator, following the prescription by [48]. Because trapped electrons with $(p, \xi)$ and $(p, -\xi)$ are completely equivalent, the equation (4.2-a) is solved only for one half of the trapped region $0 \leq \xi \leq \xi_T$ while the other half is removed from the numerical momentum space. After the distribution function is calculated on the reduced momentum space, it is extended to the full space by symmetry.

The reduced momentum space for the calculation of $f_0$ is illustrated in Fig. 4-3 where the following points are considered

| | | |
|---|---|---|
| 1 | $(i+1/2, j_T^+ - 1/2)$ | last point in the right half trapped region |
| 2 | $(i+1/2, j_T^+ + 1/2)$ | first point in the co-passing region |
| 3 | $(i+1/2, j_T^- + 1/2)$ | first point in the left half trapped region |
| 4 | $(i+1/2, j_T^- - 1/2)$ | last point in the counter-passing region |
| 5 | $(i+1/2, j_0 + 1/2)$ | first point in the right half trapped region |

(4.65)

where the indices $j_T^+$, $j_T^-$ and $j_0$ are defined such that $\xi_{j_T^+} = \xi_T$, $\xi_{j_T^-} = -\xi_T$ and $\xi_{j_0} = 0$ Note that the (non-uniform) pitch-angle grid was symmetric and defined such that $\xi_T$ and $-\xi_T$ correspond to full grid points.

This scheme requires to consider the fluxes through the trapped/passing boundary carefully. In fact, by reducing momentum space, it is necessary to account implicitly for links between points 4 and 3 by linking 4 to 1. The differential expression (4.50) is modified at the points 1→5 to account for this procedure:

- *Point 5*: By symmetry in the trapped region, the fluxes through the $\xi = 0$ axis must vanish, since $f_{i+1/2,j_0+1/2} = f_{i+1/2,j_0-1/2}$. The point 5 is linked to itself on

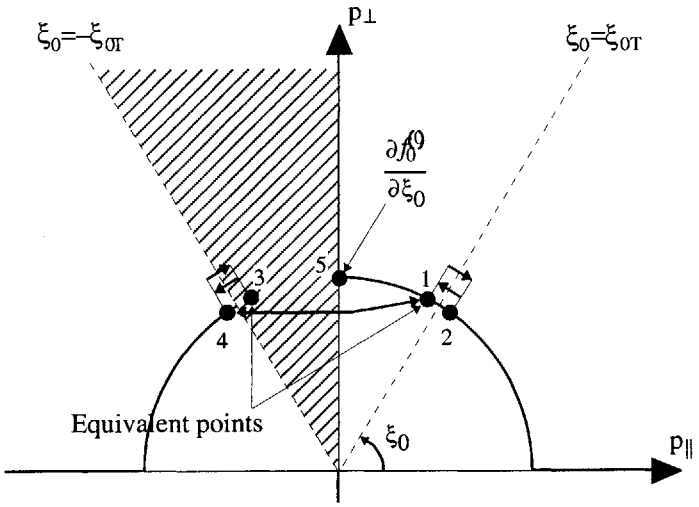


Figure 4-3: Reduced momentum space for the calculation of $f_0$.

the left

$$p^2\nabla_{\mathbf{p}}\cdot\mathbf{S}_{\mathbf{p}}\big|_{i+1/2,j_0+1/2} = \sum_{i'=i-1}^{i'=i+1} M_{i'+1/2,j_0+3/2} f_{i'+1/2,j_0+3/2} + \left(M_{i'+1/2,j_0-1/2} + M_{i'+1/2,j_0+1/2}\right) f_{i'+1/2,j_0+1/2} \tag{4.66}$$

- *Point 4*: Since points 1 and 3 are equivalent, we can replace the link between points 4 and 3 by linking 4 to 1 on the right

$$p^2\nabla_{\mathbf{p}}\cdot\mathbf{S}_{\mathbf{p}}\big|_{i+1/2,j_T^- -1/2} = \sum_{i'=i-1}^{i'=i+1} M_{i'+1/2,j_T^- -3/2} f_{i'+1/2,j_T^- -3/2} + M_{i'+1/2,j_T^- -1/2} f_{i'+1/2,j_T^- -1/2} + M_{i'+1/2,j_T^- +1/2} f_{i'+1/2,j_T^+ -1/2} \tag{4.67}$$

where the last term is the link to point 1 $f_{i'+1/2,j_T^+ -1/2}$.

- *Point 1*: Since points 1 and 3 are equivalent, we can replace the link between

points 3 and 4 by linking 1 to 4 on the right.

$$p^2\nabla_{\mathbf{p}}\cdot\mathbf{S}_{\mathbf{p}}\big|_{i+1/2,j_T^+-1/2}$$

$$=\sum_{i'=i-1}^{i'=i+1} M_{i'+1/2,j_T^+-3/2}f_{i'+1/2,j_T^+-3/2}+M_{i'+1/2,j_T^+-1/2}f_{i'+1/2,j_T^+-1/2} \tag{4.68}$$

$$+\sum_{i'=i-1}^{i'=i+1}\frac{M_{i'+1/2,j_T^++1/2}}{2}\left(f_{i'+1/2,j_T^++1/2}+f_{i'+1/2,j_T^--1/2}\right) \tag{4.69}$$

where the last term is the link to point 4 $f_{i'+1/2,j_T^--1/2}$. Note that only half of the flux from the right is accounted for - since the rest implicitly goes to the equivalent point 3.

- *Point 2*: The discretization at point 2 remains unchanged.

### Distribution function $g$

The distribution function $g$ is defined as being identically zero in the trapped region. In that case, the equation (4.2-b) is solved only in the passing region$|\xi|\geq\xi_T$. After the distribution function is calculated on the reduced momentum space, it is extended to the full space by setting $g\left(-\xi_T<\xi<\xi_T\right)=0$.

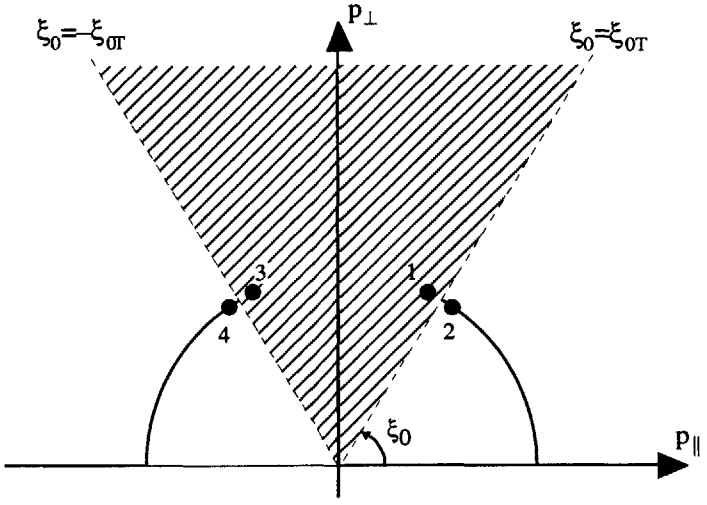


Figure 4-4: Reduced momentum space for the calculation of $g$.

The reduced momentum space for the calculation of $f_0$ is illustrated in Fig. 4-4. In

that case, there is simply no momentum flux through the trapped passing boundary. The differential expression (4.50) is modified at the points 2 and 4 to account for this procedure:

- *Point 4*: We have $f_{i+1/2,j_T^- +1/2} = 0$ because this correcponds to points 3, which is in the trapped region. We have then only

$$p^2 \nabla_{\mathbf{p}} \cdot \mathbf{S}_{\mathbf{p}}\big|_{i+1/2,j_T^- -1/2} = \sum_{i'=i-1}^{i'=i+1} M_{i'+1/2,j_T^- -3/2} f_{i'+1/2,j_T^- -3/2} + M_{i'+1/2,j_T^- -1/2} f_{i'+1/2,j_T^- -1/2} \tag{4.70}$$

- *Point 2*: We have $f_{i+1/2,j_T^+ -1/2} = 0$ because this correcponds to points 1, which is in the trapped region. We have then only

$$p^2 \nabla_{\mathbf{p}} \cdot \mathbf{S}_{\mathbf{p}}\big|_{i+1/2,j_T^+ +1/2} = \sum_{i'=i-1}^{i'=i+1} M_{i'+1/2,j_T^+ +3/2} f_{i'+1/2,j_T^+ +3/2} + M_{i'+1/2,j_T^+ +1/2} f_{i'+1/2,j_T^+ +1/2} \tag{4.71}$$

### 4.3.4 External boundary conditions

The upper limit $p_{\max}$ in momentum space is a numerical approximation because the physical space goes to $p \to \infty$. The limit $p_{\max}$ must be chosen such that the relevant physics be fully included. The condition $p_{\max} \gg 1$ is necessary in order to account for the quasi-totality of the particles for a Maxwellian distribution $\propto \exp\left[\frac{-p^2}{\gamma+1}\right]$. In order to conserve particles in the numerical scheme, the fluxes through the external boundary must be set to zero, by artificially setting $f_{n_p+1/2,j+1/2} = f_{n_p-1/2,j+1/2}$. This leads to the discretization scheme

$$\begin{aligned} p^2 \nabla_{\mathbf{p}} \cdot \mathbf{S}_{\mathbf{p}}\big|_{n_p+1/2,j+1/2} = & \sum_{j'=j-1}^{j'=j+1} M_{n_p-1/2,j'+1/2} f_{n_p-1/2,j'+1/2} \\ & + \left(M_{n_p+1/2,j'+1/2} + M_{n_p+3/2,j'+1/2}\right) f_{n_p+1/2,j'+1/2} \end{aligned} \tag{4.72}$$

## 4.4 Algorithm

### 4.4.1 Relaxation to a steady-state

In order let the equation (169)

$$\frac{\partial f}{\partial t} + \nabla_{\mathbf{p}} \cdot \mathbf{S}_{\mathbf{p}} \left( f, \mathbb{D}_{\mathbf{p}}, \mathbf{F}_{\mathbf{p}} \right) = \mathcal{I}\left( f \right) + \mathcal{S} \tag{4.73}$$

relax to a steady-state, an implicit time scheme is used. In that case, the time derivative is discretized as

$$\left. \frac{\partial f}{\partial t} \right|^{k+1} = \frac{f^{k+1} - f^{k}}{\Delta t} \tag{4.74}$$

An implicit method is used because in that case there is no fundamental limitation on the time step $\Delta t$ for this scheme to be stable, as opposed to explicit schemes (where $\frac{\partial f}{\partial t}$ is evaluated at the time step $k$) for which the maximum stable time step is related to the momentum grid size.

The integral term $\mathcal{I}\left( f \right)$, however, must be treated explicitly. In that case, the stability of the scheme can no longer be ensured, and a limitation exist on the maximum time step $\Delta t$ that can be used. Fortunately, the term $\mathcal{I}\left( f \right)$ is a small correction to the distribution function, such that in practice, a large step $\Delta t \gg 1$ can be used and the equation (4.10) converges whithin a few iteractions.

Note that it is possible to make full use of the implicit time scheme - and large time step $\Delta t$ - only if the symmetrization of the trapped region is ensured implicitly, as it is done in this code. In other codes where the symmetrization is explicit, a time step $\Delta t \lesssim 1$ must be used and the equation converges only after hundreds or thousands of iterations. The present implicit scheme thus reduces computational time by orders of magnitude.

The discretized form of equation (4.10) becomes

$$\begin{aligned} &\frac{f^{k+1}_{i+1/2,j+1/2} - f^{k}_{i+1/2,j+1/2}}{\Delta t} + \nabla_{\mathbf{p}} \cdot \mathbf{S}_{\mathbf{p}} |^{k+1}_{i+1/2,j+1/2} \\ &= \mathcal{I}\left( f^{k}_{i+1/2,j+1/2} \right) + \mathcal{S}_{i+1/2,j+1/2} \end{aligned} \tag{4.75}$$

where the $(i, j)$ indices refer to the reduced momentum space (with $n_p$ momentum and $n'_\xi$ pitch-angle grid steps), according to the procedure detailed in Section 4.3.3.

### 4.4.2 Matrix representation of the kinetic equation

As explained in Section 4.1.2, this equation is multiplied by $p^2$ to avoid singularities in $p = 0$. Using the discretized differentiation scheme developed in Section 4.2 and modified for the reduced momentum space in Section 4.3.3, we can rewrite the divergence operator in vector form as

$$p^2 \nabla_{\mathbf{p}} \cdot \mathbf{S}_{\mathbf{p}} \Big|^{k+1} = \mathbb{M} \cdot \mathbf{f}^{k+1} \tag{4.76}$$

where $\mathbf{f}^{k+1}$ is a vector of $n_p \times n'_\xi$ elements made of the discretized values of the distribution $f^{k+1}_{i+1/2,j+1/2}$, and organized as follows

$$\mathbf{f}^{k+1} = \begin{pmatrix} f^{k+1}_{1/2,1/2} \\ \vdots \\ f^{k+1}_{1/2,j+1/2} \\ \vdots \\ f^{k+1}_{1/2,n'_\xi-1/2} \\ f^{k+1}_{3/2,1/2} \\ \vdots \\ \vdots \\ f^{k+1}_{i+1/2,j+1/2} \\ \vdots \\ \vdots \\ f^{k+1}_{n_p-1/2,n'_\xi-1/2} \end{pmatrix} \tag{4.77}$$

and $\mathbb{M}$ is a matrix made of the elements $M_{i'+1/2,j'+1/2}$ in (4.50). These elements are arranged in diagonals in $\mathbb{M}$. For example, $M_{i+1/2,j+1/2}$ is the main diagonal, $M_{i+1/2,j-1/2}$ is the first lower diagonal, $M_{i-1/2,j+1/2}$ is the $n^{\text{th}}_\xi$ lower disgonal, etc.

Hence, the nine-point scheme presented in Section 4.2 leads a nine diagonals in the matrix $\mathbb{M}$. In addition, the implicit symmetrization of the trapped region requires to connect additional points, according to the procedure detailed in Section 4.3.3. The fluxes at the trapped/passing boundary thus results in an additional six diagonals, such that the differentiation matrix $\mathbb{M}$ finally contains 15 diagonals.

In vector form, the equation (4.75) (multiplied by $p^2$) can be expressed as

$$\left(\frac{\mathbb{P}}{\Delta t} + \mathbb{M}\right) \cdot \mathbf{f}^{k+1} = \frac{\mathbb{P} \cdot \mathbf{f}^k}{\Delta t} + \mathbb{P} \cdot \mathbf{I}\left(\mathbf{f}^k\right) + \mathbb{P} \cdot \mathbf{S} \tag{4.78}$$

where $\mathbb{P}$ is the diagonal matrix corresponding to the discretization of $p^2$.

### 4.4.3 Inversion of the linear equation

The equation (4.78) can be rewritten in a compact form as

$$\mathbb{A} \cdot \mathbf{f}^{k+1} = \mathbf{B}^k \tag{4.79}$$

which is a linear equation and must be inverted. Here, $\mathbb{A} = \frac{\mathbb{P}}{\Delta t} + \mathbb{M}$ and $\mathbf{B}^k = \frac{\mathbb{P} \cdot \mathbf{f}^k}{\Delta t} + \mathbb{P} \cdot \mathbf{I}\left(\mathbf{f}^k\right) + \mathbb{P} \cdot \mathbf{S}$. In order to potimize the numerical accuracy of the inversion process, the equation (4.79) is pre-conditioned such that all the coefficients of the main diagonal of $\mathbb{A}$ are 1. This is done by multiplying Eq. (4.79) by $\mathbb{C}^{-1}$ where $\mathbb{C}$ is the diagonal matrix made of the main diagonal of $\mathbb{A}$. Defining $\mathbb{A}' = \mathbb{C}^{-1} \cdot \mathbb{A}$ and $\mathbf{B}^{k\prime} = \mathbb{C}^{-1} \cdot \mathbf{B}^k$, we finally obtain the equation

$$\mathbb{A}' \cdot \mathbf{f}^{k+1} = \mathbf{B}^{k\prime} \tag{4.80}$$

The matrix $\mathbb{A}'$ is a mostly sparse matrix with only zeros except on the main diagonal, where elements are identically one, and on 14 off axis diagonals that made of elements with an absolute value between zero and one.

This equation is inverted by LU factorization, such that

$$\mathbb{A}' = \mathbb{L} \cdot \mathbb{U} \tag{4.81}$$

where $\mathbb{L}$ is a lower triangular matrix and $\mathbb{U}$ is a higher triangular matrix. The equation then reduces to the two systems

$$\begin{aligned} \mathbf{V}^{k+1} &= \mathbb{L}^{-1} \cdot \mathbf{B}^{k\prime} \\ \mathbf{f}^{k+1} &= \mathbb{U}^{-1} \cdot \mathbf{V}^{k+1} \end{aligned} \tag{4.82}$$

which are solved in order.

Although the matrix $\mathbb{A}'$ is made of only 15 non-zero diagonals, the factorization matrices $\mathbb{L}$ and $\mathbb{U}$ have far more non-zero elements, and require a large amount of computer memory. In order to limit the use of computer resources - or alternatively to extend the limits of anageable grid size - an approximate factorization procedure, called incomplete LU factorization, is used. In that case, all elements of the L and U matrices that are below some threshold $\delta_{LU}$ are discarded. Hence, only an approximate form of the equation (4.80) is solved. The procedure is iterated until the approximate solution $\mathbf{f}^{k+1}$ satisfies (4.80) within some predefined tolerance. This method allows a very significant gain in memory requirements, with only a slight increase in computation time.

## 4.5 Numerical Calculation of Bounce Integrals

The numerical calculation of bounce-averaging coefficients such as the normalized bounce time (3.81) and the generalized coefficients (3.87-3.88) requires an integration over the poloidal angle $\theta$ which can be expressed symbolically as

$$I(\psi, \xi_0) = \int_{\theta_{\min}}^{\theta_{\max}} \frac{d\theta}{2\pi} F(\psi, \theta, \xi_0; B_R, B_Z, B_\phi, R, Z) \tag{4.83}$$

where $B_R, B_Z, B_\phi, R, Z$ are functions of $(\psi, \theta)$. They are given on a uniform grid of $N_\theta$ points in $\theta$

$$\theta_j = \frac{2\pi j}{N_\theta - 1}, \; j = 0, 1, \cdots, N_\theta - 1 \tag{4.84}$$

### 4.5.1 Domain of Integration

For trapped electrons, it is important to account for the entire bounce path of the particle, including in particular the tip of banana orbits near $\theta_{T\,\min}$ and $\theta_{T\,\max}$. The contribution of these banana tips is often larger than the $d\theta = 2\pi/(N_\theta - 1)$ grid accuracy level, because $F(\theta)$ can become very large near the turning points. This is true for example in the calculation of $\lambda$, since $F(\theta) \sim 1/\xi$ and $\xi \to 0$ at the turning points. It is therefore necessary to perform the integration up to $\theta_{T\,\min}$ and $\theta_{T\,\max}$. However, these turning points are defined by (3.42)

$$B(\psi, \theta_T) = B_b(\psi, \xi_0) \equiv \frac{B_0(\psi)}{1 - \xi_0^2} \tag{4.85}$$

which in general do not coincide with any grid points in $\theta$. In order to calculate $\theta_T$, the equation (4.85) is solved by imposing that the fields $B_R, B_Z, B_\phi, R, Z$, which are given on the $(\psi, \theta)$ grid, be evaluated in $\theta_T$ by linear interpolation, while the value of $B(\psi, \theta_T)$ is obtained from (3.11)

$$B = \|\mathbf{B}\| = \sqrt{B_R^2 + B_Z^2 + B_\phi^2} \tag{4.86}$$

It is assumed that the magnetic field $B_b(\psi, \xi_0)$ at the turning point $\theta_{T\,\min}$ is located between the two (consecutive) values $B_1(\psi, \theta_1)$ and $B_2(\psi, \theta_2)$ on the $(\psi, \theta)$ grid. These values are determined from the data $B_R, B_Z, B_\phi$ (typically calculated by the equilibrium code) by (4.86)

$$\begin{aligned} B_1(\psi, \theta_1) &= \sqrt{B_R^2(\psi, \theta_1) + B_Z^2(\psi, \theta_1) + B_\phi^2(\psi, \theta_1)} \\ B_2(\psi, \theta_2) &= \sqrt{B_R^2(\psi, \theta_2) + B_Z^2(\psi, \theta_2) + B_\phi^2(\psi, \theta_2)} \end{aligned} \tag{4.87}$$

We chose to define the values of $B_R$, $B_Z$ and $B_\phi$ at the location $\theta_T$ by linear interpo-

lation

$$B_i(\psi, \theta_T) = B_{i1} + \frac{(\theta_T - \theta_1)}{(\theta_2 - \theta_1)}(B_{i2} - B_{i1}) \tag{4.88}$$

where $i = R, Z, \phi$. Then, the location $\theta_T$ of the turning point can be calculated according to the relation (4.85) which implies, using (4.86)

$$B_R^2(\psi, \theta_T) + B_Z^2(\psi, \theta_T) + B_\phi^2(\psi, \theta_T) = B_b^2(\psi, \xi_0) \tag{4.89}$$

such that the equation for $\theta_T$ is

$$\sum_{i=R,Z,\phi} \left[ B_{i1} + \frac{(\theta_T - \theta_1)}{(\theta_2 - \theta_1)}(B_{i2} - B_{i1}) \right]^2 - B_b^2(\psi, \xi_0) = 0 \tag{4.90}$$

Defining

$$\alpha = \frac{(\theta_T - \theta_1)}{(\theta_2 - \theta_1)} \tag{4.91}$$

one obtains

$$\left[ \sum_{i=R,Z,\phi} (B_{i2} - B_{i1})^2 \right] \alpha^2 + 2 \left[ \sum_{i=R,Z,\phi} B_{i1}(B_{i2} - B_{i1}) \right] \alpha + \sum_{i=R,Z,\phi} B_{i1}^2 - B_b^2(\psi, \xi_0) = 0 \tag{4.92}$$

which solves as

$$\alpha = \frac{\pm\sqrt{\left[\sum_i B_{i1}(B_{i2} - B_{i1})\right]^2 - \left[\sum_i (B_{i2} - B_{i1})^2\right]\left[\sum_i B_{i1}^2 - B_b^2\right]} - \sum_i B_{i1}(B_{i2} - B_{i1})}{\sum_i (B_{i2} - B_{i1})^2} \tag{4.93}$$

The square root transforms as

$$\begin{aligned} &\sqrt{\left[\sum_i B_{i1}(B_{i2} - B_{i1})\right]^2 - \left[\sum_i (B_{i2} - B_{i1})^2\right]\left[\sum_i B_{i1}^2 - B_b^2(\psi, \xi_0)\right]} \\ &= \sqrt{(Y - B_b^2)^2 - (B_b^2 - B_1^2)(B_b^2 - B_2^2)} \end{aligned} \tag{4.94}$$

with the definition

$$Y = B_{R1}B_{R2} + B_{Z1}B_{Z2} + B_{\phi 1}B_{\phi 2} \tag{4.95}$$

so that

$$\alpha_b = \frac{\pm\sqrt{\left(Y - B_b^2\right)^2 - \left(B_b^2 - B_1^2\right)\left(B_b^2 - B_2^2\right)} + B_1^2 - Y}{B_1^2 + B_2^2 - 2Y} \tag{4.96}$$

and finally

$$\theta_T = \theta_1 + (\theta_2 - \theta_1)\frac{B_1^2 - Y \pm \sqrt{\left(Y - B_b^2\right)^2 - \left(B_b^2 - B_1^2\right)\left(B_b^2 - B_2^2\right)}}{B_1^2 + B_2^2 - 2Y} \tag{4.97}$$

The (unique) solution that gives $0 \leq \alpha_b \leq 1$ must be chosen. Note that if the magnetic fields in points 1 and 2 are equal, we have $Y = B_1^2 = B_2^2 = B_b^2$.

### 4.5.2 Numerical Integration

The two turning points are added to the $\theta$ grid, now noted $\widetilde{\theta}_j$, $j = 0, 1, 2, \cdots N_\theta + 1$, and we define the half grid

$$\overline{\theta}_k = \frac{\left(\widetilde{\theta}_{k+1} + \widetilde{\theta}_k\right)}{2},\ k = 0, 1, 2, \cdots N_\theta \tag{4.98}$$

and calculate the discrete function

$$F_k = F\left(\psi, \overline{\theta}_k, \xi_0; B_{Rk}, B_{Zk}, B_{\phi k}, R_k, Z_k\right) \tag{4.99}$$

where $B_{Rk}, B_{Zk}, B_{\phi k}, R_k, Z_k$ have been calculated on the grid $\overline{\theta}_k$ by linear interpolation. The integral (4.83) becomes

$$I\left(\psi, \xi_0\right) = \frac{1}{2\pi}\sum_{k=0}^{N_\theta} \overline{d\theta}_k F_k \tag{4.100}$$

where the step $\overline{d\theta}_k$ are defined by

$$\overline{d\theta}_k = \widetilde{\theta}_{k+1} - \widetilde{\theta}_k,\ k = 0, 1, 2, \cdots N_\theta \tag{4.101}$$

# Chapter 5

# Current Drive by Electron Bernstein Waves

In this chapter, I calculate and describe current drive by EBWs in toroidal plasmas. First, the components of the quasilinear diffusion coefficient (3.192) are analyzed in Section 5.1 for the case of a single EBW Fourier component $(\omega, \mathbf{k})$. The interaction between electrons and EBWs is described by studying the resonance condition, and the effect of $\mathrm{Re}\,[k_\perp \rho_{Te}]$ and the polarization, which are very different for the HBF and LBF scenarios. The direction of RF diffusion is calculated. The EBW absorption coefficient and power deposition profile are evaluated in the weakly relativistic linear limit in a slab geometry. This analysis will help the interpretation of EBWCD calculations from Sections 5.3 and 5.4, which consider the LBF and HBF EBWCD scenarios respectively. The framework of these calculation is presented in Section 5.2.

## 5.1 Resonant interaction between electrons and EBWs

In quasilinear theory, the resonant interaction between electrons and EBWs leads to momentum-space diffusion of electrons, with momentum and energy transfer from the wave to the electrons. In this section, the local interaction between electrons and

a single EBW Fourier component $(\omega, \mathbf{k})$ is studied in a slab plasma. After recalling the expression of the quasilinear operator, I will focus on the wave-particle resonance condition, the direction of particle diffusion due to RF fields, the linear damping of EBWs, the power deposition profile, and the resonance overlapping problem.

### 5.1.1 RF quasilinear diffusion operator

The quasilinear operator defined in Section 3.5 is expressed here in spherical coordinates and for a single EBW Fourier component.

#### In a uniform plasma

We consider the RF quasilinear operator (3.187) for a given frequency $\omega$, given here in $(p_\perp, p_\parallel)$ coordinates (A.111)

$$\mathcal{Q}(f) = -\nabla_{\mathbf{p}} \cdot \mathbf{S}^{\mathrm{RF}} = -\frac{1}{p_\perp}\frac{\partial}{\partial p_\perp}\left(p_\perp S_\perp^{\mathrm{RF}}\right) - \frac{\partial}{\partial p_\parallel}\left(S_\parallel^{\mathrm{RF}}\right) \tag{5.1}$$

where the RF induced momentum-space flux $\mathbf{S}^{\mathrm{RF}}$ is purely diffusive (3.189) and given by (A.110)

$$\mathbf{S}^{\mathrm{RF}} = -\mathbb{D}^{\mathrm{RF}} \cdot \nabla_{\mathbf{p}} f = -\begin{pmatrix} D_{\perp\perp}^{\mathrm{RF}} & D_{\perp\parallel}^{\mathrm{RF}} \\ D_{\parallel\perp}^{\mathrm{RF}} & D_{\parallel\parallel}^{\mathrm{RF}} \end{pmatrix} \cdot \begin{pmatrix} \partial f/\partial p_\perp \\ \partial f/\partial p_\parallel \end{pmatrix} \tag{5.2}$$

and the quasilinear diffusion tensor elements are given by (B.23) which for electrons becomes (3.190) (B.43)

$$\begin{aligned}
D_{\perp\perp}^{\mathrm{RF}} &= \sum_{n=-\infty}^{+\infty} \left(\frac{n\omega_{ce}}{\gamma\omega}\right)^2 D_n^{\mathrm{RF}}(\mathbf{p}) \\
D_{\perp\parallel}^{\mathrm{RF}} &= \sum_{n=-\infty}^{+\infty} \frac{p_\perp}{p_\parallel}\frac{n\omega_{ce}}{\gamma\omega}\left(1 - \frac{n\omega_{ce}}{\gamma\omega}\right) D_n^{\mathrm{RF}}(\mathbf{p}) \\
D_{\parallel\perp}^{\mathrm{RF}} &= \sum_{n=-\infty}^{+\infty} \frac{p_\perp}{p_\parallel}\frac{n\omega_{ce}}{\gamma\omega}\left(1 - \frac{n\omega_{ce}}{\gamma\omega}\right) D_n^{\mathrm{RF}}(\mathbf{p}) \\
D_{\parallel\parallel}^{\mathrm{RF}} &= \sum_{n=-\infty}^{+\infty} \frac{p_\perp^2}{p_\parallel^2}\left(1 - \frac{n\omega_{ce}}{\gamma\omega}\right)^2 D_n^{\mathrm{RF}}(\mathbf{p})
\end{aligned} \tag{5.3}$$

where $D_n^{\mathrm{RF}}(\mathbf{p})$ is the quasilinear diffusion coefficient corresponding to resonance at harmonic $n$. It is given by (3.192) and reduces to

$$D_n^{\mathrm{RF}}(\mathbf{p}) = \frac{\pi e^2}{2} \|\mathbf{E}_\mathbf{k}\|^2 \left|\Theta_\mathbf{k}^{(n)}(\mathbf{p}, \mathbf{k}, \mathbf{e}_\mathbf{k})\right|^2 \delta\left(\omega - k_\parallel \frac{p_\parallel}{\gamma m_e} - \frac{n\omega_{ce}}{\gamma}\right) \tag{5.4}$$

for a single Fourier component $(\omega, \mathbf{k})$ with electric field amplitude $\mathbf{E}_\mathbf{k}$, and $\mathbf{e}_\mathbf{k} = |\mathbf{E}_\mathbf{k}| / \|\mathbf{E}_\mathbf{k}\|$ is the corresponding polarization vector. $\Theta_\mathbf{k}^{(n)}$ is the polarization term (3.194)

$$\Theta_\mathbf{k}^{(n)} = \frac{1}{\sqrt{2}} e_{\mathbf{k},+} e^{-i\alpha} J_{n+1}(z) + \frac{1}{\sqrt{2}} e_{\mathbf{k},-} e^{+i\alpha} J_{n-1}(z) + \frac{p_\parallel}{p_\perp} e_{\mathbf{k},\parallel} J_n(z) \tag{5.5}$$

with (3.195)

$$z = \frac{k_\perp}{\omega_{ce}} \frac{p_\perp}{m_e} \tag{5.6}$$

### Extension to a slab plasma

As seen in Appendix B.4, the diffusion coefficient (5.4), derived in a uniform plasma, can be extended to a slab geometry where the direction of inhomogeneity is perpendicular to the magnetic field. It requires that the inhomogeneity scale length $L$ is much larger than the wavelength $\lambda = 2\pi/k$, such that the WKB approximation is valid, and also much larger than the thermal electron Larmor radius $\rho_{Te} = v_{Te}/\omega_{ce}$, such that wave particle interaction remains unaffected.

The plasma electron temperature $T_e(x)$ and density $n_e(x)$ as well as the magnetic field (or gyrofrequency $\omega_{ce}(x)$) are all slowly varying functions of $x$. In that case, wave amplitude $\mathbf{E}(\mathbf{r})$, and the related polarization and energy flow, also contains a slow dependence upon $x$. However, the parallel wave vector $k_\parallel$ is conserved by symmetry.

### 5.1.2 Description of the resonant electrons

#### Resonance curves in momentum space

Considering a given Fourier component $(\omega, \mathbf{k})$, we study the condition

$$\omega = v_{\|} k_{\|} + \frac{n\omega_{ce}(x)}{\gamma} \tag{5.7}$$

for wave-particle resonance in the diffusion coefficient (5.4), which identifies the electrons - characterized by their momentum $(p_{\perp}, p_{\|})$ - that resonate at harmonic $n$ with the wave $(\omega, k_{\|})$, given the local cyclotron frequency $\omega_{ce}(x)$. These electrons are typically located (in momentum space) on a curve that depends upon two dimentionless parameters: the parallel wave number $N_{\|} = k_{\|} c/\omega$ and the frequency ratio (2.108)

$$y_n(x) = \frac{n\omega_{ce}(x)}{\omega} \tag{5.8}$$

which describes the position with respect to the $n^{\text{th}}$ harmonic resonance. The resonance condition (5.7) can be rewritten as

$$\gamma - \frac{p_{\|}}{m_e c} N_{\|} - y_n = 0 \tag{5.9}$$

Then, the equation for the resonance curve is obtained from (5.9) using (3.21)

$$\begin{aligned}
&\bullet\ \left(\frac{p_{\perp}}{mc}\right)^2 + \left(1 - N_{\|}^2\right)\left(\frac{p_{\|}}{mc} - \frac{N_{\|} y_n}{1 - N_{\|}^2}\right)^2 = \frac{y_n^2}{1 - N_{\|}^2} - 1 \quad \text{for } N_{\|}^2 < 1 \\
&\bullet\ \left(\frac{p_{\perp}}{mc}\right)^2 - 2\sigma_{\|} y_n \frac{p_{\|}}{mc} + 1 - y_n^2 = 0 \quad \text{for } N_{\|}^2 = 1 \\
&\bullet\ \left(N_{\|}^2 - 1\right)\left(\frac{p_{\|}}{mc} + \frac{N_{\|} y_n}{N_{\|}^2 - 1}\right)^2 - \left(\frac{p_{\perp}}{mc}\right)^2 = \frac{y_n^2}{N_{\|}^2 - 1} + 1 \quad \text{for } N_{\|}^2 > 1
\end{aligned} \tag{5.10}$$

where $\sigma_{\|} = \text{sign}\left(N_{\|}\right)$. The equation (5.10) shows that the resonance curve is an ellipse for $N_{\|}^2 < 1$, a parabola for $N_{\|}^2 = 1$, and a hyperbola for $N_{\|}^2 > 1$. When $N_{\|}^2 < 1$, this

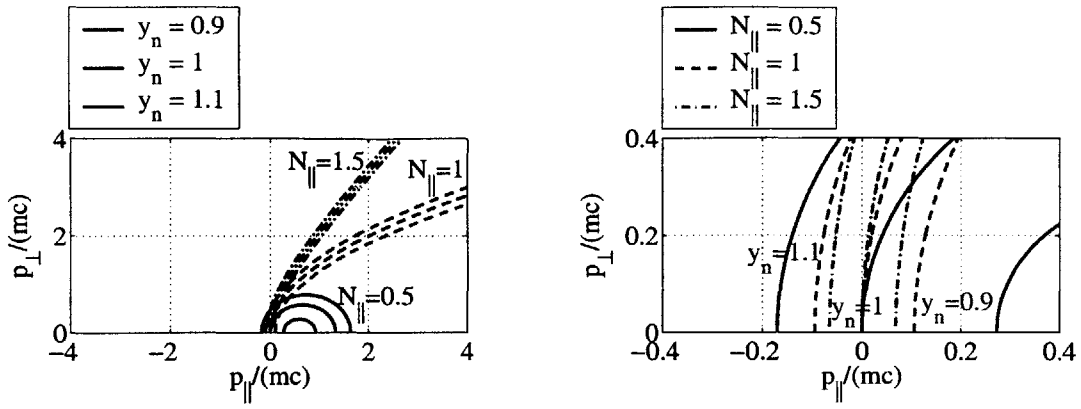


(a) (b)

Figure 5-1: Resonance curves in $(p_\perp, p_\parallel)$ momentum space corresponding to the wave numbers $N_\parallel = 0.5$ (solid lines), $N_\parallel = 1$ (dashed lines), and $N_\parallel = 1.5$ (dashed-dotted lines) and the ratios $y_n = 0.9$ (red lines), $y_n = 1$ (blue lines), and $y_n = 1.1$ (green lines). Graph (b) is a $\times 10$ zoom of graph (a).

equation has a solution only when

$$y_n > \sqrt{1 - N_\parallel^2} \tag{5.11}$$

otherwise there simply are no resonant electrons.

On Fig. 5-1 are shown the resonance curves corresponding to the wave numbers $N_\parallel = 0.5$ (solid lines), $N_\parallel = 1$ (dashed lines), and $N_\parallel = 1.5$ (dashed-dotted lines) and the ratios $y_n = 0.9$ (red lines), $y_n = 1$ (blue lines), and $y_n = 1.1$ (green lines). We observe that:

- For $y_n = 1$, the resonance curve always passes through the origin $(p_\perp, p_\parallel) = (0, 0)$. This property can be readily verified from equation (5.10).

- It can be shown that the point with minimum momentum $p$ on the resonance curve is always on the $p_\perp = 0$ axis, and can therefore be identified as $p_{\parallel\,\mathrm{min}}(N_\parallel, y_n)$. For positive $N_\parallel$, we find that $p_{\parallel\,\mathrm{min}} < 0$ for $y_n > 1$, which corresponds to a high $B$-field (HBF) approach since $n\omega_{ce} > \omega$. Also, $p_{\parallel\,\mathrm{min}} > 0$ for $y_n < 1$, which corresponds to a low $B$-field (LBF) approach since $n\omega_{ce} < \omega$. In

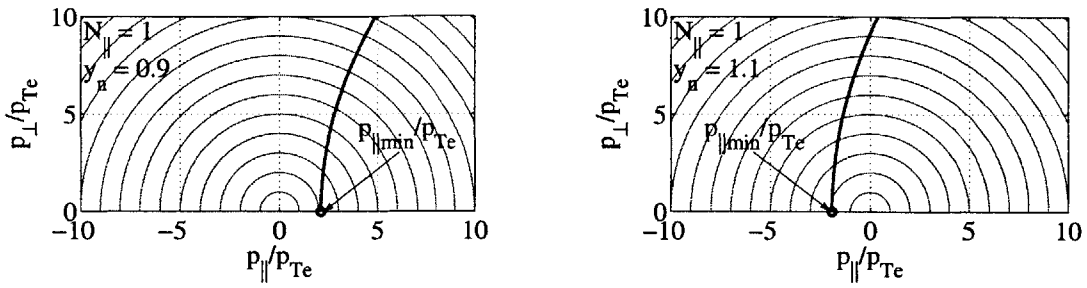


(a) (b)

Figure 5-2: The point $p_{\parallel \min}$ characterizes the location with minimum momentum $p$ on the resonance curve, in both LBF (a) and HBF (b) cases.

addition, the point $p_{\parallel \min}\left(N_\parallel, y_n\right)$ "moves in" closer to the bulk as the the wave approaches the resonance ($y_n \rightarrow 1$) from either (HBF or LBF) side.

- For a given $y_n$, $p_{\parallel \min}$ is closer to zero for larger $\left|N_\parallel\right|$, which generally means larger damping. This effect is called *Doppler shift* of resonance. In addition, the resonance curves "move" less rapidly as a function of $y_n$ for larger $\left|N_\parallel\right|$, which generally leads to wider spatial power deposition profiles. This effect is called *Doppler broadening.*

- The equation (5.10) is invariant by the transformation $\left(N_\parallel, p_\parallel\right) \rightarrow \left(-N_\parallel, -p_\parallel\right)$. Therefore, changing the sign of $N_\parallel$ requires simply to invert Fig. 5-1 with respect to $p_\parallel$.

**Expression for $p_{\parallel \min}$**

For given wave parameters $\left(N_\parallel, y_n\right)$, the value of $p_{\parallel \min}\left(N_\parallel, y_n\right)$, which is the point with minimum $p$ on the resonance curve and is on the $p_\perp = 0$ axis, has a particular importance because it strongly affects damping, as we will demonstrate in Section 5.1.6, and also the current drive efficiency. This can be understood by the fact that the momentum-space density of electrons is highest on the resonance curve at this

point. Therefore, if this point is closer to the bulk, it usually means that the damping is higher, since there are more resonant electrons.

Therefore, it is important to calculate the value of $p_{\parallel \min}$ with respect to $p_{Te}$. From (5.10), we get, setting $p_\perp = 0$,

$$\frac{p_{\parallel \min}}{p_{Te}} = \begin{cases} \bullet \ \dfrac{N_\parallel y_n - \sigma_\parallel \sqrt{y_n^2 - 1 + N_\parallel^2}}{\beta_{Te}\left(1 - N_\parallel^2\right)} & \text{for } N_\parallel^2 < 1 \\ \bullet \ \sigma_\parallel \dfrac{\left(1 - y_n^2\right)}{2\beta_{Te} y_n} & \text{for } N_\parallel^2 = 1 \\ \bullet \ \dfrac{\sigma_\parallel \sqrt{y_n^2 - 1 + N_\parallel^2} - N_\parallel y_n}{\beta_{Te}\left(N_\parallel^2 - 1\right)} & \text{for } N_\parallel^2 > 1 \end{cases} \tag{5.12}$$

with (2.103) $\beta_{Te} = p_{Te}/m_e c$. We define the parameter (2.126)

$$p_n(x) = \frac{1 - y_n(x)}{\beta_{Te} N_\parallel} \tag{5.13}$$

which measures the distance from resonance ($y_n = 1$, $n\omega_{ce} = \omega$) in terms of magnetic field variation, and accounts for the Doppler shift effect through the term $\beta_{Te} N_\parallel$. The equation (5.12) for $p_{\parallel \min}$ becomes

$$\frac{p_{\parallel \min}}{p_{Te}} = \begin{cases} \bullet \ \dfrac{N_\parallel}{\beta_{Te}\left(1 - N_\parallel^2\right)} \left(1 - \beta_{Te} N_\parallel p_n - \sqrt{1 - \dfrac{2\beta_{Te} p_n}{N_\parallel} + \beta_{Te}^2 p_n^2}\right) & \text{for } N_\parallel^2 < 1 \\ \bullet \ p_n \dfrac{\left(2 - \sigma_\parallel \beta_{Te} p_n\right)}{2\left(1 - \sigma_\parallel \beta_{Te} p_n\right)} & \text{for } N_\parallel^2 = 1 \\ \bullet \ \dfrac{N_\parallel}{\beta_{Te}\left(N_\parallel^2 - 1\right)} \left(\sqrt{1 - \dfrac{2\beta_{Te} p_n}{N_\parallel} + \beta_{Te}^2 p_n^2} - 1 + \beta_{Te} N_\parallel p_n\right) & \text{for } N_\parallel^2 > 1 \end{cases} \tag{5.14}$$

In the limit where $\beta_{Te} |p_n| \ll |N_\parallel| \lesssim 1$, which we will call *weakly relativistic approximation*, and gives with (5.13)

$$|1 - y_n(x)| \ll N_\parallel^2 \tag{5.15}$$

which is satisfied close enough to resonance, (5.14) becomes for any $N_{\|}$

$$\frac{p_{\| \min}^{\mathrm{wr}}}{p_{Te}} = p_n \left( 1 + \frac{\beta_{Te} p_n}{2N_{\|}} + O\left[ \left( \frac{\beta_{Te} p_n}{N_{\|}} \right)^2 \right] \right) \tag{5.16}$$

where the subscript "wr" refers to quantities evaluated in the weakly relativistic limit.

Note that in the non-relativistic limit ($\beta_{Te} \to 0$) we have

$$\frac{p_{\| \min}^{\mathrm{nr}}}{p_{Te}} = p_n \tag{5.17}$$

where the subscript "nr" refers to quantities evaluated in the non relativistic limit. Therefore $p_n$ (5.13) is the parallel momentum of a resonant electron on the ($p_\perp = 0$) axis in the non-relativistic limit, and the Doppler effect is well described by (5.13). In addition, we see from (5.16) that relativistic effects bring the resonance closer to the bulk in HBF approach ($y_n > 1$, $p_n$ and $N_{\|}$ are of opposite signs) but further from the bulk in LBF approach ($y_n < 1$, $p_n$ and $N_{\|}$ are of the same sign).

Therefore, the properties of EBWCD, in particular the damping and the efficiency, strongly depend upon $p_n \simeq p_{\| \min}/p_{Te}$ which determines the position of the resonant curve. The relative variations of $p_n$ depend mostly on the parameter $y_n$ because $p_n$ varies like $1 - y_n$ and we consider the vicinity of $y_n \simeq 1$. As a consequence, near the cyclotron harmonic resonance, the characteristics of EBWCD will vary primarily according to the changes in $y_n$, i.e. in the magnetic field.

### 5.1.3 Polarization term for EBWs

Because EBW waves have a mostly electrostatic polarization, as we saw in Section 2.2, we can make the following approximations (2.82)

$$\begin{aligned} e_{\mathbf{k},+} &\simeq e_{\mathbf{k},-} \simeq \frac{1}{\sqrt{2}} \\ e_{\mathbf{k},\|} &\simeq \frac{N_{\|}}{N_\perp} \text{ with } \left| e_{\mathbf{k},\|} \right| \ll 1 \end{aligned} \tag{5.18}$$

so that, using the following identity for Bessel functions

$$J_{n+1}(z) + J_{n-1}(z) = \frac{2n}{z} J_n(z) \tag{5.19}$$

the polarization term (5.5) becomes

$$\begin{aligned} \Theta_{\mathbf{k}}^{(n)} &\simeq \left[ \frac{n}{z} + \frac{N_\parallel}{N_\perp} \frac{p_\parallel}{p_\perp} \right] J_n(z) \\ &\simeq \frac{J_n(z)}{N_\perp \beta_{Te}} \frac{p_{Te}}{p_\perp} \left[ y_n + N_\parallel \beta_{Te} \frac{p_\parallel}{p_{Te}} \right] \end{aligned} \tag{5.20}$$

where we used (5.6)

$$z = k_\perp \rho_{Te} \frac{p_\perp}{p_{Te}} \tag{5.21}$$

and the definitions (5.8) and (2.103)

$$\begin{aligned} y_n &= \frac{n\omega_{ce}}{\omega} \\ \beta_{Te} &= \frac{p_{Te}}{m_e c} \end{aligned} \tag{5.22}$$

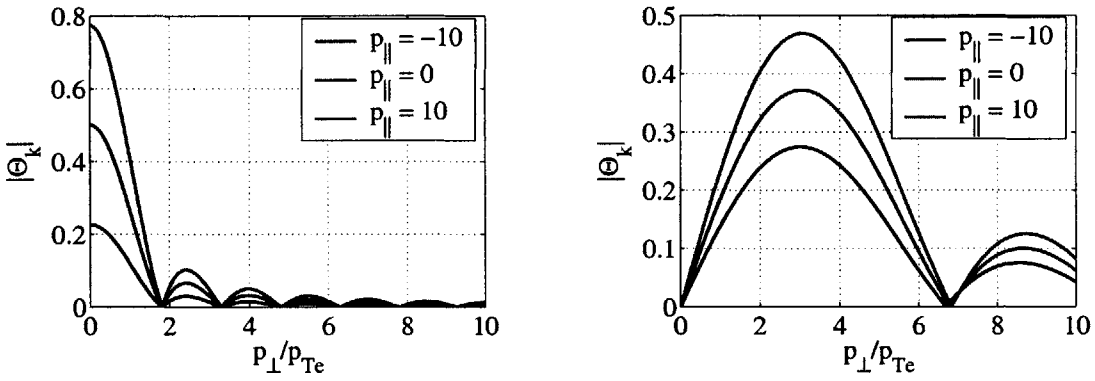


(a) (b)

Figure 5-3: Polarization term (5.5) for EBWs as a function of $p_\perp$ for several values of $p_\parallel$ and with $\beta_{Te} = 0.05$ and $N_\parallel = 1$. Graph (a) corresponds to a $n = 1$ LBF case ($y_n = 0.83$) and graph (b) corresponds to a $n = 2$ HBF case ($y_n = 1.19$).

We observe that the polarization term varies mostly like $nJ_n(z)/z$, and therefore has a band structure in $p_\perp$. The polarization term $\left|\Theta_{\mathbf{k}}^{(n)}\right|$ (5.5) is shown in Fig. 5-3 as

a function of $p_\perp$ for several values of $p_\parallel$ and with $\beta_{Te} = 0.05$ and $N_\parallel = 1$. Graph (a) corresponds to a $n = 1$ LBF case ($y_n = 0.83$) and graph (b) corresponds to a $n = 2$ HBF case ($y_n = 1.19$).

- In the $n = 1$ LBF case, the polarization term peaks at $p_\perp = 0$, in accordance with the behavior of $J_1(z)/z$ for $z \to 0$. In addition, the zeros and peaks of $\left|\Theta_{\mathbf{k}}^{(1)}\right|$ are quite close together in $p_\perp$, which is due to the large values of $k_\perp \rho_{Te}$ in (5.21) for LBF approach, as seen in Section 2.3.

- In the $n = 2$ HBF case (note that there cannot be a $n = 1$ HBF approach with EBWs), the polarization term peaks at $p_\perp \simeq 3p_{Te}$ , in accordance with the behavior of $J_2(z)/z$ which peaks at $z = 2.3$. In addition, the zeros and peaks of $\left|\Theta_{\mathbf{k}}^{(2)}\right|$ are much further apart in $p_\perp$ than in the LBF case, which is due to the smaller values of $k_\perp \rho_{Te}$ in (5.21) for HBF approach.

- We also note that the shape of $\left|\Theta_{\mathbf{k}}^{(n)}\right|$ follows closely $J_n(z)/z$ and that the parallel polarization correction is merely a scaling of this term, which confirms the approximate form (5.20).

The correction due to the parallel polarization is of order $N_\parallel \beta_{Te} p_\parallel / p_{Te}$ and is therefore expected to play a role for electrons with a large $p_\parallel$. Note that this corrective effect is proportional to the Doppler-shift factor $N_\parallel \beta_{Te}$.

### 5.1.4 Direction of diffusion for EBW-electron interaction

EBWs interact with electrons at harmonics $n > 0$ of the cyclotron frequency. We consider the vicinity of a given harmonic $n$ and assume that harmonic overlapping can be neglected. For an electron with momentum $(p_\perp, p_\parallel)$ resonating with an EBW characterized by $(\omega, k_\parallel)$, the direction of diffusion, characterized by an angle $\chi$ with respect to the perpendicular direction in momentum space, is investigated by considering (5.3) and the ratio

$$\tan\chi = \frac{D^{\mathrm{RF}}_{\perp\parallel n}}{D^{\mathrm{RF}}_{\perp\perp n}} = \frac{D^{\mathrm{RF}}_{\parallel\parallel n}}{D^{\mathrm{RF}}_{\parallel\perp n}} = \frac{p_\perp}{p_\parallel}\frac{\gamma\omega}{n\omega_{ce}}\left(1 - \frac{n\omega_{ce}}{\gamma\omega}\right) = \frac{p_\perp}{p_\parallel}\left(\frac{\gamma\omega}{n\omega_{ce}} - 1\right) \tag{5.23}$$

The resonance condition (5.9) gives

$$\gamma - \frac{p_\parallel}{m_e c} N_\parallel - y_n = 0 \tag{5.24}$$

with the ratio

$$y_n = \frac{n\omega_{ce}}{\omega} \tag{5.25}$$

so that combining equations (5.23) and (5.24) we find

$$\tan\chi = \frac{p_\perp}{p_{Te}} \frac{N_\parallel \beta_{Te}}{y_n} \tag{5.26}$$

In the non-relativistic limit, we take $c \to \infty$ and get simply

$$\tan\chi = 0 \tag{5.27}$$

meaning that the diffusion is purely perpendicular ($\chi = 0°$).

When relativistic effects are included, the diffusion is no longer purely perpendicular. Using $y_n \simeq 1$, we get

$$\tan\chi \simeq \frac{p_\perp}{p_{Te}} N_\parallel \beta_{Te} \tag{5.28}$$

where typically $N_{b\parallel}\beta_{Te} \ll 1$. Expanding $\tan\chi$, we get

$$\chi \simeq \frac{p_\perp}{p_{Te}} N_\parallel \beta_{Te} \tag{5.29}$$

which gives, for typical NSTX parameters with $\beta_{Te} \simeq 0.05$ and $p_\perp \approx 3p_{Te}$, a deviation $\chi \approx N_{b\parallel} \times 10°$. Even for large parallel wave numbers, the diffusion remains mostly perpendicular. However, the small parallel component of the diffusion can have important effect on current drive, because some parallel momentum can be transferred directly to electrons, which is more efficient than creating an asymmetric resistivity [36]. The effects can be even more important when trapped electrons effects are present. The diffusion in the parallel direction increases with both $N_{b\parallel}$ and $\beta_{Te} \propto \sqrt{T_e}$, and is of the same sign as $N_\parallel$. Because $p_{\parallel\,\mathrm{min}}$ is of the same sign as $N_\parallel$

in LBF approach, the parallel diffusion is in the same direction as $p_{\parallel \min}$. However, in HBF approach, $p_{\parallel \min} N_\parallel < 0$ and the parallel diffusion is in the opposite direction to $p_{\parallel \min}$.

### 5.1.5 Linear damping of EBWs

The density of power absorbed from RF waves at the $n^{\text{th}}$ harmonic is related to the quasilinear operator for EBW (5.1), and is given by (3.277)

$$P_{\text{abs},n}^{\text{RF}} = 2\pi \int_0^\infty dp \, \frac{p^3}{\gamma m_e} \int_{-1}^{+1} d\xi S_{p,n}^{\text{RF}}(f) \tag{5.30}$$

where $S_{p,n}^{\text{RF}}$ is the RF-induced flux (5.2) for the $n^{\text{th}}$ harmonic, projected in the $\widehat{\mathbf{p}}$ direction. This expression can be evaluated analytically in the linear electrostatic limit when the distribution function $f$ is a Maxwellian, using the weakly relativistic approximation (5.15). The derivation is detailed in Appendix B.4, and gives an expression for the absorption coefficient near the $n^{\text{th}}$ harmonic, defined as (2.50)

$$\alpha_n^{\text{RF}} = \frac{P_{\text{abs},n}^{\text{RF}}}{\|\mathbf{s}_0\|} \tag{5.31}$$

where $\|\mathbf{s}_0\|$ is the energy flow density (2.36). We find, in the weakly relativistic limit (B.162)

$$\alpha_n^{\text{RF},M\text{wr}} = \frac{1}{\sqrt{2\pi}} \frac{\omega\pi}{c} \frac{\omega_{pe}^2}{\omega_{ce}^2} \frac{1}{\beta_{Te} |N_\parallel| \Phi} \frac{\Gamma_n[\lambda_e]}{\lambda_e} \exp\left[ -\frac{1}{2} \left( p_n \left[ 1 + \frac{\beta_{Te} p_n}{2N_\parallel} \right] \right)^2 \right] \tag{5.32}$$

which becomes in the non-relativistic limit (B.160)

$$\alpha_n^{\text{RF},M\text{nr}} = \frac{1}{\sqrt{2\pi}} \frac{\omega\pi}{c} \frac{\omega_{pe}^2}{\omega_{ce}^2} \frac{1}{\beta_{Te} |N_\parallel| \Phi} \frac{\Gamma_n[\lambda_e]}{\lambda_e} \exp\left[ -\frac{p_n^2}{2} \right] \tag{5.33}$$

where $\Phi$ is the normalized energy flow density (2.36) and $p_n$ is given by (5.13). Comparing with expressions (5.16) and (5.17), we can rewrite respectively in the weakly

relativistic limit

$$\alpha_n^{\mathrm{RF},M\mathrm{wr}} = \frac{1}{\sqrt{2\pi}} \frac{\omega\pi}{c} \frac{\omega_{pe}^2}{\omega_{ce}^2} \frac{1}{\beta_{Te} \left|N_\parallel\right| \Phi} \frac{\Gamma_n\left[\lambda_e\right]}{\lambda_e} \exp\left[-\frac{\left(p_{\parallel\,\mathrm{min}}^{\mathrm{wr}}\right)^2}{2p_{Te}^2}\right] \tag{5.34}$$

and in the non-relativistic limit (B.160)

$$\alpha_n^{\mathrm{RF},M\mathrm{nr}} = \frac{1}{\sqrt{2\pi}} \frac{\omega\pi}{c} \frac{\omega_{pe}^2}{\omega_{ce}^2} \frac{1}{\beta_{Te} \left|N_\parallel\right| \Phi} \frac{\Gamma_n\left[\lambda_e\right]}{\lambda_e} \exp\left[-\frac{\left(p_{\parallel\,\mathrm{min}}^{\mathrm{nr}}\right)^2}{2p_{Te}^2}\right] \tag{5.35}$$

Therefore, the absorption coefficient of EBWs depends primarily upon $p_{\parallel\,\mathrm{min}}/p_{Te}$, as we anticipated in Section 5.1.2.

We note that the linear non-relativistic electrostatic absorption coefficient (2.120) calculated from the kinetic susceptibility tensor is retrieved in (5.33), which was expected since the two derivations are based on the same assumptions. This is a good check for the validity of our derivation of the quasilinear operator.

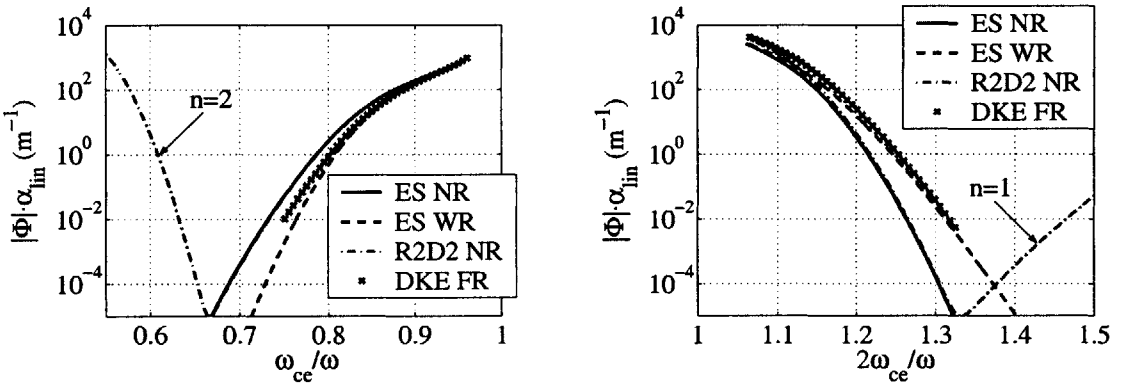


Figure 5-4: Absorption coefficient as a function of $y_n$ in the LBF case (a) and in the HBF case (b), for $\omega/2\pi = 14$ GHz, $N_\parallel = 1$, $\beta_{Te} = 0.05$ and $\omega_{pe}^2 = 12\omega^2$. The results from non-relativistic (NR) and weakly relativistic (WR) analytical results are compared with results from *R2D2* and *DKE* codes.

In order to verify our calculation of the absorption coefficient and determine if the electrostatic, weakly relativistic limit is a good approximation to the exact, fully

relativistic and electromagnetic absorption coefficient, we calculate the product $\Phi\alpha_n^{\mathrm{RF}}$ as a function of $y_n$ for a typical NSTX EBWCD scenario, with $\omega/2\pi = 14$ GHz, $N_\parallel = 1$, $\beta_{Te} = 0.05$ and $\omega_{pe}^2 = 12\omega^2$. The results are shown on Fig. 5-4 for both a LBF approach at first harmonic (a) and a HBF approach at second harmonic (b), where the product $\Phi\alpha_n^{\mathrm{RF}}$ is calculated using the non-relativistic expression (5.33) (blue solid line), the weakly relativistic expression (5.32) (green dashed line), the fully electromagnetic, non-relativistic result from *R2D2* [13] (dot-dashed red line) and the fully electromagnetic, fully relativistic code *DKE* (purple crosses). We observe that:

- In LBF approach, all calculations converge near resonance, meaning that the electrostatic approximation is very good.

- In HBF approach, the electromagnetic calculations (*DKE*, *R2D2*) differ slightly from the corresponding electrostatic calculations (WR,NR) close to the resonance. This is in accordance with the results of Section 2.3 where it was shown that electromagnetic effects were important near the resonance in HBF approach, in particular for the polarization.

- Apart from the electromagnetic effects in HBF approach, the analytic non-relativistic calculation (NR) agrees perfectly with the results from *R2D2*, which validates our derivation (and *R2D2*).

- Apart from the electromagnetic effects in HBF approach, the weakly relativistic calculation (WR) is in very good agreement with the fully relativistic calculation from *R2D2*, except in the LBF approach for $y_n < 0.8$.

- The relativistic effects lead to a reduction of the absorption in the LBF approach and an increase in the HBF approach, as found in Section 5.1.2.

- Resonance overlapping occurs around $|1 - y_n| \simeq 0.3$ in the two cases presented here. The importance of this overlapping will be asserted in Section 5.1.7.

### 5.1.6 EBW power deposition

The calculation of $\alpha_n^{\mathrm{RF}}$ is not sufficient to predict the effect of plasma and wave parameters on the damping of EBW and the driven current. In fact, it is the integration of $\alpha_n^{\mathrm{RF}}$ along the propagation that gives the deposition profile and characterizes EBW damping.

The damping region is assumed to be sufficiently narrow as compared to plasma non-uniformity scalelength $L$, so that the temperature and density can be considered as being uniform across that damping region. In addition, we assume that wave propagation characteristics such as the perpendicular wave vector $k_\perp$and the power flow $\Phi$ are also constant across the damping region. This assumption may seem questionable with regard to the rapid changes in these wave characteristics near cyclotron resonances, as a function of $y_n = n\omega_{ce}/\omega$, as demonstrated in Section 2.3 from solving the local dispersion relation. However, it will turn out that the power deposition profile is rather insensitive to the typical variations of the wave parameters across the damping region.

Indeed, the variations in the absorption coefficient $\alpha_n^{\mathrm{RF}}$ are dominated by the exponential term in (5.33) and (5.32), which is expressed as (B.133) $p_n = (1 - y_n)/\beta_{Te} N_{0\|}$. The relative variations of $p_n$ are mostly sensitive to the variations of the magnetic field, because $p_n$ depends upon the difference $(1 - y_n)$ in the vicinity of $y_n \simeq 1$. It is therefore justified to take all parameters constant in the damping region except $y_n$, that is, account for variations in the magnetic field only. In addition, the magnetic field amplitude - and thus $y_n$ - are assumed to vary linearly in space.

The equation for the location of the peak in the power deposition profile has been solved in Appendix B.4. We found that the peak position as a function of $p_n$ is given by (B.183) in the weakly relativistic limit and by (B.178) in the non relativistic limit. In either case, given that the weakly relativistic corrections matter only in the

exponential factor, one obtains

$$\frac{\left|p^{\mathrm{m}}_{\parallel\,\mathrm{min}}\right|}{p_{Te}} = p_{0,n}\exp\left[-\frac{\left|p^{\mathrm{m}}_{\parallel\,\mathrm{min}}\right|^2}{2p^2_{Te}}\right] \tag{5.36}$$

where $p_{0,n}$ is a dimentionless parameter given by (B.179)

$$p_{0,n} = \frac{1}{\sqrt{2\pi}}\frac{\omega\pi}{c}\frac{\omega^2_{pe}}{\omega^2_{ce}}\frac{L_B}{|\Phi_\perp|}\frac{\Gamma_n\left[\lambda_e\right]}{\lambda_e} \tag{5.37}$$

and where we keep in mind that $p^{\mathrm{m}}_{\parallel\,\mathrm{min}}$ is of the same sign as $\sigma N_\parallel$ where $\sigma = +1$ for low $B$-field approach (LBF) and $\sigma = -1$ for high $B$-field approach (HBF). Note that the parameter $p_{0,n}$ is simply related to the optical half-depth $\tau_{\mathbf{k},n}$ (2.129) as

$$p_{0,n} = \sqrt{\frac{2}{\pi}}\tau_{\mathbf{k},n} \tag{5.38}$$

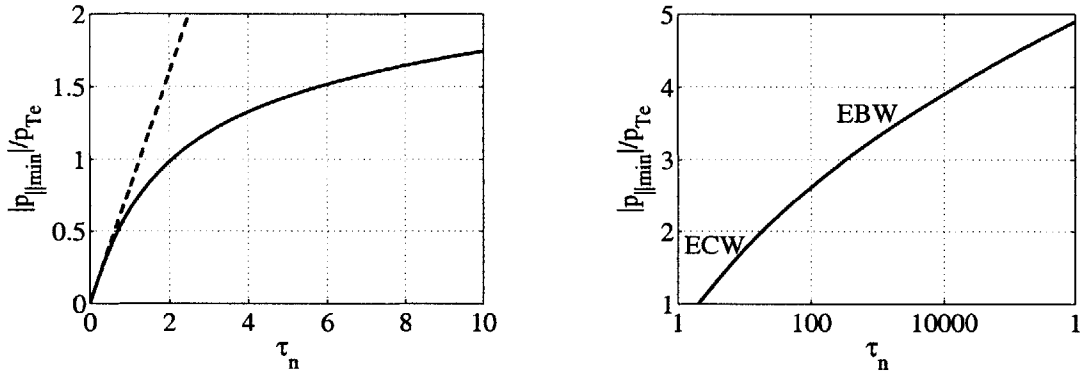


(a) (b)

Figure 5-5: Peak of deposition profile $\left|p^{\mathrm{m}}_{\parallel\,\mathrm{min}}\right|$ as a function of $\tau_{\mathbf{k},n}$ on linear (a) and logarithmic (b) scales. On graph (a), the dashed line represent the linear limit $\left|p^{\mathrm{m}}_{\parallel\,\mathrm{min}}\right| \to \sqrt{\frac{2}{\pi}}\tau_{\mathbf{k},n}$.

The equation (5.36) for $p^{\mathrm{m}}_{\parallel\,\mathrm{min}}$, which corresponds to the resonant value of $p_\parallel$ for $p_\perp = 0$ at the peak of deposition, is plotted on Fig. 5-5 as a function of the optical half-

depth $\tau_{\mathbf{k},n}$. On graph (a), the dashed line represents the linear limit $\left|p^{\mathrm{m}}_{\parallel\,\mathrm{min}}\right| \to p_{0,n}$.

As a first observation, we see that $\left|p^{\mathrm{m}}_{\parallel\,\mathrm{min}}\right|$ increases as a function of $\tau_{\mathbf{k},n}$, which means that for larger $p_{0,n}$ - or equivalently a larger optical depth - the power will be absorbed farther in the tail in momentum space. As expected from equation (5.36), and showed on graph (a), $\left|p^{\mathrm{m}}_{\parallel\,\mathrm{min}}\right|$ is linear with $p_{0,n}$ for $p_{0,n} < 1$, while $\left|p^{\mathrm{m}}_{\parallel\,\mathrm{min}}\right|$ varies very slowly with $p_{0,n}$ for $p_{0,n} > 10$; indeed, for large values of $p_{0,n}$, or for $\left|p^{\mathrm{m}}_{\parallel\,\mathrm{min}}\right| > 1$, $\left|p^{\mathrm{m}}_{\parallel\,\mathrm{min}}\right|$ varies like $\sqrt{\ln p_{0,n}}$, which is an extremely slow variation.

We point out that the validity of equation (5.36) extends to wave damping problems in general - with different expressions for $p_0$ depending on the type of wave.

- For example, in lower-hybrid current drive (LHCD) problems where wave-particle resonance occurs through Landau damping at $n = 0$, we have that $\left|p^{\mathrm{m}}_{\parallel\,\mathrm{min}}\right|$ is often set at a fixed value, typically between 3 and 4, and this is done rather independently of local wave or plasma equilibrium properties. This is because in LHCD, $p_{0,0}$ is very large (larger than 1000) and therefore $\left|p^{\mathrm{m}}_{\parallel\,\mathrm{min}}\right|$ varies very slowly with $p_{0,0}$. It is equivalent to say that spectrum components such that $N_\parallel \gtrsim 1/(3\beta_{Te})$ are strongly absorbed. We note also that in LHCD, the strongly absorbed $N_\parallel$s are then such that $\beta_{Te}/N_\parallel \lesssim 3\beta_{Te}^2 \ll 1$ and weakly relativistic effects in (5.16) can be neglected.

- In electron-cyclotron current drive, however, absorption occurs much closer to the bulk, where $\left|p^{\mathrm{m}}_{\parallel\,\mathrm{min}}\right| \simeq 1$, and therefore the power deposition profile - and consequently the CD efficiency - depends strongly on plasma and wave parameters. In other words, the LH absorption is dominated by the Gaussian dependence of the distribution function, while the EC absorption is dominated by the plasma and wave parameters.

- For EBW, it is necessary to calculate $p_{0,n}$ in order to specify which regime the evolution of $\left|p^{\mathrm{m}}_{\parallel\,\mathrm{min}}\right|$ belongs to. We recall (Section 2.3) that typical values of $\lambda_e = (k_\perp \rho_{Te})^2$ for EBWs are $\lambda_e \simeq 0.2$ for $n = 2$ HBF approach, and $\lambda_e \simeq 10$ for $n = 1$ LBF approach. We consider the asymptotic forms of $\Gamma_n[\lambda_e]/\lambda_e$:

– *Large arguments.* From [75] we get the asymptotic expansion

$$\frac{\Gamma_n[\lambda_e]}{\lambda_e} \approx \frac{1}{\sqrt{2\pi}\lambda_e^{3/2}} \quad \text{for } \lambda_e \gg 1 \tag{5.39}$$

so that for large values of $\lambda_e \simeq 10$ typically found in LBF approach, we have approximately $\Gamma_1[\lambda_e]/\lambda_e \simeq 10^{-2}$ .

– *Small arguments.* From [75] we get the power series

$$\frac{\Gamma_n[\lambda_e]}{\lambda_e} \approx \frac{\lambda_e^{n-1}}{2^n n!} \quad \text{for } \lambda_e \ll 1 \tag{5.40}$$

and we see that for small values of $\lambda_e \simeq 0.2$ typically found in second harmonic HBF approach, we have approximately $\Gamma_2[\lambda_e]/\lambda_e \simeq 10^{-2}$, which turns out to be of the same order as for LBF approach.

- We can rewrite

$$p_{0,n} \simeq \begin{cases} \dfrac{1}{\sqrt{2\pi}} \dfrac{\omega\pi}{c} \dfrac{\omega_{pe}^2}{\omega_{ce}^2} \dfrac{L_B}{|\Phi_\perp|} \dfrac{1}{\sqrt{2\pi}\left(k_\perp \rho_{Te}\right)^3} & \text{for LBF approach} \\ \dfrac{1}{\sqrt{2\pi}} \dfrac{\omega\pi}{c} \dfrac{\omega_{pe}^2}{\omega_{ce}^2} \dfrac{L_B}{|\Phi_\perp|} \dfrac{\left(k_\perp \rho_{Te}\right)^{2(n-1)}}{2^n n!} & \text{for HBF approach} \end{cases} \tag{5.41}$$

For a NSTX-type plasma with $\omega_{pe}^2 = 10\omega^2$, $\beta_{Te} = 0.05$, $\omega/2\pi = 14$ GHz, we have typically $L_B^{\text{LBF}} \simeq R_p \simeq 1$ m, while for a HBF approach near the bottom of the magnetic field well on the outboard side, $L_B^{\text{HBF}}$ depends strongly on the propagation path and can be much larger than $R_p$. Taking for example $L_B^{\text{HBF}} = 10$ m and $f_B = 1$, $p_{0,n}$ scales approximately as

$$p_{0,n} \approx \begin{cases} 1000 & \text{for } n = 1 \text{ LBF approach} \\ 200 & \text{for } n = 2 \text{ HBF approach} \end{cases} \tag{5.42}$$

As a consequence of the large values for $p_{0,n}$ for EBWs, the value of $\left|p_{\parallel \min}^{\text{m}}\right|$ is very insensitive to variations in $p_{0,n}$, which justifies a posteriori our assumption to consider wave and plasma parameters constant in the damping region, except for the

magnetic field. Considering the typical values for $p_{0,n}$ for EBWs (5.42), we observe that the location of the peak of deposition is a rather fixed quantity, and is located at $3 \lesssim p_n^{\mathrm{m}} \lesssim 3.5$. The explanation is that EBW is deposited in the tail of the distribution function, which varies so strongly as a function of $p_{\parallel \min}/p_{Te}$ that the location of deposition is a function of these variations rather than anything else.

This is an important result in the study of EBWCD, because it means that the normalized CD results will not depend much upon the parameters that typically affect greatly ECCD results, such as the density and the magnetic field scale length. Rather, we should approach EBWCD more like LHCD where the location of damping in momentum space is a fixed quantity. Another important observation is that EBWs are deposited on electrons in the tail of the distribution function, which are less collisional than bulk electrons, and therefore better current drive efficiencies than in ECCD can be anticipated.

### 5.1.7 Harmonic overlapping with EBWs

In this section, we have always assumed that harmonics could be considered separately, meaning the the wave damping was strongly dominated by the contribution of only one harmonic. As we saw on Fig. 5-4, there is a position (measured by $y_n$) between two harmonics where the contributions from the two harmonics are comparable. We will call this position the overlapping point. With (2.108) $\omega_{ce} = \omega y_n/n$, we find that the overlapping point is characterized by

$$\frac{y_n}{n} = \frac{y_{n+1}}{n+1} \tag{5.43}$$

This condition can be expressed as a function of $p_n$ according to (5.13), which gives

$$\frac{1-\beta_{Te}N_{\parallel}p_n}{n} = \frac{1-\beta_{Te}N_{\parallel}p_{n+1}}{n+1} \tag{5.44}$$

The question of the overlapping problem can then be expressed as such: under which conditions does the Doppler effects increase sufficiently such that the over-

lapping point is in the strong damping region? In that case, we will say the two harmonics overlap, and it is not possible for the wave to propagate between the two harmonics, and the corresponding region in the plasma is inaccessible, because the wave power would be absorbed before reaching this region.

The overlapping point necessarily separates a LBF approach region (near harmonic $n$) from a HBF approach region (near harmonic $n+1$). Because relativistic effects reduce the damping in one case (LBF) and increase the damping in the other case (HBF) with comparable shift in amplitude, the overall effect of relativistic corrections on the overlapping problem is mainly to move the overlapping point closer to the LBF resonance (harmonic $n$). These effects are neglected in the determination of the overlapping condition.

The strong damping region can be defined as including the locations between the resonance and the position $|p_n^{\mathrm{m}}|$ of the peak in the deposition profile when only one harmonic is considered at a time. Using (5.44) and the fact that $p_n^{\mathrm{m}}$ is of the same sign as $\sigma\sigma_{\|}$, where $\sigma = +1$ for LBF approach and $\sigma = -1$ for HBF approach and $\sigma_{\|}$ is the sign of $N_{\|}$, the overlapping point coincides with the position of peak deposition for

$$\frac{1 - \beta_{Te} \left|N_{\|}\right| \left|p_n^{\mathrm{m,LBF}}\right|}{n} = \frac{1 + \beta_{Te} \left|N_{\|}\right| \left|p_{n+1}^{\mathrm{m,HBF}}\right|}{n+1} \tag{5.45}$$

which gives an equation for $\beta_{Te} \left|N_{\|}\right|$

$$\beta_{Te} \left|N_{\|}\right| = \frac{1}{n \left|p_{n+1}^{\mathrm{m,HBF}}\right| + (n+1) \left|p_n^{\mathrm{m,LBF}}\right|} \tag{5.46}$$

According to results in Section 5.1.6, the location of the peaks of deposition between first and second harmonics is given by $\left|p_1^{\mathrm{m,LBF}}\right| \simeq \left|p_{n+1}^{\mathrm{m,HBF}}\right| \simeq 3.5$. For typical $\beta_{Te} = 0.05$, the overlapping condition becomes $\left|N_{\|}\right| \gtrsim 2$. Note that our definition of harmonic overlapping is a rather conservative one, since we impose that the peaks of one-harmonic deposition profiles must coincide. However, the profiles themselves will visibly overlap at even lower $\beta_{Te} \left|N_{\|}\right|$, as we will show in Sections 5.3 and 5.4.

We also observe that the overlapping condition becomes quickly restrictive at

higher harmonic. Even if the value of $\left|p_{n+1}^{\mathrm{m,HBF}}\right|$ decreases as higher harmonic according to (5.41), and we take the high-harmonic limit $\left|p_{n+1}^{\mathrm{m,HBF}}\right| \to 0$, we find that for $\beta_{Te} = 0.05$ and $|N_{\parallel}| \simeq 1$, harmonics completely overlap above the fourth harmonic.

## 5.2 Framework of EBWCD Calculations

### 5.2.1 Introduction

The EBW is approximated to a beam of frequency $\omega$ with Gaussian transverse amplitude profile of characteristic width $d$. We assume that the beam size $d$ is much larger than the wavelength $\lambda$. Then, the beam diffraction can be neglected and the Fourier spectrum of the beam is very localized around a central wave vector $\mathbf{k}$, since $\Delta k/k = \lambda/(2\pi d) \ll 1$. In addition, we assume that the plasma inhomogeneity scale length $L$ is also much larger than the wavelength $\lambda$, so that the WKB description of the wave is valid. With these assumptions, the local behaviour of the EBW beam can be understood by studying the uniform plasma characteristics of the linear mode $(\omega, \mathbf{k})$ corresponding to the central wave vector of the beam. Such study was done in Section 2.3 where properties of EBWs relevant to EBWCD were described by solving the local dispersion relation.

In this thesis, we restrict our calculations of EBWCD to the horizontal midplane ($Z = 0$). According to the discussion in Section 3.5.2, our quasilinear description of EBWCD is more valid near the horizontal midplane, where we can consider approximately a slab geometry, and where electrons see a quasi-uniform plasma across the EBW beam. These approximations require however that the size of the beam, projected on the poloidal field line within the flux-surface ($d_{\|P}$), be small compared to the length of the poloidal field lines: $d_{\|P} \ll 2\pi r$.

The beam size must therfore satisfy the condition

$$\lambda \ll d \ll 2\pi r, L \tag{5.47}$$

In a typical NSTX plasma, we have $\lambda \leq 0.005$ m and $2\pi r, L \geq 1$ m. The experimental beam size (which is half the beam diameter in our definitions) is typically of the order of $d = 0.05$ m [12]. Therefore, the condition (5.47) is well satisfied.

With the slab symmetry, the parallel wave number $N_{\|}$ can be taken to be approximately constant in the damping region, and the direction of the power flow

with respect to the flux-surfaces can be evaluated from solving the local dispersion relation. Thus, the propagation aspects of the EBWCD problem, such as the power deposition profile and the total driven current, can be calculated without solving the EBW propagation problem (which would otherwise require ray-tracing techniques).

In addition, the EBW electric field amplitude is assumed to be sufficiently small such that non-linear wave-particle interaction effects (trapping) can be neglected.

The calculations of EBWCD are presented in two steps: local calculations, which have a great generality, and integrated calculations, which are applied to a particular plasma and illustrate the local calculations.

### 5.2.2 Local calculations and parametric dependence

#### Definition

In order to describe the CD mechanism and study parametric dependence of the CD damping and efficiency, we first consider "local" calculations, which are independent of any particular plasma magnetic geometry or plasma profiles, and thus could apply *a priori* to any axisymmetric toroidal device - ST, tokamak or RFP - where EBWCD is considered. However, the nominal parameters of these calculations are chosen to be typical of a high-$\beta$ NSTX plasma at the location of the minimum $B$-field $X_{\mathrm{M}}$ ($R = 1.31$ m, $Z = 0$, $\rho = 0.63$) on the outboard side. The nominal plasma parameters relevant for EBWCD calculations are

| | | |
|---|---|---|
| electron temperature | $T_e \simeq 1.3$ keV | $(\beta_{Te} = 0.05)$ |
| electron density | $n_e \simeq 3.0 \times 10^{19}$ m$^{-3}$ | $(\alpha^2 = 12)$ |
| effective charge | $Z_{\mathrm{eff}} = 2$ | |
| trapped particle fraction | $f_t = 66$ % | |
| $B$-field variations length | $L_B = 1$ m | |

(5.48)

and the nominal wave parameters are

| | |
|---|---|
| frequency | $\omega/2\pi = 14$ GHz |
| parallel wave number | $N_\parallel = 1$ |
| spectral width | $\Delta N_\parallel = 0.1$ |

(5.49)

### Parametric study

The EBW approach to resonance is simulated by changing the magnetic field amplitude $B$, keeping all other plasma parameters constant. This explains the term "local" to describe these calculations. This approximation is justified from the results of Section 5.1, where it was demonstrated that both the CD mechanism - which depends mostly on the localization of resonant electrons in momentum space - and the power deposition profile were dominated by variations of the magnetic field amplitude through the parameter $y_n = n\omega_{ce}/\omega$. This approximation is advantageous because it allows to isolate the effects of various parameters and thus conduct an detailed, independent and rigorous parametric study. Indeed, in the local calculations, a "scan" of $y_n$ is done to simulate EBWCD with given plasma and wave parameters, and these are modified between scans to study their effect on EBWCD.

### Organization

We first consider the linear limit where the RF diffusion coefficient is much smaller than collisional diffusion, by considering an input wave power $P_b$ that is appropriately small (such that the CD efficiency is independent of $P_b$). In that case, the local normalized CD efficiency is expected to be independent of the diffusion coefficient factor $D_b^{\mathrm{RF}}$ (3.214), and therefore also independent of the incident normalized power flow $\Phi_{b\perp}$ and the plasma equilibrium magnetic geometry. However, it should depend upon the position of the resonance condition in momentum space, and thus, for a given $y_n = n\omega_{ce}/\omega$, upon $N_\parallel$ and the normalized temperature $\beta_{Te}$. We will also investigate the effects of the fraction of trapped particle $f_t$ and the effective charge $Z_{\mathrm{eff}}$, which strongly affect the dynamics of collisional pitch-angle scattering. Quasilinear effects

will then be investigated by varying the incident power density on the flux-surface. The plasma electron density affects the current drive efficiency through the collision frequency, but does not play a significant role in the EBW characteristics (Section 2.3), in the CD mechanism or in the power deposition (Section 5.1). It will be normalized out in our calculations.

### 5.2.3 Integrated calculations

The integrated effect of varying plasma parameters will be included in the "global" calculations at the end of the section, which are applied to a realistic NSTX geometry and used to validate our approximate local approach. Although the plasma parameters vary along the propagation, the parallel wave number is considered constant across the damping region, in accordance with our slab approximation. The interaction between EBWCD and the bootstrap current is also calculated for a realistic NSTX CD scenario.

### 5.2.4 Normalization and interpretation of CD results

In order to determine the intrinsic efficiency of EBWCD mechanisms independently of the plasma parameters, and thus conduct an independent parametric study of EBWCD, it is necessary to work with normalized units. In addition, normalized units - along with local calculations as defined in Section 5.2.2 - offer the possibility to extrapolate the CD results to different plasma conditions, rather than being tighted to a given scenario. In this section, all quantities are considered to be flux-surfaces averaged.

The natural normalized units follow the normalization used in the *DKE* code. The current and the density of power absorbed are normalized to

$$j = \frac{J}{q_e n_e v_{Te}}$$
$$p_{\text{abs}} = \frac{P_{\text{abs}}}{n_e m_e \nu_e v_{Te}^2} \tag{5.50}$$

where $J$ is measured in $\mathrm{A/m^2}$ and $P_{\mathrm{abs}}$ is measured in $\mathrm{W/m^3}$. Note that the normalized current is in the direction of the electron flow, which is the opposite direction to the actual driven current.

### Local figures of merit

The normalized CD efficiency $\eta$ is a local quantity (in $\psi$), which is given by the ratio

$$\eta = \frac{j}{p_{\mathrm{abs}}} \tag{5.51}$$

and is related to the dimensional figure of merit, defined as

$$\eta_{JP} = J/P_{\mathrm{abs}} \tag{5.52}$$

and expressed in A·m/W, by

$$\eta_{JP} = \frac{q_e}{m_e \nu_e v_{Te}} \eta \tag{5.53}$$

Inserting the expression (3.106) for the collision frequency, we find

$$\eta_{JP} = \frac{4\pi\varepsilon_0^2}{q_e^3 \ln\Lambda} \frac{\kappa T_e}{n_e} \eta \tag{5.54}$$

However, the definition (5.52) for the efficiency is seldom used. More common definitions of the efficiency relate to quantities that can be directly measured experimentally, such as the current and power deposition profiles $dI/d\psi$ and $dP/d\psi$. With the infinitesimal volume $dV/d\psi$ and poloidal surface $dS_P/d\psi$ elements of a flux-surface, given by (3.212) and (3.238) respectively

$$\begin{aligned} \frac{dV}{d\psi} &= \frac{4\pi^2 R_p \widehat{q}}{B_0} \\ \frac{dS_P}{d\psi} &= \frac{2\pi \overline{q}}{B_0} \end{aligned} \tag{5.55}$$

we find

$$\frac{dP}{d\psi} = P_{\text{abs}}\frac{dV}{d\psi} = \frac{4\pi^2 R_p \widehat{q} P_{\text{abs}}}{B_0}$$
$$\frac{dI}{d\psi} = J\frac{dS_P}{d\psi} = \frac{2\pi\overline{q}J}{B_0} \tag{5.56}$$

With the following definition of the efficiency

$$\eta_{IP} = \frac{dI}{dP} \tag{5.57}$$

expressed in A/W, we obtain

$$\eta_{IP} = \frac{\overline{q}}{\widehat{q}}\frac{\eta_{JP}}{2\pi R_p} \tag{5.58}$$

This expression can be rewritten as

$$\frac{dI}{dP} = \eta_{IP} = \frac{\overline{q}}{\widehat{q}}\frac{2\varepsilon_0^2}{q_e^3 \ln\Lambda}\frac{\kappa T_e}{R_p n_e}\eta \tag{5.59}$$

where we note that $\overline{q}/\widehat{q}$ accounts for the poloidal variations in the radial thickness of the incremental flux-surface, and that $\overline{q} = \widehat{q}$ for circular concentric flux-surfaces. Therefore, the measurable current drive efficiency $dI/dP$ increases with temperature, and decreases with density and the plasma size.

### Global figures of merit

The total driven current in the plasma is the integral over $dI$

$$I = \int_0^{\psi_a} \frac{dI}{d\psi}d\psi = \int_0^{\psi_a} \eta_{IP}\frac{dP}{d\psi}d\psi \tag{5.60}$$

When the deposition profile is narrow enough so that the efficiency is approximately constant across the damping region, where all the beam power is assumed to be absorbed, this integral approximately reduces to

$$I \simeq \eta_{IP\text{peak}} P_0 \tag{5.61}$$

where $\eta_{IP\text{peak}}$ is the value of $\eta_{IP}$ at the peak in the deposition profile and where $P_0$ is the power deposited by the EBW beam. With the expression (5.59) for the efficiency $\eta_{IP}$, we obtain

$$\frac{I}{P_0} \simeq \frac{\overline{q}}{\widehat{q}} \frac{2\varepsilon_0^2}{q_e^3 \ln\Lambda} \frac{\kappa T_e}{R_p n_e} \eta_{\text{peak}} \tag{5.62}$$

which is an approximate global efficiency in the narrow deposition profile limit. Note that this expression can be rewritten as

$$\eta_{\text{peak}} \simeq \frac{\widehat{q}}{\overline{q}} \frac{q_e^3 \ln\Lambda}{2\varepsilon_0^2} \frac{I R_p n_e}{\kappa T_e P_0} \tag{5.63}$$

and also as

$$\eta_{\text{peak}} \simeq \frac{\widehat{q}}{\overline{q}} \frac{\ln\Lambda}{2} \xi_{CD} \tag{5.64}$$

with

$$\xi_{CD} = 32.7 \frac{I R_p n_{e[20]}}{T_{e[\text{keV}]} P_0} \tag{5.65}$$

where $\xi_{CD}$ is the current drive efficiency defined in [76], $n_{e[20]}$ is the density divided by $10^{20}$ and $T_{e[\text{keV}]}$ is the temperature in keV. The efficiency $\xi_{CD}$ is therefore very similar to $\eta$ in the narrow deposition profile limit.

The total current (5.60) can also be rewritten as

$$I = \int \eta_{IP} \frac{dP}{dy_n} dy_n \tag{5.66}$$

where the integral is over the damping region in the vicinity of the $n^{\text{th}}$ harmonic resonance, where $y_n = 1$. This expression can be rewritten as (5.59)

$$I = \int \frac{\overline{q}}{\widehat{q}} \frac{2\varepsilon_0^2}{q_e^3 \ln\Lambda} \frac{T_e}{R_p n_e} \eta \frac{dP}{dy_n} dy_n \tag{5.67}$$

For "local" EBWCD calculation, as prescribed in Section 5.2.2, all parameters are assumed to be constant across the damping region except the magnetic field - or equivalently $y_n$ - whose variations strongly affects both the damping and the CD

efficiency. Hence, we can write

$$\frac{I}{P_0} = \frac{\overline{q}}{\widehat{q}} \frac{2\varepsilon_0^2}{q_e^3 \ln\Lambda} \frac{\kappa T_e}{R_p n_e} \overline{\eta} \tag{5.68}$$

where we define the integrated efficiency

$$\overline{\eta} \equiv \int \eta \left( \frac{1}{P_0} \frac{dP}{dy_n} \right) dy_n = \int \eta \left( \frac{1}{P_0} \frac{dP}{dp_n} \right) dp_n \tag{5.69}$$

The global efficiency $I/P_0$ is therefore proportional to $\overline{\eta}$, which is the efficiency $\eta$ weighted by the deposition profile $\frac{1}{P_0}\frac{dP}{dp_n}$. In local EBWCD calculations, the normalized CD efficiency $\eta$ will be plotted on the same graph as $\frac{1}{P_0}\frac{dP}{dp_n}$, with the interpretation that the integral of the product $\eta \left( \frac{1}{P_0}\frac{dP}{dp_n} \right)$ over the damping region gives the total current. Note that we can also rewrite

$$\xi_{CD} = \frac{\overline{q}}{\widehat{q}} \frac{2}{\ln\Lambda} \overline{\eta} \tag{5.70}$$

which is consistent with $\overline{\eta} \simeq \eta_{\text{peak}}$ in the narrow deposition profile limit, where $\eta_{\text{peak}}$ is taken at the peak in the deposition profile.

## 5.3 LBF ($n\omega_{ce} < \omega$) approach

We first consider a LBF scenario for EBWCD. We have seen in Section 1.3 that LBF wave-particle interaction typically takes place in the inboard side of the plasma in a high-$\beta$ plasma (see Fig. 1-9). In that case, trapped electron effects are expected to play a lesser role and therefore Fisch-Boozer effect should dominate current generation. The calculations are restricted to the horizontal inboard midplane ($\theta = 180°$), which is relevant since trapped electron effects are minimized at this location.

In our study of LBFCD, we consider only the $n = 1$ resonance, because LBFCD accessibility is very limited for harmonics $n \geq 2$, as we saw in Section 1.3.

Considering local calculations, as defined in Section 5.2.2, an example of LBF

approach to EBWCD is considered first. The CD results are explained according to the CD mechanism. By calculating the power deposition profile and comparing with the CD efficiency profile, it is possible to identify an optimization scheme for LBF-EBWCD. The parametric dependence of EBWCD on the parallel wave number, the temperature, the effective charge, and the fraction of trapped particles is calculated. Quasilinear effects on EBWCD are also investigated. Then an integrated calculation of EBWCD is presented and illustrates the LBF-EBWCD mechanism in realistic ST geometry. Finally, the effects of the interaction with the bootstrap current are described.

### 5.3.1 EBWCD calculation in LBF approach

By varying the frequency ratio $y_n$ keeping all other parameters constant, it is possible to simulate the EBW approaching the resonance and calculate analytically the power deposition - as a function of $y_n$ - by integrating over the absorption coefficient, as done in Appendix B.4. Knowledge of the power deposition profile is important in order to estimate the driven current density and optimize EBWCD.

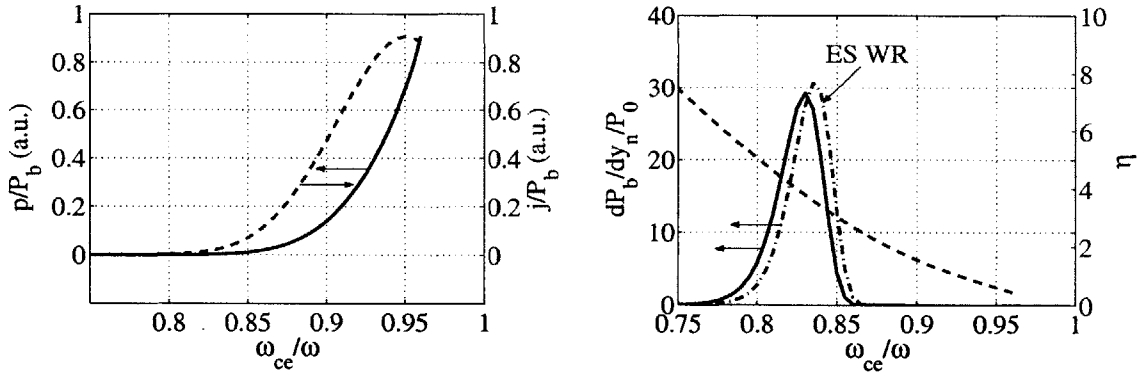


Figure 5-6: Relative evolution of (a) the current (dashed red line) and absorbed power (solid blue line) densities, and (b) the normalized efficiency $\eta$ (dashed red line) and the power deposition profile $dP_b/P_0dy_n$ (solid blue line) as a function of $\omega_{ce}/\omega$.

We consider the plasma and wave parameters given in the tables (5.48) and (5.49)

respectively. For various values of $y_n < 1$, and a given input power $P_b$, we solve the Fokker-Planck equation (3.118) and calculate the resulting normalized driven current density $j$ and absorbed power density $p_{\text{abs}}$. The results are shown on Fig. 5-6, graph (a), where the blue solid line is $p_{\text{abs}}/P_b$ and the dashed red line is $j/P_b$, normalized to the input power density. As expected from the results of Section 5.1.5, the absorbed power density increases as $y_n$ increases towards $y_n = 1$ and the wave approaches resonance. The current density picks up further from the resonance and then saturates. Consequently, the normalized current drive efficiency, defined as $\eta = j/p_{\text{abs}}$ and shown on graph (b) as a red dashed line, decreases steadily towards resonance.

### 5.3.2 Current drive mechanism

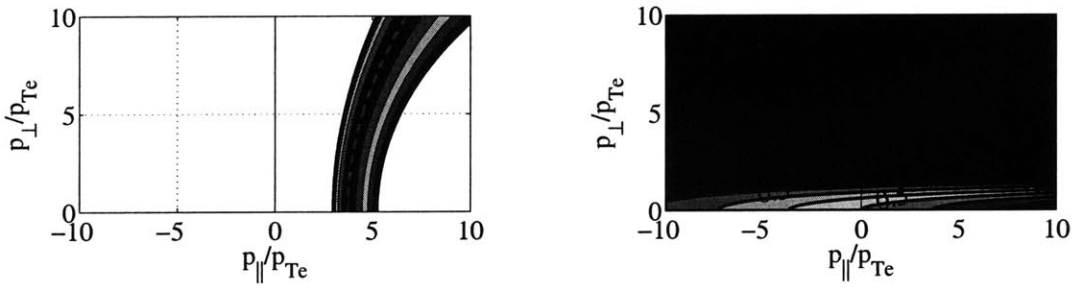


(a) (b)

Figure 5-7: Resonance condition term $\delta\left(N_{\|\text{res}}(\mathbf{p}) - N_{\|}, \Delta N_{\|}\right)$ (a), and polarization term $|\Theta^1|$ (b) contributing to the diffusion coefficient in momentum space, for $y_n = 0.83$.

The current drive mechanism can be understood by considering the various components of the RF diffusion coefficient (3.205), namely the resonance term

$$\delta\left(N_{\|\text{res}} - N_{\|}, \Delta N_{\|}\right) \equiv \frac{1}{\sqrt{\pi}\Delta N_{\|}} \exp\left[-\frac{\left(N_{\|\text{res}} - N_{\|}\right)^2}{\Delta N_{\|}^2}\right] \tag{5.71}$$

and the polarization term $\left|\Theta^{(1)}\right|$ (3.194), plotted in momentum space as contour plots in Fig. 5-7 on graphs (a) and (b) respectively. Calculations are done for $y_n = 0.83$. As expected, the resonance condition leads to a diffusion confined around the central resonance curve, characterized by $\left(y_n, N_\parallel\right)$ (5.10) and shown as a red dashed line, with a characteristic width in $p_\parallel$: $\Delta p_\parallel \sim p_\parallel \Delta N_\parallel / N_\parallel$. Because we took $N_\parallel = 1$, the resonance curve is a parabola in momentum space. In the limit of electrostatic polarization, the term $\left|\Theta^{(1)}(\mathbf{p})\right|$ can be rewritten approximately as (5.20), where $J_1(z)/z$ peaks at the origin and has a first zero for $z \simeq 3.8$. Because of the large value of $k_\perp \rho_{Te} \simeq 2.1$ in LBF approach, as seen in Section 2.3, $z = k_\perp \rho_{Te} p_\perp / p_{Te}$ (5.21) corresponds to a relatively small value of $p_\perp = 1.8 p_{Te}$, and therefore most of the interaction is confined to $p_\perp < 1.8 p_{Te}$, that is, electrons with mostly parallel momentum. We also note that the effect of the parallel component of the polarization, which explains the strong $p_\parallel$ asymmetry in $\left|\Theta^{(1)}\right|$, is quite important because the small amplitude of $e_\parallel$ is compensated by the factor $p_\parallel / p_\perp$ which can be very large since the polarization term contribution is confined to a narrow band near the $p_\perp = 0$ axis. Because $e_\parallel \simeq N_\parallel / N$, larger $N_\parallel$ are expected to have a positive effect of this term and increase the diffusion coefficient.

The resulting diffusion coefficient is shown on Fig. 5-8, graph (b), where its magnitude is represented by a contour plot and the dashed red and blue lines represent the central $N_\parallel$ resonance curve and the first zero of $\left|\Theta^{(1)}\right|$ (3.194), respectively. The RF diffusion is therefore mostly confined around the resonance curve and under the first zero line, with a much weaker secondary peak above the line. The black arrows indicate the direction of RF diffusion, where the angle of diffusion is given by (5.26) and the direction of diffusion is given by $-\partial f / \partial p$, which is the direction of rising $p$'s for a Maxwellian. We observe that the diffusion is mostly in the perpendicular direction, as expected for cyclotron harmonic resonance. Because wave-particle interaction occurs on the inboard midplane ($\theta_b = 180°$), there are no resonant trapped electrons and the current is generated by Fisch-Boozer effect [28]. As a consequence of Fisch-Boozer CD, electron flow (opposite to the driven current since electrons carry a negative charge) is driven in the same direction as the resonant $p_{\parallel\,\mathrm{min}}$. In LBF

approach, the resonant $p_{\parallel \min}$ is also of the same sign as $N_\parallel$. We note that in LBF EBWCD, the diffusion coefficient is located near and along the $p_\perp = 0$ axis, which is favorable for Fisch-Boozer CD because the resonant electrons are located far from the trapped region and have a large parallel velocity, which generates a large anisotropy in the distribution function.

### 5.3.3 Power deposition and CD optimization

In order to estimate the actual driven current density in such scenario, it is necessary to calculate the power deposition profile, calculated by *DKE* for a density $n_e \simeq 3.0 \times 10^{19}$ m$^{-3}$ ($\alpha^2 = 12$) and $L_B = 1$ m and shown on Fig. 5-6, graph (b) as a solid blue line. The deposition profile results from the balance between increasing damping, as $y_n$ increases, and reduction in the power density carried by the wave, as the wave is being damped. This calculation of the power deposition profile is compared with the weakly relativistic calculation (green dash-dotted line), based on the expression (5.32) for the absorption coefficient. We see that the two calculations agree fairly well, which is in accordance with the results shown on Fig. 5-4.

Because of the monotonically decreasing efficiency, an increasing damping rate - which shifts the power deposition to lower $y_n$ and thus further in the tail of the distribution function - would increase the normalized driven current. According to the results of Section 5.1.6, the location of the peak of deposition - with respect to $p_n$ - is a rather fixed quantity at the value $p_n \simeq 3.5$. However, it is sentitive to relativistic effects, which we will investigate further in this section.

### 5.3.4 Interpretation of CD results

In order to explain the variations of $j$, $p_{\text{abs}}$ and $\eta$ with $y_n$, we calculate the diffusion coefficient (3.205) and show its magnitude in momentum space on Fig. 5-8, for three values of $y_n = 0.73$ (a), $y_n = 0.83$ (b) and $y_n = 0.93$ (c). We see that the main effect of increasing $y_n$ is to move the resonance curves in momentum space closer to the bulk, in accordance with Fig. 5-1. Therefore, as the wave moves closer to resonance,

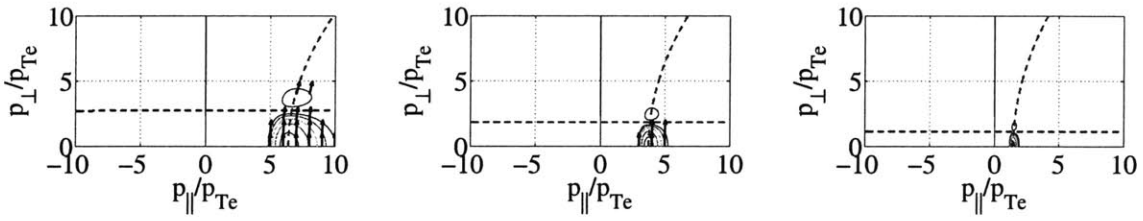


(a) (b) (c)

Figure 5-8: Contour plot of the RF diffusion coefficient in momentum space for $N_{||} = 1$ and (a) $y_n = 0.73$, (b)$y_n = 0.83$, and (c) $y_n = 0.93$. Black arrows give the direction of diffusion.

increasing $y_n$ leads to increasing damping, since the number of resonant electrons increases, but also decreasing efficiency, because resonant electrons have a decreasing parallel momentum $p_{||}$ and an increasing collisionality.

### 5.3.5 Role of $N_{||}$ in LBF EBWCD

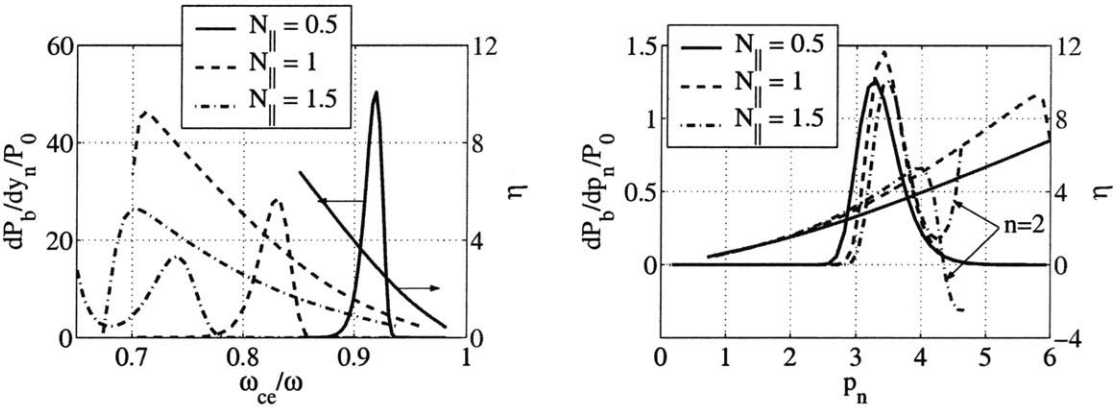


(a) (b)

Figure 5-9: Normalized efficiency $\eta$ and power deposition profile $dP_b/P_0dy_n$ as a function of $y_n = \omega_{ce}/\omega$ (a) and as a function of $p_n$ (b), for three different values of the parallel wave number: $N_{||} = 0.5$, $N_{||} = 1$ and $N_{||} = 1.5$.

On Fig. 5-9, graph (a), we show the normalized efficiency $\eta$ and power deposition profile $dP_b/dy_nP_0$ as a function of $y_n = n\omega_{ce}/\omega < 1$ (LBF), for the same parameters as

in Section 5.3.1, but for three different values of the parallel wave number, $N_{\|} = 0.5$, $N_{\|} = 1$ and $N_{\|} = 1.5$. We observe that:

- The CD calculation for $N_{\|} = 0.5$ is limited to $y_n \gtrsim 0.86$ because of the condition (5.11) for the existence of resonant electrons.

- For a given $y_n$, we saw in Fig. 5-1 that the resonance curves are closer to the bulk for larger $N_{\|}$, which is the Doppler shift effect. This explains why the profiles of power deposition $dP_b$ and of efficiency $\eta$ are shifting away from resonance ($y_n = 1$) as $N_{\|}$ increases.

- The slower variations of $dP_b$ and $\eta$ for larger $N_{\|}$ are due to the Doppler broadening effect (see Section 5.1.2).

- For a large $N_{\|} = 1.5$, the $n = 1$ and $n = 2$ resonance overlap, meaning that the deposition profiles corresponding to each harmonic cannot be separated. In other words (see Section 5.1.7), the wave cannot propagate undamped between these two harmonics for $N_{\|} = 1.5$.

Because the Doppler shift and broadening effects dominate the variations of both $dP_b$ and $\eta$, we normalize the position $y_n$ with respect to $N_{\|}$ as (B.133) $p_n = (1 - y_n) / N_{\|}\beta_{Te}$ and plot the profiles of $dP_b/dp_n P_0$ and $\eta$ as a function of $p_n$. This choice of normalization is motivated by the results of Section 5.1.2 where we saw that $p_n$ corresponds approximately to the value of $p_{\|\,\mathrm{min}}$, which is the position on the resonance curve closest to the bulk. As expected, with the Doppler effects accounted for, the profiles are now much closer and it is possible to compare the results in more detail. We observe that:

- The deposition profiles are shifting away from the resonance ($p_n = 0$) as $N_{\|}$ increases, in particular between $N_{\|} = 0.5$ and $N_{\|} = 1$. This result can be understood as a relativistic effect on power absorption. Indeed, we saw in Section 5.1.6 that relativistic effects bring the deposition closer to resonance for LBF approach, and that the relativistic shift varies as (5.36) $\beta_{Te}/\left|N_{\|}\right|$, meaning

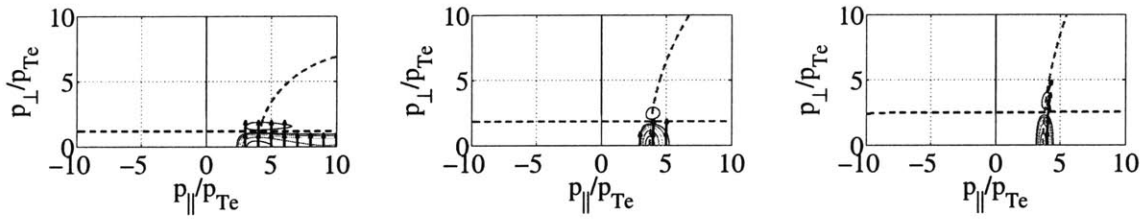


Figure 5-10: Contour plot of the RF diffusion coefficient in momentum space for (a) $N_{\|} = 0.5$ and $y_n = 0.92$, (b) $N_{\|} = 1.0$ and $y_n = 0.83$, and (c) $N_{\|} = 1.5$ and $y_n = 0.74$. Black arrows give the direction of diffusion.

it decreases with increasing $|N_{\|}|$, which is consistent with our observations on Fig. 5-9, graph (b).

- At constant $p_n$, the CD efficiency $\eta$ increases with $|N_{\|}|$. This result can be explained by the contribution of the parallel component in the RF diffusion. We showed in Section 5.1.4 that there is a small parallel component in the RF diffusion due the relativistic effects, such that the angle of diffusion with respect to perpendicular is $\chi \simeq \frac{p_{\perp}}{p_{Te}} N_{\|} \beta_{Te}$ (5.26). This angle increases with $N_{\|}$, and this effect is enhanced by the fact that resonant $p_{\perp}/p_{Te}$ also increase with $N_{\|}$. Indeed, Doppler effect shifts the power deposition further from resonance, where $k_{\perp}\rho_{Te}$ is lower, and resonant $p_{\perp}/p_{Te}$ verify $p_{\perp}/p_{Te} < z_1/(k_{\perp}\rho_{Te})$, where $z_1$ is the first zero of $J_1(z)/z$ (5.20).

The effect of parallel diffusion can be seen of Fig. 5-10, where we calculate the diffusion coefficient (3.205) and show its magnitude in momentum space at the peak location of deposition profile for (a) $N_{\|} = 0.5$ ($y_n = 0.92$), (b) $N_{\|} = 1.0$ ($y_n = 0.83$), and (c) $N_{\|} = 1.5$ ($y_n = 0.74$). The black arrows indicate the direction of RF diffusion. The increase of the angle $\chi$ with $N_{\|}$ and the increase in resonant $p_{\perp}/p_{Te}$ are clearly visible. An increased parallel diffusion leads to a consequent increase in efficiency, because direct parallel momentum is transfered to electrons. By extension, a fully parallel diffusion would lead to normalized efficiencies comparable to LHCD, $\eta \gtrsim 15$.

| $N_\parallel$ | 0.5 | 1.0 | 1.5 |
|---|---|---|---|
| $\eta_{\text{peak}}$ | 2.9 | 3.7 | 4.2 |

Table 5.1: CD efficiency $\eta$ measured at the peak of deposition profile for various values of $N_\parallel$.

An estimation of the total driven current efficiency is $\eta_{\text{peak}}$ (5.62), the efficiency measured at the peak of deposition profile $y_{n,\text{peak}}$ or $p_{n,\text{peak}}$. The results are shown in Table 5.1. The combined effect of a shift of the deposition profile (in $p_n$) and an increase of the CD efficiency (at fixed $p_n$) result in a significant increase in the peak current drive efficiency with $N_\parallel$. The conclusion is that a higher $N_\parallel$ is better as long as the harmonics do not overlap.

### 5.3.6 Role of the temperature in LBF EBWCD

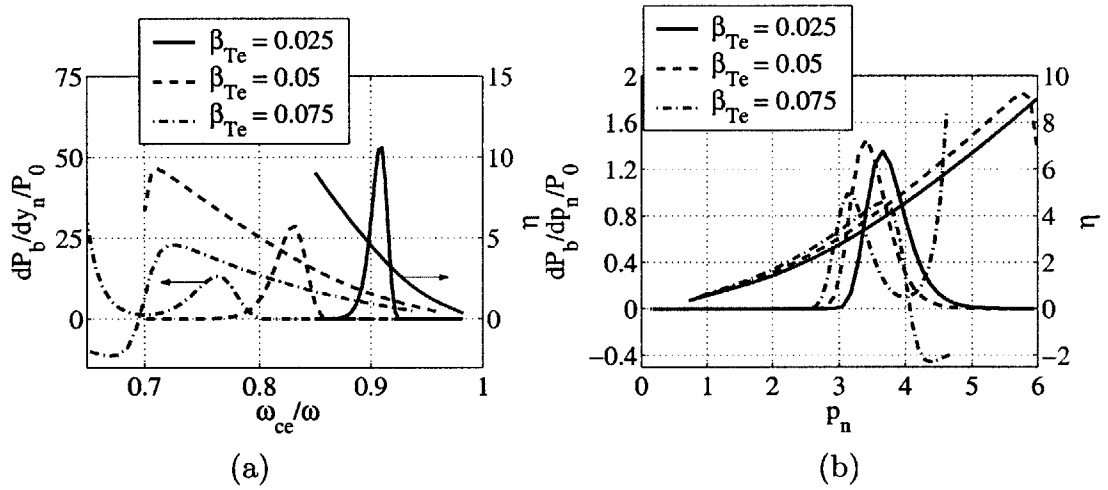


Figure 5-11: Normalized efficiency $\eta$ and power deposition profile $dP_b/P_0 dy_n$ as a function of $y_n = \omega_{ce}/\omega$ (a) and as a function of $p_n$ (b), for three different values of the normalized temperature, $\beta_{Te} = 0.025$, $\beta_{Te} = 0.05$ and $\beta_{Te} = 0.075$.

On Fig. 5-11, graph (a), we show the normalized efficiency $\eta$ and power deposition profile $dP_b/dy_n P_0$ as a function of $y_n = n\omega_{ce}/\omega < 1$ (LBF), for the same parameters as in Section 5.3.1, with $N_\parallel = 1$, but for three different values of the normalized temperature $\beta_{Te} = \sqrt{T_e/(m_e c^2)}$: $\beta_{Te} = 0.025$, $\beta_{Te} = 0.05$ and $\beta_{Te} = 0.075$, which correspond to $T_e = 0.3$ keV, $T_e = 1.3$ keV, and $T_e = 2.9$ keV respectively. We observe

that:

- For given $y_n$ and $N_\parallel$, the position of the resonance curves (5.10) is not a function of temperature in the momentum space $\left(p_\perp/m_ec, p_\parallel/m_ec\right)$, but it is clearly a function of temperature in the space $\left(p_\perp/p_{Te}, p_\parallel/p_{Te}\right)$, which is relative to the distribution function, as a result of the change of coordinates. The Doppler shift effect is therefore proportional to $p_{Te}/m_ec = \beta_{Te}$, as seen on garph (a).

- The slower variations of $dP_b$ and $\eta$ for larger $N_\parallel$ are due to the Doppler broadening effect (see Section 5.1.2).

- For a large $\beta_{Te} = 0.075$, the $n = 1$ and $n = 2$ resonance overlap, meaning that the deposition profiles corresponding to each harmonic cannot be separated. In this way, $\beta_{Te}$ and $N_\parallel$ have similar effects since the overlapping condition (5.46) is a condition on $\beta_{Te}\left|N_\parallel\right|$.

In order to isolate the Doppler shift and broadening effects, we normalize again the position $y_n$ as (B.133) $p_n = \left(1 - y_n\right)/N_\parallel\beta_{Te}$ and plot the profiles of $dP_b/dp_nP_0$ and $\eta$ as a function of $p_n$. With the Doppler effects accounted for, the profiles are now much closer and it is possible to compare the results in more details. We observe that:

- Unlike the case of increasing $N_\parallel$, the deposition profiles are shifting towards the resonance ($p_n = 0$) as $\beta_{Te}$ increases, which is again a relativistic effect on power absorption. Indeed, we saw in Section 5.1.6 that relativistic effects bring the deposition closer to resonance for LBF approach, and that the relativistic shift varies as (5.36) $\beta_{Te}/\left|N_\parallel\right|$, meaning it increases with $\beta_{Te}$, which is consistent with our observations on Fig. 5-11, graph (b).

- At constant $p_n$, the CD efficiency $\eta$ increases with $\beta_{Te}$. This result can again be explained by the contribution of the parallel component in the RF diffusion. We showed in Section 5.1.4 that the angle of diffusion with respect to perpendicular is $\chi \simeq \frac{p_\perp}{p_{Te}}N_\parallel\beta_{Te}$ (5.26). This angle increases with $\beta_{Te}$, and this effect is

| $\beta_{Te}$ | 0.025 | 0.050 | 0.075 |
|---|---|---|---|
| $\eta_{\text{peak}}$ | 3.8 | 3.7 | 3.7 |

Table 5.2: CD efficiency $\eta$ measured at the peak of deposition profile for various values of $\beta_{Te}$.

enhanced by the fact that resonant $p_\perp/p_{Te}$ also increase with $\beta_{Te}$, since Doppler effect shifts the power deposition further from resonance, where $k_\perp \rho_{Te}$ is lower, and resonant $p_\perp/p_{Te}$ verify $p_\perp/p_{Te} < z_1/(k_\perp \rho_{Te})$, where $z_1$ is the first zero of $J_1(z)/z$ (5.20).

An estimation of the total driven current efficiency is $\eta_{\text{peak}}$, the efficiency measured at the peak of deposition profile $y_{n,\text{peak}}$ or $p_{n,\text{peak}}$. The results are shown in Table 5.2. The negative effect of an increasing shift of the deposition profile (in $p_n$) and the positive effect of an increase of the CD efficiency (at fixed $p_n$), as $\beta_{Te}$ increases, almost cancel so that the total effect of $\beta_{Te}$ on the normalized efficiency is negligeable, as the harmonics do not overlap. However, we should keep in mind that for a fixed $\eta$, the absolute current drive efficiency $\eta_{JP}$ (5.54) increases linearly as a function of $\beta_{Te}$, when the normalization is taken into account. This increase results from the reduction of collisionality at higher temperature.

### 5.3.7 Collisional response: role of $Z_{\text{eff}}$ and electron trapping

In the linear limit, $Z_{\text{eff}}$ and electron trapping do not affect the power deposition profile. However, they affect the collisional response of the plasma, and thus the current drive efficiency.

On Fig. 5-12, we show the normalized efficiency $\eta$ and power deposition profile $dP_b/dy_n P_0$ as a function of $y_n = n\omega_{ce}/\omega < 1$ (LBF), for the same parameters as in Section 5.3.1, but either (a) for three different values of the effective charge $Z_{\text{eff}} = 1$, $Z_{\text{eff}} = 2$ and $Z_{\text{eff}} = 3$, or (b) for three different values of the trapped electron fraction, $f_t = 47$ %, $f_t = 66$ % and $f_t = 81$ %. As expected, the linear power deposition profile is independent of $Z_{\text{eff}}$ and $f_t$.

Considering the effect of $Z_{\text{eff}}$, we see that the current drive efficiency decreases ste-

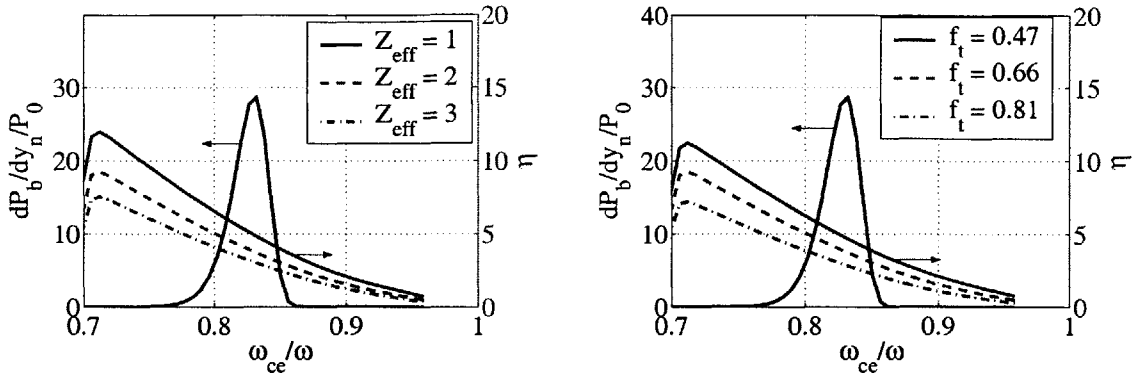


Figure 5-12: Normalized efficiency $\eta$ and power deposition profile $dP_b/P_0dy_n$ as a function of $\omega_{ce}/\omega$ for (a) three different values of the effective charge $Z_{\text{eff}} = 1$, $Z_{\text{eff}} = 2$ and $Z_{\text{eff}} = 3$, and for (b) three different values of the trapped electron fraction, $f_t = 47$ %, $f_t = 66$ % and $f_t = 81$ %.

dily with $Z_{\text{eff}}$ (graph a), which is a general characteristic of any current drive scenario. Indeed, the collisional pitch-angle scattering of electrons on ions, which increases proportionally to $Z_{\text{eff}}$, tends to isotropize the distribution function and therefore reduces the parallel current.

Despite the fact that there are no trapped electrons at the location of wave-particle resonance ($\theta = 180°$), trapped electrons affect the current drive efficiency $\eta$, which decreases when the trapped fraction $f_t$ increases (graph b). Indeed, resonant electrons rapidly move back and forth from inboard to outboard sides, because of fast motion along the field lines. When they are on the outboard side, they exchange momentum with trapped particles through collisions. Because of the fast bounce motion of trapped electrons, this momentum can almost immediately be transferred to counter-passing electrons. In other words, the trapped region acts as a short-circuit in collisional pitch-angle scattering, thus increasing the collisional isotropization of the distribution function.

An estimation of the total driven current efficiency is $\eta_{\text{peak}}$, the efficiency measured at the peak of deposition profile $y_{n,\text{peak}}$ or $p_{n,\text{peak}}$. The results are shown in Table 5.3 as a function of $Z_{\text{eff}}$ (a) and $f_t$ (b).

| $Z_{\text{eff}}$ | 1 | 2 | 3 |
|---|---|---|---|
| $\eta_{\text{peak}}$ | 4.8 | 3.7 | 3.0 |

(a)

| $f_t$ | 47 % | 66 % | 81 % |
|---|---|---|---|
| $\eta_{\text{peak}}$ | 4.6 | 3.7 | 2.8 |

(b)

Table 5.3: CD efficiency $\eta$ measured at the peak of deposition profile for various values of (a) $Z_{\text{eff}}$ and (b) $f_t$.

### 5.3.8 Quasilinear effects on EBWCD

The calculations so far were done in the linear limit. The quasilinear effects on EBWCD can be investigated by increasing the incident power in the EBW beam.

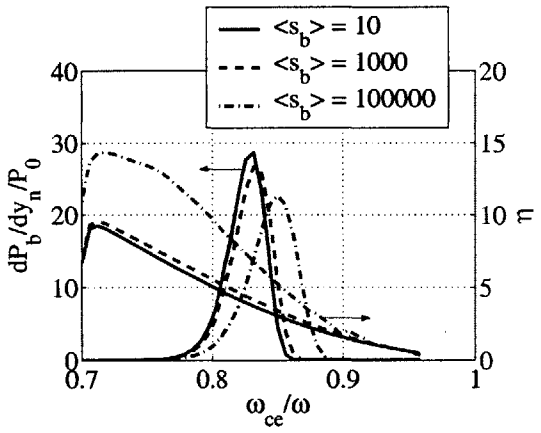


Figure 5-13: Normalized efficiency $\eta$ and power deposition profile $dP_b/P_0 dy_n$ as a function of $\omega_{ce}/\omega$, for three different values of the incident energy flow: $s_{\text{inc}} = 0.01$ kW/m$^2$, $s_{\text{inc}} = 1$ kW/m$^2$ and $s_{\text{inc}} = 100$ kW/m$^2$.

On Fig. 5-13, graph (a), we show the normalized efficiency $\eta$ and power deposition profile $dP_b/dy_n P_0$ as a function of $y_n = n\omega_{ce}/\omega < 1$ (LBF), for the same parameters as in Section 5.3.1, but for three different values of the incident energy flow density $s_{\text{inc}} = 0.01$ kW/m$^2$, $s_{\text{inc}} = 1$ kW/m$^2$ and $s_{\text{inc}} = 100$ kW/m$^2$. This last value corresponds to experimental power levels (about one Megawatt in NSTX) and approaches the limit of validity of our quasilinear operator with respect to non-linear effects, according to results from Section 3.5.3.

The difference between $s_{\text{inc}} = 0.01$ kW/m$^2$, $s_{\text{inc}} = 1$ kW/m$^2$ does not affect the CD results significantly, which means that the linear regime still prevails. However, for $s_{\text{inc}} = 100$ kW/m$^2$, we observe a significant shift of the power deposition profile towards the resonance, combined with a strong increase in the efficiency $\eta$ at fixed $y_n$.

These effects can be understood by the flattening of the distribution function due to quasilinear diffusion. The modifications of the distribution function due to quasilinear diffusion can be observed on Fig. 5-14, where the steady-state distribution function was calculated for $y_n = 0.83$ and $s_{\text{inc}} = 100$ kW/m$^2$.

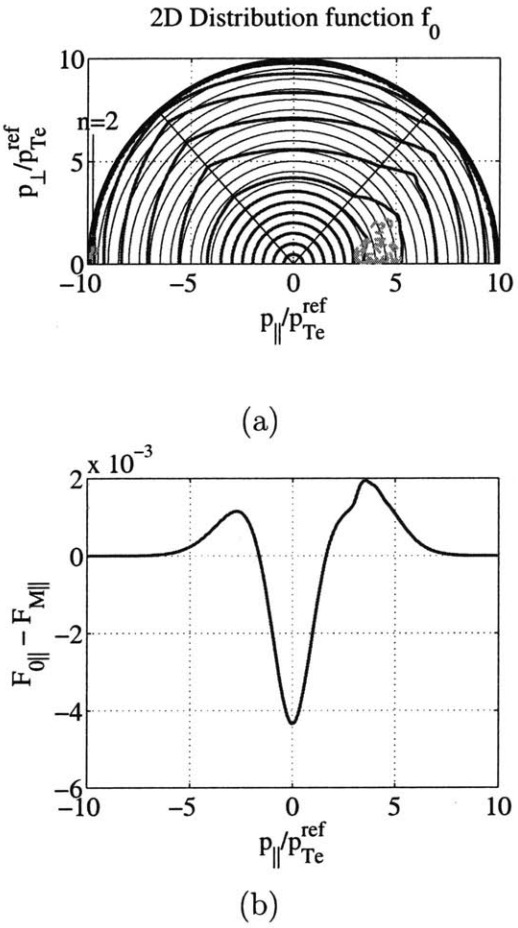


Figure 5-14: (a) Contour plot of the distribution function $f_0$ in LBF-EBWCD. The thin blue lines represent the Maxwellian distribution, and the green contours represent the magnitude of the diffusion coefficient. (b) $F_0$: same distribution integrated over the perpendicular momentum.

On graph (a), the steady-state distribution function $f_0$ is shown as a contour plot in momentum space, while on graph (b) it is integrated over the perpendicular momentum as

$$F_0\left(p_{\|}\right) = 2\pi \int_0^{\infty} p_{\perp} dp_{\perp}\, f_0\left(p_{\|}, p_{\perp}\right) \tag{5.72}$$

| $s_{\text{inc}}$ (kW/m$^2$) | 0.01 | 1 | 100 |
|---|---|---|---|
| $\eta_{\text{peak}}$ | 3.7 | 4.1 | 5.2 |

Table 5.4: CD efficiency $\eta$ measured at the peak of deposition profile for various values of $s_{\text{inc}}$.

On graph (a), the thin blue lines represents the circular contours of a Maxwellian distribution, while the thick red lines are contours of the distribution function with strong RF diffusion. The dashed green contours reprensent the magnitude of the diffusion coefficient. In the region of strong diffusion, the quasilinear distortion of the distribution function is clearly visible. This flattening is in the direction of diffusion, and leads to a decrease in the density of absorbed power (normalized to the incident power) relative to the linear case, where the distribution remains Maxwellian. This reduction in the relative density of absorbed power $p_{\text{abs}}$ leads to a higher peak CD efficiency $\eta$, since $\eta = j/p_{\text{abs}}$, but also a shift of the power deposition profile towards resonance. The overall effect is positive, however, as we can see from the results of Table 5.4.

### 5.3.9 Integrated calculation of LBF EBWCD for actual ST scenario

In order to validate the parametric study presented in this section, an actual LBF EBWCD scenario in a NSTX plasma is considered. A EBW beam of frequency $\omega/2\pi = 12$ GHz is assumed to propagate along the horizontal midplane, with a constant $N_{\|} = 0.5$, as shown of Fig. 5-15 graph (a). For such parameters, the inboard side of the plasma is accessible, as shown on graph (b) where the frequency profile on the horizontal midplane shows the cyclotron harmonics including the Doppler shift $\omega = n\omega_{ce} \pm 3.5 v_{Te} k_{\|}$. The wave characteristics, power deposition and driven current are calculated along the beam path, for an initial power $P = 1$ MW in the beam. The power and current density deposition profiles are shown on graph (c). The power deposition profile peaks at the radial location $\rho \simeq 0.50$. The current is driven by Fisch-Boozer effect and peaks sightly before, meaning that the CD efficiency is decreasing

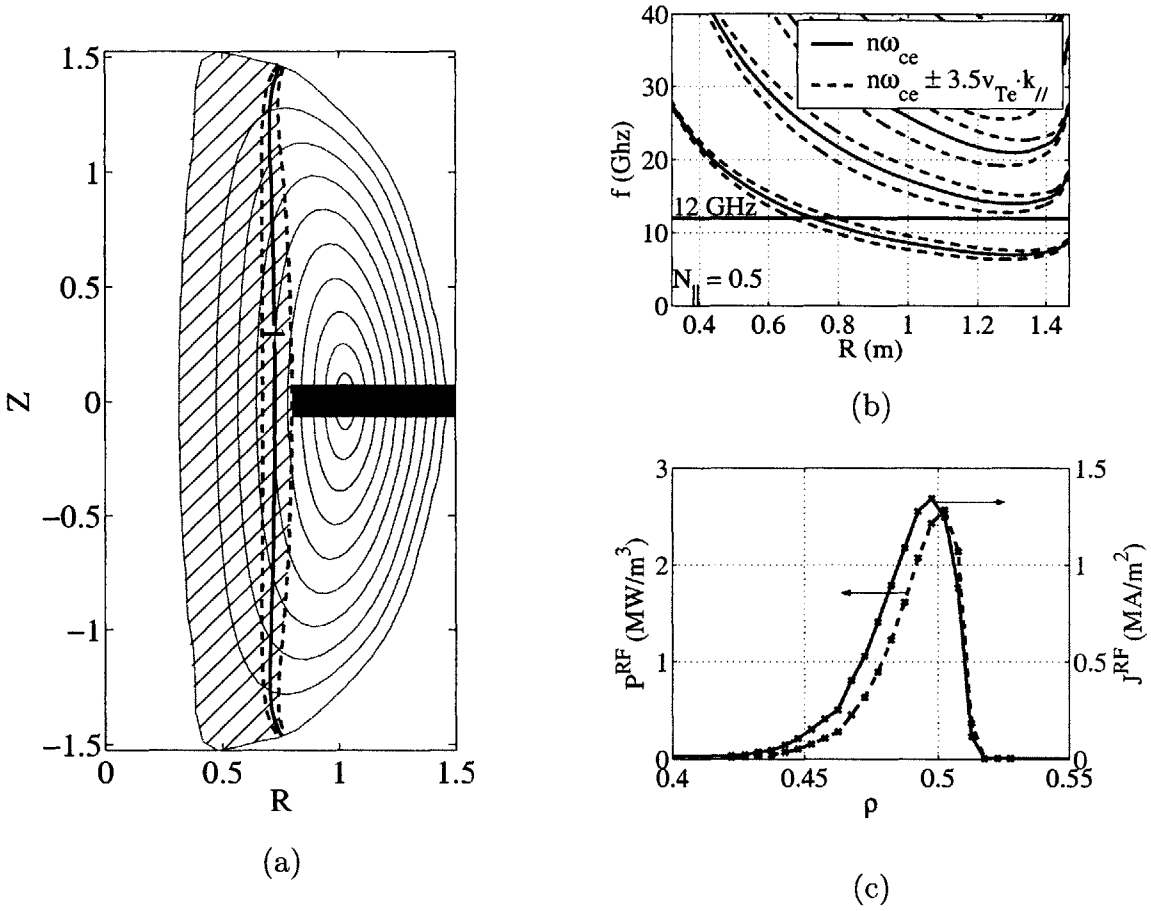


Figure 5-15: (a) Same as Fig. 1-9 for $f = 12$ GHz and $N_{\|} = 0.5$. (b) Frequency profile of the cyclotron harmonics - including the Doppler shift $\omega = n\omega_{ce} \pm 3v_{Te}k_{\|}$ - on the horizontal midplane. (c) Density of current and power deposited at a function of radius.

as expceted as the wave moves towards resonance. The normalized efficiency at the peak of power absorption is $\eta \simeq 3.7$, and the total driven current is $I = 99$ kA, so that the CD efficiency is approximately $I/P = 0.1$ A/W. In terms of normalized global efficiency as defined in (5.65), we find $\xi_{CD} = 0.67$, which is significantly higher than typical ECCD efficiencies. The power deposition profile is very narrow: $\Delta\rho = 0.04$, because of a small Doppler effect ($N_{\|} = 0.5$) and the small value of the magnetic field variations scale length on the inboard side of the plasma.

### 5.3.10 Interaction between LBF EBWCD and the bootstrap current

Because the LBF interaction between EBWs and electrons occurs on the inboard side of the plasma, where there are no trapped electrons, the interaction between the bootstrap current and EBWCD is expected to be small. To illustrate this, we consider the location of the peak in the power deposition profile calculated for the integrated LBFCD calculation in NSTX presented in Section 5.3.9. The radial location is $\rho = 0.50$. The distribution function $f_1$, which accounts for the effects of the drifts, is calculated in the absence of EBWCD - when $f_0$ is Maxwellian - which gives the bootstrap current. At this location, the bootstrap current density is $J^{\mathrm{BC}} = 0.13$ MA/m$^2$. When the effect of EBWs is included, the current calculated from $f_0$ gives the EBWCD density, $J^{\mathrm{RF}} = 1.03$ MA/m$^2$, and the current calculated from $f_1$ give the bootstrap current with synergistic effects, $J_1 = 0.15$ MA/m$^2$. Substracting $J^{\mathrm{BC}}$ from this value, we obtain the synergistic current $J^{\mathrm{syn}} = 0.02$ MA/m$^2$. This current represents about 2% of the EBW driven current and is not significant.

## 5.4 HBF ($n\omega_{ce} > \omega$) approach

We now consider a HBF scenario for EBWCD. We have seen in Section 1.3 that HBF wave-particle interaction typically takes place in the outboard side of the plasma where the dip in the magnetic field is located in a high-$\beta$ plasma. (see Fig. 1-9). This dip is located far off-axis near the midplane, such that trapped electron effects are expected to play an important role and Ohkawa effect should dominate current generation. Since trapped electron effects are maximized near the inboard horizontal midplane, restricting our calculations to $\theta = 0^{\circ}$ is relevant for HBFCD.

Because the EBW frequency is necessary higher than the electron cyclotron frequency, a HBF approach ($n\omega_{ce} > \omega$) can only be considered for $n \geq 2$. In our study of HBFCD, we consider only the $n = 2$ resonance, but many results and their interpretation can be extrapolated to higher harmonics.

Considering local calculations, as defined in Section 5.2.2, an example of HBF approach to EBWCD is considered first. The CD results are explained according to the CD mechanism. By calculating the power deposition profile and comparing with the CD efficiency profile, it is possible to identify an optimization scheme for HBF-EBWCD. The parametric dependence of EBWCD is calculated upon the parallel wave number, the temperature, the effective charge and the fraction of trapped particles. Quasilinear effects on EBWCD are also investigated. Then an integrated calculation of EBWCD is presented and illustrates the HBF-EBWCD mechanism in realistic ST geometry. Finally, the effects of the interaction with the bootstrap current are described.

### 5.4.1 EBWCD calculation in HBF approach

By varying the frequency ratio $y_n$ keeping all other parameters constant, it is possible to simulate the EBW approaching the resonance and calculate analytically the power deposition - as a function of $y_n$ - by integrating over the absorption coefficient, as done in Appendix B.4. Knowledge of the power deposition profile is important in order to estimate the driven current density and optimize EBWCD.

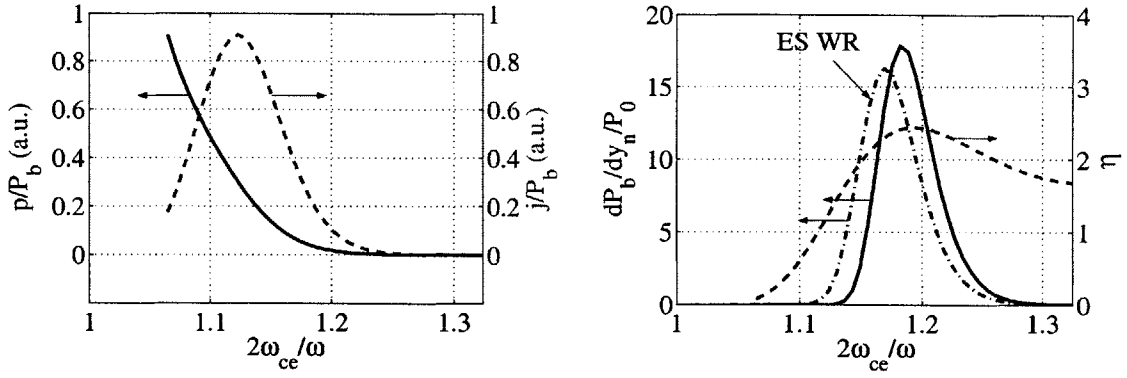


Figure 5-16: Relative evolution of (a) the current (dashed red line) and absorbed power (solid blue line) densities, and (b) the normalized efficiency $\eta$ (dashed red line) and the power deposition profile $dP_b/P_0dy_n$ (solid blue line) as a function of $y_2 = 2\omega_{ce}/\omega$.

We consider the plasma and wave parameters given in the tables (5.48) and (5.49) respectively. These parameters correspond approximately to the plasma conditions near the bottom of the dip in the magnetic field profile on NSTX, and the wave frequency $\omega/2\pi = 14$ GHz is chosen to match the second harmonic at that point. For various values of $y_n > 1$, and a given input power $P_b$, we solve the Fokker-Planck equation (3.118) and calculate the resulting normalized driven current density $j$ and absorbed power density $p_{\text{abs}}$. The results are shown on Fig. 5-16, graph (a), where the blue solid line is $p_{\text{abs}}/P_b$ and the dashed red line is $j/P_b$, normalized to the input power density. As expected from the results of Section 5.1.5, the absorbed power density increases as $y_2$ decreases towards 1 - or the wave approaches resonance. However, the current density increases and then decreases after some peak location. The normalized current drive efficiency $\eta = j/p_{\text{abs}}$ is shown on graph (b) as a red dashed line. It slowly increases as $y_n$ decreases towards 1 until some maximum value, beyond which the efficiency rapidly decreases to 0.

### 5.4.2 Current drive mechanism

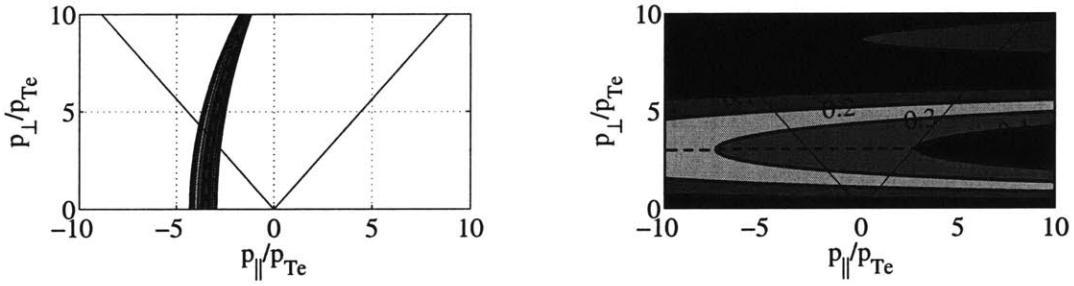


(a) (b)

Figure 5-17: Resonance condition term $\delta\left(N_{\|\text{res}}(\mathbf{p}) - N_{\|}, \Delta N_{\|}\right)$ (a), and polarization term $|\Theta^2|$ (b) contributing to the diffusion coefficient in momentum space for $y_2 = 1.19$.

The current drive mechanism can be understood by considering the various com-

ponents of the RF diffusion coefficient (3.205), namely the resonance condition

$$\delta\left(N_{\parallel \mathrm{res}}-N_{\parallel}, \Delta N_{\parallel}\right) \equiv \frac{1}{\sqrt{\pi} \Delta N_{\parallel}} \exp\left[-\frac{\left(N_{\parallel \mathrm{res}}-N_{\parallel}\right)^{2}}{\Delta N_{\parallel}^{2}}\right] \tag{5.73}$$

and the polarization term $\left|\Theta^{(2)}\right|$ (3.194), plotted in momentum space as contour plots in Fig. 5-17 on graphs (a) and (b) respectively. Calculations are done for $y_2 = 1.19$, which corresponds to the peak in the efficiency profile. As expected, the resonance condition leads to a diffusion confined around the central resonance curve, characterized by $\left(y_n, N_{\parallel}\right)$ (5.10) and shown as a red dashed line, with a characteristic width in $p_{\parallel}$: $\Delta p_{\parallel} \sim p_{\parallel} \Delta N_{\parallel} / N_{\parallel}$. Because we took $N_{\parallel} = 1$, the resonance curve is a parabola in momentum space. In the limit of electrostatic polarization, the term $\left|\Theta^{(2)}(\mathbf{p})\right|$ can be rewritten approximately as (5.20), where $J_2(z)/z$ peaks at $z \simeq 2.3$ between the two first zeros at $z = 0$ and $z \simeq 5.1$. Because of the smaller value of $k_{\perp}\rho_{Te} \simeq 0.7$ in HBF approach, as seen in Section 2.3, $z = k_{\perp}\rho_{Te}p_{\perp}/p_{Te}$ corresponds to large peak value at $p_{\perp} = 3.3 p_{Te}$, which is higher than typical resonant $p_{\perp}/p_{Te}$ in LBF approach. The interaction occurs over a wide range of $0 < p_{\perp} < 7.3\ p_{\perp}/p_{Te}$, and resonant electrons have a significant perpendicular momentum component. We also note that the effect of the parallel component of the polarization, which explains the strong $p_{\parallel}$ asymmetry in $\left|\Theta^{(2)}\right|$, is quite important because $e_{\parallel}$ is larger than for LBFCD (since $e_{\parallel} \simeq N_{\parallel}/N$ and $N$ is smaller) despite the fact that the factor $p_{\parallel}/p_{\perp}$ is smaller in this case. The asymmetry reduces $\left|\Theta^{(2)}\right|$ on the resonant side and therefore larger $N_{\parallel}$ are expected to have a negative effect of this term and decrease the magnitude of the diffusion coefficient.

The resulting diffusion coefficient is shown on Fig. 5-18, graph (b), where its magnitude is represented by a contour plot and the dashed red and blue lines represent the central $N_{\parallel}$ resonance curve and the peak of $\left|\Theta^{(2)}\right|$, respectively. The RF diffusion is therefore mostly confined around the resonance curve and peaks near where this curve crosses the blue line, with a much weaker secondary peak well above. The black arrows indicate the direction of RF diffusion, where the angle of diffusion is given by (5.26) and the direction of diffusion is given by $-\partial f/\partial p$, which is the direc-

tion of rising $p$'s for a Maxwellian. We observe that the diffusion is again mostly in the perpendicular direction, as expected for cyclotron harmonic resonance. Because wave-particle interaction occurs on the outboard midplane ($\theta_b = 0°$) and the trapped particle fraction is large (about 2/3), perpendicular diffusion leads to significant electron trapping and therefore Ohkawa current is generated [29]. As a consequence of Ohkawa CD, electron flow (opposite to the driven current since electrons carry a negative charge) is driven in the opposite direction to the resonant $p_{\parallel \min}$. However, in a HBF approach, resonant $p_{\parallel \min}$ are of opposite sign to $N_\parallel$, and therefore current is generated in the same direction as for LBF FBCD. We see that in HBF EBWCD, the diffusion coefficient is located at rather high values of $p_\perp$, which is favorable for Ohkawa CD because the resonant electrons are located close to the trapped region and significant wave-induced trapping can be expected.

### 5.4.3 Interpretation of CD results

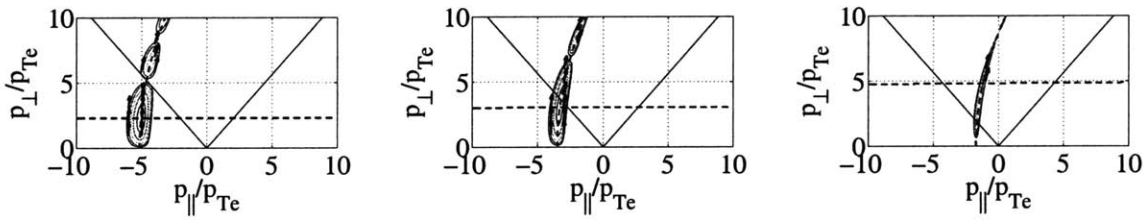


Figure 5-18: Contour plot of the RF diffusion coefficient in momentum space for $N_\parallel = 1$ and (a) $y_n = 1.29$, (b)$y_n = 1.19$, and (c) $y_n = 1.09$. Black arrows give the direction of diffusion.

In order to explain the variations of $j$, $p_{\text{abs}}$ and $\eta$ with $y_n$, we calculate the diffusion coefficient (3.205) and show its magnitude in momentum space on Fig. 5-18, for three values of $y_n = 1.29$ (a), $y_n = 1.19$ (b) and $y_n = 1.09$ (c). We see that the main effect of increasing $y_n$ is to move the resonance curves in momentum space closer to the bulk ($\left|p_{\parallel \min}\right|$ decreases), in accordance with Fig. B.149. Therefore, as the wave moves closer to resonance, decreasing $y_n$ leads to increasing damping, since the number of

resonant electrons increases, which explains the evolution of $p_{\text{abs}}$ on Fig. 5-16.

- Concerning the current density $j$, it first increases as the wave moves closer to resonance and $y_n$ decreases (a $\rightarrow$ b), mainly because the number of resonant electrons increases.

- However, even closer to the resonance (c), most of the wave power couples to trapped electrons, which do not carry any current. This explained the decreasing current density for $y_n < 1.13$. This current reduction leads to a corresponding decrease in the efficiency, which is further enhanced by the fact that the few remaining resonant electrons of the passing region have a decreasing parallel momentum $p_{\|}$ and an increasing collisionality (c).

- Note however that the heating of trapped electrons may result in changes in the bootstrap current, which will be investigated in Section 5.4.10.

- The small decrease in the efficiency as the resonance curves move away from the bulk for increasing $y_n$ (b $\rightarrow$ a) beyond the peak value $y_n = 1.19$ is the result of the balance between having less collisional resonant electrons with larger $p_{\|}$ - a positive effect - and the Fisch-Boozer effect of creating an asymmetric resistivity, which increases as the resonance moves further from the trapped region, and drives a current in the opposite direction.

- It is not surprising that the peak efficiency is obtained when the diffusion coefficient peaks just below the trapped/passing boundary (b) and perpendicular diffusion leads to maximum wave-induced trapping.

### 5.4.4 Power deposition and CD optimization

In order to estimate the actual driven current density in such scenario, it is necessary to calculate the power deposition profile, calculated by *DKE* for a density $n_e \simeq 3.0 \times 10^{19}$ m$^{-3}$ ($\alpha^2 = 12$) and $L_B = 1$ m and shown on Fig. 5-16, graph (b) as a solid blue line. The deposition profile results from the balance between increasing

damping, as $y_n$ increases, and reduction in the power density carried by the wave, as the wave is being damped. This calculation of the power deposition profile is compared with the weakly relativistic calculation (green dash-dotted line), based on the expression (5.32) for the absorption coefficient. We see that the two calculations agree fairly well, but not as well as for the LBFCD case. This is due to the fact that the electrostatic approximation, used in the calculation of (5.32), fails down near the resonance in HBF appraoch, in particular regarding the polarization (See Fig. 2-5), which is in accordance with the results shown on Fig. 5-4.

Because of the peaked efficiency profile, CD is be optimized if the peaks in the deposition profile and the efficiency coincide. According to the results of Section 5.1.6, the location of the peak of power deposition is always about $p_n \simeq 3.5$. Therefore, the optimization of HBF EBWCD requires to adjust the location of the peak in the efficiency profile accordingly, by controling the location of deposition and $N_{||}$, which will be adressed in the coming sections.

### 5.4.5 Role of $N_{||}$ in HBF EBWCD

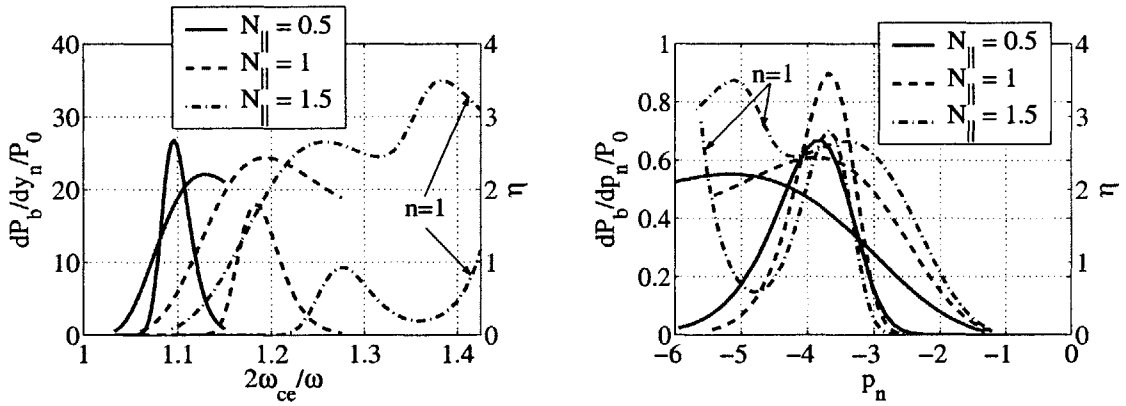


Figure 5-19: Normalized efficiency $\eta$ and power deposition profile $dP_b/P_0 dy_n$ as a function of $y_2 = 2\omega_{ce}/\omega$ (a) and as a function of $p_n$ (b), for three different values of the parallel wave number: $N_{||} = 0.5$, $N_{||} = 1$ and $N_{||} = 1.5$.

On Fig. 5-19, graph (a), we show the normalized efficiency $\eta$ and power deposition

profile $dP_b/dy_n P_0$ as a function of $y_n = n\omega_{ce}/\omega > 1$ (HBF), for the same parameters as in Section 5.4.1, but for three different values of the parallel wave number, $N_\parallel = 0.5$, $N_\parallel = 1$ and $N_\parallel = 1.5$.

- For a given $y_n$, we saw on Fig. 5-1 that the resonance curves are closer to the bulk for larger $N_\parallel$, which corresponds to the resonance Doppler shift effect. This explains why the profiles of power deposition $dP_b$ and of efficiency $\eta$ are shifting away from resonance ($y_n = 1$) as $N_\parallel$ increases.

- The slower variations of $dP_b$ and $\eta$ for larger $N_\parallel$ are due to the Doppler broadening effect (see Section 5.1.2).

- The peak value for $\eta$ increases as $N_\parallel$ increases, and the Doppler shifts of the peaks for $\eta$ and $dP_b$ are different, such that these two peaks coincide for $N_\parallel = 1$, while power deposition occurs too far away from resonance for $N_\parallel = 1.5$ and too close to the resonance for $N_\parallel = 0.5$.

- For a large $N_\parallel = 1.5$, the $n = 1$ and $n = 2$ resonance overlap, meaning that the deposition profiles corresponding to each harmonic cannot be separated. In other words (see Section 5.1.7), the wave cannot propagate undamped between these two harmonics for $N_\parallel = 1.5$.

Because the Doppler shift and broadening effects dominate the variations of both $dP_b$ and $\eta$, we normalize the position $y_n$ with respect to $N_\parallel$ as (B.133) $p_n = (1 - y_n)/N_\parallel \beta_{Te}$ and plot the profiles of $dP_b/dp_n P_0$ and $\eta$ as a function of $p_n$. This choice of normalization is motivated by the results of Section 5.1.2 where we saw that $p_n$ corresponds approximately to the value of $p_{\parallel \min}$, which is the position on the resonance curve closest to the bulk. As expected, with the Doppler effects accounted for, the profiles are now much closer and it is possible to compare the results in more details. We observe that:

- The deposition profiles moving closer to the resonance ($p_n = 0$) as $N_\parallel$ increases, in particular between $N_\parallel = 0.5$ and $N_\parallel = 1$. This result can be understood as

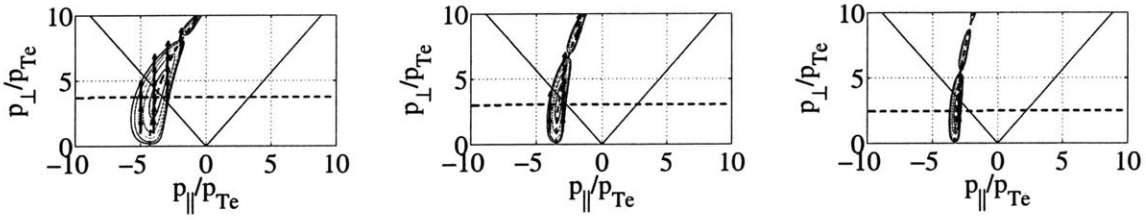


Figure 5-20: Contour plot of the RF diffusion coefficient in momentum space for (a) $N_{\|} = 0.5$ and $y_n = 1.13$, (b) $N_{\|} = 1.0$ and $y_n = 1.19$, and (c) $N_{\|} = 1.5$ and $y_n = 1.26$. Black arrows give the direction of diffusion.

a relativistic effect on power absorption. Indeed, we saw in Section 5.1.6 that relativistic effects move the power deposition away from resonance for HBF approach, and that the relativistic shift varies as (5.36) $\beta_{Te}/\left|N_{\|}\right|$, meaning it decreases with $\left|N_{\|}\right|$, which is consistent with our observations on Fig. 5-9, graph (b). In other words, the positive relativistic effects are larger for small $\left|N_{\|}\right|$.

- The peak value of $\eta$ increases with $N_{\|}$. This result can be explained by the contribution of the parallel component in the RF diffusion. We showed in Section 5.1.4 that there is a small parallel component in the RF diffusion due the relativistic effects, such that the angle of diffusion with respect to perpendicular is $\chi \simeq \frac{p_\perp}{p_{Te}} N_{\|}\beta_{Te}$ (5.26). This angle therefore increases with $N_{\|}$. Unlike the LBF CD case, the variation of resonant $p_\perp/p_{Te}$ as $N_{\|}$ changes should not be important in this case because resonant $p_\perp/p_{Te}$ are spread over a large range, a consequence of small $(k_\perp \rho_{Te})$ (5.20). The effect of parallel diffusion can be seen of Fig. 5-20, where we calculate the diffusion coefficient (3.205) and show its magnitude in momentum space at the peak location of deposition profile for (a) $N_{\|} = 0.5$ ($y_n = 1.13$), (b) $N_{\|} = 1.0$ ($y_n = 1.19$), and (c) $N_{\|} = 1.5$ ($y_n = 1.26$). The black arrows indicate the direction of RF diffusion. The increase of the angle $\chi$ with $N_{\|}$ is clearly visible. Unlike the LFBCD case, the parallel diffusion now faces towards lower $\left|p_{\|}\right|$ and so toward the bulk. Because the CD mechanism is the Ohkawa effect, this parallel component has a positive

| $N_\parallel$ | 0.5 | 1.0 | 1.5 |
|---|---|---|---|
| $\eta_{\text{peak}}$ | 1.8 | 2.4 | 2.6 |

Table 5.5: CD efficiency $\eta$ measured at the peak of deposition profile for various values of $N_\parallel$.

effect as it reduces the incidence angle between the direction of diffusion and the normal to the trapped/passing boundary. The RF diffusion is directed more toward the trapped/passing boundary. Therefore, the peak value of $\eta$ increases with $N_\parallel$.

- On Fig. 5-20, we see that for each $N_\parallel$, the largest current drive efficiency is obtained when the diffusion region peaks right beneath the trapped/passing boundary, so that wave-induced trapping is maximum.

- The profiles for the CD efficiency $\eta$ move closer to the resonance (with respect to $p_n$) as $|N_\parallel|$ increases. A possible explanation for this result is the effect of curvature in the resonance curve, which decreases as $|N_\parallel|$ increases. Therefore, in order to have the diffusion region peaking near the trapped passing boundary, the value of $|p_{\parallel\,\min}| \simeq |p_n|$ must be smaller for large $N_\parallel$. Another explanation is the variation of the peak in resonant $p_\perp/p_{Te}$ (blue dashed lines on Fig. 5-20), which moves down as $|N_\parallel|$ increases, such that the value of $|p_{\parallel\,\min}| \simeq |p_n|$ must be smaller for large $N_\parallel$.

We note that, as $|N_\parallel|$ increases, the shifts of the power deposition and efficiency profiles with respect to $p_n$ are in the same direction, which means that the range of $|N_\parallel|$ over which the two profiles coincide - and HBF Ohkawa CD is optimized - is quite large.

An estimation of the total driven current efficiency is $\eta_{\text{peak}}$ (5.62), the efficiency measured at the peak of deposition profile $y_{n,\text{peak}}$ or $p_{n,\text{peak}}$. The results are shown in Table 5.5. At $N_\parallel = 1$, the two profiles coincide, and the peak efficiency is higher than for $N_\parallel = 0.5$, which explains the large difference on $\eta_{\text{peak}}$. Between $N_\parallel = 1$ and $N_\parallel = 1.5$, the increase in the peak efficiency with $N_\parallel$ dominates the fact that the two profiles do not coincide for $N_\parallel = 1.5$, and $\eta_{\text{peak}}$ increases slightly.

### 5.4.6 Role of the temperature in HBF EBWCD

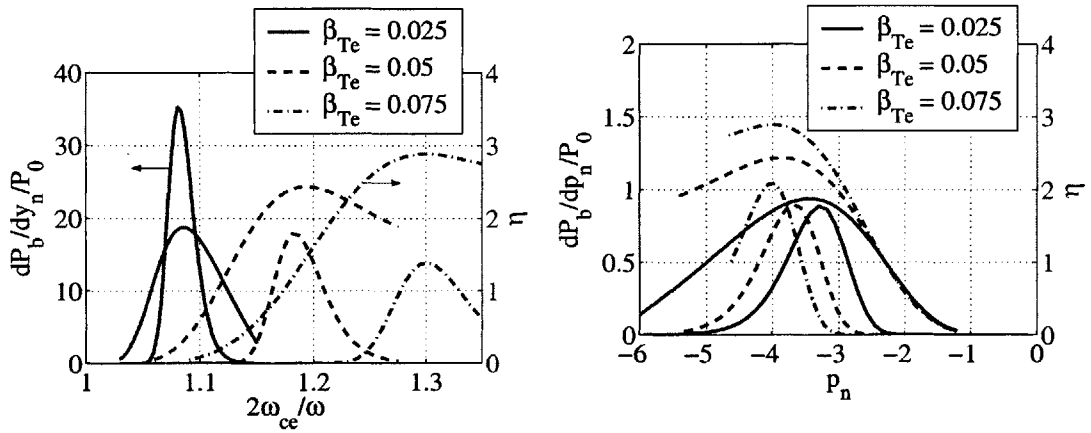


Figure 5-21: Normalized efficiency $\eta$ and power deposition profile $dP_b/P_0 dy_n$ as a function of $y_2 = 2\omega_{ce}/\omega$ (a) and as a function of $p_n$ (b), for three different values of the normalized temperature, $\beta_{Te} = 0.025$, $\beta_{Te} = 0.05$ and $\beta_{Te} = 0.075$.

On Fig. 5-21, graph (a), we show the normalized efficiency $\eta$ and power deposition profile $dP_b/dy_n P_0$ as a function of $y_n = n\omega_{ce}/\omega > 1$ (HBF), for the same parameters as in Section 5.4.1, with $N_\parallel = 1$, but for three different values of the normalized temperature $\beta_{Te} = \sqrt{T_e/(m_e c^2)}$: $\beta_{Te} = 0.025$, $\beta_{Te} = 0.05$ and $\beta_{Te} = 0.075$, which correspond to $T_e = 0.3$ keV, $T_e = 1.3$ keV, and $T_e = 2.9$ keV respectively. We observe that:

- For given $y_n$ and $N_\parallel$, the position of the resonance curves (5.10) is not a function of temperature in the momentum space $(p_\perp/m_e c, p_\parallel/m_e c)$, but it is clearly a function of temperature in the space $(p_\perp/p_{Te}, p_\parallel/p_{Te})$, which is relative to the distribution function, as a result of the change of coordinates. The Doppler shift effect is therefore proportional to $p_{Te}/m_e c = \beta_{Te}$, as seen on graph (a).

- The slower variations of $dP_b$ and $\eta$ for larger $N_\parallel$ are due to the Doppler broadening effect (see Section 5.1.2).

In order to isolate the Doppler shift and broadening effects, we normalize again the position $y_n$ as (B.133) $p_n = (1 - y_n)/N_\parallel \beta_{Te}$ and plot the profiles of $dP_b/dp_n P_0$

| $\beta_{Te}$ | 0.025 | 0.050 | 0.075 |
|---|---|---|---|
| $\eta_{\text{peak}}$ | 1.9 | 2.4 | 2.9 |

Table 5.6: CD efficiency $\eta$ measured at the peak of deposition profile for various values of $\beta_{Te}$.

and $\eta$ as a function of $p_n$. With the Doppler effects accounted for, the profiles are now much closer and it is possible to compare the results in more details. We observe that:

- Unlike the case of increasing $N_{\|}$, the deposition profiles are shifting away from the resonance ($p_n = 0$) as $\beta_{Te}$ increases, which is again a relativistic effect on power absorption. Indeed, we saw in Section 5.1.6 that relativistic effects move the deposition profile away from resonance for HBF approach, and that the relativistic shift varies as (5.36) $\beta_{Te}/\left|N_{\|}\right|$, meaning it increases with $\beta_{Te}$, which is consistent with our observations on Fig. 5-21, graph (b).

- At constant $p_n$, the CD efficiency $\eta$ increases with $\beta_{Te}$. This result can again be explained by the contribution of the parallel component in the RF diffusion. We showed in Section 5.1.4 that the angle of diffusion with respect to perpendicular is $\chi \simeq N_{\|}\beta_{Te}p_{\perp}/p_{Te}$ (5.26). This angle increases with $\beta_{Te}$. The effect of $\beta_{Te}$ on the efficiency is therefore very similar to the effect of $N_{\|}$.

- There is a shift of the $\eta$ profile away from resonance as $\beta_{Te}$ increases. Like in the case of varying $N_{\|}$, the power deposition and efficiency profiles shift in the same direction as $\beta_{Te}$ increases, which means that the range of $\beta_{Te}$ over which the two profiles coincide - and HBF Ohkawa CD is optimized - is quite large.

An estimation of the total driven current efficiency is $\eta_{\text{peak}}$, the efficiency measured at the peak of deposition profile $y_{n,\text{peak}}$ or $p_{n,\text{peak}}$. The results are shown in Table 5.6. Because the power deposition and efficiency profiles coincide quite well for all these values of $\beta_{Te}$, the increase in the peak efficiency results from the increase in the maximum efficiency with $\beta_{Te}$.

### 5.4.7 Collisional response and Ohkawa effect: role of $Z_{\text{eff}}$ and electron trapping

In the linear limit, $Z_{\text{eff}}$ and electron trapping are not assumed to affect the power deposition profile. However, they affect the collisional response of the plasma, and thus the current drive efficiency. In addition, the Ohkawa CD mechanism is very dependent on the location of the trapped/passing boundary in momentum space, and therefore on the fraction of trapped electrons.

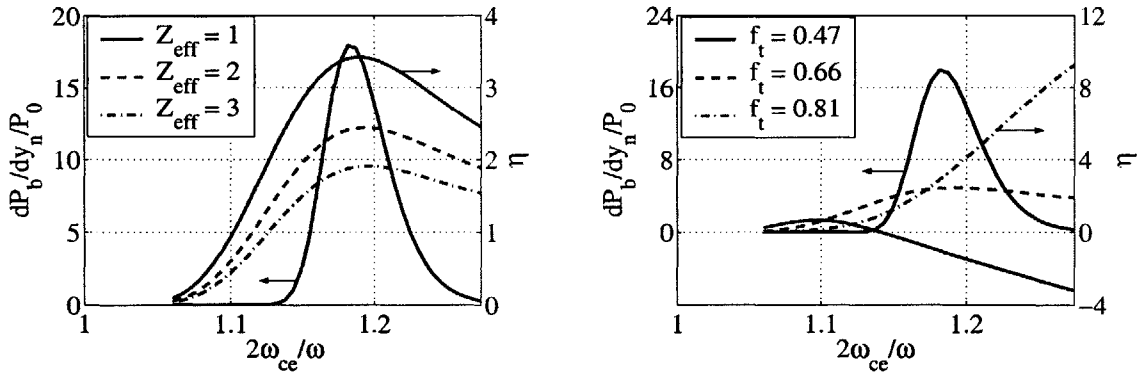


Figure 5-22: Normalized efficiency $\eta$ and power deposition profile $dP_b/P_0dy_n$ as a function of $y_2 = 2\omega_{ce}/\omega$ for (a) three different values of the effective charge $Z_{\text{eff}} = 1$, $Z_{\text{eff}} = 2$ and $Z_{\text{eff}} = 3$, and for (b) three different values of the trapped electron fraction, $f_t = 47$ %, $f_t = 66$ % and $f_t = 81$ %.

On Fig. 5-22, we show the normalized efficiency $\eta$ and power deposition profile $dP_b/dy_nP_0$ as a function of $y_n = n\omega_{ce}/\omega > 1$ (HBF), for the same parameters as in Section 5.4.1, but either (a) for three different values of the effective charge $Z_{\text{eff}} = 1$, $Z_{\text{eff}} = 2$ and $Z_{\text{eff}} = 3$, or (b) for three different values of the trapped electron fraction, $f_t = 47$ %, $f_t = 66$ % and $f_t = 81$ %. As expected, the linear power deposition profile is independent of $Z_{\text{eff}}$ and $f_t$.

Considering the effect of $Z_{\text{eff}}$, we see that the current drive efficiency decreases stedily with $Z_{\text{eff}}$ (graph a), which is a general characteristic of any current drive scenario. Indeed, the collisional pitch-angle scattering of electrons on ions, which increases pro-

| $Z_{\text{eff}}$ | 1 | 2 | 3 |
|---|---|---|---|
| $\eta_{\text{peak}}$ | 3.4 | 2.4 | 1.9 |

(a)

| $f_t$ | 47 % | 66 % | 81 % |
|---|---|---|---|
| $\eta_{\text{peak}}$ | $-1.1$ | 2.4 | 3.0 |

(b)

Table 5.7: CD efficiency $\eta$ measured at the peak of deposition profile for various values of (a) $Z_{\text{eff}}$ and (b) $f_t$.

portionally to $Z_{\text{eff}}$, tends to isotropize the distribution function and therefore reduces the parallel current.

The CD efficiency profile depends dramatically upon the fraction of trapped electrons.

- When the trapped fraction is small (case with $f_t = 47$ %) and the trapped region in momentum space is narrow, the peak in the profile of CD efficiency is close to the bulk. Further from the resonance, the driven current becomes actually negative, which means that the Fisch Boozer effect dominates. For the present power deposition profile, shown on Fig. 5-22, the total driven current would definitely be negative Fisch-Boozer current

- With a very large trapped fraction (case with $f_t = 81$ %, which would correspond to NSTX locations very close to the edge), the efficiency increases stedily away from the resonance. This means that the Fisch-Boozer current effects are negligeable, and the increase in efficiency results from the fact that the resonant electrons are further in the bulk and thus less collisional.

- Because of the strong variations in the efficiency profile when the trapped fraction is changed, the region of the plasma where Ohkawa CD is possible is limited to the far off-axis locations of the plasma.

An estimation of the total driven current efficiency is $\eta_{\text{peak}}$, the efficiency measured at the peak of deposition profile $y_{n,\text{peak}}$ or $p_{n,\text{peak}}$. The results are shown in Table 5.7 as a function of $Z_{\text{eff}}$ (a) and $f_t$ (b).

### 5.4.8 Quasilinear effects on EBWCD

The calculations so far were done in the linear limit. The quasilinear effects on EBWCD can be investigated by increasing the incident power in the EBW beam.

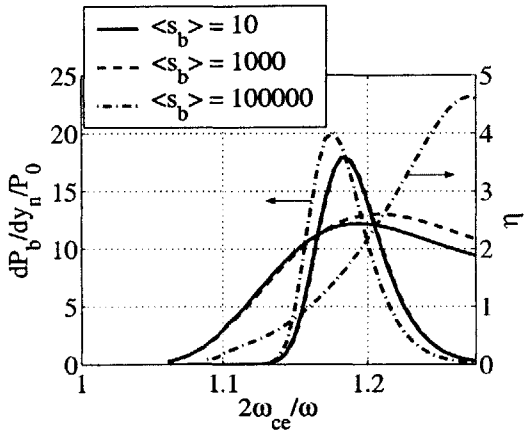


Figure 5-23: Normalized efficiency $\eta$ and power deposition profile $dP_b/P_0dy_n$ as a function of $y_2 = 2\omega_{ce}/\omega$, for three different values of the incident energy flow: $s_{\text{inc}} = 0.01$ kW/m$^2$, $s_{\text{inc}} = 1$ kW/m$^2$ and $s_{\text{inc}} = 100$ kW/m$^2$.

On Fig. 5-23, graph (a), we show the normalized efficiency $\eta$ and power deposition profile $dP_b/dy_nP_0$ as a function of $y_n = n\omega_{ce}/\omega > 1$ (HBF), for the same parameters as in Section 5.4.1, but for three different values of the incident energy flow density $s_{\text{inc}} = 0.01$ kW/m$^2$, $s_{\text{inc}} = 1$ kW/m$^2$ and $s_{\text{inc}} = 100$ kW/m$^2$. This last value corresponds to experimental power levels and approaches the limit of validity of our quasilinear operator with respect to non-linear effects, according to results from Section 3.5.3.

The difference between $s_{\text{inc}} = 0.01$ kW/m$^2$, $s_{\text{inc}} = 1$ kW/m$^2$ does not affect the CD results significantly, which means that the linear regime still prevails. However, for $s_{\text{inc}} = 100$ kW/m$^2$, we observe a shift of the power deposition profile towards the resonance, combined with a strong increase in the peak efficiency $\eta$ and a large shift of the efficiency profile away from the resonance.

These effects can be understood by the flattening of the distribution function due to quasilinear diffusion. The modifications of the distribution function due to quasilinear diffusion can be observed on Fig. 5-24, where the steady-state distribution function was calculated for $y_n = 1.19$ and $s_{\text{inc}} = 100$ kW/m$^2$.

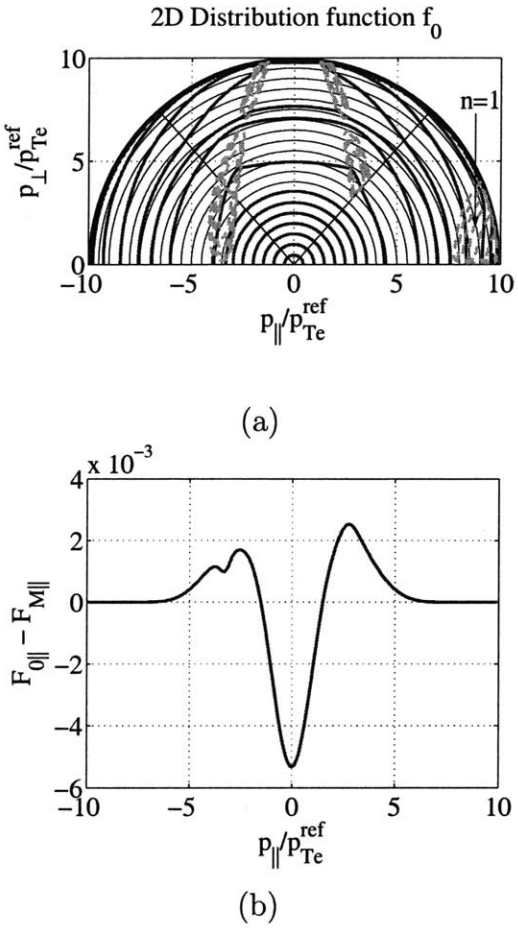


Figure 5-24: (a) Contour plot of the distribution function $f_0$ in HBF-EBWCD. The thin blue lines represent the Maxwellian distribution, and the green contours represent the magnitude of the diffusion coefficient. (b) $F_0$: same distribution integrated over the perpendicular momentum.

On graph (a), the steady-state distribution function $f_0$ is shown as a contour plot in momentum space, while on graph (b) it is integrated over the perpendicular momentum as

$$F_0\left(p_\parallel\right) = 2\pi \int_0^\infty p_\perp dp_\perp \; f_0\left(p_\parallel, p_\perp\right) \tag{5.74}$$

On graph (a), the thin blue lines represents the circular contours of a Maxwellian distribution, while the thick red lines are contours of the distribution function with strong RF diffusion. The dashed green contours reprensent the magnitude of the diffusion coefficient. In the region of strong diffusion, the quasilinear distortion of the

| $s_{inc}$ (kW/m$^2$) | 0.01 | 1 | 100 |
|---|---|---|---|
| $\eta_{peak}$ | 2.4 | 2.5 | 1.4 |

Table 5.8: CD efficiency $\eta$ measured at the peak of deposition profile for various values of $s_{inc}$.

distribution function is clearly visible. This flattening is in the direction of diffusion, and leads to a decrease in the density of absorbed power (normalized to the incident power) relative to the linear case, where the distribution remains Maxwellian. This reduction in the relative density of absorbed power $p$ leads to a higher peak CD efficiency $\eta$, since $\eta = j/p$, but also a shift of the power deposition profile towards resonance. In addition, a large shift of the efficiency profile occurs. This shift is also a consequence of the flattening of the distribution function, for which a given contour of the distribution "reaches" the trapped/passing boundary further away from the resonance.

Because the peaks in the profiles for the power deposition and the driven current do not coincide for the large energy flow density case, the overall effect can be negative, as we can see from the results of Table 5.8.

### 5.4.9 Integrated calculation of HBF EBWCD for actual ST scenario

In order to validate the parametric study presented in this section, an actual HBF EBWCD scenario in a NSTX plasma is considered. A EBW beam of frequency $\omega/2\pi = 12$ GHz is assumed to propagate along the horizontal midplane, with a constant $N_{||} = 1.0$, as shown of Fig. 5-25 graph (a). For such parameters, the beam reaches a Doppler-shifted harmonic on the outboard side near the botton of the magnetic well, as shown on graph (b) where the frequency profile on the horizontal midplane shows the cyclotron harmonics including the Doppler shift $\omega = n\omega_{ce} \pm 3.5 v_{Te} k_{||}$. The wave characteristics, power deposition and driven current are calculated along the beam path, for an initial power $P = 1$ MW in the beam. The power and current density deposition profiles are shown on graph (c). The power deposition

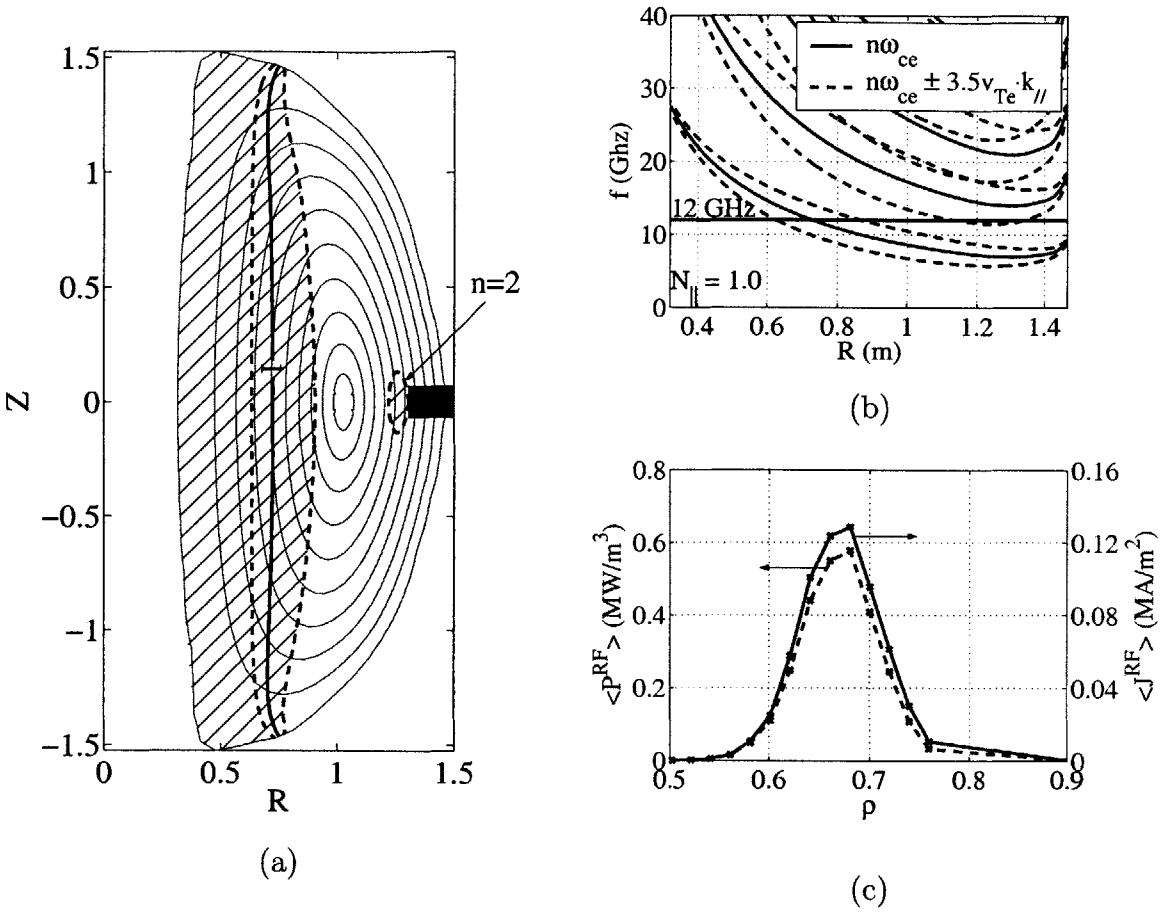


Figure 5-25: (a) Same as Fig. 1-9 for $f = 12$ GHz and $N_{||} = 1.0$. (b) Frequency profile of the cyclotron harmonics - including the Doppler shift $\omega = n\omega_{ce} \pm 3.5 v_{Te} k_{||}$ - on the horizontal midplane. (c) Density of current and power deposited at a function of radius.

profile peaks at the radial location $\rho \simeq 0.68$. The current is driven by Ohkawa effect and peaks at the same location as the power deposited. The normalized efficiency at the peak of power absorption is $\eta \simeq 1.6$, and the total driven current is $I = 41$ kA, so that the CD efficiency is approximately $I/P = 0.04$ A/W. In terms of normalized global efficiency as defined in (5.65), we find $\xi_{CD} = 0.37$, which is significantly higher than typical off-axis ECCD efficiencies. The power deposition profile is rather broad: $\Delta\rho = 0.12$, because of the large Doppler effect ($N_{||} = 1.0$) and the large value of the magnetic field variations scale length near the bottom of the magnetic well.

### 5.4.10 Interaction between HBF EBWCD and the bootstrap current

Because the HBF interaction between EBWs and electrons occurs on the outboard side of the plasma, where the fraction of trapped electrons is maximum, the interaction between the bootstrap current and EBWCD is expected to be significant. To illustrate this, we consider the location of the peak in the power deposition profile calculated for the integrated HBFCD calculation in NSTX presented in Section 5.4.9. The radial location is $\rho = 0.68$. The distribution function $f_1$, which accounts for the effects of the drifts, is calculated in the absence of EBWCD, when $f_0$ is Maxwellian, which gives the bootstrap current. At this location, the bootstrap current density is $J^{\mathrm{BC}} = 120$ kA/m$^2$. When the effect of EBWs is included, the current calculated from $f_0$ gives the EBWCD density, $J^{\mathrm{RF}} = 133$ kA/m$^2$, and the current calculated from $f_1$ give the bootstrap current with synergistic effects, $J_1 = 146$ kA/m$^2$. Substracting $J^{\mathrm{BC}}$ from this value, we obtain the synergistic current $J^{\mathrm{syn}} = 26$ kA/m$^2$. This current represents about 20% of the EBW driven current. Note that the EBW driven current density in that case in much lower than the LBF case because the deposition profile is much broader.

The strong synergism between HBF EBWCD and the bootstrap current can be understood from the plot of the distribution function $f_1$ on Fig. 5-26. The thin lines represent the bootstrap current distribution, while thick lines are the contours of $f_1$ in the presence of EBWCD. The distribution is negative on the side $p_\parallel < 0$ and positive on the $p_\parallel > 0$ side. The green contours represent the magnitude of the diffusion coefficient. The deformation of the bootstrap distribution function due to interaction with EBWs in clearly visible. On graph (b), the same distribution is integrated over the perpendicular momentum, as

$$F_1\left(p_\parallel\right) = 2\pi \int_0^\infty p_\perp dp_\perp \, f_1\left(p_\parallel, p_\perp\right) \tag{5.75}$$

which shows that the synergistic current is driven in the tail of the bootstrap distribution function, which drives significant current.

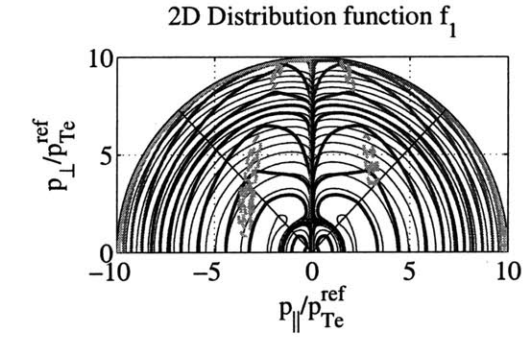


(a)

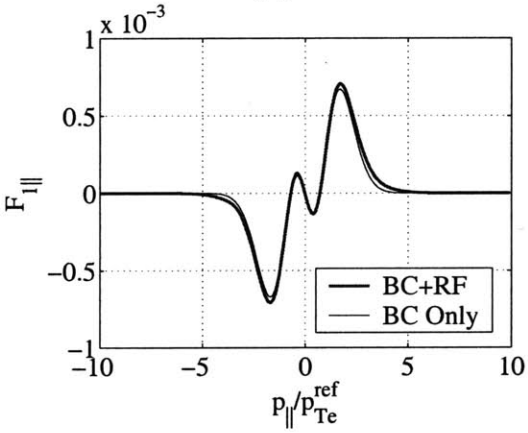


(b)

Figure 5-26: (a) Contour plot of the distribution function $f_1$ in HBF-EBWCD. The thin lines represent the bootstrap current distribution, while thick lines are the contours of $f_1$ in the presence of EBWCD. The green contours represent the magnitude of the diffusion coefficient. (b) $F_1$: same distribution integrated over the perpendicular momentum.

# Chapter 6

# Summary and Conclusions

## 6.1 Electron Bernstein wave current drive modeling

Electrons Bernstein waves (EBW) are kinetic waves, for which the wavelength can be of the order of the electron Larmor radius or even smaller. They do not exist in a cold plasma wave description. The fundamentals of the kinetic theory of plasma waves have been reviewed. An analytical description of EBWs characteristics has been undertaken in the electrostatic limit for a non-relativistic plasma, and expressions for the wave energy flow density and absorption coefficient have been derived for the first time. This analytical work has been used for the guidance and interpretation of EBWCD calculations. This model has been validated by comparison with the exact calculations using the numerical code *R2D2* [13], which includes full electromagnetic effects. The characteristics of EBWs have been systematically described, as a function of the wave and plasma parameters.

The description of the resonant interaction between electrons and EBWs also involves kinetic theory, in the form of a RF quasilinear diffusion operator for electrons in momentum space, which calculates the transfer of momentum from radio-frequency (RF) waves to the resonant electrons. Based on earlier works on quasilinear theory [41], a new fully-relativistic quasi-linear operator describing the interaction between

electrons and a Gaussian EBW beam has been derived for a slab plasma.

The calculation of current drive (CD) by EBWs in toroidal plasmas involves the solution of the fully-relativistic electron drift-kinetic equation with Fokker-Planck collisions and RF quasilinear diffusion. This equation, which accounts for particle orbit effects such as magnetic trapping and radial drifts, has been derived in a general formalism that is valid for an arbitrary axisymmetric magnetic geometry, and thus is adapted to the strongly shaped plasmas of spherical tokamaks.

In typical fusion plasmas, the radial drift velocity of electron is much smaller than their parallel velocity, and thus the radial extent of trapped particule (banana) orbits is small. In addition, the collisionality is low, meaning that particles can complete many poloidal orbits before strong collisional effects occurs, and as a results the particle orbits are well defined. In that case the 4D drift-kinetic equation (2D in axisymmetric configuration space, 2D in gyro-averaged momentum space) is reduced to a set of two bounce-averaged 2D equations in momentum space.

Solving these two partial integral-differential equations requires numerical techniques, and a new code named *DKE* [73] has been developed for this purpose. It uses a completely implicit technique to solve the differential part of the equations, in the sense that the symmetrization of the distribution function in the trapped region, which results from the fast parallel motion, is ensured implicitly, with an appropriate treatments of the fluxes at the trapped/passing boundary in momentum space. This fully implicit scheme makes calculations several order of magnitude faster than the commonly used half-implicit schemes. Because radial drifts are properly accounted for in the kinetic equations, the *DKE* code also calculates the bootstrap current correctly. In addition, it consistently includes the calculation of CD by any kind of RF wave interacting with electrons, provided that this interaction can be described by quasilinear theory. Therefore, the range of applications for the present formalism and the *DKE* code reaches far beyond the scope of this thesis, and the code has been successfully used for many CD calculations, including the first accurate calculation of Ohkawa CD with electron cyclotron (EC) waves [31] and several investigations of the kinetic interaction between the bootstrap current and RF waves [77] [30] [33] [34]

[35] [78].

The description of EBWs and the EBWCD calculations both derive from kinetic theory. The consistency between the two models has been verified by demonstrating that the EBW absorption coefficient, calculated using the analytical linear model for EBWs, is retrieved both analytically and numerically from the quasilinear operator in the non-relativistic electrostatic limit. Along with this calculation, a new expression for the linear absorption coefficient has been derived within the weakly-relativistic approximation. The resulting relativistic effects on the power deposition are found to be important.

## 6.2 Electron Bernstein waves characteristics

The systematic study of EBW characteristics has led to the following observations, relevant for EBWCD calculations:

- In high-$\beta$ plasmas, EBWs are generated at the edge of the plasma, in the mode-conversion region near the upper-hybrid resonance, which is characterized mainly by density variations. Once EBWs propagate inside the plamas, however, their behaviour is dominated by magnetic field variations. Indeed, EBWs can propagate between two harmonics of the cyclotron resonance, but are completely damped at the Doppler-shifted resonance of any harmonic.

- The absorption of EBWs is independent of the plasma density, a property of waves for which the energy density flow is mostly due to the coherent motion of particles.

- The ratio of the gyroradius to the wavelength is measured by the expression $\mathrm{Re}\,[k_\perp \rho_{Te}]$, which is obtained from solving the dispersion relation. It is found that $\mathrm{Re}\,[k_\perp \rho_{Te}]$ does not vary significantly as a function of parallel wave number $N_\parallel$, the temperature, or the density (away from the mode-conversion region).

- The properties of EBWs vary primarily with variations in the magnetic field,

and can be characterized with respect to the location of cyclotron harmonic resonances. For this purpose, we have defined the parameter $y_n = n\omega_{ce}/\omega$.

- In particular, if the wave approaches the $n^{\text{th}}$ harmonic resonance from a lower $B$-field region (LBF) ($n\omega_{ce} < \omega$), the wave is characterized by a large perpendicular wave vector, a completely electrostatic polarization, and a large electric field amplitude for a given energy flow density.

- However, if the wave approaches the $n^{\text{th}}$ harmonic resonance from a higher $B$-field region (HBF) ($n\omega_{ce} > \omega$), the wave is characterized by a smaller perpendicular wave vector, strong electromagnetic effects in the polarization, and a smaller electric field amplitude for the same energy flow density.

## 6.3 Damping of EBWs and power deposition profile

- As EBWs approach a cyclotron harmonic resonance, they are absorbed in the tail of the distribution function, for typical values of the parallel momentum such that $3 \leq p_{\|}/p_{Te} \leq 3.5$, where $p_{Te} = \sqrt{m_e T_e}$ is the thermal momentum. As a consequence, the location of power deposition in momentum space, along the resonance curve, is determined by the rapid Gaussian variations of the distribution function at large $p_{\|}$. As a result, parameters such as the geometry of the flux-surfaces (plasma shaping) and the scale length of magnetic field variations, which for example strongly affect the ECCD deposition profile and thus the CD efficiency, have little effect on EBWCD.

- In the vicinity of a resonance ($y_n \simeq 1$), the position of resonance curves in momentum space changes mostly as a function of the distance from the magnetic field, or $(1 - y_n)$. Therefore, the damping of EBWs is dominated by changes in the magnitude of the magnetic field.

- There is an important shift and broadening of the power deposition profile in

configuration space, due to the Doppler effect, which scales like $N_{\|}\beta_{Te}$, where $\beta_{Te} = \sqrt{T_e/(m_e c^2)}$. This effect is accounted for by measuring the distance to the resonance using the parameter $p_n = (1 - y_n) / (N_{\|}\beta_{Te})$, which accounts for the variation is the magnetic field as well as the Doppler shift.

- In addition, the power deposition profile is subject to significant relativistic effects, which are found to scale like $\beta_{Te}/N_{\|}$ withing the weakly relativistic approximation. Relativistic effects shift the deposition towards the resonance in LBF approach, and away from the resonance in HBF approach

- For large values of the Doppler shift, two consecutive harmonics can overlap and thus the wave cannot propagate between these harmonics any longer. In a 1 keV plasma, significant overlapping occurs between first and second harmonic for $N_{\|} \gtrsim 1.5$. In a 10 keV plasma, the overlapping threshold drops to $N_{\|} \gtrsim 0.5$. In addition, overlapping increases with the harmonic number. For example, between the third and the fourth harmonic, significant overlapping occurs for $N_{\|} \gtrsim 0.5$ in a 1 keV plasma.

- The diffusion of electrons due to interaction with EBWs is mostly in the perpendicular direction in momentum space. However, there is a small component of the diffusion in the parallel direction, which scale like $N_{\|}\beta_{Te}$ and is in the direction of the parallel wave vector $\mathbf{k}_{\|}$.

## 6.4 Spherical tokamaks and framework of EBWCD calculations

Spherical tokamaks are high-$\beta$ plasma devices with a very small aspect ratio and thus a tight toroidal geometry. Consequently, RF waves must be launched from the outboard side of the plasma. A particularity of high-$\beta$ toroidal plasmas is the existence of a dip in the magnetic field profile, located off-axis on the outboard side of the plasma. Therefore, in a high-$\beta$ plasma, it is possible to approch a harmonic

resonance from either the LBF or the HBF region, with launching from the outboard side. In that case, LBF CD is located on the inboard side while HBF CD is located on the outboard side.

The EBWCD calculations presented in this thesis apply to the vicinity of the horizontal midplane, where the plasma is locally in a slab geometry so that the quasilinear operator is valid. This approximation requires that the EBW beam size be much larger than the wavelength, so that the wave is well defined in Fourier spectrum, but also much smaller than the length of poloidal field lines, so that the slab approximation applies. In that case, EBW damping and current drive can be calculated without ray-tracing techniques.

Because the EBW characteristics are very different depending whether the resonance is approached from a HBF or a LBF region, and because the corresponding locations in the plasma are different, these two scenarios are considered separately. Even though the calculations are limited to the horizontal midplane, the relevant physics of EBW CD mechanisms is included in our models, since we consider both the location with maximum trapped electron effects (HBF at $\theta = 0°$) and the location with minimum trapped electron effects (LBF at $\theta = 0°$).

## 6.5 Low $B$-field ($n\omega_{ce} < \omega$) current drive

- Since LBFCD occurs on the inboard side of the plasma, the LBFCD mechanism is the Fisch-Boozer effect, which results from the plasma collisional response to an asymmetric resistivity (in $p_\parallel$) created by asymmetric perpendicular heating of the distribution function.

- The CD efficiency decreases as the wave moves closer to the cyclotron harmonic resonance and the resonance curves move correspondingly closer to the bulk in momentum space, where resonant electrons are more collisional and carry less parallel momentum.

- The large value of $\mathrm{Re}\,[k_\perp \rho_{Te}]$ in LBFCD results in confining the interaction to

the vicinity of the $p_\perp = 0$ axis, which is favorable for Fisch-Boozer current drive because the resonance region is far from the trapped/passing boundary.

- The parallel component of the quasilinear diffusion - a relativistic effect - is directed towards the tail of the distribution in LBFCD, which is favorable for Fisch-Boozer current drive because more efficient direct parallel momentum is transmitted to the electrons.

- In LBFCD, the shift of power deposition due to relativisic effects is directed toward the resonance, which has a negative effect on CD since the CD efficiency is decreasing monotonically towards the resonance.

- As a consequence of these two relativistic effects, the normalized LBF driven current increases with $N_\parallel$ and remains rather independent of temperature.

- The effect of electron trapping is to reduce the CD efficiency, because the effect of collisional pitch-angle scattering is enhanced by trapped electrons.

- Quasilinear effects typically increase the LBF Fisch-Boozer CD efficiency.

- In HBFCD, the overlapping of harmonics is always deleterious because the mechanism for $n = 2$ HBFCD is dominated by the Fisch-Boozer effect on the inboard side of the plasma, where there are no trapped electrons. This effect can be observed in Fig. (5-9). Because the HBF approach to the $n = 2$ resonance is on the opposite side in $p_\parallel$ (see Fig. 5-14-a), current is driven in the opposite direction.

## 6.6 High $B$-field ($n\omega_{ce} < \omega$) current drive

- Since HBFCD occurs on the outboard side of the plasma and far off-axis, the HBFCD mechanism is the Ohkawa effect, which results from the asymmetric trapping (in $p_\parallel$) induced by the wave when barely-passing electrons are heated perpendicularly.

- The CD efficiency peaks at some distance from the resonance that corresponds to a situation where the diffusion coefficient in momentum space is located in the vicinity of the trapped-passing boundary, and thus wave-induced magnetic trapping is at its maximum. Farther from the resonance, the Fisch-Boozer effect counteracts the Ohkawa effect and the CD efficiency is reduced. Closer to the resonance, most of the power is coupled to the trapped electrons, which drive no current.

- Because of the smaller value of $\mathrm{Re}\,[k_\perp \rho_{Te}]$ in HFBCD, the interaction is located at larger $p_\perp$, which is favorable for Ohkawa current drive because the resonance region is close to the trapped/passing boundary, and large wave-induced trapping can occur.

- The parallel component of the quasilinear diffusion is directed towards the bulk of the distribution in HBFCD, which is favorable for Ohkawa current drive because wave-induced trapping is increased.

- In HBFCD, the shift of power deposition due to relativisic effects is directed away from the resonance. Its effect on CD depends on the relative positions of the CD efficiency and power deposition profiles.

- As a consequence of these two relativistic effects, the normalized HBF driven current increases with both $N_\parallel$ and the temperature.

- Optimizing OKCD requires a much larger fraction of trapped electrons than for ECCD, in order for the diffusion coefficient to be located close to the trapped/passing boundary in momentum space. Fortunately, STs typically have very large fractions of trapped particles, because of their small aspect ratio.

- In order to optimize OKCD, the fraction of trapped electrons - and thus the location of deposition - must be adjusted with quasilinear effects such that the peaks in the CD efficiency and power deposition profiles coincide.

| | LBF-EBWCD | HBF-EBWCD |
|---|---|---|
| Definition (vs. $n^{\text{th}}$ harmonic) | $n\omega_{ce} < \omega$ | $n\omega_{ce} > \omega$ |
| Localization in high-$\beta$ plasma | inboard side | outboard side |
| CD mechanism | Fisch-Boozer | Ohkawa |
| CD direction | opposite to $\mathbf{k}_{\|}$ | opposite to $\mathbf{k}_{\|}$ |
| Accessibility | restricted on midplane | very good on midplane |
| Accessible harmonics | only $n = 1$ | any $n \geq 2$ |
| Radial locations (in NSTX) | $0 \lesssim \rho \lesssim 0.6$ | $0.6 \lesssim \rho \lesssim 1$ |
| Deposition profile | very narrow | narrow to broad |
| Increasing $N_{\|}$ | increases $\eta$ | increases $\eta$ |
| Increasing electron trapping | reduces $\eta$ | increases $\eta$ |
| Increasing temperature | little effect on $\eta$ | increases $\eta$ |
| $\Longrightarrow$ effect of increased $\rho$ | $\eta$ decreases | $\eta$ increases |
| Typical norm. CD efficiency | $\xi_{CD} \sim 0.67$ | $\xi_{CD} \sim 0.37$ |
| Typical CD efficiency in NSTX | $I/P \sim 0.1$ A/W | $I/P \sim 0.04$ A/W |

Table 6.1: Comparison between the HBF and LBF EBWCD schemes.

- In HBFCD, the overlapping of harmonics is not necessarily deleterious because the mechanism for $n = 1$ LBFCD, far from the resonance, is dominated by the Fisch-Boozer effect, even on the outboard side of the plasma. This effect can be observed in Fig. (5-19). Because the LBF approach to the $n = 1$ resonance is on the opposite side in $p_{\|}$ (see Fig. 5-24-a), current is driven in the same direction.

## 6.7 Comparison and conclusions

A comparison between LBF and HBF approaches is presented in Table 6.1.

For a given $N_{\|}$, LBF Fisch-Boozer CD and HBF Ohkawa CD are in the same direction, because the resonance curves in momentum space are located on opposite sides of the $p_{\|} = 0$ axis. This could be an important (and favorable) factor if part of the RF power happens to be absorbed in LBF approach on the inboard side and part of it in HBF approach on the outboard side.

The typical EBWCD efficiencies are significantly higher than ECCD efficiencies because the power - and the current - are deposited in the tail of the distribution function. For comparison, typical normalized ECCD efficiencies measured in comparable

D3D plasmas are $\xi_{CD} \sim 0.3$ in the core and $\xi_{CD} \sim 0$ for $\rho \geq 0.4$. However, efficiencies are lower than for lower-hybrid current drive, because the diffusion is mostly in the perpendicular direction.

In general, a higher $N_{\|}$ leads to higher CD efficiencies for both Fisch-Boozer LBFCD and Ohkawa HBFCD. However, if $N_{\|}$ becomes too large, two harmonics can overlap. As for any current drive mechanism, an increased effective charge reduces both Fisch-Boozer LBFCD and Ohkawa HBFCD, because it tends to isotropize the distribution function.

Because of the particular magnetic geometry of high-$\beta$ ST plasmas, LBFCD occurs on the inboard side and is possible only between first and second harmonic, and at radial locations $0 \lesssim \rho \lesssim 0.6$. Its efficiency generally decreases with $\rho$ because of the larger fraction of trapped particles.

On the other side, the high-$\beta$ ST plasma geometry limits HBFCD to the outboard side at locations $0.6 \lesssim \rho \lesssim 1$, where the mechanism is Ohkawa current drive. The variations of the CD efficiency with $\rho$ depend upon many parameters, in particular the fraction of trapped electrons.

The radial width of the power deposition profile increases with the magnetic field variations scale length $L_B$ and the Doppler broadening effect, proportional to $N_{\|}\beta_{Te}$. In HBFCD, it is possible to obtain very wide deposition profiles by driving current near the bottom of the dip in the magnetic field profile, where $L_B$ becomes very large.

In conclusion, current can be efficiently driven by electron Bernstein waves in most radial locations in the plasma, provided the wave is launched near the midplane. The current drive mechanism is the Fisch-Boozer effect when the EC resonance is approached from a lower $B$-field region in the center of the plasma, and it is the Ohkawa effect when it is approached from a higher $B$-field region far off-axis on the outboard side.

# Appendix A

# Properties of Curvilinear Systems

The particular geometries and symmetries of toroidal magnetic equilibrium (in configuration space) and gyromotion (in momentum space) require to use several curvilinear coordinate systems. The geometrical properties of these systems (metric factors, elementary distances, surfaces and volumes) and differential operators are used extensively in this work. Some general properties and identities of curvilinear systems are first presented; then, they are applied to the particular coordinate systems used through this work.

## A.1 General Case $(u^1, u^2, u^3)$

We note $\mathbf{X} = x\widehat{\mathbf{x}} + y\widehat{\mathbf{y}} + z\widehat{\mathbf{z}}$ the vector position in the space under consideration, where $(x, y, z)$ is the initial, cartesian coordinate system. We consider the curvilinear coordinate system $(u^1, u^2, u^3)$.

### A.1.1 Covariant (tangent) basis

The covariant, or tangent vector basis $(\mathbf{e}_1, \mathbf{e}_2, \mathbf{e}_3)$ is defined as

$$\mathbf{e}_i = \frac{\partial \mathbf{X}}{\partial u^i} \tag{A.1}$$

where the $\mathbf{e}_i$ are tangent to the curvilinear lines.

### A.1.2 Contravariant (reciprocal) basis

The gradient $\nabla f$ of a function $f$ being defined by the differential

$$df = \nabla f \cdot d\mathbf{X} \tag{A.2}$$

we apply to $u^i$ which gives

$$du^i = \nabla u^i \cdot d\mathbf{X} \tag{A.3}$$

By chain rule, we have

$$d\mathbf{X} = \frac{\partial \mathbf{X}}{\partial u^j} du^j = \mathbf{e}_j du^j \tag{A.4}$$

so that

$$du^i = \nabla u^i \cdot \mathbf{e}_j du^j \tag{A.5}$$

which implies

$$\nabla u^i \cdot \mathbf{e}_j = \delta^i_j \tag{A.6}$$

thus defining two reciprocal basis $(\nabla u^i, \mathbf{e}_j)$ of vectors. The reciprocal basis vectors are also called contravariant, and noted

$$\mathbf{e}^i \equiv \nabla u^i \tag{A.7}$$

These vectors are perpendicular to the surfaces of constant $u^i$.

From the properties of reciprocal basis, we can calculate a vector from the three vectors of the reciprocal basis, such that

$$\mathbf{e}^i = \nabla u^i = \frac{\mathbf{e}_j \times \mathbf{e}_k}{\mathbf{e}_i \cdot \mathbf{e}_j \times \mathbf{e}_k} \tag{A.8}$$

$$\mathbf{e}_i = \frac{\partial \mathbf{X}}{\partial u^i} = \frac{\mathbf{e}^j \times \mathbf{e}^k}{\mathbf{e}^i \cdot \mathbf{e}^j \times \mathbf{e}^k} \tag{A.9}$$

### A.1.3 Metric coefficients

They are defined as

$$g_{ij} = \mathbf{e}_i \cdot \mathbf{e}_j \tag{A.10}$$
$$g^{ij} = \mathbf{e}^i \cdot \mathbf{e}^j$$

With the differential vector given in (A.4), we see that the differential arc length along a curve is

$$dl = |d\mathbf{X}| = \sqrt{d\mathbf{X} \cdot d\mathbf{X}} = \sqrt{g_{ij} du^i du^j} \tag{A.11}$$

In addition, we have the relations

$$\mathbf{e}_i = g_{ij}\mathbf{e}^j \tag{A.12}$$
$$\mathbf{e}^i = g^{ij}\mathbf{e}_j$$

We also see that

$$[g_{ij}] = \left[g^{ij}\right]^{-1} \tag{A.13}$$
$$\left[g^{ij}\right] = [g_{ij}]^{-1} \tag{A.14}$$

so that, defining

$$g = \det [g_{ij}] \tag{A.15}$$

we find

$$g^{-1} = \det \left[g^{ij}\right] \tag{A.16}$$

### A.1.4 Jacobian

We define the Jacobian

$$J \equiv \frac{\partial(x,y,z)}{\partial(u^1,u^2,u^3)} = \det \begin{pmatrix} \partial x/\partial u^1 & \partial x/\partial u^2 & \partial x/\partial u^3 \\ \partial y/\partial u^1 & \partial y/\partial u^2 & \partial y/\partial u^3 \\ \partial z/\partial u^1 & \partial z/\partial u^2 & \partial z/\partial u^3 \end{pmatrix} \tag{A.17}$$

which gives

$$J = \frac{\partial \mathbf{X}}{\partial u^1} \cdot \frac{\partial \mathbf{X}}{\partial u^2} \times \frac{\partial \mathbf{X}}{\partial u^3} = \mathbf{e}_1 \cdot \mathbf{e}_2 \times \mathbf{e}_3 \tag{A.18}$$

and the reciprocal Jacobian

$$\mathcal{J} \equiv \frac{\partial(u^1,u^2,u^3)}{\partial(x,y,z)} = \det \begin{pmatrix} \partial u^1/\partial x & \partial u^1/\partial y & \partial u^1/\partial z \\ \partial u^2/\partial x & \partial u^2/\partial y & \partial u^2/\partial z \\ \partial u^3/\partial x & \partial u^3/\partial y & \partial u^3/\partial z \end{pmatrix} \tag{A.19}$$

which gives

$$\mathcal{J} = \nabla u^1 \cdot \nabla u^2 \times \nabla u^3 = \mathbf{e}^1 \cdot \mathbf{e}^2 \times \mathbf{e}^3 \tag{A.20}$$

We can show that

$$\mathcal{J} = J^{-1} \tag{A.21}$$

and the relations (A.8-A.9) become

$$\mathbf{e}^i = \frac{1}{J}\left(\mathbf{e}_j \times \mathbf{e}_k\right) \tag{A.22}$$

$$\mathbf{e}_i = J\left(\mathbf{e}^j \times \mathbf{e}^k\right) \tag{A.23}$$

Also,

$$g = J^2 \tag{A.24}$$

### A.1.5 Vector identities

With

$$\mathbf{A} = (\mathbf{A} \cdot \mathbf{e}_i)\, \mathbf{e}^i = A_i \mathbf{e}^i \tag{A.25}$$

$$\mathbf{A} = \left(\mathbf{A} \cdot \mathbf{e}^i\right) \mathbf{e}_i = A^i \mathbf{e}_i \tag{A.26}$$

we find

$$\mathbf{A} \cdot \mathbf{B} = g_{ij} A^i B^j = g^{ij} A_i B_j \tag{A.27}$$

so that

$$A = |\mathbf{A}| = \sqrt{g_{ij} A^i A^j} = \sqrt{g^{ij} A_i A_j} \tag{A.28}$$

We also find

$$\mathbf{A} \times \mathbf{B} = A^i B^j \mathbf{e}_i \times \mathbf{e}_j = A_i B_j \mathbf{e}^i \times \mathbf{e}^j \tag{A.29}$$

which gives

$$(\mathbf{A} \times \mathbf{B})_k = \varepsilon_{ijk} J A^i B^j = \frac{\varepsilon^{ijk}}{J} A_i B_j \tag{A.30}$$

Note that from (A.12),

$$A_i = g_{ij} A^j \tag{A.31}$$

$$A^i = g^{ij} A_j \tag{A.32}$$

### A.1.6 Differential elements

**differential length along $u^i$**

$$dl\,(i) = |d\mathbf{X}\,(i)| = h_i du^i = \sqrt{g_{ii}} du^i \tag{A.33}$$

Equivalently,

$$dl\,(i) = J \left|\nabla u^j \times \nabla u^k\right| du^i \tag{A.34}$$

**Differential area in surface of constant $u^i$**

Using

$$dS(i) = |d\mathbf{X}(j) \times d\mathbf{X}(k)| = |\mathbf{e}_j \times \mathbf{e}_k| \, du^j du^k \tag{A.35}$$

which becomes

$$dS(i) = \sqrt{g_{jj}g_{kk} - g_{jk}^2} du^j du^k \tag{A.36}$$

Equivalently

$$dS(i) = J \left|\nabla u^i\right| du^j du^k \tag{A.37}$$

so that

$$d\mathbf{S}(i) = \pm J du^j du^k \nabla u^i \tag{A.38}$$

**Differential volume element**

$$d^3\mathbf{X} = d\mathbf{X}(1) \cdot d\mathbf{X}(2) \times d\mathbf{X}(3) = J du^1 du^2 du^3 \tag{A.39}$$

### A.1.7 Operator $\nabla$

The operator $\nabla$ can be decomposed in the curvilinear coordinates as

$$\nabla = \nabla u^i \frac{\partial}{\partial u^i} = \mathbf{e}^i \frac{\partial}{\partial u^i} \tag{A.40}$$

We then find the following differential operations:

**Gradient**

It follows simply that

$$\nabla f = \nabla u^i \frac{\partial f}{\partial u^i} = \frac{\partial f}{\partial u^i} \mathbf{e}^i \tag{A.41}$$

so that

$$(\nabla f)_i = (\nabla f \cdot \mathbf{e}_i) = \frac{\partial f}{\partial u^i} \tag{A.42}$$

**Divergence**

It can be shown that the divergence is expressed as

$$\nabla \cdot \mathbf{A} = \frac{1}{J} \frac{\partial}{\partial u^i} \left( J A^i \right) \tag{A.43}$$

**Curl**

It becomes, a compact notations,

$$\nabla \times \mathbf{A} = \frac{\varepsilon^{ijk}}{J} \frac{\partial A_j}{\partial u^i} \mathbf{e}_k \tag{A.44}$$

or is extended as

$$(\nabla \times \mathbf{A})^k = \frac{1}{J} \left( \frac{\partial A_j}{\partial u^i} - \frac{\partial A_i}{\partial u^j} \right) \tag{A.45}$$

## A.2 Configuration space

### A.2.1 System $(R, Z, \phi)$

The coordinates $(R, Z, \phi)$ are defined on the space $0 \leq R < \infty$, $-\infty \leq Z < \infty$, $0 \leq \phi < 2\pi$, and they are related to $(x, y, z)$ by

$$\begin{aligned} R &= \sqrt{x^2 + y^2} \\ Z &= -z \\ \phi &= \arctan(y/x) + \pi H(-x) \quad [2\pi] \end{aligned} \tag{A.46}$$

which is inverted to

$$\begin{aligned} x &= R \cos \phi \\ y &= R \sin \phi \\ z &= -Z \end{aligned} \tag{A.47}$$

The position vector is

$$\mathbf{X} = R \widehat{\mathbf{R}} + Z \widehat{\mathbf{Z}} \tag{A.48}$$

where we define a local orthonormal basis $\left(\widehat{\mathbf{R}}, \widehat{\mathbf{Z}}, \widehat{\phi}\right)$ as

$$\begin{aligned}
\widehat{\mathbf{R}} &= \cos\phi\,\widehat{\mathbf{x}} + \sin\phi\,\widehat{\mathbf{y}} \\
\widehat{\mathbf{Z}} &= -\widehat{\mathbf{z}} \\
\widehat{\phi} &= \widehat{\mathbf{R}} \times \widehat{\mathbf{Z}} = -\sin\phi\,\widehat{\mathbf{x}} + \cos\phi\,\widehat{\mathbf{y}}
\end{aligned} \tag{A.49}$$

The covariant vector basis is defined in (A.1), which gives in the $(R, Z, \phi)$ coordinates system

$$(\mathbf{e}_R, \mathbf{e}_Z, \mathbf{e}_\phi) \equiv \left(\frac{\partial \mathbf{X}}{\partial R}, \frac{\partial \mathbf{X}}{\partial Z}, \frac{\partial \mathbf{X}}{\partial \phi}\right) = \left(\widehat{\mathbf{R}}, \widehat{\mathbf{Z}}, R\widehat{\phi}\right) \tag{A.50}$$

The Contravariant vector basis is defined in (A.7), which gives

$$\left(\mathbf{e}^R, \mathbf{e}^Z, \mathbf{e}^\phi\right) \equiv (\nabla R, \nabla Z, \nabla\phi) = \left(\widehat{\mathbf{R}}, \widehat{\mathbf{Z}}, \frac{\widehat{\phi}}{R}\right) \tag{A.51}$$

We note that the normalized reciprocal basis is colinear with the normalized tangent basis, which was expected since both bases are orthogonal. The Jacobian of the transformation is

$$J = R \tag{A.52}$$

The differential elements associated with this system are:

- the infinitesimal distance element along each coordinate

$$\begin{aligned}
dl\,(R) &= dR \\
dl\,(Z) &= dZ \\
dl\,(\phi) &= Rd\phi
\end{aligned} \tag{A.53}$$

- the infinitesimal surface element of constant coordinate

$$\begin{aligned}
d\mathbf{S}\,(R) &= RdZd\phi\,\widehat{\mathbf{R}} \\
d\mathbf{S}\,(Z) &= RdRd\phi\,\widehat{\mathbf{Z}} \\
d\mathbf{S}\,(\phi) &= dRdZ\,\widehat{\phi}
\end{aligned} \tag{A.54}$$

- the infinitesimal volume element

$$d^3\mathbf{X} = RdRdZd\phi \tag{A.55}$$

Finally, the differential operators are

- Gradient

$$\nabla f = \frac{\partial f}{\partial R}\widehat{\mathbf{R}} + \frac{\partial f}{\partial Z}\widehat{\mathbf{Z}} + \frac{1}{R}\frac{\partial f}{\partial \phi}\widehat{\phi} \tag{A.56}$$

- Divergence

$$\nabla \cdot \mathbf{A} = \frac{1}{R}\frac{\partial}{\partial R}\left(R\mathbf{A}\cdot\widehat{\mathbf{R}}\right) + \frac{\partial}{\partial Z}\left(\mathbf{A}\cdot\widehat{\mathbf{Z}}\right) + \frac{1}{R}\frac{\partial}{\partial \phi}\left(\mathbf{A}\cdot\widehat{\phi}\right) \tag{A.57}$$

- Curl

$$\begin{aligned}
(\nabla \times \mathbf{A})\cdot\widehat{\mathbf{R}} &= \frac{\partial}{\partial Z}\left(\mathbf{A}\cdot\widehat{\phi}\right) - \frac{1}{R}\frac{\partial}{\partial \phi}\left(\mathbf{A}\cdot\widehat{\mathbf{Z}}\right) \\
(\nabla \times \mathbf{A})\cdot\widehat{\mathbf{Z}} &= \frac{1}{R}\frac{\partial}{\partial \phi}\left(\mathbf{A}\cdot\widehat{\mathbf{R}}\right) - \frac{1}{R}\frac{\partial}{\partial R}\left(R\mathbf{A}\cdot\widehat{\phi}\right) \\
(\nabla \times \mathbf{A})\cdot\widehat{\phi} &= \frac{\partial}{\partial R}\left(\mathbf{A}\cdot\widehat{\mathbf{Z}}\right) - \frac{\partial}{\partial Z}\left(\mathbf{A}\cdot\widehat{\mathbf{R}}\right)
\end{aligned} \tag{A.58}$$

### A.2.2 System $(r, \theta, \phi)$

The coordinates $(r, \theta, \phi)$ are defined from an origin $(R_p, Z_p)$ on the space $0 \leq r < \infty$, $0 \leq \theta < 2\pi$, and they are related to $(R, Z, \phi)$ by

$$\begin{aligned}
r &= \sqrt{(R - R_p)^2 + (Z - Z_p)^2} \\
\theta &= \arctan\left((Z - Z_p)/(R - R_p)\right) + \pi H\left(R_p - R\right) \quad [2\pi]
\end{aligned} \tag{A.59}$$

which is inverted to

$$\begin{aligned}
R &= R_p + r\cos\theta \\
Z &= Z_p + r\sin\theta
\end{aligned} \tag{A.60}$$

The position vector is

$$\mathbf{X} = R_p\widehat{\mathbf{R}} + Z_p\widehat{\mathbf{Z}} + r\widehat{\mathbf{r}} \tag{A.61}$$

where we define a local orthonormal basis $\left(\widehat{\mathbf{r}}, \widehat{\theta}, \widehat{\phi}\right)$ as

$$\begin{aligned} \widehat{\mathbf{r}} &= \cos\theta\, \widehat{\mathbf{R}} + \sin\theta\, \widehat{\mathbf{Z}} \\ \widehat{\theta} &= \widehat{\phi} \times \widehat{\mathbf{r}} = -\sin\theta\, \widehat{\mathbf{R}} + \cos\theta\, \widehat{\mathbf{Z}} \end{aligned} \tag{A.62}$$

The covariant vector basis (A.1) is

$$(\mathbf{e}_r, \mathbf{e}_\theta, \mathbf{e}_\phi) \equiv \left(\frac{\partial \mathbf{X}}{\partial r}, \frac{\partial \mathbf{X}}{\partial \theta}, \frac{\partial \mathbf{X}}{\partial \phi}\right) = \left(\widehat{\mathbf{r}}, r\widehat{\theta}, R\widehat{\phi}\right) \tag{A.63}$$

The Contravariant vector basis (A.7) is

$$\left(\mathbf{e}^r, \mathbf{e}^\theta, \mathbf{e}^\phi\right) \equiv (\nabla r, \nabla\theta, \nabla\phi) = \left(\widehat{\mathbf{r}}, \frac{\widehat{\theta}}{r}, \frac{\widehat{\phi}}{R}\right) \tag{A.64}$$

and again, the normalized reciprocal basis is colinear with the normalized tangent basis. The Jacobian of the transformation is

$$J = rR \tag{A.65}$$

The differential elements associated with this system are:

- the infinitesimal distance element along each coordinate

$$\begin{aligned} dl\,(r) &= dr \\ dl\,(\theta) &= rd\theta \\ dl\,(\phi) &= Rd\phi \end{aligned} \tag{A.66}$$

- the infinitesimal surface element of constant coordinate

$$\begin{aligned} d\mathbf{S}\,(r) &= rRd\theta d\phi\, \widehat{\mathbf{r}} \\ d\mathbf{S}\,(\theta) &= Rdrd\phi\, \widehat{\theta} \\ d\mathbf{S}\,(\phi) &= rdrd\theta\, \widehat{\phi} \end{aligned} \tag{A.67}$$

- the infinitesimal volume element

$$d^3\mathbf{X} = rRdrd\theta d\phi \tag{A.68}$$

Finally, the differential operators are

- Gradient

$$\nabla f = \frac{\partial f}{\partial r}\widehat{\mathbf{r}} + \frac{1}{r}\frac{\partial f}{\partial \theta}\widehat{\theta} + \frac{1}{R}\frac{\partial f}{\partial \phi}\widehat{\phi} \tag{A.69}$$

- Divergence

$$\nabla \cdot \mathbf{A} = \frac{1}{rR}\frac{\partial}{\partial r}\left(rR\mathbf{A}\cdot\widehat{\mathbf{r}}\right) + \frac{1}{rR}\frac{\partial}{\partial \theta}\left(R\mathbf{A}\cdot\widehat{\theta}\right) + \frac{1}{R}\frac{\partial}{\partial \phi}\left(\mathbf{A}\cdot\widehat{\phi}\right) \tag{A.70}$$

- Curl

$$\begin{aligned}
(\nabla \times \mathbf{A})\cdot\widehat{\mathbf{r}} &= \frac{1}{rR}\frac{\partial}{\partial \theta}\left(R\mathbf{A}\cdot\widehat{\phi}\right) - \frac{1}{R}\frac{\partial}{\partial \phi}\left(\mathbf{A}\cdot\widehat{\theta}\right) \\
(\nabla \times \mathbf{A})\cdot\widehat{\theta} &= \frac{1}{R}\frac{\partial}{\partial \phi}\left(\mathbf{A}\cdot\widehat{\mathbf{r}}\right) - \frac{1}{R}\frac{\partial}{\partial r}\left(R\mathbf{A}\cdot\widehat{\phi}\right) \\
(\nabla \times \mathbf{A})\cdot\widehat{\phi} &= \frac{1}{r}\frac{\partial}{\partial r}\left(r\mathbf{A}\cdot\widehat{\theta}\right) - \frac{1}{r}\frac{\partial}{\partial \theta}\left(\mathbf{A}\cdot\widehat{\mathbf{r}}\right)
\end{aligned} \tag{A.71}$$

### A.2.3 System $(\psi, s, \phi)$

The coordinates $(\psi, s, \phi)$ are used to parametrize non-circular closed flux-surfaces, are defined from the origin $(R_p, Z_p)$, on the space $\min(\psi_0, \psi_a) \leq \psi \leq \max(\psi_0, \psi_a)$, $s_{\min}(\psi) \leq s \leq s_{\max}(\psi)$, and they are related to $(r, \theta, \phi)$ by a general

$$\begin{aligned}
\psi &= \psi(r, \theta) \\
s &= s(r, \theta)
\end{aligned} \tag{A.72}$$

which is inverted to

$$\begin{aligned}
r &= r(\psi, s) \\
\theta &= \theta(\psi, s)
\end{aligned} \tag{A.73}$$

Note that $\psi(r, \theta)$ must be a monotonic function of $r$ from $\psi_0$ at the center $(R_p, Z_p)$ to $\psi_a$ at the edge. It is the case for nested flux-surfaces. We define a local orthonormal

basis $\left(\widehat{\psi}, \widehat{\mathbf{s}}, \widehat{\phi}\right)$ with

$$\begin{aligned} \widehat{\psi} &= \frac{\nabla\psi}{\|\nabla\psi\|} \\ \widehat{\mathbf{s}} &= \widehat{\phi} \times \widehat{\psi} = \frac{R}{\|\nabla\psi\|}\nabla\phi \times \nabla\psi \end{aligned} \tag{A.74}$$

The transformation from $\left(\widehat{\mathbf{r}}, \widehat{\theta}\right)$ to $\left(\widehat{\psi}, \widehat{\mathbf{s}}\right)$ is a rotation of angle $\alpha(\psi, s)$ such that

$$\begin{pmatrix} \widehat{\psi} \\ \widehat{\mathbf{s}} \end{pmatrix} = \begin{pmatrix} \cos\alpha & -\sin\alpha \\ \sin\alpha & \cos\alpha \end{pmatrix} \cdot \begin{pmatrix} \widehat{\mathbf{r}} \\ \widehat{\theta} \end{pmatrix} \tag{A.75}$$

The position vector remains

$$\mathbf{X} = R_p\widehat{\mathbf{R}} + Z_p\widehat{\mathbf{Z}} + r\widehat{\mathbf{r}} \tag{A.76}$$

The covariant vector basis (A.1) is

$$(\mathbf{e}_\psi, \mathbf{e}_s, \mathbf{e}_\phi) \equiv \left(\frac{\partial\mathbf{X}}{\partial\psi}, \frac{\partial\mathbf{X}}{\partial s}, \frac{\partial\mathbf{X}}{\partial\phi}\right) = \left(\frac{\widehat{\psi}}{\|\nabla\psi\|}, \widehat{\mathbf{s}}, R\widehat{\phi}\right) \tag{A.77}$$

The Contravariant vector basis (A.7) is

$$\left(\mathbf{e}^\psi, \mathbf{e}^s, \mathbf{e}^\phi\right) \equiv (\nabla\psi, \nabla s, \nabla\phi) = \left(\|\nabla\psi\|\,\widehat{\psi}, \widehat{\mathbf{s}}, \frac{\widehat{\phi}}{R}\right) \tag{A.78}$$

and again, the normalized reciprocal basis is colinear with the normalized tangent basis. The Jacobian of the transformation is

$$J = \frac{R}{\|\nabla\psi\|} \tag{A.79}$$

The differential elements associated with this system are:

- the infinitesimal distance element along each coordinate

$$\begin{aligned} dl(\psi) &= \frac{d\psi}{\|\nabla\psi\|} \\ dl(s) &= ds \\ dl(\phi) &= Rd\phi \end{aligned} \tag{A.80}$$

- the infinitesimal surface element of constant coordinate

$$\begin{aligned} d\mathbf{S}(\psi) &= Rdsd\phi\,\widehat{\psi} \\ d\mathbf{S}(s) &= \frac{R}{\|\nabla\psi\|}d\psi d\phi\,\widehat{\mathbf{s}} \\ d\mathbf{S}(\phi) &= \frac{1}{\|\nabla\psi\|}d\psi ds\,\widehat{\phi} \end{aligned} \tag{A.81}$$

- the infinitesimal volume element

$$d^3\mathbf{X} = \frac{R}{\|\nabla\psi\|}d\psi dsd\phi \tag{A.82}$$

Finally, the differential operators are

- Gradient

$$\nabla f = \|\nabla\psi\|\frac{\partial f}{\partial\psi}\widehat{\psi} + \frac{\partial f}{\partial s}\widehat{\mathbf{s}} + \frac{1}{R}\frac{\partial f}{\partial\phi}\widehat{\phi} \tag{A.83}$$

- Divergence

$$\nabla\cdot\mathbf{A} = \frac{\|\nabla\psi\|}{R}\frac{\partial}{\partial\psi}\left(R\mathbf{A}\cdot\widehat{\psi}\right) + \frac{\|\nabla\psi\|}{R}\frac{\partial}{\partial s}\left(\frac{R}{\|\nabla\psi\|}\mathbf{A}\cdot\widehat{\mathbf{s}}\right) + \frac{1}{R}\frac{\partial}{\partial\phi}\left(\mathbf{A}\cdot\widehat{\phi}\right) \tag{A.84}$$

- Curl

$$\begin{aligned} (\nabla\times\mathbf{A})\cdot\widehat{\psi} &= \frac{1}{R}\frac{\partial}{\partial s}\left(R\mathbf{A}\cdot\widehat{\phi}\right) - \frac{1}{R}\frac{\partial}{\partial\phi}\left(\mathbf{A}\cdot\widehat{\mathbf{s}}\right) \\ (\nabla\times\mathbf{A})\cdot\widehat{\mathbf{s}} &= \frac{1}{R}\frac{\partial}{\partial\phi}\left(\mathbf{A}\cdot\widehat{\psi}\right) - \frac{\|\nabla\psi\|}{R}\frac{\partial}{\partial\psi}\left(R\mathbf{A}\cdot\widehat{\phi}\right) \\ (\nabla\times\mathbf{A})\cdot\widehat{\phi} &= \|\nabla\psi\|\frac{\partial}{\partial\psi}\left(\mathbf{A}\cdot\widehat{\mathbf{s}}\right) - \|\nabla\psi\|\frac{\partial}{\partial s}\left(\frac{\mathbf{A}\cdot\widehat{\psi}}{\|\nabla\psi\|}\right) \end{aligned} \tag{A.85}$$

### A.2.4 System $(\psi, \theta, \phi)$

The coordinates $(\psi, \theta, \phi)$ are an alternative to $(\psi, \theta, \phi)$ and is defined from the origin $(R_p, Z_p)$ and is related to $(r, \theta, \phi)$ by

$$\psi = \psi(r, \theta) \tag{A.86}$$

which is inverted to

$$r = r(\psi, \theta) \tag{A.87}$$

The position vector then becomes

$$\mathbf{X} = R_p \widehat{\mathbf{R}} + Z_p \widehat{\mathbf{Z}} + r(\psi, \theta)\, \widehat{\mathbf{r}} \tag{A.88}$$

The covariant vector basis (A.1) is

$$(\mathbf{e}_\psi, \mathbf{e}_\theta, \mathbf{e}_\phi) \equiv \left( \frac{\partial \mathbf{X}}{\partial \psi}, \frac{\partial \mathbf{X}}{\partial \theta}, \frac{\partial \mathbf{X}}{\partial \phi} \right) = \left( \frac{\widehat{\mathbf{r}}}{\|\nabla \psi\| \cos\alpha}, \frac{r\widehat{\mathbf{s}}}{\cos\alpha}, R\widehat{\phi} \right) \tag{A.89}$$

where ()

$$\cos\alpha = \left| \widehat{\psi} \cdot \widehat{\mathbf{r}} \right| \tag{A.90}$$

The Contravariant vector basis (A.7) is

$$\left(\mathbf{e}^\psi, \mathbf{e}^\theta, \mathbf{e}^\phi\right) \equiv (\nabla\psi, \nabla\theta, \nabla\phi) = \left( \|\nabla\psi\|\, \widehat{\psi}, \frac{\widehat{\theta}}{r}, \frac{\widehat{\phi}}{R} \right) \tag{A.91}$$

Note that the two based are not colinear in this case, because $\left(\widehat{\psi}, \widehat{\theta}, \widehat{\phi}\right)$ is not orthogonal. The Jacobian of the transformation is

$$J = \frac{Rr}{\|\nabla\psi\| \cos\alpha} \tag{A.92}$$

The differential elements associated with this system are:

- the infinitesimal distance element along each coordinate

$$\begin{aligned} dl(\psi) &= \frac{d\psi}{\|\nabla\psi\|\cos\alpha} \\ dl(\theta) &= \frac{r}{\cos\alpha}d\theta \\ dl(\phi) &= Rd\phi \end{aligned} \tag{A.93}$$

- the infinitesimal surface element of constant coordinate

$$\begin{aligned} d\mathbf{S}(\psi) &= \frac{Rr}{\cos\alpha}d\theta d\phi\,\widehat{\psi} \\ d\mathbf{S}(\theta) &= \frac{R}{\|\nabla\psi\|\cos\alpha}d\psi d\phi\,\widehat{\mathbf{s}} \\ d\mathbf{S}(\phi) &= \frac{r}{\|\nabla\psi\|\cos\alpha}d\psi d\theta\,\widehat{\phi} \end{aligned} \tag{A.94}$$

- the infinitesimal volume element

$$d^3\mathbf{X} = \frac{Rr}{\|\nabla\psi\|\cos\alpha}d\psi d\theta d\phi \tag{A.95}$$

Finally, the differential operators are

- Gradient

$$\nabla f = \|\nabla\psi\|\frac{\partial f}{\partial\psi}\widehat{\psi} + \frac{1}{r}\frac{\partial f}{\partial\theta}\widehat{\theta} + \frac{1}{R}\frac{\partial f}{\partial\phi}\widehat{\phi} \tag{A.96}$$

- Divergence

$$\begin{aligned} \nabla\cdot\mathbf{A} = &\frac{\|\nabla\psi\|\cos\alpha}{Rr}\frac{\partial}{\partial\psi}\left(\frac{Rr}{\cos\alpha}\mathbf{A}\cdot\widehat{\psi}\right) \\ &+ \frac{\|\nabla\psi\|\cos\alpha}{Rr}\frac{\partial}{\partial\theta}\left(\frac{R}{\|\nabla\psi\|\cos\alpha}\mathbf{A}\cdot\widehat{\theta}\right) + \frac{1}{R}\frac{\partial}{\partial\phi}\left(\mathbf{A}\cdot\widehat{\phi}\right) \end{aligned} \tag{A.97}$$

- Curl

$$
\begin{aligned}
(\nabla \times \mathbf{A}) \cdot \widehat{\psi} &= \frac{\cos\alpha}{Rr} \frac{\partial}{\partial \theta} \left( R\mathbf{A} \cdot \widehat{\phi} \right) - \frac{1}{R} \frac{\partial}{\partial \phi} \left( \mathbf{A} \cdot \widehat{\mathbf{s}} \right) \\
(\nabla \times \mathbf{A}) \cdot \widehat{\theta} &= \frac{1}{R} \frac{\partial}{\partial \phi} \left( \mathbf{A} \cdot \widehat{\mathbf{r}} \right) - \frac{|\nabla \psi| \cos\alpha}{R} \frac{\partial}{\partial \psi} \left( R\mathbf{A} \cdot \widehat{\phi} \right) \\
(\nabla \times \mathbf{A}) \cdot \widehat{\phi} &= \frac{|\nabla \psi| \cos\alpha}{r} \frac{\partial}{\partial \psi} \left( \frac{r\mathbf{A} \cdot \widehat{\mathbf{s}}}{\cos\alpha} \right) - \frac{|\nabla \psi| \cos\alpha}{r} \frac{\partial}{\partial \theta} \left( \frac{\mathbf{A} \cdot \widehat{\mathbf{r}}}{|\nabla \psi| \cos\alpha} \right)
\end{aligned}
\tag{A.98}
$$

## A.3 Momentum Space

We consider a cartesian momentum space in coordinates $(p_x, p_y, p_z)$ along axes $(\widehat{\mathbf{x}}, \widehat{\mathbf{y}}, \widehat{\mathbf{z}})$. The vector position is momentum space is written

$$
\mathbf{P} = p_x \widehat{\mathbf{x}} + p_y \widehat{\mathbf{y}} + p_z \widehat{\mathbf{z}} \tag{A.99}
$$

We consider the two following curvilinear systems:

### A.3.1 System $\left(p_{\parallel}, p_{\perp}, \varphi\right)$

The coordinates $\left(p_{\parallel}, p_{\perp}, \varphi\right)$ are defined on the space $-\infty \leq p_{\parallel} < \infty$, $0 \leq p_{\perp} < \infty$, $0 \leq \varphi < 2\pi$ and is related to $(p_x, p_y, p_z)$ by

$$
\begin{aligned}
p_{\parallel} &= p_z \\
p_{\perp} &= \sqrt{p_x^2 + p_y^2} \\
\varphi &= \arctan\left(p_y / p_x\right) + \pi H\left(-p_x\right) \quad [2\pi]
\end{aligned}
\tag{A.100}
$$

which is inverted to

$$
\begin{aligned}
p_x &= p_{\perp} \cos\varphi \\
p_y &= p_{\perp} \sin\varphi \\
p_z &= p_{\parallel}
\end{aligned}
\tag{A.101}
$$

The position vector in momentum space then becomes

$$
\mathbf{P} = p_{\perp} \widehat{\perp} + p_{\parallel} \widehat{\parallel} \tag{A.102}
$$

where we define a local orthonormal basis $\left(\widehat{\parallel}, \widehat{\perp}, \widehat{\varphi}\right)$ as

$$\begin{aligned}
\widehat{\parallel} &= \widehat{\mathbf{z}} \\
\widehat{\perp} &= \cos\varphi\, \widehat{\mathbf{x}} + \sin\varphi\, \widehat{\mathbf{y}} \\
\widehat{\varphi} &= \widehat{\parallel} \times \widehat{\perp} = -\sin\varphi\, \widehat{\mathbf{x}} + \cos\varphi\, \widehat{\mathbf{y}}
\end{aligned} \tag{A.103}$$

The covariant vector basis (A.1) is

$$\left(\mathbf{e}_{\parallel}, \mathbf{e}_{\perp}, \mathbf{e}_{\varphi}\right) \equiv \left(\frac{\partial \mathbf{P}}{\partial p_{\parallel}}, \frac{\partial \mathbf{P}}{\partial p_{\perp}}, \frac{\partial \mathbf{P}}{\partial \varphi}\right) = \left(\widehat{\parallel}, \widehat{\perp}, p_{\perp}\widehat{\varphi}\right) \tag{A.104}$$

The Contravariant vector basis (A.7) is

$$\left(\mathbf{e}^{\parallel}, \mathbf{e}^{\perp}, \mathbf{e}^{\varphi}\right) \equiv \left(\nabla_{\mathbf{p}} p_{\parallel}, \nabla_{\mathbf{p}} p_{\perp}, \nabla_{\mathbf{p}} \varphi\right) = \left(\widehat{\parallel}, \widehat{\perp}, \frac{\widehat{\varphi}}{p_{\perp}}\right) \tag{A.105}$$

The Jacobian is

$$J = p_{\perp} \tag{A.106}$$

The differential elements associated with this system are:

- the infinitesimal distance element along each coordinate

$$\begin{aligned}
dl\left(p_{\parallel}\right) &= dp_{\parallel} \\
dl\left(p_{\perp}\right) &= dp_{\perp} \\
dl\left(\varphi\right) &= p_{\perp} d\varphi
\end{aligned} \tag{A.107}$$

- the infinitesimal surface element of constant coordinate

$$\begin{aligned}
d\mathbf{S}\left(p_{\parallel}\right) &= p_{\perp} dp_{\perp} d\varphi\, \widehat{\parallel} \\
d\mathbf{S}\left(p_{\perp}\right) &= p_{\perp} dp_{\parallel} d\varphi\, \widehat{\perp} \\
d\mathbf{S}\left(\varphi\right) &= dp_{\parallel} dp_{\perp}\, \widehat{\varphi}
\end{aligned} \tag{A.108}$$

- the infinitesimal volume element

$$d^3\mathbf{X} = p_{\perp} dp_{\parallel} dp_{\perp} d\varphi \tag{A.109}$$

Finally, the differential operators are

- Gradient

$$\nabla_{\mathbf{p}} f = \frac{\partial f}{\partial p_{\parallel}} \widehat{\parallel} + \frac{\partial f}{\partial p_{\perp}} \widehat{\perp} + \frac{1}{p_{\perp}} \frac{\partial f}{\partial \varphi} \widehat{\varphi} \tag{A.110}$$

- Divergence

$$\nabla_{\mathbf{p}} \cdot \mathbf{A} = \frac{\partial}{\partial p_{\parallel}} \left( \mathbf{A} \cdot \widehat{\parallel} \right) + \frac{1}{p_{\perp}} \frac{\partial}{\partial p_{\perp}} \left( p_{\perp} \mathbf{A} \cdot \widehat{\perp} \right) + \frac{1}{p_{\perp}} \frac{\partial}{\partial \varphi} \left( \mathbf{A} \cdot \widehat{\varphi} \right) \tag{A.111}$$

- Curl

$$\begin{aligned} (\nabla_{\mathbf{p}} \times \mathbf{A}) \cdot \widehat{\parallel} &= \frac{\partial}{\partial p_{\perp}} \left( p_{\perp} \mathbf{A} \cdot \widehat{\varphi} \right) - \frac{1}{p_{\perp}} \frac{\partial}{\partial \varphi} \left( \mathbf{A} \cdot \widehat{\perp} \right) \\ (\nabla_{\mathbf{p}} \times \mathbf{A}) \cdot \widehat{\perp} &= \frac{1}{p_{\perp}} \frac{\partial}{\partial \varphi} \left( \mathbf{A} \cdot \widehat{\parallel} \right) - \frac{\partial}{\partial p_{\parallel}} \left( \mathbf{A} \cdot \widehat{\varphi} \right) \\ (\nabla_{\mathbf{p}} \times \mathbf{A}) \cdot \widehat{\varphi} &= \frac{\partial}{\partial p_{\parallel}} \left( \mathbf{A} \cdot \widehat{\perp} \right) - \frac{\partial}{\partial p_{\perp}} \left( \mathbf{A} \cdot \widehat{\parallel} \right) \end{aligned} \tag{A.112}$$

### A.3.2 System $(p, \xi, \varphi)$

The coordinates $(p, \xi, \varphi)$ are defined on the space $0 \leq p < \infty$, $-1 \leq \xi < 1$, $0 \leq \varphi < 2\pi$ and is related to $(p_{\parallel}, p_{\perp}, \varphi)$ by

$$\begin{aligned} p &= \sqrt{p_{\parallel}^2 + p_{\perp}^2} \\ \xi &= \frac{p_{\parallel}}{\sqrt{p_{\parallel}^2 + p_{\perp}^2}} \end{aligned} \tag{A.113}$$

which is inverted to

$$\begin{aligned} p_{\parallel} &= p\xi \\ p_{\perp} &= p\sqrt{1 - \xi^2} \end{aligned} \tag{A.114}$$

The position vector in momentum space then becomes

$$\mathbf{P} = p\widehat{\mathbf{p}} \tag{A.115}$$

where we define a local orthonormal basis $\left(\widehat{\mathbf{p}}, \widehat{\xi}, \widehat{\varphi}\right)$ as

$$\begin{aligned} \widehat{\mathbf{p}} &= \sqrt{1-\xi^2}\widehat{\perp} + \xi \widehat{\parallel} \\ \widehat{\xi} &= \widehat{\varphi} \times \widehat{\mathbf{p}} = \xi\widehat{\perp} - \sqrt{1-\xi^2}\,\widehat{\parallel} \end{aligned} \tag{A.116}$$

The covariant vector basis (A.1) is

$$\left(\mathbf{e}_p, \mathbf{e}_\xi, \mathbf{e}_\varphi\right) \equiv \left(\frac{\partial \mathbf{P}}{\partial p}, \frac{\partial \mathbf{P}}{\partial \xi}, \frac{\partial \mathbf{P}}{\partial \varphi}\right) = \left(\widehat{\mathbf{p}}, -\frac{p}{\sqrt{1-\xi^2}}\widehat{\xi}, p\sqrt{1-\xi^2}\widehat{\varphi}\right) \tag{A.117}$$

The Contravariant vector basis (A.7) is

$$\left(\mathbf{e}^p, \mathbf{e}^\xi, \mathbf{e}^\varphi\right) \equiv \left(\nabla_{\mathbf{p}} p, \nabla_{\mathbf{p}} \xi, \nabla_{\mathbf{p}} \varphi\right) = \left(\widehat{\mathbf{p}}, -\frac{\sqrt{1-\xi^2}}{p}\widehat{\xi}, \frac{1}{p\sqrt{1-\xi^2}}\widehat{\varphi}\right) \tag{A.118}$$

The Jacobian is

$$J = p^2 \tag{A.119}$$

The differential elements associated with this system are:

- the infinitesimal distance element along each coordinate

$$\begin{aligned} dl\left(p\right) &= dp \\ dl\left(\xi\right) &= \frac{p}{\sqrt{1-\xi^2}} d\xi \\ dl\left(\varphi\right) &= p\sqrt{1-\xi^2} d\varphi \end{aligned} \tag{A.120}$$

- the infinitesimal surface element of constant coordinate

$$\begin{aligned} d\mathbf{S}\left(p\right) &= p^2 d\xi d\varphi\, \widehat{\mathbf{p}} \\ d\mathbf{S}\left(\xi\right) &= -p\sqrt{1-\xi^2} dp d\varphi\, \widehat{\xi} \\ d\mathbf{S}\left(\varphi\right) &= \frac{p}{\sqrt{1-\xi^2}} dp d\xi\, \widehat{\varphi} \end{aligned} \tag{A.121}$$

- the infinitesimal volume element

$$d^3\mathbf{X} = p^2 dp d\xi d\varphi \tag{A.122}$$

Finally, the differential operators are

- Gradient

$$\nabla_{\mathbf{p}} f = \frac{\partial f}{\partial p}\widehat{\mathbf{p}} - \frac{\sqrt{1-\xi^2}}{p}\frac{\partial f}{\partial \xi}\widehat{\xi} + \frac{1}{p\sqrt{1-\xi^2}}\frac{\partial f}{\partial \varphi}\widehat{\varphi} \tag{A.123}$$

- Divergence

$$\nabla_{\mathbf{p}} \cdot \mathbf{A} = \frac{1}{p^2}\frac{\partial}{\partial p}\left(p^2 \mathbf{A}\cdot\widehat{\mathbf{p}}\right) - \frac{1}{p}\frac{\partial}{\partial \xi}\left(\sqrt{1-\xi^2}\mathbf{A}\cdot\widehat{\xi}\right) + \frac{1}{p\sqrt{1-\xi^2}}\frac{\partial}{\partial \varphi}\left(\mathbf{A}\cdot\widehat{\varphi}\right) \tag{A.124}$$

- Curl

$$\begin{aligned}
(\nabla\times\mathbf{A})\cdot\widehat{\mathbf{p}} &= \frac{1}{p}\frac{\partial}{\partial \xi}\left(\sqrt{1-\xi^2}\mathbf{A}\cdot\widehat{\varphi}\right) + \frac{1}{p\sqrt{1-\xi^2}}\frac{\partial}{\partial \varphi}\left(\mathbf{A}\cdot\widehat{\xi}\right) \\
(\nabla\times\mathbf{A})\cdot\widehat{\xi} &= \frac{1}{p}\frac{\partial}{\partial p}\left(p\mathbf{A}\cdot\widehat{\varphi}\right) - \frac{1}{p\sqrt{1-\xi^2}}\frac{\partial}{\partial \varphi}\left(\mathbf{A}\cdot\widehat{\mathbf{p}}\right) \\
(\nabla\times\mathbf{A})\cdot\widehat{\varphi} &= -\frac{1}{p}\frac{\partial}{\partial p}\left(p\mathbf{A}\cdot\widehat{\xi}\right) - \frac{\sqrt{1-\xi^2}}{p}\frac{\partial}{\partial \xi}\left(\mathbf{A}\cdot\widehat{\mathbf{p}}\right)
\end{aligned} \tag{A.125}$$

# Appendix B

# Quasilinear Operator in an Infinite Uniform Plasma

## B.1 Introduction

We consider an infinite uniform collisionless plasma in a constant, uniform magnetic field of magnitude $B$ associated with the electron gyrofrequency $\omega_{ce} = eB/m_e$. Steady-state radio-frequency (RF) fields are applied to this plasma. The RF electric field is assumed to be decomposed into a discrete set of monochromatic waves with frequency $\omega_b$

$$\mathbf{E}(\mathbf{r},t) = \sum_b \mathbf{E}_b(\mathbf{r})\, e^{-i\omega_b t} \tag{B.1}$$

with each monochromatic wave being decomposed into Fourier components, such that

$$\mathbf{E}_b(\mathbf{r}) = \iiint \frac{d^3k}{(2\pi)^3} \mathbf{E}_{\mathbf{k},b}(\mathbf{k})\, e^{i\mathbf{k}\cdot\mathbf{r}} \tag{B.2}$$

where each Fourier component is given by

$$\mathbf{E}_{\mathbf{k},b}(\mathbf{k}) = \iiint d^3r\ \mathbf{E}_b(\mathbf{r})\, e^{-i\mathbf{k}\cdot\mathbf{r}} \tag{B.3}$$

The quasilinear operator describing the slow evolution of the macroscopic distribution function $f$ under the effect of the fields has been derived by Kennel & Engelmann

[41] and extended by Lerche [42] to relativistic plasmas. In order to apply this operator to our study of EBWCD, we proceed in three steps: first, the operator derived by Lerche is transformed in order to be expressed in a conservative form, as the divergence of a RF-driven flux, which is essential for a proper use in a kinetic code in which particles conservation must be ensured. The second step consist of transforming the quasilinear operator using the reality of the electric field. Third, this operator is applied to the case of a quasi-Gaussian RF beam, which is a generally a good approximation for experimental EBWs. The use of this operator - derived for an infinite uniform plasma - in a bounded, non-uniform tokamak plasma is discussed and justified in Section 3.5.2. In the fourth section, we extend our operator to a slab geometry and use the energy equation to calculate the power deposition profile for EBWs.

## B.2 Quasilinear operator in a conservative form

The quasilinear operator derived by Lerche for a relativistic infinite uniform plasma assumed a field with a single monochromatic frequency $\omega$. The generalization for a discrete set of frequencies is immediate and will be done at the end of the section. The operator derived by Lerche [42] is expressed as

$$\begin{aligned} Q(f) = -\frac{e^2}{(2\pi)^3} \lim_{V\to\infty} \frac{1}{V} \sum_{n=-\infty}^{\infty} \iiint d^3k \\ \left[ \left( P_\parallel^* E_{\mathbf{k},\parallel}^* J_n + \left[ P_\perp^* - \frac{1}{p_\perp} \left( \frac{k_\parallel v_\parallel}{\omega^*} - 1 \right) \right] E_{\mathbf{k},\perp}^* \right) \right. \\ \left. \frac{i}{\left[ n\Omega + k_\parallel v_\parallel - \omega \right]} \left( E_{\mathbf{k},\parallel} J_n P_\parallel + E_{\mathbf{k},\perp} P_\perp \right) f \right] \end{aligned} \tag{B.4}$$

with the momentum-space differential operators

$$\begin{aligned} P_\parallel &= \frac{\partial}{\partial p_\parallel} - \frac{n\Omega}{\omega v_\perp} \left( v_\perp \frac{\partial}{\partial p_\parallel} - v_\parallel \frac{\partial}{\partial p_\perp} \right) \\ P_\perp &= \frac{\partial}{\partial p_\perp} + \frac{k_\parallel}{\omega} \left( v_\perp \frac{\partial}{\partial p_\parallel} - v_\parallel \frac{\partial}{\partial p_\perp} \right) \end{aligned} \tag{B.5}$$

and

$$E_{\mathbf{k},\perp} = \frac{1}{\sqrt{2}}\left(E_{\mathbf{k},-}e^{i\alpha}J_{n+1} + E_{\mathbf{k},+}e^{-i\alpha}J_{n-1}\right) \tag{B.6}$$

where a Fourier component $\mathbf{E}_\mathbf{k}$ (B.3) of the electric field is projected on the rotating field frame

$$\begin{aligned} E_{\mathbf{k},\pm} &= \frac{1}{\sqrt{2}}\left(E_{\mathbf{k},x} \pm iE_{\mathbf{k},y}\right) \\ E_{\mathbf{k},\parallel} &= E_{\mathbf{k},z} \end{aligned} \tag{B.7}$$

The wave vector is expressed in cylindrical coordinates as

$$\begin{aligned} k_x &= k_\perp \cos\alpha \\ k_y &= k_\perp \sin\alpha \\ k_z &= k_\parallel \end{aligned}$$

and the argument of the Bessel functions is $k_\perp v_\perp/\Omega$ where the relativistic cyclotron frequency is

$$\Omega = \frac{q_e B}{\gamma m_e} = -\frac{\omega_{ce}}{\gamma} \tag{B.8}$$

The differential operators (B.5) can be rewritten in divergence form as

$$\begin{aligned} P_\parallel \mathcal{A} &= \frac{\partial}{\partial p_\parallel}\left[\left(1 - \frac{n\Omega}{\omega}\right)\mathcal{A}\right] + \frac{1}{p_\perp}\frac{\partial}{\partial p_\perp}\left(p_\perp \frac{n\Omega}{\omega}\frac{p_\parallel}{p_\perp}\mathcal{A}\right) \\ P_\perp \mathcal{A} &= \frac{\partial}{\partial p_\parallel}\frac{k_\parallel v_\perp}{\omega}\mathcal{A} + \frac{1}{p_\perp}\frac{\partial}{\partial p_\perp}\left[p_\perp\left(1 - \frac{k_\parallel v_\perp}{\omega}\right)\mathcal{A}\right] + \frac{1}{p_\perp}\left(\frac{k_\parallel v_\perp}{\omega} - 1\right)\mathcal{A} \end{aligned} \tag{B.9}$$

where we used the identity

$$\frac{\partial \gamma}{\partial p_\parallel} = \frac{p_\parallel}{\gamma m^2 c^2} = \frac{p_\parallel}{p_\perp}\frac{\partial \gamma}{\partial p_\perp} \tag{B.10}$$

Consequently, (B.4) can be rewritten in a conservative form as

$$\mathcal{Q}(f) = -\nabla_\mathbf{p} \cdot \mathbf{S}^{\mathrm{RF}} = -\frac{1}{p_\perp}\frac{\partial}{\partial p_\perp}\left(p_\perp S_\perp^{\mathrm{RF}}\right) - \frac{\partial}{\partial p_\parallel}\left(S_\parallel^{\mathrm{RF}}\right) \tag{B.11}$$

where we see from the expression (B.4) and (B.5) that the fluxes are purely diffusive,

such that we can write

$$\mathbf{S}^{\mathrm{RF}} = -\mathbb{D}^{\mathrm{RF}} \cdot \nabla_{\mathbf{p}} f = -\begin{pmatrix} D_{\perp\perp}^{\mathrm{RF}} & D_{\perp\parallel}^{\mathrm{RF}} \\ D_{\parallel\perp}^{\mathrm{RF}} & D_{\parallel\parallel}^{\mathrm{RF}} \end{pmatrix} \cdot \begin{pmatrix} \partial f/\partial p_{\perp} \\ \partial f/\partial p_{\parallel} \end{pmatrix} \tag{B.12}$$

with the following diffusion tensor elements

$$\begin{aligned}
D_{\perp\perp}^{\mathrm{RF}} &= -\sum_{n=-\infty}^{+\infty} \frac{e^2}{(2\pi)^3} \lim_{V\to\infty} \frac{1}{V} \iiint d^3k \left[ \left( \frac{n\Omega}{\omega^*} \frac{p_{\parallel}}{p_{\perp}} E_{\mathbf{k},\parallel}^* J_n + \left[ 1 - \frac{k_{\parallel} v_{\perp}}{\omega^*} \right] E_{\mathbf{k},\perp}^* \right) \right. \\
&\quad \left. \frac{i}{\left[ n\Omega + k_{\parallel} v_{\parallel} - \omega \right]} \left( \frac{n\Omega}{\omega} \frac{v_{\parallel}}{v_{\perp}} E_{\mathbf{k},\parallel} J_n + \left[ 1 - \frac{k_{\parallel} v_{\perp}}{\omega} \right] E_{\mathbf{k},\perp} \right) \right] \\
D_{\perp\parallel}^{\mathrm{RF}} &= -\sum_{n=-\infty}^{+\infty} \frac{e^2}{(2\pi)^3} \lim_{V\to\infty} \frac{1}{V} \iiint d^3k \left[ \left( \frac{n\Omega}{\omega^*} \frac{p_{\parallel}}{p_{\perp}} E_{\mathbf{k},\parallel}^* J_n + \left[ 1 - \frac{k_{\parallel} v_{\perp}}{\omega^*} \right] E_{\mathbf{k},\perp}^* \right) \right. \\
&\quad \left. \frac{i}{\left[ n\Omega + k_{\parallel} v_{\parallel} - \omega \right]} \left( \left[ 1 - \frac{n\Omega}{\omega} \right] E_{\mathbf{k},\parallel} J_n + \frac{k_{\parallel} v_{\perp}}{\omega} E_{\mathbf{k},\perp} \right) \right] \\
D_{\parallel\perp}^{\mathrm{RF}} &= -\sum_{n=-\infty}^{+\infty} \frac{e^2}{(2\pi)^3} \lim_{V\to\infty} \frac{1}{V} \iiint d^3k \left[ \left( \left[ 1 - \frac{n\Omega}{\omega^*} \right] E_{\mathbf{k},\parallel}^* J_n + \frac{k_{\parallel} v_{\perp}}{\omega^*} E_{\mathbf{k},\perp}^* \right) \right. \\
&\quad \left. \frac{i}{\left[ n\Omega + k_{\parallel} v_{\parallel} - \omega \right]} \left( \frac{n\Omega}{\omega} \frac{v_{\parallel}}{v_{\perp}} E_{\mathbf{k},\parallel} J_n + \left[ 1 - \frac{k_{\parallel} v_{\perp}}{\omega} \right] E_{\mathbf{k},\perp} \right) \right] \\
D_{\parallel\parallel}^{\mathrm{RF}} &= -\sum_{n=-\infty}^{+\infty} \frac{e^2}{(2\pi)^3} \lim_{V\to\infty} \frac{1}{V} \iiint d^3k \left[ \left( \left[ 1 - \frac{n\Omega}{\omega^*} \right] E_{\mathbf{k},\parallel}^* J_n + \frac{k_{\parallel} v_{\perp}}{\omega^*} E_{\mathbf{k},\perp}^* \right) \right. \\
&\quad \left. \frac{i}{\left[ n\Omega + k_{\parallel} v_{\parallel} - \omega \right]} \left( \left[ 1 - \frac{n\Omega}{\omega} \right] E_{\mathbf{k},\parallel} J_n + \frac{k_{\parallel} v_{\perp}}{\omega} E_{\mathbf{k},\perp} \right) \right]
\end{aligned} \tag{B.13}$$

In the limit of a resonant diffusion,

$$\frac{1}{\left[ n\Omega + k_{\parallel} v_{\parallel} - \omega \right]} \to i\pi\delta\left( \omega - k_{\parallel} v_{\parallel} - n\Omega \right) \tag{B.14}$$

and, using the resonance condition

$$k_{\parallel} v_{\parallel} = \omega - n\Omega \tag{B.15}$$

the frequency $\omega$ must be real and the RF diffusion tensor elements may be expressed

in a simple form

$$
\begin{aligned}
D_{\perp\perp}^{\mathrm{RF}} &= \sum_{n=-\infty}^{+\infty} \left(\frac{n\Omega}{\omega}\right)^2 D_n^{\mathrm{RF}}(\mathbf{p}) \\
D_{\perp\parallel}^{\mathrm{RF}} &= \sum_{n=-\infty}^{+\infty} \frac{p_\perp}{p_\parallel}\frac{n\Omega}{\omega}\left(1-\frac{n\Omega}{\omega}\right) D_n^{\mathrm{RF}}(\mathbf{p}) \\
D_{\parallel\perp}^{\mathrm{RF}} &= \sum_{n=-\infty}^{+\infty} \frac{p_\perp}{p_\parallel}\frac{n\Omega}{\omega}\left(1-\frac{n\Omega}{\omega}\right) D_n^{\mathrm{RF}}(\mathbf{p}) \\
D_{\parallel\parallel}^{\mathrm{RF}} &= \sum_{n=-\infty}^{+\infty} \frac{p_\perp^2}{p_\parallel^2}\left(1-\frac{n\Omega}{\omega}\right)^2 D_n^{\mathrm{RF}}(\mathbf{p})
\end{aligned}
\tag{B.16}
$$

where the diffusion coefficient, common to all tensor elements, is

$$
D_n^{\mathrm{RF}}(\mathbf{p}) = \lim_{V\to\infty}\frac{\pi e^2}{V}\iiint\frac{d^3k}{(2\pi)^3}\left|E_{\mathbf{k},\perp}+\frac{p_\parallel}{p_\perp}E_{\mathbf{k},\parallel}J_n\right|^2\delta\left(\omega-k_\parallel v_\parallel-n\Omega\right) \tag{B.17}
$$

which can be rewritten as

$$
D_n^{\mathrm{RF}}(\mathbf{p}) = \lim_{V\to\infty}\frac{\pi e^2}{V}\iiint\frac{d^3k}{(2\pi)^3}\left\|\mathbf{E}_\mathbf{k}\right\|^2\left|\Theta_\mathbf{k}^{(n)}\right|^2\delta\left(\omega-k_\parallel v_\parallel-n\Omega\right) \tag{B.18}
$$

where we refer to $\Theta_\mathbf{k}^{(n)}$ as the polarization term associated with a particular Fourier component $\mathbf{E}_\mathbf{k} = |\mathbf{E}_\mathbf{k}|\,e^{i\varphi_\mathbf{k}}$. It is expressed as

$$
\Theta_\mathbf{k}^{(n)} = \frac{1}{\sqrt{2}}e_{\mathbf{k},+}e^{-i\alpha}J_{n-1}\left(\frac{k_\perp v_\perp}{\Omega}\right)+\frac{1}{\sqrt{2}}e_{\mathbf{k},-}e^{+i\alpha}J_{n+1}\left(\frac{k_\perp v_\perp}{\Omega}\right)+\frac{p_\parallel}{p_\perp}e_{\mathbf{k},\parallel}J_n\left(\frac{k_\perp v_\perp}{\Omega}\right) \tag{B.19}
$$

where the polarization vector $\mathbf{e}_\mathbf{k} = |\mathbf{E}_\mathbf{k}|\,/\,\|\mathbf{E}_\mathbf{k}\|$ is decomposed as

$$
\begin{aligned}
e_{\mathbf{k},+} &= \frac{|E_{\mathbf{k},x}|+i\,|E_{\mathbf{k},y}|}{\sqrt{2}\,\|\mathbf{E}_\mathbf{k}\|} \\
e_{\mathbf{k},-} &= \frac{|E_{\mathbf{k},x}|-i\,|E_{\mathbf{k},y}|}{\sqrt{2}\,\|\mathbf{E}_\mathbf{k}\|} \\
e_{\mathbf{k},\parallel} &= \frac{|E_{\mathbf{k},z}|}{\|\mathbf{E}_\mathbf{k}\|}
\end{aligned}
\tag{B.20}
$$

and where the phase $\varphi_{\mathbf{k},b}$ diseappeared because only the module of $\Theta_\mathbf{k}^{(n)}$ is used.

### B.2.1 Discrete set of monochromatic waves

The extension of the quasilinear operator to a discrete set of monochromatic waves is immediate provided that wave-wave coupling phenomena are neglected. With the electric field given by (B.1), the RF flux (B.12) is the sum over the contributions from each frequency

$$\mathbf{S}^{\mathrm{RF}} = \sum_b \mathbf{S}_b^{\mathrm{RF}}\left(\omega_b, \mathbf{E}_b\right) \tag{B.21}$$

with

$$\mathbf{S}_b^{\mathrm{RF}}\left(\omega_b, \mathbf{E}_b\right) = -\mathbb{D}_b^{\mathrm{RF}}\left(\omega_b, \mathbf{E}_b\right) \cdot \nabla_{\mathbf{p}} f \tag{B.22}$$

where the diffusion tensor elements (B.16) for a given $(\omega_b, \mathbf{E}_b)$ are

$$\begin{aligned}
D_{b,\perp\perp}^{\mathrm{RF}} &= \sum_{n=-\infty}^{+\infty} \left(\frac{n\Omega}{\omega_b}\right)^2 D_n^{\mathrm{RF}}\left(\mathbf{p}, \omega_b, \mathbf{E}_b\right) \\
D_{b,\perp\parallel}^{\mathrm{RF}} &= \sum_{n=-\infty}^{+\infty} \frac{p_\perp}{p_\parallel} \frac{n\Omega}{\omega_b}\left(1 - \frac{n\Omega}{\omega_b}\right) D_n^{\mathrm{RF}}\left(\mathbf{p}, \omega_b, \mathbf{E}_b\right) \\
D_{b,\parallel\perp}^{\mathrm{RF}} &= \sum_{n=-\infty}^{+\infty} \frac{p_\perp}{p_\parallel} \frac{n\Omega}{\omega_b}\left(1 - \frac{n\Omega}{\omega_b}\right) D_n^{\mathrm{RF}}\left(\mathbf{p}, \omega_b, \mathbf{E}_b\right) \\
D_{b,\parallel\parallel}^{\mathrm{RF}} &= \sum_{n=-\infty}^{+\infty} \frac{p_\perp^2}{p_\parallel^2}\left(1 - \frac{n\Omega}{\omega_b}\right)^2 D_n^{\mathrm{RF}}\left(\mathbf{p}, \omega_b, \mathbf{E}_b\right)
\end{aligned} \tag{B.23}$$

The diffusion coefficient (B.18) associated with a particular harmonic $n$ and the wave parameters $(\omega_b, \mathbf{E}_b)$ is given by

$$D_n^{\mathrm{RF}}\left(\mathbf{p}, \omega_b, \mathbf{E}_b\right) = \lim_{V\to\infty} \frac{\pi e^2}{V} \iiint \frac{d^3k}{(2\pi)^3} \left\|\mathbf{E}_{\mathbf{k},b}\right\|^2 \left|\Theta_{\mathbf{k}}^{(n)}\left(\mathbf{k}, \mathbf{e}_{\mathbf{k},b}\right)\right|^2 \delta\left(\omega_b - k_\parallel v_\parallel - n\Omega\right) \tag{B.24}$$

where $\Theta_{\mathbf{k}}^{(n)}$, which accounts for the polarization and the intensity of the RF wave, is given by (B.19)

$$\begin{aligned}
\Theta_{\mathbf{k}}^{(n)}\left(\mathbf{k}, \mathbf{e}_{\mathbf{k},b}\right) = {} & \frac{1}{\sqrt{2}} e_{\mathbf{k},b,+} e^{-i\alpha} J_{n-1}\left(\frac{k_\perp v_\perp}{\Omega}\right) + \frac{1}{\sqrt{2}} e_{\mathbf{k},b,-} e^{+i\alpha} J_{n+1}\left(\frac{k_\perp v_\perp}{\Omega}\right) \\
& + \frac{p_\parallel}{p_\perp} e_{\mathbf{k},b,\parallel} J_n\left(\frac{k_\perp v_\perp}{\Omega}\right)
\end{aligned} \tag{B.25}$$

and $\mathbf{E}_{\mathbf{k},b}(\mathbf{k})$ is obtained from the Fourier transform (B.3) with $\mathbf{e}_{\mathbf{k},b} = |\mathbf{E}_{\mathbf{k},b}| / \|\mathbf{E}_{\mathbf{k},b}\|$.

### B.2.2 Reality of the electric field

Because the electric field is a real quantity, it must be of the form

$$\mathbf{E}(\mathbf{r},t) = \frac{1}{2}\sum_b \left[\mathbf{E}_b(\mathbf{r})\, e^{-i\omega_b t} + \mathbf{E}_b^*(\mathbf{r})\, e^{i\omega_b t}\right] \tag{B.26}$$

where $\mathbf{E}(\mathbf{r},t) = \mathbf{E}^*(\mathbf{r},t)$ is immediately verified. As a consequence, the total RF flux can be rewritten as

$$\mathbf{S}^{\mathrm{RF}} = \sum_b \mathbf{S}_b^{\mathrm{RF}}\left(\omega_b, \frac{\mathbf{E}_b}{2}\right) + \mathbf{S}_b^{\mathrm{RF}}\left(-\omega_b, \frac{\mathbf{E}_b^*}{2}\right) \tag{B.27}$$

Considering the expression (B.23) for the diffusion tensor elements, we can use the transformation $n \to -n$ and the sum over all $n$'s to obtain the identity

$$\begin{aligned}
D_{b,\perp\perp}^{\mathrm{RF}}\left(-\omega_b, \frac{\mathbf{E}_b^*}{2}\right) &= \sum_{n=-\infty}^{+\infty}\left(\frac{n\Omega}{\omega_b}\right)^2 D_{-n}^{\mathrm{RF}}\left(\mathbf{p}, -\omega_b, \frac{\mathbf{E}_b^*}{2}\right) \\
D_{b,\perp\parallel}^{\mathrm{RF}}\left(-\omega_b, \frac{\mathbf{E}_b^*}{2}\right) &= \sum_{n=-\infty}^{+\infty}\frac{p_\perp}{p_\parallel}\frac{n\Omega}{\omega_b}\left(1-\frac{n\Omega}{\omega_b}\right) D_{-n}^{\mathrm{RF}}\left(\mathbf{p}, -\omega_b, \frac{\mathbf{E}_b^*}{2}\right) \\
D_{b,\parallel\perp}^{\mathrm{RF}}\left(-\omega_b, \frac{\mathbf{E}_b^*}{2}\right) &= \sum_{n=-\infty}^{+\infty}\frac{p_\perp}{p_\parallel}\frac{n\Omega}{\omega_b}\left(1-\frac{n\Omega}{\omega_b}\right) D_{-n}^{\mathrm{RF}}\left(\mathbf{p}, -\omega_b, \frac{\mathbf{E}_b^*}{2}\right) \\
D_{b,\parallel\parallel}^{\mathrm{RF}}\left(-\omega_b, \frac{\mathbf{E}_b^*}{2}\right) &= \sum_{n=-\infty}^{+\infty}\frac{p_\perp^2}{p_\parallel^2}\left(1-\frac{n\Omega}{\omega_b}\right)^2 D_{-n}^{\mathrm{RF}}\left(\mathbf{p}, -\omega_b, \frac{\mathbf{E}_b^*}{2}\right)
\end{aligned} \tag{B.28}$$

which is identical to (B.23) with the transformation $D_n^{\mathrm{RF}}(\mathbf{p}, \omega_b, \mathbf{E}_b) \to D_{-n}^{\mathrm{RF}}\left(\mathbf{p}, -\omega_b, \frac{\mathbf{E}_b^*}{2}\right)$. The Fourier component of $\mathbf{E}_b^*$ associated with the wavevector $\mathbf{k}$ is given by

$$(\mathbf{E}_b^*)_{\mathbf{k},b}(\mathbf{k}) = \iiint d^3r\, \mathbf{E}_b^*(\mathbf{r})\, e^{-i\mathbf{k}\cdot\mathbf{r}} = [\mathbf{E}_{\mathbf{k},b}(-\mathbf{k})]^* \tag{B.29}$$

so that $\left\|\left(\mathbf{E}_b^*\right)_{\mathbf{k},b}(\mathbf{k})\right\|^2 = \left\|\mathbf{E}_{\mathbf{k},b}(-\mathbf{k})\right\|^2$ and

$$\frac{\left|\left(\mathbf{E}_b^*\right)_{\mathbf{k},b}(\mathbf{k})\right|}{\left\|\left(\mathbf{E}_b^*\right)_{\mathbf{k},b}(\mathbf{k})\right\|} = \frac{\left|\mathbf{E}_{\mathbf{k},b}(-\mathbf{k})\right|}{\left\|\mathbf{E}_{\mathbf{k},b}(-\mathbf{k})\right\|} = \mathbf{e}_{\mathbf{k},b}(-\mathbf{k}) \tag{B.30}$$

Consequently, we get the following expression from (B.24)

$$D_{-n}^{\mathrm{RF}}\left(\mathbf{p}, -\omega_b, \frac{\mathbf{E}_b^*}{2}\right) = \lim_{V\to\infty} \frac{\pi e^2}{V} \iiint \frac{d^3k}{(2\pi)^3} \frac{1}{4} \left\|\mathbf{E}_{\mathbf{k},b}(-\mathbf{k})\right\|^2 \tag{B.31}$$
$$\times \left|\Theta_{\mathbf{k}}^{(-n)}\left[\mathbf{k}, \mathbf{e}_{\mathbf{k},b}(-\mathbf{k})\right]\right|^2 \delta\left(-\omega_b - k_{\|}v_{\|} + n\Omega\right)$$

and can use the transform $\mathbf{k} \to -\mathbf{k}$ and the symmetry of the delta function to get

$$D_{-n}^{\mathrm{RF}}\left(\mathbf{p}, -\omega_b, \mathbf{E}_b^*\right) = \lim_{V\to\infty} \frac{\pi e^2}{4V} \iiint \frac{d^3k}{(2\pi)^3} \left\|\mathbf{E}_{\mathbf{k},b}(\mathbf{k})\right\|^2 \tag{B.32}$$
$$\times \left|\Theta_{\mathbf{k}}^{(-n)}\left[-\mathbf{k}, \mathbf{e}_{\mathbf{k},b}(\mathbf{k})\right]\right|^2 \delta\left(\omega_b - k_{\|}v_{\|} - n\Omega\right) \tag{B.33}$$

with

$$\Theta_{\mathbf{k}}^{(-n)}\left[-\mathbf{k}, \mathbf{e}_{\mathbf{k},b}(\mathbf{k})\right] = \frac{1}{\sqrt{2}} e_{\mathbf{k},b,+} e^{-i(\alpha+\pi)} J_{-n-1}\left(\frac{k_{\perp}v_{\perp}}{\Omega}\right) \tag{B.34}$$
$$+ \frac{1}{\sqrt{2}} e_{\mathbf{k},b,-} e^{+i(\alpha+\pi)} J_{-n+1}\left(\frac{k_{\perp}v_{\perp}}{\Omega}\right) + \frac{p_{\|}}{p_{\perp}} e_{\mathbf{k},b,\|} J_{-n}\left(\frac{k_{\perp}v_{\perp}}{\Omega}\right)$$

where we used the fact that $\mathbf{k} \to -\mathbf{k}$ leads to $\alpha \to \alpha + \pi$ and $k_{\perp} \to k_{\perp}$. With the property of the Bessel functions $J_n(z) = (-1)^n J_{-n}(z)$, and using $e^{-i\pi} = -1$, we get

$$\Theta_{\mathbf{k}}^{(-n)}\left[-\mathbf{k}, \mathbf{e}_{\mathbf{k},b}(\mathbf{k})\right] = (-1)^n \left[\frac{1}{\sqrt{2}} e_{\mathbf{k},b,+} e^{-i\alpha} J_{n+1}\left(\frac{k_{\perp}v_{\perp}}{\Omega}\right)\right. \tag{B.35}$$
$$\left. + \frac{1}{\sqrt{2}} e_{\mathbf{k},b,-} e^{+i\alpha} J_{n-1}\left(\frac{k_{\perp}v_{\perp}}{\Omega}\right) + \frac{p_{\|}}{p_{\perp}} e_{\mathbf{k},b,\|} J_n\left(\frac{k_{\perp}v_{\perp}}{\Omega}\right)\right]$$

In addition, we see from (B.20) that

$$\begin{aligned} e_{\mathbf{k},b,+} &= \left(e_{\mathbf{k},b,-}\right)^* \\ e_{\mathbf{k},b,-} &= \left(e_{\mathbf{k},b,+}\right)^* \\ e_{\mathbf{k},b,\parallel} &= \left(e_{\mathbf{k},b,\parallel}\right)^* \end{aligned} \tag{B.36}$$

so that we get the identity

$$\Theta_{\mathbf{k}}^{(-n)}\left[-\mathbf{k}, \mathbf{e}_{\mathbf{k},b}\left(\mathbf{k}\right)\right] = (-1)^n \left[\Theta_{\mathbf{k}}^{(n)}\left(\mathbf{k}, \mathbf{e}_{\mathbf{k},b}\right)\right]^* \tag{B.37}$$

Inserting back into (B.32), and comparing with (B.24), we find

$$D_{-n}^{\mathrm{RF}}\left(\mathbf{p}, -\omega_b, \frac{\mathbf{E}_b^*}{2}\right) = D_n^{\mathrm{RF}}\left(\mathbf{p}, \omega_b, \frac{\mathbf{E}_b}{2}\right) = \frac{1}{4} D_n^{\mathrm{RF}}\left(\mathbf{p}, \omega_b, \mathbf{E}_b\right) \tag{B.38}$$

so that finally, for a real field expressed as (B.26)

$$\mathbf{E}\left(\mathbf{r}, t\right) = \sum_b \mathrm{Re}\left[\mathbf{E}_b\left(\mathbf{r}\right) e^{-i\omega_b t}\right] \tag{B.39}$$

the RF fluxes can be expressed again as (B.21)

$$\mathbf{S}^{\mathrm{RF}} = \sum_b \mathbf{S}_b^{\mathrm{RF}}\left(\omega_b, \mathbf{E}_b\right) \tag{B.40}$$

where $\mathbf{S}_b^{\mathrm{RF}}$ is given by (B.22) and $\mathbb{D}_b^{\mathrm{RF}}$ is given by (B.23), and where we redefine (B.24) for real fields as

$$D_n^{\mathrm{RF}}\left(\mathbf{p}, \omega_b, \mathbf{E}_b\right) = \lim_{V\to\infty} \frac{\pi e^2}{2V} \iiint \frac{d^3k}{\left(2\pi\right)^3} \left\|\mathbf{E}_{\mathbf{k},b}\right\|^2 \left|\Theta_{\mathbf{k}}^{(n)}\left(\mathbf{k}, \mathbf{e}_{\mathbf{k},b}\right)\right|^2 \delta\left(\omega_b - k_\parallel v_\parallel - n\Omega\right) \tag{B.41}$$

### B.2.3 Expression in spherical momentum coordinates

While cylindrical momentum coordinates $\left(p_\parallel, p_\perp\right)$ are the natural set of coordinates for describing wave-particle interaction, the kinetic equation is rather solved in the

spherical $(p, \xi)$ system, which has the natural symmetry of collisions. To obtain the expression for the coefficient in spherical coordinates, we use the coordinate transformation

$$\begin{aligned} p &= \sqrt{p_\parallel^2 + p_\perp^2} \\ \xi &= \frac{p_\parallel}{\sqrt{p_\parallel^2 + p_\perp^2}} \end{aligned} \tag{B.42}$$

which is associated with the following diffusion tensor coordinates transformation

$$\begin{pmatrix} D_{pp} \\ D_{p\xi} \\ D_{\xi p} \\ D_{\xi\xi} \end{pmatrix} = \begin{pmatrix} (1-\xi^2) & \xi\sqrt{1-\xi^2} & \xi\sqrt{1-\xi^2} & \xi^2 \\ \xi\sqrt{1-\xi^2} & -(1-\xi^2) & \xi^2 & -\xi\sqrt{1-\xi^2} \\ \xi\sqrt{1-\xi^2} & \xi^2 & -(1-\xi^2) & -\xi\sqrt{1-\xi^2} \\ \xi^2 & -\xi\sqrt{1-\xi^2} & -\xi\sqrt{1-\xi^2} & (1-\xi^2) \end{pmatrix} \cdot \begin{pmatrix} D_{\perp\perp} \\ D_{\perp\parallel} \\ D_{\parallel\perp} \\ D_{\parallel\parallel} \end{pmatrix} \tag{B.43}$$

and, using (B.23), leads to the following RF diffusion tensor elements

$$\begin{aligned} D_{b,pp}^{\mathrm{RF}} &= \sum_{n=-\infty}^{+\infty} (1-\xi^2)\, D_n^{\mathrm{RF}}(\mathbf{p}, \omega_b, \mathbf{E}_b) \\ D_{b,p\xi}^{\mathrm{RF}} &= \sum_{n=-\infty}^{+\infty} -\frac{\sqrt{1-\xi^2}}{\xi}\left(1-\xi^2-\frac{n\Omega}{\omega_b}\right) D_n^{\mathrm{RF}}(\mathbf{p}, \omega_b, \mathbf{E}_b) \\ D_{b,\xi p}^{\mathrm{RF}} &= \sum_{n=-\infty}^{+\infty} -\frac{\sqrt{1-\xi^2}}{\xi}\left(1-\xi^2-\frac{n\Omega}{\omega_b}\right) D_n^{\mathrm{RF}}(\mathbf{p}, \omega_b, \mathbf{E}_b) \\ D_{b,\xi\xi}^{\mathrm{RF}} &= \sum_{n=-\infty}^{+\infty} \frac{1}{\xi^2}\left(1-\xi^2-\frac{n\Omega}{\omega_b}\right)^2 D_n^{\mathrm{RF}}(\mathbf{p}, \omega_b, \mathbf{E}_b) \end{aligned} \tag{B.44}$$

## B.3 Diffusion coefficient for a Gaussian beam

### B.3.1 Electric field with Gaussian transverse amplitude profile

We propose to calculate the diffusion coefficient for a beam of limited transverse extend with Gaussian profile. Note that it is somewhat incorrect to name such wave a Gaussian beam, since this denomination has a precise meaning in optics and refers to modes that include diffraction and are exact solutions of the wave equation.

In the present case, we neglect the effects of diffraction and simply assume a field of the form

$$\mathbf{E}(\mathbf{r},t) = \mathbf{E}_0(\mathbf{r}_0)\cos[\mathbf{k}_0\cdot\mathbf{r} - \omega_0 t + \varphi_0]\exp\left(-\frac{|\mathbf{r}-\mathbf{r}_0|^2}{2d^2}\right) \tag{B.45}$$

where $\mathbf{E}_0(\mathbf{r}_0)$ is a real field, $\mathbf{r}$ is the position vector

$$\mathbf{r} = x\widehat{x} + y\widehat{y} + z\widehat{z} \tag{B.46}$$

and $\mathbf{r}_0$ is the corresponding "ray location", which is the projection of $\mathbf{r}$ on the central line of wavepacket energy propagation, which is along the group velocity $\mathbf{v}_g$, so that

$$\mathbf{r}_0 = \frac{(\mathbf{r}\cdot\mathbf{v}_g)\,\mathbf{v}_g}{v_g^2} \tag{B.47}$$

The frequency $\omega_0$ and the parallel wave vector $k_{0\|}$ are arbitrarily chosen. Then the perpendicular wave vector $k_{0\perp}$ is obtained from solving the dispersion relation $D(\omega_0, k_{0\|}, k_{0\perp})$, so that the wave vector $\mathbf{k}_0$ is known. The group velocity $\mathbf{v}_g$ is also determined from the dispersion relation, as $\mathbf{v}_g = \left.\dfrac{\partial\omega_0}{\partial\mathbf{k}_0}\right|_{D(\omega_0,k_{0\|},k_{0\perp})=0}$.

We stress the point that the expression (B.45) is in fact an approximation because diffraction is neglected. In order to fully satisfy the wave equation, this beam cannot strictly speaking have a constant width. This approximation is more valid if the beam width is large compared to the wavelength

$$k_0 d \gg 1 \tag{B.48}$$

This is the limit where the beam is not well focused and is apparented to a plane wave near the axis of propagation $\mathbf{r}_0$. A corollary is that the spectral width $\Delta k$ of the beam is small compared to $k_0$, since $\Delta k \sim 1/d$. Within this approximation $\Delta k \ll k_0$, it is also valid to require that the dispersion relation $D(\omega_0, k_{0\|}, k_{0\perp}) = 0$ be satisfied for the central value $\mathbf{k}_0$ only.

The real field (B.45) can be expressed in the form (B.26) as

$$\mathbf{E}(\mathbf{r},t) = \frac{1}{2}\left[\widetilde{\mathbf{E}}(\mathbf{r})\, e^{-i\omega_0 t} + \widetilde{\mathbf{E}}^*(\mathbf{r})\, e^{i\omega_0 t}\right] \tag{B.49}$$

with the complex field

$$\widetilde{\mathbf{E}}(\mathbf{r}) = \mathbf{E}_0(\mathbf{r}_0)\, e^{i\mathbf{k}_0\cdot\mathbf{r}+i\varphi_0} \exp\left(-\frac{|\mathbf{r}-\mathbf{r}_0|^2}{2d^2}\right) \tag{B.50}$$

To simplify the Fourier transform operation, we define a fixed coordinate system $(x', y', z')$ such that $x'$ be in the direction of energy propagation $\mathbf{v}_g$ and the wave vector $\mathbf{k}_0$ lies within the $(\widehat{x}', \widehat{z}')$ plane, which gives

$$\mathbf{r}_0 = x'\widehat{x}' \tag{B.51}$$

$$\mathbf{k}_0 = k'_{0x}\widehat{x}' + k'_{0z}\widehat{z}' \tag{B.52}$$

Within this system, the electric field (B.50) is expressed as

$$\widetilde{\mathbf{E}}(\mathbf{r}) = \mathbf{E}_0(x')\, e^{ik'_{0x}x'+ik'_{0z}z'+i\varphi_0} \exp\left[-\frac{(y'^2+z'^2)}{2d^2}\right] \tag{B.53}$$

### B.3.2 Fourier transform of the electric field

The Fourier transform of the field is

$$\mathbf{E}_\mathbf{k}(\mathbf{k}) = \iiint d^3r\; e^{-i\mathbf{k}\cdot\mathbf{r}}\widetilde{\mathbf{E}}(\mathbf{r}) \tag{B.54}$$

With $\mathbf{k}\cdot\mathbf{r} = k'_x x' + k'_y y' + k'_z z'$ we find

$$\begin{aligned}\mathbf{E}_\mathbf{k}(\mathbf{k}) &= \mathbf{E}_0 \iiint d^3\mathbf{r}\; e^{-i\mathbf{k}\cdot\mathbf{r}} e^{ik'_{0x}x'+ik'_{0z}z'+i\varphi_0} \exp\left[-\frac{(y'^2+z'^2)}{2d^2}\right] \\ &= 2\pi\mathbf{E}_0 e^{i\varphi_0}\delta(k'_x - k'_{0x}) \int \exp\left[-ik'_y y' - \frac{y'^2}{2d^2}\right] dy' \\ &\quad \times \int \exp\left[-i(k'_z - k'_{0z})z' - \frac{z'^2}{2d^2}\right] dz'\end{aligned} \tag{B.55}$$

The integrals are separated and can be solved analytically

$$\int \exp\left[-ik'_y y' - \frac{y'^2}{2d^2}\right] dy' = \sqrt{2\pi} d \exp\left[-\frac{k'^2_y d^2}{2}\right] \tag{B.56}$$

$$\int \exp\left[-i\left(k'_z - k'_{0z}\right) z' - \frac{z'^2}{2d^2}\right] dz' = \sqrt{2\pi} d \exp\left[-\frac{\left(k'_z - k'_{0z}\right)^2 d^2}{2}\right] \tag{B.57}$$

and (B.55) becomes

$$\mathbf{E}_{\mathbf{k}}(\mathbf{k}) = \frac{(2\pi)^2}{\Delta k_0^2} \mathbf{E}_0 e^{i\varphi_0} \delta\left(k'_x - k'_{0x}\right) \exp\left[-\frac{k'^2_y + \left(k'_z - k'_{0z}\right)^2}{2\Delta k_0^2}\right] \tag{B.58}$$

where we defined

$$\Delta k_0 = \frac{1}{d} \tag{B.59}$$

Note that we can re-express the Fourier field independently of the coordinate system: using the conditions $k'_x = \pm k'_{0x}$ in (B.58) and $k'_{0y} = 0$, we can rewrite

$$\mathbf{E}_{\mathbf{k}}(\mathbf{k}) = \frac{(2\pi)^2}{\Delta k_0^2} \mathbf{E}_0 e^{i\varphi_0} \delta\left(k'_x - k'_{0x}\right) \exp\left[-\frac{\|\mathbf{k} - \mathbf{k}_0\|^2}{2\Delta k_0^2}\right] \tag{B.60}$$

and given that $k'_x = \mathbf{k} \cdot \widehat{\mathbf{\Phi}}_0$ and $k'_{0x} = \mathbf{k}_0 \cdot \widehat{\mathbf{\Phi}}_0$, where $\widehat{\mathbf{\Phi}}_0 = \mathbf{v}_g / v_g$ is the unit vector in the direction of the energy density flow (2.43), the expression (B.58) becomes

$$\mathbf{E}_{\mathbf{k}}(\mathbf{k}) = \frac{(2\pi)^2}{\Delta k_0^2} \mathbf{E}_0 e^{i\varphi_0} \delta\left[(\mathbf{k} - \mathbf{k}_0) \cdot \widehat{\mathbf{\Phi}}_0\right] \exp\left[-\frac{\|\mathbf{k} - \mathbf{k}_0\|^2}{2\Delta k_0^2}\right] \tag{B.61}$$

### B.3.3 Power carried by the beam

The time-averaged energy density flow related to a Fourier component of the field is normalized according to (2.36) as

$$\mathbf{s}_{\mathbf{k}}(\mathbf{k}) = \frac{\varepsilon_0 c}{2} \|\mathbf{E}_{\mathbf{k}}(\mathbf{k})\|^2 \mathbf{\Phi}_{\mathbf{k}}(\mathbf{k}) \tag{B.62}$$

where the normalized power flow $\mathbf{\Phi}_{\mathbf{k}}(\mathbf{k})$ is a smooth function of $\mathbf{k}$, and since we assumed $\Delta k_0 \ll k_0$, we can take $\mathbf{\Phi}_{\mathbf{k}}(\mathbf{k}) \simeq \mathbf{\Phi}_{\mathbf{k}}(\mathbf{k}_0) \equiv \mathbf{\Phi}_0$. The total energy flow in

the beam is the sum over all Fourier contributions, and is therefore given by

$$\mathbf{S} = \iiint \frac{d^3k}{(2\pi)^3}\, \mathbf{s}_{\mathbf{k}}(\mathbf{k}) \tag{B.63}$$

$$\simeq \frac{\varepsilon_0 c}{2}\mathbf{\Phi}_0 \frac{(2\pi)^4}{\Delta k_0^4} \|\mathbf{E}_0\|^2 \iiint \frac{d^3k}{(2\pi)^3}\delta^2(k'_x - k'_{0x}) \exp\left[-\frac{k_y'^2 + (k'_z - k'_{0z})^2}{\Delta k_0^2}\right] \tag{B.64}$$

$$= \frac{\varepsilon_0 c}{2}\mathbf{\Phi}_0 \frac{(2\pi)^2 \pi}{\Delta k_0^2} \|\mathbf{E}_0\|^2 \int \frac{dk'_x}{2\pi}\delta^2(k'_x - k'_{0x}) \tag{B.65}$$

where we used Parseval's theorem

$$\int \frac{dk'_x}{2\pi}\ |F_{\mathbf{k}}(k'_x)|^2 = \int dx'\ |F(x')|^2 \tag{B.66}$$

with $F_{\mathbf{k}}(k'_x) = \delta(k'_x - k'_{0x})$ such that

$$F(x') = \int \frac{dk'_x}{2\pi} e^{ik'_x x'} \delta(k'_x - k'_{0x}) = \frac{1}{2\pi} e^{ik'_{0x}x'} \tag{B.67}$$

We get

$$\mathbf{S} = \pi d^2 L'_x \frac{\varepsilon_0 c}{2}\mathbf{\Phi}_0 \|\mathbf{E}_0\|^2 \tag{B.68}$$

where $L'_x$ is the plasma size in $x'$ direction in which the beam propagates. We also get an integrated formulation of (2.43) for the Gaussian beam

$$\mathbf{S} = W\mathbf{v}_g \tag{B.69}$$

where

$$W = \pi d^2 L'_x \frac{\varepsilon_0}{2} \|\mathbf{E}_0\|^2 \Sigma_{\mathbf{k}} \tag{B.70}$$

is the total energy in the beam of effective volume $\pi d^2 L'_x$.

The power carried by the beam is the total energy flow per unit length along the beam propagation path, and is therefore given by $P = \|\mathbf{S}\| / L'_x$ so that

$$P = \pi d^2 \frac{\varepsilon_0 c}{2} \|\mathbf{\Phi}_0\| \|\mathbf{E}_0\|^2 \tag{B.71}$$

### B.3.4 Diffusion coefficient

For a Gaussian beam characterized by a single frequency $\omega_0$, and the parameters $\mathbf{k}_0$, $\mathbf{E}_0$ and $\Delta k_0$, the diffusion coefficient for harmonic $n$ is (B.41)

$$D_n^{\mathrm{RF}}(\mathbf{p}) = \lim_{V\to\infty} \frac{\pi e^2}{2V} \iiint \frac{d^3k}{(2\pi)^3} \|\mathbf{E}_\mathbf{k}\|^2 \left|\Theta_\mathbf{k}^{(n)}(\mathbf{k}, \mathbf{e}_0)\right|^2 \delta\left(\omega_0 - k_\parallel v_\parallel - n\Omega\right) \tag{B.72}$$

with (B.19)

$$\Theta_\mathbf{k}^{(n)} = \frac{1}{\sqrt{2}} e_{0,+} e^{-i\alpha} J_{n-1}\left(\frac{k_\perp v_\perp}{\Omega}\right) + \frac{1}{\sqrt{2}} e_{0,-} e^{+i\alpha} J_{n+1}\left(\frac{k_\perp v_\perp}{\Omega}\right) + \frac{p_\parallel}{p_\perp} e_{0,\parallel} J_n\left(\frac{k_\perp v_\perp}{\Omega}\right) \tag{B.73}$$

where, using (B.61), we defined the polarization vector

$$\mathbf{e}_0 \equiv \frac{|\mathbf{E}_\mathbf{k}(\mathbf{k})|}{\|\mathbf{E}_\mathbf{k}(\mathbf{k})\|} = \frac{|\mathbf{E}_0|}{\|\mathbf{E}_0\|} \tag{B.74}$$

Because the polarization term $\Theta_\mathbf{k}^{(n)}$ (B.73) is a smooth function of $\mathbf{k}$ and since we assumed $\Delta k_0 \ll k_0$, we can make the approximation $\Theta_\mathbf{k}^{(n)}(\mathbf{k}, \mathbf{e}_0) \simeq \Theta_\mathbf{k}^{(n)}(\mathbf{k}_0, \mathbf{e}_0) \equiv \Theta_0^{(n)}$ using the Gaussian term. In addition, we can be rewrite the resonance condition as

$$\delta\left(\omega_0 - k_\parallel v_\parallel - n\Omega\right) = \frac{1}{|v_\parallel|} \delta\left(k_\parallel - k_{\parallel\mathrm{res}}\right) \tag{B.75}$$

where

$$k_{\parallel\mathrm{res}} = \frac{\omega_0 - n\Omega}{v_\parallel} \tag{B.76}$$

Then, using (B.61), the diffusion coefficient (B.41) can then be rewritten as

$$D_n^{\mathrm{RF}}(\mathbf{p}) \simeq \lim_{V\to\infty} \frac{\pi e^2 \|\mathbf{E}_0\|^2}{2V} \frac{2\pi}{|v_\parallel| \Delta k_0^4} \left|\Theta_0^{(n)}\right|^2 I^{(n)}(\mathbf{p}, \omega_0, \mathbf{k}_0) \tag{B.77}$$

where we need to evaluate the integral

$$\mathcal{I}^{(n)}(\mathbf{p}, \omega_0, \mathbf{k}_0) = \iiint d^3k\, \delta\left(k_\parallel - k_{\parallel\mathrm{res}}\right) \delta^2\left[(\mathbf{k} - \mathbf{k}_0)\cdot\widehat{\mathbf{\Phi}}\right] \exp\left[-\frac{\|\mathbf{k} - \mathbf{k}_0\|^2}{\Delta k_0^2}\right] \tag{B.78}$$

Using the expression (B.71) for the power carried by the beam, we can rewrite (B.77) as

$$D_n^{\mathrm{RF}}(\mathbf{p}) = \lim_{V\to\infty} \frac{P}{V} \frac{2\pi e^2}{\varepsilon_0 c \|\mathbf{\Phi}_0\| |v_\parallel| \Delta k_0^2} \left|\Theta_0^{(n)}\right|^2 I^{(n)}(\mathbf{p}, \omega_0, \mathbf{k}_0) \tag{B.79}$$

**Evaluation of the integral $\mathcal{I}^{(n)}$**

We define the coordinate system $(x, y, z)$ such that the magnetic field is along the $\widehat{z}$ axis, and the group velocity $\mathbf{v}_g$ - and the unit vector $\widehat{\mathbf{\Phi}}$ - lie within the $(\widehat{x}, \widehat{z})$ plane. Because of the cylindrical symmetry of the plasma around the $\widehat{z}$ axis, the power flow must be within the $(\mathbf{k}_0, \widehat{z})$ plane (see Section 2.1.1), and we define then

$$\mathbf{k}_0 = k_{0\parallel}\widehat{z} + k_{0\perp}\widehat{x} \tag{B.80}$$

along with

$$\widehat{\mathbf{\Phi}} = \cos\beta\widehat{z} + \sin\beta\widehat{x} \tag{B.81}$$

which gives

$$\begin{aligned} \cos\beta &= \frac{\Phi_{0\parallel}}{\|\mathbf{\Phi}_0\|} \\ \sin\beta &= \frac{\Phi_{0\perp}}{\|\mathbf{\Phi}_0\|} \end{aligned} \tag{B.82}$$

so that

$$\begin{aligned} (\mathbf{k} - \mathbf{k}_0)\cdot\widehat{\Phi} &= \cos\beta\left(k_\parallel - k_{0\parallel}\right) + \sin\beta\left(k_x - k_{0\perp}\right) \\ \|\mathbf{k} - \mathbf{k}_0\|^2 &= \left(k_\parallel - k_{0\parallel}\right)^2 + \left(k_x - k_{0\perp}\right)^2 + k_y^2 \end{aligned} \tag{B.83}$$

Integrating (B.78) over $k_\parallel$ then gives

$$\mathcal{I}^{(n)}(\mathbf{p}, \omega_0, \mathbf{k}_0) = \exp\left[-\frac{\left(k_{\parallel\mathrm{res}} - k_{0\parallel}\right)^2}{\Delta k_0^2}\right] \iint d^2k_\perp \tag{B.84}$$

$$\times\delta^2\left[\cos\beta\left(k_{\parallel\mathrm{res}} - k_{0\parallel}\right) + \sin\beta\left(k_x - k_{0\perp}\right)\right] \exp\left[-\frac{\left(\left[k_x - k_{0\perp}\right]^2 + k_y^2\right)}{\Delta k_0^2}\right]$$

In the two-dimensional space $\mathbf{k}_\perp$, for any integrable function $F_{\mathbf{k}}(\mathbf{k}_\perp)$, Parseval's theorem gives

$$\iint \frac{d^2k_\perp}{(2\pi)^2} \left|F_{\mathbf{k}}(\mathbf{k}_\perp)\right|^2 = \iint d^2r_\perp \left|F(\mathbf{r}_\perp)\right|^2 \tag{B.85}$$

where $\mathbf{r}_\perp$ is the corresponding real space and $F(\mathbf{r}_\perp)$ is given by

$$F(\mathbf{r}_\perp) = \iint \frac{d^2k_\perp}{(2\pi)^2} e^{i\mathbf{k}_\perp \cdot \mathbf{r}_\perp} F_{\mathbf{k}}(\mathbf{k}_\perp) \tag{B.86}$$

In order to apply Parseval's theorem to (B.84) where

$$F_{\mathbf{k}}(\mathbf{k}_\perp) = \delta\left[\cos\beta\left(k_{\parallel \mathrm{res}} - k_{0\parallel}\right) + \sin\beta\left(k_x - k_{0\perp}\right)\right] \exp\left[-\frac{\left(\left[k_x - k_{0x}\right]^2 + k_y^2\right)}{2\Delta k_0^2}\right] \tag{B.87}$$

we first do the Fourier inverse transform (B.86)

$$\begin{aligned} F(\mathbf{r}_\perp) = \iint \frac{d^2k_\perp}{(2\pi)^2} e^{ik_x x + ik_y y} \delta\left[\cos\beta\left(k_{\parallel \mathrm{res}} - k_{0\parallel}\right) + \sin\beta\left(k_x - k_{0\perp}\right)\right] \\ \times \exp\left[-\frac{\left(\left[k_x - k_{0\perp}\right]^2 + k_y^2\right)}{2\Delta k_0^2}\right] \end{aligned} \tag{B.88}$$

Integrating over $k_x$, we obtain

$$\begin{aligned} (2\pi)^2 F(\mathbf{r}_\perp) = \frac{1}{\sin\beta} \exp\left[-\frac{\cot^2\beta\left(k_{\parallel \mathrm{res}} - k_{0\parallel}\right)^2}{2\Delta k_0^2} + i\left(k_{0\perp} - \cot\beta\left[k_{\parallel \mathrm{res}} - k_{0\parallel}\right]\right)x\right] \\ \times \int dk_y \exp\left[-\frac{k_y^2}{2\Delta k_0^2} + ik_y y\right] \end{aligned} \tag{B.89}$$

and now, integrating over $k_y$,

$$\begin{aligned} (2\pi)^2 F(\mathbf{r}_\perp) = \frac{1}{\sin\beta} \exp\left[-\frac{\cot^2\beta\left(k_{\parallel \mathrm{res}} - k_{0\parallel}\right)^2}{2\Delta k_0^2} + i\left(k_{0\perp} - \cot\beta\left[k_{\parallel \mathrm{res}} - k_{0\parallel}\right]\right)x\right] \\ \times \sqrt{2\pi}\Delta k_0 \exp\left[-\frac{y^2\Delta k_0^2}{2}\right] \end{aligned} \tag{B.90}$$

Inserting (B.90) into (B.85), we find

$$\begin{aligned}\iint d^2k_\perp \left|F_{\mathbf{k}}\left(\mathbf{k}_\perp\right)\right|^2 &= (2\pi)^2 \iint d^2r_\perp \ \left|F\left(\mathbf{r}_\perp\right)\right|^2 \\ &= \frac{\Delta^2 k_0}{2\pi \sin^2\beta} \exp\left[-\frac{\cot^2\beta\left(k_{\parallel\mathrm{res}}-k_{0\parallel}\right)^2}{\Delta k_0^2}\right] \\ &\times \iint d^2r_\perp \exp\left[-y^2\Delta k_0^2\right]\end{aligned} \tag{B.91}$$

and integrate

$$\iint d^2r_\perp \exp\left[-y^2\Delta k_0^2\right] = L_x\frac{\sqrt{\pi}}{\Delta k_0} \tag{B.92}$$

where $L_x$ is the space extent in the $x$ direction. The integral (B.84) therefore becomes

$$\mathcal{I}^{(n)}\left(\mathbf{p},\omega_0,\mathbf{k}_0\right) = \frac{\sqrt{\pi}L_x\Delta k_0}{2\pi\sin^2\beta}\exp\left[-\frac{\left(k_{\parallel\mathrm{res}}-k_{0\parallel}\right)^2}{\sin^2\beta\Delta k_0^2}\right]$$

**Diffusion coefficient**

The diffusion coefficient (B.79) now becomes

$$D_n^{\mathrm{RF}}\left(\mathbf{p}\right) = \lim_{V\to\infty}\frac{PL_x'}{V}\frac{e^2\pi}{\varepsilon_0 c\Phi_0\left|v_\parallel\right|}\left|\Theta_0^{(n)}\right|^2\frac{1}{\sqrt{\pi}\Delta k_{0\parallel}}\exp\left[-\frac{\left(k_{\parallel\mathrm{res}}-k_{0\parallel}\right)^2}{\Delta k_{0\parallel}^2}\right] \tag{B.93}$$

where $\Phi_0 = \|\mathbf{\Phi}_0\|$ and where we defined

$$\Delta k_{0\parallel}^2 = \sin^2\beta\Delta k_0^2 \tag{B.94}$$

and used (B.81)

$$L_x = L_x'\left|\sin\beta\right| \tag{B.95}$$

Using (B.82), we can rewrite

$$\Delta k_{0\parallel} = \frac{\left|\Phi_{0\perp}\right|}{\Phi_0}\Delta k_0 \tag{B.96}$$

**Limit of a plane wave**

The limit of a plane wave can be retrieved from the expression (B.93) by taking the limit $\Delta k_{0\|} \to 0$ for which we have the following asymptotic expression

$$\frac{1}{\sqrt{\pi}\Delta k_{0\|}} \exp\left[-\frac{\left(k_{\|\mathrm{res}} - k_{0\|}\right)^2}{\Delta k_{0\|}^2}\right] \to \delta\left(k_{\|\mathrm{res}} - k_{0\|}\right) \tag{B.97}$$

$$\frac{PL_x'}{V} \to \frac{\varepsilon_0 c}{2}\Phi_0 \left\|\mathbf{E}_0\right\|^2 \tag{B.98}$$

where we used (B.71) and let the volume $\pi d^2 L_x' \Longleftrightarrow V$ go to infinity as $\Delta k_{0\|} \to 0$. This gives

$$D_n^{\mathrm{RF}}(\mathbf{p}) \to \frac{e^2\pi}{2}\left\|\mathbf{E}_0\right\|^2 \left|\Theta_0^{(n)}\right|^2 \delta\left(\omega_0 - k_{0\|}v_{\|} - n\Omega\right) \tag{B.99}$$

which is the same expression as found in Refs. [58] and [59].

# B.4 Diffusion coefficient in a slab geometry

## B.4.1 Diffusion coefficient for a Gaussian beam

The diffusion coefficient for a Gaussian beam in a uniform plasma (B.93) can be extended to a slab geometry where the inhomogeneity scale length $L$ is much larger than the wavelength $\lambda_0 = 2\pi/k_0$ , such that the WKB approximation is valid, and also much larger than the thermal electron Larmor radius $\rho_{Te} = v_{Te}/\omega_{ce}$, such that wave particle interaction remains unaffected. With the magnetic field still is in the $\widehat{\mathbf{z}}$ direction, we assume that the inhomogeneity is in the $\widehat{\mathbf{x}}''$ direction, and define $\widehat{\mathbf{y}}'' = \widehat{\mathbf{z}}'' \times \widehat{\mathbf{x}}''$. The parallel component of the wave vector $k_{0\|}$ and the component perpendicular to both the field direction and the inhomogeneity, $k_{0y}''$, are conserved. Because $k_{0y}''$ is conserved while $k_{0\perp}$ undergoes a large upshift in the mode conversion region, we have typically $k_{0y}'' \ll k_{0\perp}$. Therefore, the perpendicular wave vector is directed in the direction of inhomogeneity, and we have $k_{0x}'' = k_{0x} = k_{0\perp}$. The inhomogeneity is therefore in the $\widehat{\mathbf{x}}$ direction.

Because the normalized power flow $\mathbf{\Phi}_0$ is in the $(\widehat{\mathbf{x}}, \widehat{\mathbf{z}})$ plane by symmetry in the

dispersion relation (B.81), we have (B.82)

$$\begin{aligned}\Phi_{0x} &= \Phi_{0\perp} \\ \Phi_{0z} &= \Phi_{0\parallel}\end{aligned} \tag{B.100}$$

In a slab geometry, it is therefore possible to determine the direction of $\mathbf{\Phi}_0$ with respect to the direction of inhomogeneity $\widehat{\mathbf{x}}$ simply from solving the dispersion relation, which gives $\Phi_{0\perp}$ and $\Phi_{0\parallel}$.

The plasma electron temperature $T_e(x)$ and density $n_e(x)$ as well as the magnetic field (or gyrofrequency $\omega_{ce}(x)$) are all slowly varying functions of $x$. In that case, the beam power $P(x)$, perpendicular wave vector $k_{0\perp}(x)$, power flow $\mathbf{\Phi}_0(x)$ and polarization $\mathbf{e}_0(x)$ are also slowly varying functions of $x$. Across an infinitesimal flux-surface of width $\Delta x(x)$, the beam path $L'_x$ becomes

$$L'_x(x) = \Delta x(x) \frac{\Phi_0(x)}{|\Phi_{0\perp}(x)|} \tag{B.101}$$

and the diffusion coefficient for a Gaussian beam (B.93) becomes in a slab plasma

$$D_n^{\mathrm{RF}}(\mathbf{p}, x) = D_{n,0}^{\mathrm{RF}}(x) \frac{v_{Te}}{|v_\parallel|} \frac{\omega_0}{c} \left|\Theta_0^{(n)}(x)\right|^2 \frac{1}{\sqrt{\pi}\Delta k_{0\parallel}(x)} \exp\left[-\frac{\left(k_{\parallel\mathrm{res}}(x) - k_{0\parallel}\right)^2}{\Delta k_{0\parallel}^2(x)}\right] \tag{B.102}$$

with the constant factor

$$D_{n,0}^{\mathrm{RF}}(x) = \lim_{V\to\infty} \frac{P(x)}{A} \frac{e^2\pi}{\varepsilon_0\omega_0 |\Phi_{0\perp}(x)| v_{Te}} \tag{B.103}$$

where we defined

$$\frac{\Delta x(x)}{\Delta V(x)} = A \tag{B.104}$$

with $A$ being the area of the flux-surface $(\widehat{\mathbf{y}}, \widehat{\mathbf{z}})$.

### B.4.2 Limit of a plane wave

In order to simplify the calculation of the absorption coefficient and power deposition profile, we take the limit of a plane wave, based on the condition (B.48) which gives $\Delta k_0 \ll k_0$. Applying the limit $\Delta k_0 \to 0$ in (B.102) we get the asymptotic expression (B.97)

$$\frac{1}{\sqrt{\pi}\Delta k_{0\|}} \exp\left[-\frac{\left(k_{\|\mathrm{res}} - k_{0\|}\right)^2}{\Delta k_{0\|}^2}\right] \to \delta\left(k_{\|\mathrm{res}} - k_{0\|}\right) = \left|v_\|\right| \delta\left(\omega_0 - v_\| k_{0\|} - \frac{n\omega_{ce}}{\gamma}\right) \tag{B.105}$$

and $\lim_{A\to\infty} \frac{P(x)}{A} = s_{\mathrm{inc}}(x)$, where $s_{\mathrm{inc}}(x)$ is the incident energy density flow on the flux-surface $(\widehat{\mathbf{y}}, \widehat{\mathbf{z}})$. The diffusion coefficient (B.102) becomes

$$D_n^{\mathrm{RF}}(\mathbf{p}, x) = D_{n,0}^{\mathrm{RF}}(x) \frac{v_{Te}}{c} \left|\Theta_0^{(n)}(x)\right|^2 \delta\left(1 - \frac{v_\| k_{0\|}}{\omega_0} - \frac{n\omega_{ce}(x)}{\gamma\omega_0}\right) \tag{B.106}$$

with (B.103)

$$D_{n,0}^{\mathrm{RF}}(x) = \frac{e^2 \pi s_{\mathrm{inc}}(x)}{\varepsilon_0 \omega_0 \left|\Phi_{0\perp}(x)\right| v_{Te}} \tag{B.107}$$

### B.4.3 Density of power absorbed in the linear limit

We propose to calculate the density of power absorbed using the quasilinear operator in the linear limit.

#### General expression

The expression for the density of power absorbed from RF waves is given by (3.277)

$$P_{\mathrm{abs}}^{\mathrm{RF}} = 2\pi \int_0^\infty dp \frac{p^3}{\gamma m_e} \int_{-1}^{+1} d\xi S_p^{\mathrm{RF}}(f) \tag{B.108}$$

where $S_p^{\mathrm{RF}}(f)$ is the RF induced flux (B.12) in the momentum direction $\widehat{p}$, with the expression (A.123) for the gradient in spherical momentum coordinates

$$S_p^{\mathrm{RF}}(f) = -D_{pp}^{\mathrm{RF}} \frac{\partial f}{\partial p} + \frac{\sqrt{1-\xi^2}}{p} D_{p\xi}^{\mathrm{RF}} \frac{\partial f}{\partial \xi} \tag{B.109}$$

The corresponding quasilinear diffusion tensor elements are (B.44), expressed here with the transformation $n \rightarrow -n$ for electrons (see Section 3.5)

$$\begin{aligned} D_{pp}^{\mathrm{RF}} &= \sum_{n=-\infty}^{+\infty} \left(1-\xi^2\right) D_n^{\mathrm{RF}}(\mathbf{p}) \\ D_{p\xi}^{\mathrm{RF}} &= \sum_{n=-\infty}^{+\infty} -\frac{\sqrt{1-\xi^2}}{\xi}\left[1-\xi^2-\frac{n\omega_{ce}}{\gamma\omega_0}\right] D_n^{\mathrm{RF}}(\mathbf{p}) \end{aligned} \tag{B.110}$$

with the RF quasilinear diffusion coefficient (B.106)

$$D_n^{\mathrm{RF}}(\mathbf{p}) = D_{n,0}^{\mathrm{RF}} \frac{v_{Te}}{c}\left|\Theta_0^{(n)}\right|^2 \delta\left(1-\frac{v_{\parallel}k_{0\parallel}}{\omega_0}-\frac{n\omega_{ce}}{\gamma\omega_0}\right) \tag{B.111}$$

For electrons, the polarization term (B.73) can be written as (3.194) with $\alpha = 0$ since $k_{0\perp} = k_{0x}$, which gives

$$\Theta_0^{(n)} = \frac{1}{\sqrt{2}} e_{0,+} J_{n+1}(z) + \frac{1}{\sqrt{2}} e_{0,-} J_{n-1}(z) + \frac{p_{\parallel}}{p_{\perp}} e_{0,\parallel} J_n(z) \tag{B.112}$$

with (3.195)

$$z = \frac{k_{0\perp}}{\omega_{ce}} \frac{p_{\perp}}{m_e} \tag{B.113}$$

### Polarization term for electrostatic EBWs

Assuming that EBWs have an electrostatic polarization, the polarization term can be approximated to (5.20)

$$\Theta_0^{(n)} \simeq \frac{J_n(z)}{N_{0\perp}\beta_{Te}} \frac{p_{Te}}{p_{\perp}} \left[y_n + N_{0\parallel}\beta_{Te}\frac{p_{\parallel}}{p_{Te}}\right] \tag{B.114}$$

with the definitions (2.108) and (2.103)

$$\begin{aligned} y_n &= \frac{n\omega_{ce}}{\omega_0} \\ \beta_{Te} &= \frac{p_{Te}}{m_e c} \end{aligned} \tag{B.115}$$

### Relativistic Maxwellian distribution

When the evolution of the electrons is dominated by collisions, we tend to the linear limit where the electron distribution function is a Maxwellian, given by

$$f_M(p) = \frac{n_e}{4\pi m_e^2 c T_e} \frac{1}{K_2\left(\frac{m_e c^2}{T_e}\right)} \exp\left[-\frac{\gamma m_e c^2}{T_e}\right] \tag{B.116}$$

where $\gamma$ is the relativistic factor (3.21)

$$\gamma = \sqrt{1 + \frac{p^2}{m_e^2 c^2}} \tag{B.117}$$

In order to make the non- and weakly-relativistic limits more apparent for further approximations, we rewrite (B.116) as

$$f_M = \frac{n_e}{(2\pi m_e T_e)^{3/2}} R\left(\frac{T_e}{m_e c^2}\right) \exp\left[-\frac{p^2}{(\gamma+1) m_e T_e}\right] \tag{B.118}$$

where $R(x)$ is a normalization factor defined as

$$R(x) = \sqrt{\frac{\pi}{2}} x^{1/2} \frac{1}{K_2\left(\frac{1}{x}\right)} \exp\left[-\frac{1}{x}\right] \tag{B.119}$$

which has the following Taylor expansion

$$R(x) = \left[1 + \frac{15x}{8} + \frac{105}{128}x^2 + \mathcal{O}\left(x^3\right)\right] \tag{B.120}$$

The derivative of $f_M$ with respect to $p$ is

$$\frac{\partial f_M}{\partial p} = \frac{d\gamma}{dp}\frac{\partial f_M}{\partial \gamma} = -\frac{p}{\gamma m_e T_e} f_M(p) \tag{B.121}$$

while the derivative of $f_M$ with respect to $\xi$ is zero since the Maxwellian distribution is isotropic.

Therefore, in the linear limit with a relativistic Maxwellian distribution, the den-

sity of power absorbed (B.108) reduces to

$$P_{\text{abs}}^{\text{RF},M} = 2\pi \int_0^{\infty} dp \, \frac{p^4}{\gamma^2 m_e^2 T_e} \int_{-1}^{+1} d\xi \sum_{n=-\infty}^{+\infty} \left(1-\xi^2\right) D_n^{\text{RF}}(\mathbf{p}) f_M(p) \tag{B.122}$$

where we inserted (B.109) and (B.110). The density of power absorbed can be decomposed into the contribution of each harmonic

$$P_{\text{abs}}^{\text{RF},M} = \sum_{n=-\infty}^{+\infty} P_{\text{abs},n}^{\text{RF},M} \tag{B.123}$$

with

$$P_{\text{abs},n}^{\text{RF},M} = 2\pi \int_0^{\infty} dp \, \frac{p^4}{\gamma^2 m_e^2 T_e} \int_{-1}^{+1} d\xi \left(1-\xi^2\right) D_n^{\text{RF}}(\mathbf{p}) f_M(p) \tag{B.124}$$

which we will consider separately from now on.

### Expression in cylindrical coordinates

From here on, it is easier to work in cylindrical coordinates $\left(p_{\parallel}, p_{\perp}\right)$, with the transformation (A.114)

$$\begin{aligned} p_{\parallel} &= p\xi \\ p_{\perp} &= p\sqrt{1-\xi^2} \end{aligned} \tag{B.125}$$

and (B.124) becomes

$$P_{\text{abs},n}^{\text{RF},M} = 2\pi \int_0^{\infty} p_{\perp} dp_{\perp} \int_{-\infty}^{+\infty} dp_{\parallel} \, \frac{p_{\perp}^2}{\gamma^2 m_e^2 T_e} D_n^{\text{RF}}(\mathbf{p}) f_M(p) \tag{B.126}$$

### Normalization

The momentum coordinates are normalized to the thermal momentum according to

$$\begin{aligned} p_{\parallel} &\longrightarrow p_{Te} p_{\parallel} \\ p_{\perp} &\longrightarrow p_{Te} p_{\perp} \end{aligned} \tag{B.127}$$

so that (B.126) becomes

$$P_{\mathrm{abs},n}^{\mathrm{RF},M} = 2\pi \frac{n_e}{m_e} \int_0^{\infty} p_\perp dp_\perp \int_{-\infty}^{+\infty} dp_\parallel \, \frac{p_\perp^2}{\gamma^2} D_n^{\mathrm{RF}}(\mathbf{p}) \overline{f}_M(p) \tag{B.128}$$

with the normalized Maxwellian distribution (B.118)

$$\overline{f}_M = \frac{1}{(2\pi)^{3/2}} R\left(\beta_{Te}^2\right) \exp\left[-\frac{\left(p_\parallel^2 + p_\perp^2\right)}{(\gamma+1)}\right] \tag{B.129}$$

The diffusion coefficient (B.111) becomes

$$D_n^{\mathrm{RF}}(\mathbf{p}) = D_{n,0}^{\mathrm{RF}} \beta_{Te} \left|\Theta_0^{(n)}\right|^2 \delta\left(1 - \frac{p_\parallel}{\gamma}\beta_{Te}N_{0\parallel} - \frac{y_n}{\gamma}\right) \tag{B.130}$$

with (B.114), (5.21), (B.117)

$$\begin{aligned} \Theta_0^{(n)} &= \frac{J_n(z)}{N_{0\perp}\beta_{Te}p_\perp}\left[y_n + N_{0\parallel}\beta_{Te}p_\parallel\right] \\ z &= N_{0\perp}\frac{\omega_0}{\omega_{ce}}p_\perp\beta_{Te} \\ \gamma &= \sqrt{1 + \left(p_\parallel^2 + p_\perp^2\right)\beta_{Te}^2} \end{aligned} \tag{B.131}$$

**Expression with EBW polarization**

We can transform

$$\delta\left(1 - \frac{p_\parallel}{\gamma}\beta_{Te}N_{0\parallel} - \frac{y_n}{\gamma}\right) = \frac{\gamma}{\left|N_{0\parallel}\right|\beta_{Te}}\delta\left(p_\parallel - p_n - \frac{[\gamma-1]}{\beta_{Te}N_{0\parallel}}\right) \tag{B.132}$$

with the definition (5.13)

$$p_n = \frac{(1-y_n)}{\beta_{Te}N_{0\parallel}} \tag{B.133}$$

so that, inserting (B.130) and (B.131), (B.128) becomes

$$P_{\mathrm{abs},n}^{\mathrm{RF},M} = 2\pi \frac{n_e D_{n,0}^{\mathrm{RF}}}{m_e N_{0\perp}^2 \beta_{Te}^2 \left|N_{0\|}\right|} \times \int_0^{\infty} p_\perp dp_\perp \int_{-\infty}^{+\infty} dp_\| \, \frac{1}{\gamma} J_n^2(z) \left[y_n + N_{0\|}\beta_{Te} p_\|\right]^2 \delta\left(p_\| - p_n - \frac{[\gamma - 1]}{\beta_{Te} N_{0\|}}\right) \overline{f}_M \tag{B.134}$$

The integration cannot be performed exactly because dependence upon $(p_\|, p_\perp)$ in the relativistic factor $\gamma$. However, it is possible to obtain approximate analytical expressions in the non- and weakly relativistic limits.

### Non-relativistic limit

To obtain an expression for the density of power absorbed in the non-relativistic limit, we simply need to take the limit $\gamma \to 1$ in the expression (B.134), which gives

$$P_{\mathrm{abs},n}^{\mathrm{RF},M\mathrm{nr}} = 2\pi \frac{n_e D_{n,0}^{\mathrm{RF}}}{m_e N_{0\perp}^2 \beta_{Te}^2 \left|N_{0\|}\right|} \int_0^{\infty} dp_\perp \, p_\perp \int_{-\infty}^{+\infty} dp_\| J_n^2(z) \left[y_n + N_{0\|}\beta_{Te} p_\|\right]^2 \delta\left(p_\| - p_n\right) \overline{f}_{M\mathrm{nr}} \tag{B.135}$$

where the non-relativistic Maxwellian is derived from (B.129)

$$\overline{f}_{M\mathrm{nr}} = \frac{1}{(2\pi)^{3/2}} \exp\left[-\frac{\left(p_\|^2 + p_\perp^2\right)}{2}\right] \tag{B.136}$$

The integration in $p_\|$ is straightforward, using the resonance condition

$$P_{\mathrm{abs},n}^{\mathrm{RF},M\mathrm{nr}} = \frac{1}{\sqrt{2\pi}} \frac{n_e D_{n,0}^{\mathrm{RF}}}{m_e N_{0\perp}^2 \beta_{Te}^2 \left|N_{0\|}\right|} \exp\left[-\frac{p_n^2}{2}\right] \int_0^{\infty} dp_\perp \, p_\perp J_n^2(z) \exp\left[-\frac{p_\perp^2}{2}\right] \tag{B.137}$$

where we used

$$y_n + N_{0\|}\beta_{Te} p_n = 1 \tag{B.138}$$

The integration in $p_\perp$ is performed using the identity [[59]]

$$\int_0^{\infty} dw \, w J_n^2(aw) \exp\left[-bw^2\right] = \frac{1}{2b} \exp\left[-\frac{a^2}{2b}\right] I_n\left(\frac{a^2}{2b}\right) \tag{B.139}$$

which gives

$$\int_0^\infty dp_\perp \, p_\perp J_n^2 \left( N_{0\perp} \beta_{Te} \frac{\omega_0}{\omega_{ce}} p_\perp \right) \exp\left[ -\frac{p_\perp^2}{2} \right] = \exp\left[ -\lambda_e \right] I_n\left[ \lambda_e \right] \tag{B.140}$$

with

$$\lambda_e = \left( k_{0\perp} \rho_{Te} \right)^2 = \left( N_{0\perp} \beta_{Te} \frac{\omega_0}{\omega_{ce}} \right)^2 \tag{B.141}$$

We get an analytical expression for the density of power absorbed in the non-relativistic limit

$$P_{\mathrm{abs},n}^{\mathrm{RF},M\mathrm{nr}} = \frac{1}{\sqrt{2\pi}} \frac{n_e D_{n,0}^{\mathrm{RF}}}{m_e N_{0\perp}^2 \beta_{Te}^2 \left| N_{0\parallel} \right|} \Gamma_n\left[ \lambda_e \right] \exp\left[ -\frac{p_n^2}{2} \right] \tag{B.142}$$

where

$$\Gamma_n\left[ \lambda_e \right] = \exp\left[ -\lambda_e \right] I_n\left[ \lambda_e \right] \tag{B.143}$$

We recall (B.107)

$$D_{n,0}^{\mathrm{RF}} = \frac{e^2 \pi s_{\mathrm{inc}}}{\varepsilon_0 \omega_0 \left| \Phi_{0\perp} \right| v_{Te}} \tag{B.144}$$

so that

$$P_{\mathrm{abs},n}^{\mathrm{RF},M\mathrm{nr}} = \frac{1}{\sqrt{2\pi}} \frac{1}{N_{0\perp}^2 \beta_{Te}^3 \left| N_{0\parallel} \right|} \frac{\omega_{pe}^2}{\omega_0^2} \frac{\omega_0 \pi}{c} \frac{s_{\mathrm{inc}}}{\left| \Phi_{0\perp} \right|} \Gamma_n\left[ \lambda_e \right] \exp\left[ -\frac{p_n^2}{2} \right] \tag{B.145}$$

where the electron plasma frequency is (2.60)

$$\omega_{pe} = \sqrt{\frac{e^2 n_e}{\varepsilon_0 m_e}} \tag{B.146}$$

**Weakly relativistic limit**

In the weakly limit, we do a Taylor expansion of the gamma relativistic factor for small $\beta_{Te}$

$$\begin{aligned} \gamma &= \sqrt{1 + \left( p_\parallel^2 + p_\perp^2 \right) \beta_{Te}^2} \\ &= 1 + \frac{1}{2} \left( p_\parallel^2 + p_\perp^2 \right) \beta_{Te}^2 + \mathcal{O}\left( \beta_{Te}^4 \right) \end{aligned} \tag{B.147}$$

When considering the expression for the power absorbed (B.134) with the Maxwellian distribution (B.129), we see that relativistic corrections (B.147) will come to the order $\beta_{Te}^2$ everywhere, except in the resonance condition, where the relativistic corrections are of order $\beta_{Te}/N_{0\|}$. Therefore, we only keep relativistic effects in the resonance condition in (B.134), which becomes

$$P_{\mathrm{abs},n}^{\mathrm{RF},M\mathrm{wr}} = 2\pi \frac{n_e D_{n,0}^{\mathrm{RF}}}{m_e N_{0\perp}^2 \beta_{Te}^2 \left|N_{0\|}\right|} \times \int_0^\infty p_\perp dp_\perp \int_{-\infty}^{+\infty} dp_\| \; J_n^2(z) \left[y_n + N_{0\|}\beta_{Te}p_\|\right]^2 \delta\left[p_\| - p_n - \frac{(\gamma-1)}{\beta_{Te}N_\|}\right] \overline{f}_{M\mathrm{nr}} \tag{B.148}$$

where the non-relativistic maxwellian in given by (B.136). This correction of order $\beta_{Te}/N_{0\|}$ can be significant, and corresponds to a relativistic shift of the resonance curve $p_\| = p_n + (\gamma-1)/\beta_{Te}N_{0\|}$ in momentum space, towards higher $p_\|$ when $N_{0\|} > 0$, and towards lower $p_\|$ when $N_{0\|} < 0$. The consequence of this shift is therefore a relativistic increase of the damping for HBF approach, and a relativistic reduction of the damping for LBF approach.

### Case with $\left|N_{0\|}\right| \lesssim \beta_{Te}$

When $N_{0\|} \lesssim \beta_{Te}$, it is not possible to use a perturbative approach in calculating $p_\|$ from the resonance condition. In fact, the existence of resonant electrons imposes a condition on $p_n$. From the resonance condition

$$p_\| = p_n + \frac{(\gamma-1)}{\beta_{Te}N_{0\|}} \tag{B.149}$$

we obtain the same expression as in (5.10) and get a minimal ($p_\perp = 0$) condition for the existence of resonant electrons (5.11)

$$y_n > \sqrt{1 - N_{0\|}^2} \tag{B.150}$$

which affects the LBF approach ($y_n < 1$).

**Case with $|N_{0\|}| \gg \beta_{Te}$**

This inequality is generally valid in EBWCD, where typically $|N_{0\|}| \sim 1$ and $\beta_{Te} \lesssim 0.1$. In that case, to which we restrict ourselves in the remaining of this section, we can calculate $p_\|$ perturbatively from the resonance condition, which gives

$$p_\| = p_n + \frac{\beta_{Te}}{2N_{0\|}}\left(p_n^2 + p_\perp^2\right) + \mathcal{O}\left(\beta_{Te}^3/\left|N_{0\|}\right|\right) \tag{B.151}$$

**Resonance in $|p_\|| \gg p_\perp$ limit**

In order to obtain an analytical expression for the density of power absorbed in the weakly relativistic limit, we have to neglect the relativistic corrections involving $p_\perp$, meaning that we assume that resonant electrons satisfy $|p_\|| \gg p_\perp$. This approximation is very good in the LBF approach, as we saw in section 5.3, but not in the HBF approach where we have typically $|p_\|| \sim p_\perp$. Dropping $p_\perp$ terms in the relativistic correction means that we neglect the curvature of the resonance line.

Then, in the limit $|p_\|| \gg p_\perp$ the approximate resonance condition in the weakly relativistic limit (B.151) gives simply

$$p_\| \simeq p_n\left(1 + \frac{\beta_{Te}p_n}{2N_{0\|}}\right) = p_n\left(1 + \frac{[1-y_n]}{2N_{0\|}^2}\right) \tag{B.152}$$

where we observe that the weakly relativistic correction are independent of $\beta_{Te}$.

Using the resonance condition, the integration in $p_\|$ gives

$$P_{\mathrm{abs},n}^{\mathrm{RF},M\mathrm{wr}} = \frac{1}{\sqrt{2\pi}}\frac{n_e D_{n,0}^{\mathrm{RF}}}{m_e N_{0\perp}^2 \beta_{Te}^2 \left|N_{0\|}\right|}\left[y_n + N_{0\|}\beta_{Te}p_n\right]^2 \times \exp\left[-\frac{1}{2}\left(p_n\left[1 + \frac{(1-y_n)}{2N_{0\|}^2}\right]\right)^2\right]\int_0^\infty p_\perp dp_\perp\, J_n^2(z)\exp\left[-\frac{p_\perp^2}{2}\right] \tag{B.153}$$

where the weakly relativistic correction (B.152) was not kept in the $y_n + N_{0\|}\beta_{Te}p_\|$ term because $N_{0\|}\beta_{Te}p_\|$ is itself a corrective term. The integral over $p_\perp$ is done in

(B.140), giving

$$P_{\mathrm{abs},n}^{\mathrm{RF},M\mathrm{wr}} = \frac{1}{\sqrt{2\pi}} \frac{n_e D_{n,0}^{\mathrm{RF}}}{m_e N_{0\perp}^2 \beta_{Te}^2 \left|N_{0\parallel}\right|} \Gamma_n\left[\lambda_e\right] \exp\left[-\frac{1}{2}\left(p_n\left[1+\frac{(1-y_n)}{2N_{0\parallel}^2}\right]\right)^2\right] \tag{B.154}$$

where we used (B.138). We recall (B.107)

$$D_{n,0}^{\mathrm{RF}} = \frac{e^2 \pi s}{\varepsilon_0 \omega_0 \left|\Phi_{0\perp}\right| v_{Te}} \tag{B.155}$$

so that the weakly relativistic density of power absorbed becomes

$$P_{\mathrm{abs},n}^{\mathrm{RF},M\mathrm{wr}} = \frac{1}{\sqrt{2\pi}} \frac{1}{N_{0\perp}^2 \beta_{Te}^3 \left|N_{0\parallel}\right|} \frac{\omega_{pe}^2}{\omega^2} \frac{\omega\pi}{c} \frac{s_{\mathrm{inc}}}{\left|\Phi_{0\perp}\right|} \Gamma_n\left[\lambda_e\right] \exp\left[-\frac{1}{2}\left(p_n\left[1+\frac{(1-y_n)}{2N_{0\parallel}^2}\right]\right)^2\right] \tag{B.156}$$

### B.4.4 Absorption coefficient

The absorption coefficient defined in (2.50) is expressed here as a function of power absorbed related to the RF quasilinear operator, which for the $n^{\mathrm{th}}$ harmonic contribution gives

$$\alpha_n^{\mathrm{RF}} = \frac{P_{\mathrm{abs},n}^{\mathrm{RF}}}{\|\mathbf{s}_0\|} \tag{B.157}$$

where $\|\mathbf{s}_0\|$ is the energy density flow, which is directed along $\mathbf{\Phi}_0$ (2.36) such that

$$\frac{s_{\mathrm{inc}}}{\|\mathbf{s}_0\|} = \frac{\left|\Phi_{0\perp}\right|}{\Phi_0} \tag{B.158}$$

and we find

$$\alpha_n^{\mathrm{RF}} = \frac{P_{\mathrm{abs},n}^{\mathrm{RF}}}{s_{\mathrm{inc}}} \frac{\left|\Phi_{0\perp}\right|}{\Phi_0} \tag{B.159}$$

In the linear limit where the distribution function is a Maxwellian, we find, using (B.145) and (B.156):

- In the non-relativistic limit

$$\alpha_n^{\mathrm{RF},M\mathrm{nr}} = \frac{1}{\sqrt{2\pi}}\frac{\omega_0\pi}{c}\frac{\omega_{pe}^2}{\omega_0^2}\frac{1}{N_{0\perp}^2\beta_{Te}^3\left|N_{0\|}\right|\Phi_0}\Gamma_n\left[\lambda_e\right]\exp\left[-\frac{p_n^2}{2}\right] \tag{B.160}$$

$$= \frac{1}{\sqrt{2\pi}}\frac{\omega_0\pi}{c}\frac{\omega_{pe}^2}{\omega_{ce}^2}\frac{1}{\beta_{Te}\left|N_{0\|}\right|\Phi_0}\frac{\Gamma_n\left[\lambda_e\right]}{\lambda_e}\exp\left[-\frac{p_n^2}{2}\right] \tag{B.161}$$

- and in the weakly relativistic limit

$$\alpha_n^{\mathrm{RF},M\mathrm{wr}} = \frac{1}{\sqrt{2\pi}}\frac{\omega_0\pi}{c}\frac{\omega_{pe}^2}{\omega_0^2}\frac{1}{N_{0\perp}^2\beta_{Te}^3\left|N_{0\|}\right|\Phi_0}\Gamma_n\left[\lambda_e\right]\exp\left[-\frac{1}{2}\left(p_n\left[1+\frac{(1-y_n)}{2N_{0\|}^2}\right]\right)^2\right] \tag{B.162}$$

$$= \frac{1}{\sqrt{2\pi}}\frac{\omega_0\pi}{c}\frac{\omega_{pe}^2}{\omega_{ce}^2}\frac{1}{\beta_{Te}\left|N_{0\|}\right|\Phi_0}\frac{\Gamma_n\left[\lambda_e\right]}{\lambda_e}\exp\left[-\frac{1}{2}\left(p_n\left[1+\frac{(1-y_n)}{2N_{0\|}^2}\right]\right)^2\right] \tag{B.163}$$

where we recall (2.108) (B.115)

$$\begin{aligned} y_n &= \frac{n\omega_{ce}}{\omega_0} \\ p_n &= \frac{(1-y_n)}{\beta_{Te}N_{0\|}} \end{aligned} \tag{B.164}$$

### B.4.5 Power deposition profile

#### Evolution of the incident power density

In our slab geometry, we consider the case of a EBW propagating towards the $n^{\mathrm{th}}$ cyclotron harmonic resonance where it is completely damped. The magnetic field variations are assumed to be monotonic and increasing in the positive $\widehat{\mathbf{x}}$ direction, and the $n^{\mathrm{th}}$ cyclotron harmonic resonance is located at $x = 0$.

Assuming that harmonics do not overlap, so that we can consider separately the damping near harmonic $n$, the energy equation (2.21) gives, in steady-state and in slab geometry

$$\frac{ds_{0x}}{dx} = -\sigma P_{\mathrm{abs},n}^{\mathrm{RF}} \tag{B.165}$$

where $s_{0x} = s_{\text{inc}}$ and $\sigma = +1$ for low $B$-field approach (LBF) where $x < 0$ and is increasing towards resonance, and $\sigma = -1$ for high $B$-field approach (HBF) where $x > 0$ and is decreasing towards resonance. Introducing the absorption coefficient (B.159), we get

$$\frac{ds_{\text{inc}}}{dx} = -\sigma \frac{\Phi_0}{|\Phi_{0\perp}|} \alpha_n^{\text{RF}} s_{\text{inc}} \tag{B.166}$$

We assume that the wave propagates towards the $n^{\text{th}}$ harmonic resonance from a position $x_0$ (negative for LBF approach, positive for HBF approach) where the initial incident power density is $s_{\text{inc},0}$. The evolution of the incident power density is then

$$s_{\text{inc}}(x) = s_{\text{inc},0} e^{-\int_{x_0}^{x} \sigma \frac{\Phi_0}{|\Phi_{0\perp}|} \alpha_n^{\text{RF}} dx} \tag{B.167}$$

### Narrow damping region approximation

The damping region is assumed to be sufficiently narrow as compared to plasma non-uniformity scalelength $L$, such that the plasma properties such that temperature and density can be considered as being uniform across that damping region. In addition, we assume that wave propagation characteristics such as the perpendicular wave vector $k_{0\perp}$, the polarization vector $\mathbf{e}_0$, and the power flow $\mathbf{\Phi}_0$ are also constant across the damping region. This assumption may seem questionable with regards to the rapid changes in these wave characteristics near cyclotron resonances, as a function of $y_n = n\omega_{ce}/\omega$, as demonstrated in Section 2.3 from solving the local dispersion relation. However, it will turn out that the power deposition profile is rather insensitive to the typical variations of the wave parameters across the damping region.

Indeed, the variations in the absorption coefficient $\alpha_n^{\text{RF}}$ are dominated by the exponential term in (B.160) and (B.162), which is expressed as (B.133) $p_n = (1 - y_n)/\beta_{Te} N_{0\|}$. The relative variations of $p_n$ are mostly sensitive to the variations of the magnetic field, because $p_n$ depends upon the difference $(1 - y_n)$ in the vicinity of $y_n \simeq 1$. It is therefore justified to take all parameters constant in the damping region except $y_n$.

We can define the magnetic field amplitude variations scalelength $L_B > 0$ such

that

$$\frac{dB}{dx} = \frac{B}{L_B(x)} \tag{B.168}$$

Near the damping region, the variations of $B$ are assumed to be apprximately linear so that $L_B$ is a constant. We can rewrite the power deposition profile (B.166) as

$$\frac{ds_{\text{inc}}}{dy_n} = -\sigma L_B \frac{\Phi_0}{|\Phi_{0\perp}|} \alpha_n^{\text{RF}}(y_n)\, s_{\text{inc}}(y_n) \tag{B.169}$$

where we used $y_n = enB/(m_e\omega_0) \simeq 1$. With the following identity, obtained from (B.133)

$$dp_n = -\frac{dy_n}{\beta_{Te} N_{0\parallel}} \tag{B.170}$$

we can rewrite (B.169) as

$$\frac{ds_{\text{inc}}}{dp_n} = \sigma L_B \beta_{Te} N_{0\parallel} \frac{\Phi_0}{|\Phi_{0\perp}|} \alpha_n^{\text{RF}}(y_n)\, s_{\text{inc}}(y_n) \tag{B.171}$$

The peak $p_n^{\text{m}}$ in the profile is then given by

$$\left.\frac{d^2 s_{\text{inc}}}{dp_n^2}\right|_{p_n = p_n^{\text{m}}} = 0 \tag{B.172}$$

which leads to

$$\begin{aligned}\left.\frac{d\alpha_n^{\text{RF}}}{dp_n}\right|_{p_n=p_n^{\text{m}}} s_{\text{inc}}(p_n^{\text{m}}) &= -\alpha_n(p_n^{\text{m}}) \left.\frac{ds_{\text{inc}}}{dp_n}\right|_{p_n=p_n^{\text{m}}} \\ &= -\sigma L_B \beta_{Te} N_{0\parallel} \frac{\Phi_0}{|\Phi_{0\perp}|} \left[\alpha_n^{\text{RF}}(p_n^{\text{m}})\right]^2 s_{\text{inc}}(p_n^{\text{m}})\end{aligned} \tag{B.173}$$

such that the location $p_n^{\text{m}}$ of the peak in power deposition profile is given by

$$\left[\frac{d\alpha_n^{\text{RF}}}{dp_n} + \sigma L_B \beta_{Te} N_{0\parallel} \frac{\Phi_0}{|\Phi_{0\perp}|} \left(\alpha_n^{\text{RF}}\right)^2\right]_{p_n=p_n^{\text{m}}} = 0 \tag{B.174}$$

### Linear non-relativistic limit

In the linear limit without relativistic effects, the absorption coefficient is given by (B.160)

$$\alpha_n^{\mathrm{RF},M\mathrm{nr}}(p_n) = \alpha_{0,n} \exp\left[-\frac{p_n^2}{2}\right] \tag{B.175}$$

where we define the coefficient

$$\alpha_{0,n} = \frac{1}{\sqrt{2\pi}} \frac{\omega_0 \pi}{c} \frac{\omega_{pe}^2}{\omega_{ce}^2} \frac{1}{\beta_{Te} \left|N_{0\|}\right| \Phi_0} \frac{\Gamma_n\left[\lambda_e\right]}{\lambda_e} \tag{B.176}$$

which is assumed to be constant across the resonance region. We find

$$\frac{d\alpha_n^{\mathrm{RF},M\mathrm{nr}}}{dp_n} = -\alpha_n^{\mathrm{RF},M\mathrm{nr}} p_n \tag{B.177}$$

which is inserted in (B.174), so that we get an equation for $p_n^{\mathrm{m},M\mathrm{nr}}$ in the non-relativistic limit

$$\left|p_n^{\mathrm{m},M\mathrm{nr}}\right| = p_{0,n} \exp\left[-\frac{\left|p_n^{\mathrm{m},M\mathrm{nr}}\right|^2}{2}\right] \tag{B.178}$$

where we keep in mind that $p_n^{\mathrm{m},M\mathrm{nr}}$ is of the same sign as $\sigma N_{\|}$ for either HBF or LBF approach, and where we defined the dimensionless parameter

$$\begin{aligned} p_{0,n} &\equiv L_B \beta_{Te} \left|N_{0\|}\right| \frac{\Phi_0}{\left|\Phi_{0\perp}\right|} \alpha_{0,n} \\ &= \frac{1}{\sqrt{2\pi}} \frac{\omega_0 \pi}{c} \frac{\omega_{pe}^2}{\omega_{ce}^2} \frac{L_B}{\left|\Phi_{0\perp}\right|} \frac{\Gamma_n\left[\lambda_e\right]}{\lambda_e} \end{aligned} \tag{B.179}$$

### Linear weakly relativistic limit

In the linear limit with weakly relativistic effects, the absorption coefficient is given by (B.160)

$$\alpha_n^{\mathrm{RF},M\mathrm{wr}}(p_n) = \alpha_{0,n} \exp\left[-\frac{1}{2}\left(p_n\left[1 + \frac{\beta_{Te} p_n}{2N_{\|}}\right]\right)^2\right] \tag{B.180}$$

so that

$$\frac{d\alpha_n^{\mathrm{RF},M\mathrm{wr}}}{dp_n} \simeq -\alpha_n^{\mathrm{RF},M\mathrm{wr}} p_n \tag{B.181}$$

where the weakly relativistic correction is dropped in the terms outside the exponential, consistently with our narrow damping region approximation. Inserting in (B.174), we get an equation for $p_n^{\mathrm{m},M\mathrm{wr}}$ in the weakly relativistic limit

$$\left|p_n^{\mathrm{m},M\mathrm{wr}}\right| = p_{0,n} \exp\left[-\frac{1}{2}\left(p_n^{\mathrm{m},M\mathrm{wr}}\left[1+\frac{\beta_{Te} p_n^{\mathrm{m},M\mathrm{wr}}}{2N_{\|}}\right]\right)^2\right] \tag{B.182}$$

where we keep in mind that $p_n^{\mathrm{m},M\mathrm{nr}}$ is of the same sign as $\sigma N_{\|}$ for either HBF or LBF approach, so that we get

$$\left|p_n^{\mathrm{m},M\mathrm{wr}}\right| = p_{0,n} \exp\left[-\frac{1}{2}\left(\left|p_n^{\mathrm{m},M\mathrm{wr}}\right|\left[1+\frac{\sigma\beta_{Te}\left|p_n^{\mathrm{m},M\mathrm{wr}}\right|}{2\left|N_{\|}\right|}\right]\right)^2\right] \tag{B.183}$$

# Appendix C

# Differential Operator in the *DKE* code

In the *DKE* code, the differential operators in the kinetic equations (3.118-3.122) are bounce-averaged and solved as a function of $(p, \xi_0)$, where the pitch-angle coordinate $\xi_0$ represents the value of $\xi$ as the electron passes through the point of minimum $B$-field on a given flux-surface $\psi$. For the sake of readability, we will omit the superscripts $^{(0)}$ and subscripts $_0$ refering to bounce-averaged quantities in this chapter, keeping in mind that all operators are assumed to apply to the $(p, \xi_0)$ space and all fields are bounce-averaged. More explicitly, one can refer to the notation equivalence prescribed in (4.1):

$$\begin{aligned} \xi_0 &\longleftrightarrow \xi \\ f_0^{(0)} &\longleftrightarrow f_0 \\ g^{(0)} &\longleftrightarrow g \\ \widetilde{f}^{(0)} &\longleftrightarrow \widetilde{f} \\ \mathbf{S}_\mathbf{p}^{(0)} &\longleftrightarrow \mathbf{S}_\mathbf{p} \\ \mathbb{D}_\mathbf{p}^{(0)} &\longleftrightarrow \mathbb{D}_\mathbf{p} \\ \mathbf{F}_\mathbf{p}^{(0)} &\longleftrightarrow \mathbf{F}_\mathbf{p} \end{aligned} \tag{C.1}$$

We need to calculate the momentum space differential operators (4.2) corresponding to the fluxes $\mathbf{S}_\mathbf{p}(f_0, \mathbb{D}_\mathbf{p}, \mathbf{F}_\mathbf{p})$, $\mathbf{S}_\mathbf{p}(g, \mathbb{D}_\mathbf{p}, \mathbf{F}_\mathbf{p})$ and $\mathbf{S}_\mathbf{p}\left(\widetilde{f}, \widetilde{\mathbb{D}}_\mathbf{p}, \widetilde{\mathbf{F}}_\mathbf{p}\right)$. On a given flux-

surface $\psi_l$ at time $t_k$ (the field dependence upon $l$ and $k$ will be kept implicit in this chapter), the operator associated with the diffusion tensor $\mathbb{D}_{\mathbf{p}}$ and the convector vector $\mathbf{F}_{\mathbf{p}}$ and acting on the distribution function $f$ is discretized according to this operator is expressed as (4.23)

$$p^2 \nabla_{\mathbf{p}} \cdot \mathbf{S}_{\mathbf{p}}\big|_{i+1/2,j+1/2} = \sum_{i'=i-1}^{i'=i+1} \sum_{j'=j-1}^{j'=j+1} M_{i'+1/2,j'+1/2} f_{i'+1/2,j'+1/2} \tag{C.2}$$

Using the operator differentiation scheme (4.23) with (4.24), the flux decomposition (4.25), the gradient differentiation schemes (4.26) and (4.29) and the interpolation scheme (4.32), the elements $M_{i'+1/2,j'+1/2}$ are given by

$$\begin{aligned} M_{i'+3/2,j'+3/2} = & \frac{p_{i+1}}{\Delta p_{i+1/2}} \frac{\sqrt{1-\xi_{j+1/2}^2}}{\Delta \xi_{j+1} + \Delta \xi_j} D_{p\xi,i+1,j+1/2} \left(1 - \delta_{p,i+1,j+3/2}\right) \\ & + \frac{\lambda_{j+1}}{\lambda_{j+1/2}} \frac{p_{i+1/2}}{\Delta p_{i+1} + \Delta p_i} \frac{\sqrt{1-\xi_{j+1}^2}}{\Delta \xi_{j+1/2}} D_{\xi p,i+1/2,j+1} \left(1 - \delta_{\xi,i+3/2,j+1}\right) \end{aligned} \tag{C.3}$$

$$\begin{aligned} M_{i'+1/2,j'+3/2} = & -\frac{\lambda_{j+1}}{\lambda_{j+1/2}} \frac{\left(1-\xi_{j+1}^2\right)}{\Delta \xi_{j+1/2} \Delta \xi_{j+1}} D_{\xi\xi,i+1/2,j+1} \\ & + \frac{p_{i+1}}{\Delta p_{i+1/2}} \frac{\sqrt{1-\xi_{j+1/2}^2}}{\Delta \xi_{j+1} + \Delta \xi_j} D_{p\xi,i+1,j+1/2} \delta_{p,i+1,j+3/2} \\ & - \frac{p_i}{\Delta p_{i+1/2}} \frac{\sqrt{1-\xi_{j+1/2}^2}}{\Delta \xi_{j+1} + \Delta \xi_j} D_{p\xi,i,j+1/2} \left(1 - \delta_{p,i,j+3/2}\right) \\ & - \frac{\lambda_{j+1}}{\lambda_{j+1/2}} \frac{p_{i+1/2}\sqrt{1-\xi_{j+1}^2}}{\Delta \xi_{j+1/2}} F_{\xi,i+1/2,j+1} \left(1 - \delta_{\xi,i+1/2,j+1}\right) \end{aligned} \tag{C.4}$$

$$\begin{aligned} M_{i'-1/2,j'+3/2} = & -\frac{p_i}{\Delta p_{i+1/2}} \frac{\sqrt{1-\xi_{j+1/2}^2}}{\Delta \xi_{j+1} + \Delta \xi_j} D_{p\xi,i,j+1/2} \delta_{p,i,j+3/2} \\ & - \frac{\lambda_{j+1}}{\lambda_{j+1/2}} \frac{p_{i+1/2}}{\Delta p_{i+1} + \Delta p_i} \frac{\sqrt{1-\xi_{j+1}^2}}{\Delta \xi_{j+1/2}} D_{\xi p,i+1/2,j+1} \left(1 - \delta_{\xi,i-1/2,j+1}\right) \end{aligned} \tag{C.5}$$

$$
\begin{aligned}
M_{i'+3/2,j'+1/2} = & -\frac{p_{i+1}^2}{\Delta p_{i+1/2}\Delta p_{i+1}} D_{pp,i+1,j+1/2} \\
& + \frac{p_{i+1}^2}{\Delta p_{i+1/2}} F_{p,i+1,j+1/2}\left(1-\delta_{p,i+1,j+1/2}\right) \\
& + \frac{\lambda_{j+1}}{\lambda_{j+1/2}} \frac{p_{i+1/2}}{\Delta p_{i+1}+\Delta p_i} \frac{\sqrt{1-\xi_{j+1}^2}}{\Delta \xi_{j+1/2}} D_{\xi p,i+1/2,j+1}\delta_{\xi,i+3/2,j+1} \\
& - \frac{\lambda_j}{\lambda_{j+1/2}} \frac{p_{i+1/2}}{\Delta p_{i+1}+\Delta p_i} \frac{\sqrt{1-\xi_j^2}}{\Delta \xi_{j+1/2}} D_{\xi p,i+1/2,j}\left(1-\delta_{\xi,i+3/2,j}\right)
\end{aligned} \tag{C.6}
$$

$$
\begin{aligned}
M_{i'+1/2,j'+1/2} = & \frac{p_{i+1}^2}{\Delta p_{i+1/2}\Delta p_{i+1}} D_{pp,i+1,j+1/2} \\
& + \frac{p_i^2}{\Delta p_{i+1/2}\Delta p_i} D_{pp,i,j+1/2} \\
& + \frac{\lambda_{j+1}}{\lambda_{j+1/2}} \frac{\left(1-\xi_{j+1}^2\right)}{\Delta \xi_{j+1/2}\Delta \xi_{j+1}} D_{\xi\xi,i+1/2,j+1} \\
& + \frac{\lambda_j}{\lambda_{j+1/2}} \frac{\left(1-\xi_j^2\right)}{\Delta \xi_{j+1/2}\Delta \xi_j} D_{\xi\xi,i+1/2,j} \\
& + \frac{p_{i+1}^2}{\Delta p_{i+1/2}} F_{p,i+1,j+1/2}\delta_{p,i+1,j+1/2} \\
& - \frac{p_i^2}{\Delta p_{i+1/2}} F_{p,i,j+1/2}\left(1-\delta_{p,i,j+1/2}\right) \\
& - \frac{\lambda_{j+1}}{\lambda_{j+1/2}} \frac{p_{i+1/2}\sqrt{1-\xi_{j+1}^2}}{\Delta \xi_{j+1/2}} F_{\xi,i+1/2,j+1}\delta_{\xi,i+1/2,j+1} \\
& + \frac{\lambda_j}{\lambda_{j+1/2}} \frac{p_{i+1/2}\sqrt{1-\xi_j^2}}{\Delta \xi_{j+1/2}} F_{\xi,i+1/2,j}\left(1-\delta_{\xi,i+1/2,j}\right)
\end{aligned} \tag{C.7}
$$

$$
\begin{aligned}
M_{i'-1/2,j'+1/2} = & -\frac{p_i^2}{\Delta p_{i+1/2}\Delta p_i} D_{pp,i,j+1/2} \\
& - \frac{p_i^2}{\Delta p_{i+1/2}} F_{p,i,j+1/2}\delta_{p,i,j+1/2} \\
& - \frac{\lambda_{j+1}}{\lambda_{j+1/2}} \frac{p_{i+1/2}}{\Delta p_{i+1} + \Delta p_i} \frac{\sqrt{1-\xi_{j+1}^2}}{\Delta \xi_{j+1/2}} D_{\xi p,i+1/2,j+1}\delta_{\xi,i-1/2,j+1} \\
& + \frac{\lambda_j}{\lambda_{j+1/2}} \frac{p_{i+1/2}}{\Delta p_{i+1} + \Delta p_i} \frac{\sqrt{1-\xi_j^2}}{\Delta \xi_{j+1/2}} D_{\xi p,i+1/2,j} \left(1 - \delta_{\xi,i-1/2,j}\right)
\end{aligned} \tag{C.8}
$$

$$
\begin{aligned}
M_{i'+3/2,j-1/2} = & -\frac{p_{i+1}}{\Delta p_{i+1/2}} \frac{\sqrt{1-\xi_{j+1/2}^2}}{\Delta \xi_{j+1} + \Delta \xi_j} D_{p\xi,i+1,j+1/2} \left(1 - \delta_{p,i+1,j-1/2}\right) \\
& - \frac{\lambda_j}{\lambda_{j+1/2}} \frac{p_{i+1/2}}{\Delta p_{i+1} + \Delta p_i} \frac{\sqrt{1-\xi_j^2}}{\Delta \xi_{j+1/2}} D_{\xi p,i+1/2,j}\delta_{\xi,i+3/2,j}
\end{aligned} \tag{C.9}
$$

$$
\begin{aligned}
M_{i'+1/2,j-1/2} = & -\frac{\lambda_j}{\lambda_{j+1/2}} \frac{\left(1-\xi_j^2\right)}{\Delta \xi_{j+1/2}\Delta \xi_j} D_{\xi\xi,i+1/2,j} \\
& - \frac{p_{i+1}}{\Delta p_{i+1/2}} \frac{\sqrt{1-\xi_{j+1/2}^2}}{\Delta \xi_{j+1} + \Delta \xi_j} D_{p\xi,i+1,j+1/2}\delta_{p,i+1,j-1/2} \\
& + \frac{p_i}{\Delta p_{i+1/2}} \frac{\sqrt{1-\xi_{j+1/2}^2}}{\Delta \xi_{j+1} + \Delta \xi_j} D_{p\xi,i,j+1/2} \left(1 - \delta_{p,i,j-1/2}\right) \\
& + \frac{\lambda_j}{\lambda_{j+1/2}} \frac{p_{i+1/2}\sqrt{1-\xi_j^2}}{\Delta \xi_{j+1/2}} F_{\xi,i+1/2,j}\delta_{\xi,i+1/2,j}
\end{aligned} \tag{C.10}
$$

$$
\begin{aligned}
M_{i'-1/2,j'-1/2} = & \frac{p_i}{\Delta p_{i+1/2}} \frac{\sqrt{1-\xi_{j+1/2}^2}}{\Delta \xi_{j+1} + \Delta \xi_j} D_{p\xi,i,j+1/2}\delta_{p,i,j-1/2} \\
& + \frac{\lambda_j}{\lambda_{j+1/2}} \frac{p_{i+1/2}}{\Delta p_{i+1} + \Delta p_i} \frac{\sqrt{1-\xi_j^2}}{\Delta \xi_{j+1/2}} D_{\xi p,i+1/2,j}\delta_{\xi,i-1/2,j}
\end{aligned} \tag{C.11}
$$

# Bibliography


[1] I.B. Bernstein. *Phys. Rev.*, 109:10, 1958.

[2] F.W. Crawford, G.S. Kino, and H.H. Weiss. Excitation of cyclotron harmonic resonances in a mercury-vapor discharge. *Phys. Rev. Lett.*, 13(7):229–232, 1964.

[3] K.C. Wu, A.K. Ram, A. Bers, and S.D. Schultz. Coupling to ebw in tokamaks. In *12th Conference on Radio Frequency Power in Plasmas, AIP Conference Proceedings*, pages 207–210, 1997.

[4] A. Bers, S.D. Schultz, and A.K. Ram. Coupling to electron Bernstein waves in tokamaks. In *2nd Europhysics Conference on RF Heating and Current Drive*, pages 237–240, 1998.

[5] R.A. Cairns and C.N. Lashmore-Davies. The prospects for electron Bernstein wave heating of spherical tokamaks. *Phys. Plasmas*, 7(10):4126–4134, 2000.

[6] G. Gantenbein et al. Complete suppression of neoclassical tearing modes with current drive at the electron-cyclotron-resonance frequency in ASDEX upgrade tokamak. *Phys. Rev. Lett.*, 85(6):1242–1245, 2000.

[7] J. Preinhaelter and V. Kopecky. *J. Plasma Phys.*, 10:1, 1973.

[8] A.K. Ram and S.D. Schultz. Excitation, propagation, and damping of electron Bernstein waves in tokamaks. *Phys. Plasmas*, 7(10):4084–4094, 2000.

[9] V. Shevchenko, Y. Baranov, M. OBrien, and A. Saveliev. Generation of noninductive current by electron-Bernstein waves on the COMPASS-D tokamak. *Phys. Rev. Lett.*, 89(26):2650054–2650057, 2002.

[10] H. P. Laqua *et al.* Electron-Bernstein-wave current drive in an overdense plasma at the Wendelstein 7-AS stellarator. *Phys. Rev. Lett.*, 90(7):0750031–0750034, 2003.

[11] C. Forest, P.K. Chattopadhyay, R.W. Harvey, and A.P. Smirnov. Off-midplane launch of electron Bernstein waves for current drive in overdense plasmas. *Phys. Plasmas*, 7(5):1352–1355, 2000.

[12] G. Taylor *et al.* Efficient generation of noninductive, off-axis, ohkawa current, driven by electron bernstein waves in high-$\beta$, spherical torus plasmas. *Phys. Plasmas*, 11(10):4733–4739, 2004.

[13] A.K. Ram, J. Decker, A. Bers, R.A. Cairns, and C.N. Lashmore-Davies. Relativistic effects in heating and current drive by electron Bernstein waves. In *15th Conference on Radio Frequency Power in Plasmas, AIP Conference Proceedings*, volume 694, pages 392–395, 2003.

[14] H. Sugai *et al. J. Phys. Soc. Japan*, 56(11):3779–3782, 1987.

[15] S. Morimoto. *Nucl. Fusion*, 29:1697, 1989.

[16] H.P. Laqua *et al.* Resonant and nonresonant electron cyclotron heating at densities above the plasma cutoff by O-X-B mode conversion at the W7-AS stellarator. *Phys. Rev. Lett.*, 78(18):3467–3470, 1997.

[17] S. Nakajima and H. Abe. Mode-conversion process and overdense-plasma heating in the electron cyclotron range of frequencies. *Phys. Rev. A*, 38(8):4373–4376, 1988.

[18] H. Sugai. Mode conversion and local heating below the second electron cyclotron harmonic. *Phys. Rev. Lett.*, 47(26):1889–1902, 1981.

[19] G. Taylor *et al.* In *12th joint Workshop on ECE and ECH, AIP Conference Proceedings*, page 151, 2002.

[20] C.B. Forest *et al.* In *12th joint Workshop on ECE and ECH, AIP Conference Proceedings*, page 17, 2002.

[21] A. Bers and A.K. Ram. Symmetries in dissipation-free linear mode conversion. *Phys. Lett. A*, 301:442–445, 2002.

[22] A.K. Ram, A. Bers, and C.N. Lashmore-Davies. Emission of electron Bernstein waves in plasmas. *Phys. Plasmas*, 9(2):409–418, 2002.

[23] A. Bers and N.J. Fisch. A steady state toroidal reactor driven by microwave power in the lower-hybrid range of frequencies. In *Third Conference on Radio Frequency Power in Plasmas, AIP Conference Proceedings*, pages E5–1,E5–4, 1978.

[24] N.J. Fisch. Confining a tokamak plasma with RF-driven currents. *Phys. Rev. Lett.*, 41(13):873–876, 1978.

[25] N.J. Fisch and A. Bers. Current generation by high-power RF fields. In *Third Conference on Radio Frequency Power in Plasmas, AIP Conference Proceedings*, pages E6–1,E6–4, 1978.

[26] C.F.F. Karney and N.J. Fisch. Numerical studies of current generation by radio-frequency traveling waves. *Phys. Fluids*, 22(9):1817–1824, 1979.

[27] V. Fuchs et al. A one-dimensional model for lower hybrid current drive including perpendicular dynamics. *Phys. Fluids*, 28(12):3619–3628, 1985.

[28] N.J. Fisch and A.H. Boozer. Creating an asymmetric plasma resistivity with waves. *Phys. Rev. Lett.*, 45(9):720–722, 1980.

[29] T. Ohkawa. Steady-state operation of tokamaks by RF heating. Technical Report 4356.007.001, General Atomic, 1976.

[30] J. Decker, Y. Peysson, A. Bers, and A.K. Ram. Self-consistent ECCD calculations with bootstrap current. *in Proc. EC-12 Conference*, pages 113–118, 2002.

[31] J. Decker. ECCD for advanced tokamak operations; Fisch-Boozer versus Ohkawa methods. In *15th Conference on Radio Frequency Power in Plasmas, AIP Conference Proceedings*, volume 694, pages 447–454, 2003.

[32] S. Schultz. *Lower Hybrid and Electron Cyclotron Current Drive With Bootstrap Current in Tokamaks.* PhD thesis, MIT, 1999.

[33] J. Decker, Y. Peysson, A. Bers, and A.K. Ram. On synergism between boostrap and radio-frequency driven currents. *in Proc. 29th EPS Conference on Plasma Phys. and Cont. Fusion*, pages O–1.05, 2002.

[34] Y. Peysson, J. Decker, A. Bers, and A.K. Ram. Selfconsistent RF driven and bootstrap current. *in Proc. 19th IAEA Fusion Energy Conference*, pages TH/P3–22, 2002.

[35] J. Decker, A. Bers, A.K. Ram, and Y. Peysson. Electron cyclotron current drive by the Ohkawa method in the presence of boostrap current. *in Proc. 30th EPS Conference on Plasma Phys. and Cont. Fusion*, pages P–3.205, 2003.

[36] N.J. Fisch. Theory of current drive in plasmas. *Rev. Mod. Phys.*, 59(1):175–234, 1987.

[37] B.J. Braams and C.F.F Karney. Conductivity of a relativistic plasma. *Phys. Fluids B*, 1(7):1355–1368, 1989.

[38] T.M. Antonsen Jr. and K.R. Chu. Radio frequency current generation by waves in toroidal geometry. *Phys. Fluids*, 25(8):1295–1296, 1982.

[39] R.H. Cohen. Effect of trapped electrons on current drive. *Phys. Fluids*, 30(8):2442–2449, 1987.

[40] R.H. Cohen. Erratum:"effect of trapped electrons on current drive" [phys. fluids 30, 2442 (1987). *Phys. Fluids*, 31(2):2421, 1988.

[41] C.F. Kennel and F. Engelmann. Velocity space diffusion from weak plasma turbulence in a magnetic field. *Phys. Fluids*, 9(12):2377–2387, 1966.

[42] I. Lerche. Quasilinear theory of resonant diffusion in a magneto-active relativistic plasma. *Phys. Fluids*, 11(8):1720–1726, 1968.

[43] H.L. Berk. Derivation of the quasi-linear equation in a magnetic field. *J. Plasma Phys.*, 20(2):205–219, 1977.

[44] I.B. Bernstein and D.C. Baxter. Relativistic theory of electron cyclotron resonance heating. *Phys. Fluids*, 24(1):108–126, 1981.

[45] A.N. Kaufmann. Resonant interactions between particles and normal modes in a cylindrical plasma. *Phys. Fluids*, 14(1):387, 1972.

[46] A.J. Brizard and A.A. Chan. Relativistic bounce-averaged quasilinear diffusion equation for low-frequency electromagnetic fluctuations. *Phys. Plasmas*, 8(11):4762–4771, 2001.

[47] D.D. Kerbel and M.G. McCoy. Kinetic theory and simulation of multispecies plasmas in tokamaks excited with electromagnetic waves in the ion-cyclotron range of frequencies. *Phys. Fluids*, 28(12):3629–3653, 1985.

[48] J. Killeen, *et al. Computational Methods for Kinetic Models of Magnetically Confined Plasmas.* Springer-Verlag, 1986.

[49] R.W. Harvey and M.G. McCoy. The CQL3D Fokker-Planck code. In *IAEA Technical Committee on Advances in Simulation and Modeling of Thermonuclear Plasmas*, page 489, 1993.

[50] C.F.F. Karney and N.J. Fisch. Efficiency of current drive by fast waves. *Phys. Fluids*, 28(1):116–126, 1985.

[51] G. Giruzzi, I. Fidone, and X. Garbet. Kinetic effects of magnetic turbulence in tokamaks. *Nuclear Fusion*, 32(6):1011–1021, 1992.

[52] J.P.S Bizarro and P. Rodrigues. Fast and accurate two dimentional Fokker-Planck calculations in velocity space for RF heating and current drive. *Nuclear Fusion*, 37(11):1509–1513, 1997.

[53] M. Shoucri and I. Shkarofsky. A fast 2D Fokker-Planck solver with synergistic effects. *Comp. Phys. Comm.*, 82:287–305, 1994.

[54] I.P. Shkarofsky and M.M. Shoucri. Modelling of lower hybrid current drive in the presence of spacial radial diffusion. *Nuclear Fusion*, 37(4):539–547, 1997.

[55] Y. Peysson and M. Shoucri. An approximate factorization procedure for solving nine-point elliptic difference equations. application for a fast 2-D relativistic Fokker-Planck solver. *Comp. Phys. Comm.*, 109:55–80, 1998.

[56] C.F.F. Karney. Fokker-Planck and quasilinear codes. *Comp. Phys. Rep*, 4:183–244, 1986.

[57] G. Taylor and C. Kessel. Private communications, 2004.

[58] T.H. Stix. *Waves in Plasmas.* American Institute of Physics, 1992.

[59] M. Brambilla. *Kinetic Theory of Plasma Waves.* Oxford Science Publications, 1998.

[60] A. Bers. Kinetic theory of waves and instabilities in a magnetic field - homogeneous plasmas. MIT Course 6.652 Notes, 2002.

[61] A. Bers. *Plasma Physics - Les Houches*, chapter Linear Waves and Instabilities. Gordon and breach Science Publishers, 1975.

[62] J.D. Huba. *NRL Plasma Formulary.* Naval Research Laboratory.

[63] J. Freidberg. *Ideal Magnetohydrodynamics.* Plenum Press, 1987.

[64] J.D. Meiss R.D. Hazeltine. *Plasma Confinement.* Addison-Wesley Publishing Company, 1991.

[65] T.G. Northrop. *The adiabatic motion of charged particles.* Interscience Publishers, 1963.

[66] T.G. Northrop and J.A. Rome. Extensions of guiding center motion to higher order. *Phys. Fluids*, 21(3):384–389, 1978.

[67] R.G. Littlejohn. Hamiltonian formulation of guiding center motion. *Phys. Fluids*, 24:1730–1749, 1981.

[68] A.J. Brizard. A guiding-center fokker–planck collision operator for nonuniform magnetic fields. *Phys. Plasmas*, 11(9):4429–4438, 2004.

[69] M. N. Rosenbluth, R. D. Hazeltine, and F. L. Hinton. Plasma transport in toroidal confinement systems. *Phys. Fluids*, 15(1):116–140, 1972.

[70] V. Fuchs et al. Diffusion of electrons by coherent wavepackets. *Physica D*, 14:141–160, 1983.

[71] R. Kamendje et al. Modeling of nonlinear electron cyclotron resonance heating and current drive in a tokamak. *Phys. Plasmas*, 12:012502, 2005.

[72] G.R. Smith and A.N. Kaufman. Stochastic acceleration by a single wave in a magnetic field. *Phys. Rev. Lett.*, 34(26):16131616, 1975.

[73] J. Decker and Y. Peysson. Dke: A fast numerical solver for the 3d drift kinetic equation. report EUR-CEA-FC-1736, Euratom-CEA, 2004.

[74] J.S. Chang and G Cooper. A practical difference scheme for fokker-planck equations. *J. Comp. Phys.*, 6(1):1–16, 1970.

[75] M. Abramovitz and I.A. Stegun. *Handbood of mathematical functions.* Dover Publications, 1970.

[76] T.C. Luce. *Electron Cyclotron Current Drive in DIII-D.* Proc. of 13th Topical Conference on RF Power in Plasmas. Stephano Bernabei, editor, Annapolis, MD, 1999.

[77] J. Decker. Synergism of radio-frequency current drive with the bootstrap current. Master's thesis, MIT, Dept of Electrical Engineering and Computer Science, 2002.

[78] Y. Peysson, J. Decker, V. Basiuk, A. Bers, G. Huysmans, and A. K. Ram. Rf current drive in internal transport barrier. In *16th Conference on Radio Frequency Power in Plasmas, AIP Conference Proceedings*, 2005.